The environments of extreme star-forming galaxies across cosmic time

Thomas Cornish

Physics

Department of Physics

Lancaster University

December 3, 2023

A thesis submitted to Lancaster University for the degree of
Doctor of Philosophy in the Faculty of Science and Technology,

Supervised by Dr Julie Wardlow

Abstract

Unravelling the histories of massive elliptical galaxies in the local Universe is a monumental task. In the hierarchical paradigm which appears to govern structure formation in our Universe, these galaxies are thought to have complex histories rich with galaxy mergers. Furthermore, since they tend to reside in regions with high galaxy density such as galaxy clusters, their environments play a significant role in shaping their evolution. Significant progress has been made in recent years toward predicting how these galaxies evolve with cosmic time using both observations and simulations, but a definitive picture is yet to emerge. In this thesis we investigate the evolution of massive ellipticals through the environments of their expected progenitors at $z > 1$. Submillimetre galaxies (SMGs) are the sites of some of the most extreme star-forming activity in the Universe, and represent one such population of candidate progenitors. We thus begin with a wide-field narrowband survey of the environments of three spectroscopically-confirmed SMGs and search for signs of protocluster-like environments via overdensities of Hα and [O III] emitters. We first present the VLT/HAWK-I observations used for this study and the bespoke data reduction pipeline written to process these data. After combining these data with archival observations covering the (observed-frame) UV-to-MIR parts of the spectrum, we fit spectral energy distributions to obtain photometric redshifts for our HAWK-I detections, from which we identify candidate companions for each target SMG and compare their densities with expected values for the coeval blank field. We find that two of the three SMGs reside in galaxy overdensities spanning scales of ~ 4 Mpc, whose present-day mass estimates are consistent with local galaxy clusters; these SMGs therefore reside in potential protoclusters, as expected of the progenitors of local massive ellipticals. The third SMG also resides in an overdensity, but on a smaller physical scale of ~ 1.6 Mpc, with a present-day mass estimate indicative of either a galaxy cluster or a galaxy group. We then use JCMT/SCUBA-2 submillimetre observations from the S2COSMOS survey to measure the density of SMGs in the environments of massive ($M_\star > 10^{11}$ M$_\odot$), radio-quiet ($L_{500\ \mathrm{MHz}} \lesssim 10^{25}$ W Hz^{-1}) galaxies at $z = 1$–3. Observations in this wavelength regime trace dust-obscured star formation, which is expected to contribute significantly to the total star formation at these epochs. By searching for overdensities of SMGs we assess whether these massive radio-quiet galaxies reside in the most massive dark matter halos, as is the case for the radio-loud galaxies of similar mass which are the suspected progenitors of local brightest cluster galaxies (BCGs). SMG number counts reveal no significant overdensities in the environments of massive radio-quiet galaxies relative to blank-field expectations. Tentative signs of weak overdensities are seen on small ($\lesssim 0.5$ Mpc radius) scales when counting peaks in the S2COSMOS SNR map. However our overall results suggest that massive radio-quiet galaxies do not reside in significant SMG overdensities and thus occupy less massive dark matter halos than their radio-loud counterparts. This implies that strong radio emission is intrinsically linked with the density of the surrounding environment. Overall we find that SMGs are good candidates for being a progenitor phase in the formation of local massive early-type galaxies, but massive, high-redshift radio-quiet galaxies likely occupy regions of lower SMG density.

This thesis is dedicated to Slinky the cat, my oldest friend and first stargazing companion. The sky took on a different light after you passed.

Acknowledgements

I would like to begin by thanking my supervisor, Julie Wardlow. At all stages of this PhD it has been abundantly clear that she wants only the best for her students, and I believe that she has been successful in ensuring that for me. This thesis would not have been possible without her guidance and support, and I am grateful to have been her student for these last four years.

My time at Lancaster has been utterly fantastic, and I will miss working with the Astro group immensely. Thank you to every member of the group present during my PhD: John Stott, Isobel Hook, Brooke Simmons, Matt Pitkin, David Sobral, Klaas Wiersema, Young-Lo Kim, Danil Kuzin, Heather Wade, Pascale Desmet, David O'Ryan, Izzy Garland, Jamie Dumayne, Nick Amos, Matthew Chan, Jon Carrick, Sergio Santos, João Calhau, Matt Thorne, Amy Hewitt, Rahul Rana, Harry Stephenson, Andrew Milligan, Aruba Mohammed, Matt Fahey, and eV Day. You all created such a welcoming environment and helped to shape my experience into something truly unforgettable. Leaving this group truly feels like leaving a family.

Thank you to my friend and flatmate Juliane Bjerkan, for making the last four years of living in Lancaster such an enjoyable experience. Even the various lockdowns didn't feel so bad with you as my flatmate.

I also wish to thank my family for their unwavering support, and for always believing in me.

A special thanks is in order for Heather Wade, to whom I owe more than I can say. Despite all the stress that this PhD may have brought, I feel no reservation in saying that it has been the best time of my life because it brought me closer to you.

Finally, I acknowledge funding from Lancaster University and STFC, without which this PhD would not have been possible.

Declaration

This thesis is my own work and no portion of the work referred to in this thesis has been submitted in support of an application for another degree or qualification at this or any other institute of learning.

Chapters 2 and 3 include work that is featured in Cornish et al. (in prep), which is under second review of coauthors before submission to MNRAS. Most of Chapter 4 is part of a Radio Galaxy Environment Reference Survey (RAGERS) paper (Cornish et al., in prep) which is under coauthor review and will be submitted to MNRAS. Appendix A.2 includes a use case submitted for the Atacama Large Aperture Sub-mm/mm Telescope (AtLAST) design study (Cornish, Wardlow & Ramasawmy 2021).

Data Access
Raw data for Chapters 2 and 3 can be accessed from the ESO Science Archive under Program ID: 0103.A-0668(A), PI: Wardlow. The data used in Chapter 4 were previously published in Weaver et al. (2022, ApJS, 258, 11) and Simpson et al. (2019, ApJ, 880, 43) and are available as described in those publications. The Weaver et al. (2022) COSMOS2020 dataset can be directly accessed from this link. SCUBA-2 catalogues are available from VizieR and raw data are available from the JCMT data archive.

“There is nothing like looking, if you want to find something. You certainly usually find something, if you look, but it is not always quite the something you were after.”

— J. R. R. Tolkien (The Hobbit, 1937)

Contents

List of Figures

List of Tables

Relevant Publications by the Author

Chapters 2 and 3

- "An ALMA survey of submillimetre galaxies in the Extended *Chandra* Deep Field South: an unbiased study of SMG environments measured with narrowband imaging"; **Cornish, T.**, Wardlow, J., Wade, H., Sobral, D., Brandt, N., Cox, P., Dannerbauer, H., Decarli, R., Greve, T., Gullberg, B., Knudsen, K., Smail, I., Stott, J., Swinbank, M., Walter, F., van der Werf, P. **(in prep.)**

Chapter 4

- "The Radio Galaxy Environment Reference Survey (RAGERS): a submillimetre study of the environments of massive radio-quiet galaxies at $z = 1$–3"; **Cornish, T.**, Wardlow, J., Greve, T. & the RAGERS collaboration **(in prep.)**

Chapter 5

- "The Atacama Large Aperture Submillimetre Telescope: key science drivers"; Ramasawmy, J. Klaassen, Pamela D., Cicone, C., Mroczkowski, T., Chen, C., **Cornish, T.**, da Cunha, E., Hatziminaoglou, E., Johnstone, D., Liu, D., Perrott, Y., Schimek, A., Stanke, T., Wedemeyer, S., **2022, SPIE Proceedings, 12190, 19**.

Chapter 1

Introduction

1.1 Background Cosmology

Astronomy can be broadly divided into two subdisciplines: astrophysics and cosmology. While astrophysics focuses on applying the laws of physics to explain the nature of celestial objects, cosmology is dedicated to studying the overall nature and origin of the Universe. A symbiosis between these two fields is needed in order to understand the extraterrestrial Universe: astrophysical observations are needed to inform cosmological theories, and cosmological theories are required to explain various aspects of astrophysics.

1.1.1 The ΛCDM model

Modern cosmological models describe a Universe that began in an extremely hot, dense state, and has been expanding and cooling ever since. This 'Big Bang' theory was first proposed by Lemaître (1927), and major evidence in favour of it has been found through measurements of the recessional velocities of galaxies (Hubble 1929; Slipher 1917) and via the detection of the cosmological microwave background (CMB; Penzias & Wilson 1965). The CMB is thought to be the redshifted remnant of radiation emitted at the epoch of 'recombination', which is when the Universe had expanded and cooled sufficiently (from the hot, dense primeval state predicted by the Big Bang model) for free electrons to become bound to protons.

With the Big Bang model widely accepted, a concordance model of cosmology began to form, with evidence of a significant ‘dark’ component mounting over the last few decades. Invisible ‘dark matter’ was proposed as a means of explaining orbital speeds in galaxies and galaxy clusters that were far too high to be constrained by the visible matter in these structures (Rubin et al. 1980; Zwicky 1933; see also §1.2.6 and §1.3.1). Meanwhile ‘dark energy’ was introduced into the models in order to explain the accelerating expansion of the Universe evidenced by supernovae whose brightnesses could not be explained with a constant or slowing expansion rate (Perlmutter et al. 1998; Riess et al. 1998).

Today the ‘Λ Cold Dark Matter’ (ΛCDM) model is the accepted concordance cosmology. In this model the energy density of the Universe is split into four components: matter (m), radiation (γ), curvature (k), and dark energy (Λ). The relative contribution of a given component, i, at a given time can be described using the corresponding density parameter:

$$\Omega_i = \frac{\rho_i}{\rho_c}, \tag{1.1}$$

where ρ_i is the energy density of the component, and ρ_c is the ‘critical density’ required for a geometrically flat universe. The most recent measurements of the present-day density parameters obtained by the Planck Collaboration (2020) are $\Omega_m = 0.3153 \pm 0.0073$, $\Omega_\Lambda = 0.6847 \pm 0.0073$, $\Omega_\gamma \sim 0$ and $\Omega_k \sim 0$. The matter component of the Universe can also be divided into baryonic and dark matter components, whose density parameters are measured to be $\Omega_b = 0.04930 \pm 0.00086$ and $\Omega_c = 0.26447 \pm 0.0058$, respectively (Planck Collaboration 2020). These parameters are consistent with a universe that is geometrically flat and dominated by dark energy and dark matter, with baryonic matter constituting only $\sim$5 percent of the total energy density.

1.1.2 Structure formation in a ΛCDM universe

When viewed at sufficiently large scales, the Universe is homogeneous and isotropic – this is the so-called ‘cosmological principle’, and is a fundamental notion in modern cosmology. However, this is only true on cosmological scales; we know, for instance, that the distribution of galaxies is not uniform across the sky (e.g. Cole et al. 2005). It is now widely accepted that these heterogeneities in the distribution of matter originated as quantum fluctuations in the scalar field that drove inflation, a period of extremely rapid expansion occurring shortly after the Big Bang (e.g. Bardeen et al. 1983; Guth & Pi 1982; Starobinsky 1982). Due to this rapid expansion, the quantum fluctuations were stretched to macroscopic scales, resulting in perturbations in the energy density throughout the Universe spanning various physical scales but with approximately equal amplitudes. These amplitudes are defined via $\delta(\mathbf{x}) = (\rho(\mathbf{x})/\bar{\rho}) - 1$, where $\rho(\mathbf{x})$ is the energy density within a specified region at position $\mathbf{x}$ and $\bar{\rho}$ is the average energy density of the Universe. Following inflation, when the mean density of the Universe was still very high, all density perturbations had amplitudes $\delta \ll 1$. While radiation dominated the energy density of the Universe the amplitudes of these perturbations showed little growth, but once in the matter-dominated era they began to increase linearly with the cosmological scale factor, a. When the amplitude of a given perturbation reaches $\delta \sim 1$ it enters the ‘non-linear regime’, at which point the gravitational potential generated by the matter within the density perturbation is great enough to ‘break away’ from the expansion and collapse in on itself.

The time at which a given density perturbation breaks away from the cosmological expansion of the Universe depends on its physical extent. Perturbations spanning smaller physical scales (and thus generally containing less matter) are the first to overcome the cosmological expansion of the Universe and collapse, and the resultant dark matter halos successively merge together to form larger structures as the Universe evolves (e.g. Davis et al. 1985; Peebles 1982; Press & Schechter 1974).

Cold dark matter is the first to fall into the collapsing density perturbations, settling into virialised[1] halos consisting of particles orbiting common centres of mass. Baryonic matter can only begin to follow the resultant gravitational potential after recombination. In early models of hierarchical structure formation, it was believed that gas accreting onto a dark matter halo is shock heated to the virial temperature of the halo near its virial radius, producing a diffuse halo of hot gas (Cole et al. 2000; Rees & Ostriker 1977; White & Frenk 1991; White & Rees 1978). However, more recent simulations have shown that a second mode of accretion exists by which gas flowing along dark matter filaments is accreted onto the central structure (e.g. a galaxy) without being shock-heated near the virial radius of the halo (e.g. Dekel & Birnboim 2006; Dekel et al. 2009; Faucher-Giguère et al. 2011; Kereš et al. 2005; Ocvirk et al. 2008; van de Voort et al. 2011). This cold mode is thought to dominate in halos below a critical mass of $M_{\rm crit} \sim 10^{12}$ $\mathrm{M}_{\odot}$; halos above this critical mass can undergo both cold and hot modes of accretion, particularly at earlier epochs (e.g. Dekel & Birnboim 2006).

In summary, structure formation in the hierarchical paradigm begins with the collapse of low-mass dark matter halos, which then merge to form halos of progressively greater masses. As these halos grow and accrete gas they can form stars and galaxies, which over time evolve into the Universe we see today.

1.2 Physical properties of galaxies

The Universe has long been known to host a menagerie of galaxies displaying a vast array of properties, and understanding these properties and their evolution throughout the Universe's history is a central focus of extragalactic astronomy. Despite almost a century of progress since Edwin Hubble first settled the Shapley-Curtis debate by concluding that the 'spiral nebulae' seen in the sky were in fact other galaxies (Trimble 1995), our understanding of galaxies and their evolution is still far from complete.

---

[1] The term 'virialised' is used to describe a system of gravitationally interacting particles that has attained stability. According to the virial theorem, a system reaches virialisation when the (time-averaged) magnitude of its total gravitational potential energy is twice that of its total kinetic energy. Related quantities include the 'virial radius' (the radius within which a system obeys the virial theorem) and the 'virial temperature' (the temperature related to the kinetic energy of the system).

Significant advances in astrophysics have been made over the last century, with the advent of increasingly powerful telescopes targeting various regions of the electromagnetic spectrum consistently improving our ability to observationally dissect all things extraterrestrial. Concurrently the vast improvements in computer technology have enabled progressively more detailed interpretations of the physical mechanisms driving the observed properties of galaxies.

In this section I discuss some of the main physical properties of galaxies in the local Universe and the imprints they have on the galaxy spectral energy distribution (SEDs), as well as how these properties are known to evolve with time.

1.2.1 Morphologies

In the early 20th century Hubble attempted to categorise galaxies in the local Universe according to their morphology, in what has since become known as the 'Hubble sequence' or the 'Hubble tuning fork' (Hubble 1926; see Figure 1.1). In the Hubble sequence, galaxies are broadly split into elliptical galaxies (denoted 'E') and spiral galaxies (denoted 'S'), with the latter forking into two branches depending on the presence of a bar in its structure. Connecting the elliptical and spiral branches are lenticular galaxies (denoted 'S0'), which comprise a central bulgy component surrounded by a disk, but without any trace of spiral structure within the disk. Elliptical and lenticular galaxies are collectively known as 'early-type' galaxies; spiral galaxies are described as 'late-type'. Finally, galaxies with morphologies not befitting any of these categories are called 'irregular'.

Hubble further subcategorised galaxies along each branch of the tuning fork, as shown in Figure 1.1. Elliptical galaxies are split into eight subcategories according to their apparent ellipticity, ranging from E0 (spherical) to E7 (the highest known ellipticity). Spiral galaxies (barred and unbarred) are similarly divided into subcategories ranging from 'a' to 'd' depending on the tightness of their spiral arms, with 'a' being designated to spirals with the most tightly wound arms. Hubble even split the irregular galaxies into two groups: 'Irr-I' describes irregular galaxies with some semblance of spiral structure, while 'Irr-II' is used for galaxies with no discernibly organised structure.

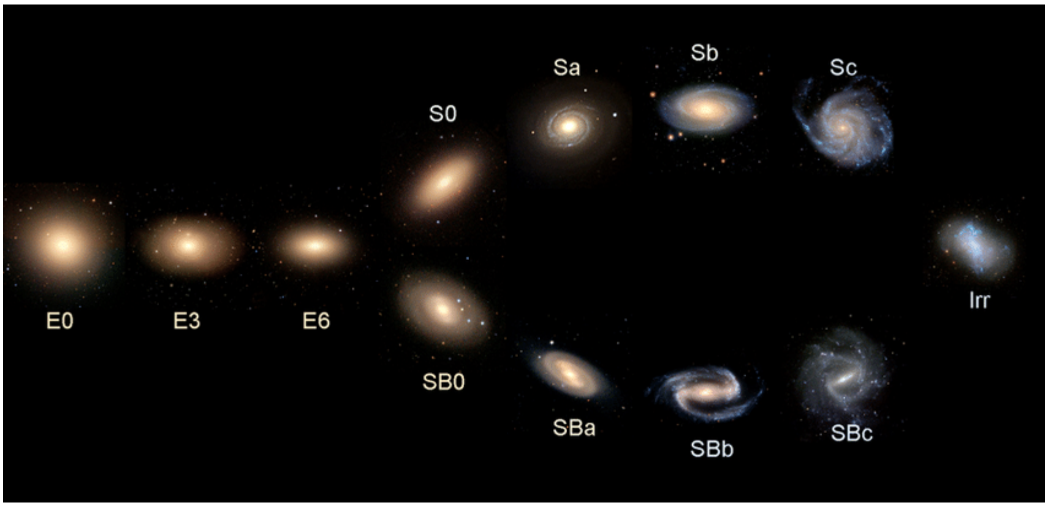

Figure 1.1: Diagram representing the Hubble tuning fork (Hubble 1926), with examples of galaxies falling under each category. Early-type elliptical and lenticular galaxies occupy the left-hand side of the diagram, while late-type spiral and irregular galaxies lie on the right. Chromatic variation can also be seen between the morphological classifications: this is driven by differences in their stellar populations (see §1.2.2). Figure from Cui et al. (2014).

Hubble envisaged the tuning fork as an evolutionary sequence, purporting that galaxies transitioned from an elliptical morphology to either a barred or unbarred spiral – hence the terminology 'early-type' and 'late-type'. Despite it now being known that this is not the case, Hubble's prescription is still widely used to describe galaxy morphologies.

Since the inception of the Hubble sequence it has become clear that the variety displayed between galaxies across the Universe is far more faceted than just their global morphologies. Galaxies are complex structures consisting primarily of stars, an interstellar medium of gas and dust, and dark matter, with the majority of galaxies also harbouring a supermassive black hole in their centres. These components can vary greatly even between galaxies with the same morphology.

1.2.2 Stellar component

Stars are the dominant source of rest-frame UV, optical and near-IR light emitted by galaxies. The variety amongst stars (e.g. less massive, cooler M-type stars compared with more massive, hotter O-types), is reflected in the stellar populations of galaxies. Herein lies the source of a second dichotomy between early-type and late-type galaxies (beyond the morphological differences): early-type galaxies typically have redder colours in the optical part of the spectrum than late-type galaxies. This contrast is driven by an abundance of bluer, hotter O and B stars in late-type galaxies, which are absent in early-type galaxies. Since these stars are generally more luminous than their cooler, less massive counterparts, they dominate the optical emission and give rise to the characteristic blue appearance of spiral galaxies. Without the presence of these stars, the cooler stars dominate and the peak of the emission consequently shifts to longer wavelengths, hence the redder colours seen in elliptical and lenticular galaxies. Given their short lifespans ($\sim 10^{7–8}$ yr), the presence of O and B stars in a galaxy is usually indicative of ongoing star formation; late-types are therefore more actively forming stars than early-types.

The stellar components of galaxies can exhibit a wide range of masses: spiral galaxies typically have stellar masses of $M_\star \sim 10^{9–12}$ $\mathrm{M}_\odot$, while for elliptical galaxies these masses can range from as low as $M_\star \sim 10^5$ $\mathrm{M}_\odot$ to as high as $M_\star \sim 10^{13}$ $\mathrm{M}_\odot$.

1.2.3 Interstellar medium

The ability of a galaxy to produce stars is dependent on the content and properties of its interstellar medium (ISM). The ISM describes the matter situated between stars in a galaxy, and is composed of gas and dust. The gas component consists primarily of hydrogen in either molecular (H_2), neutral atomic (HI) or ionised (HII) states. Regions dominated by HII are generally found around newly formed stars, where the UV photons from O and B stars ionise the surrounding medium. The subsequent recombination of electrons and protons is typically followed by a ‘cascade’ as the electron falls to lower energy levels; these cascades are often detected via Balmer emission lines such as Hα ($n = 3 \rightarrow 2$). Conversely, HI and H_2 can only exist far away from these stars. With no high-energy radiation to even excite the electrons, the atomic hydrogen found in HI regions exists in its ground state ($n = 1$). HI regions can therefore only be directly detected through the emission line that occurs when the electron in the hydrogen atom changes its spin state to be anti-aligned with that of the proton, which occurs at a wavelength of 21 cm in the rest frame. Finally, H_2 is only found in regions where the gas is dense enough and cold enough for HI atoms to bond with each other. These molecules are the main fuel for star formation in galaxies. Star formation thus generally occurs in massive (10^4–10^6 $M_\odot$), dense ($n(H_2) \sim 10^2$–10^5 cm^{-3}), cold ($T \sim 10$–50 K) giant molecular clouds (GMCs; e.g. Kennicutt & Evans 2012). H_2 is difficult to observe directly and is instead usually traced via emission lines from other molecules such as carbon monoxide (CO; e.g. Bolatto et al. 2013; Solomon & Vanden Bout 2005).

'Dust' is a term used to describe small, optically-thick grains composed of metals such as carbon and silicon. These grains are thought to form in galaxies via two main sources: the atmospheres of low-to-intermediate mass (1–4 $M_\odot$) asymptotic giant branch stars, which then disperse it into the ISM via stellar winds (Ferrarotti & Gail 2006; Gehrz 1989; Sargent et al. 2010); and the supernova explosions of massive stars (Barlow et al. 2010; Dunne et al. 2009; Rho et al. 2008). As well as being a by-product of star formation, dust also has the ability to catalyse the formation of new stars via the condensation of atomic hydrogen onto its surface and subsequent conversion to molecular hydrogen (e.g. Cazaux et al. 2016). Dust in galaxies is known to reprocess UV/optical photons emitted by stars and re-radiate them in the FIR (Hildebrand 1983); the bulk of this emission is often modelled using a modified blackbody prescription (e.g. Barger et al. 2012; Bianchi 2013; Blain et al. 2002) with typical temperatures of ∼20–40 K (e.g. Hwang et al. 2010).

As a galaxy evolves it will deplete its ISM through star formation, unless new cold gas is supplied from some external source. The ISM therefore becomes more gas-poor as a galaxy evolves. Early-type galaxies have a gas-poor ISM, having effectively run out of star formation fuel, while late-type galaxies still have a reservoir of cold gas enabling their ongoing star formation. As will be discussed later on (§1.2.4, §1.2.5, §1.3.1 and §1.4.1 in particular), the evolution of the ISM can be more complex, with mechanisms existing through which a galaxy can replenish its cold gas reservoirs or lose it more quickly.

1.2.4 Star formation rates

The rate at which a galaxy can form stars can vary significantly depending on the properties of the ISM. Locally, gas-poor early-type galaxies have star formation rates (SFRs) significantly lower than $\sim$1 $\mathrm{M}_\odot$ yr^{-1}, while the gas-rich ISM of a typical late-type galaxy can drive SFRs of up to $\sim$20 $\mathrm{M}_\odot$ yr^{-1} (e.g. Calvi et al. 2018; Gao & Solomon 2004; Kennicutt 1983). Some local galaxies can even reach SFRs in excess of $\gtrsim$100 $\mathrm{M}_\odot$ yr^{-1}, and are consequently known as 'starburst' galaxies (e.g. Kennicutt & De Los Reyes 2021).

Star formation activity creates signatures in the emission from a galaxy, which can thus be used to estimate its SFR. Commonly used tracers include: the copious amounts of UV radiation emitted by newly-formed stars; FIR emission from dust after reprocessing the UV/optical radiation from these stars; nebular emission lines such as Lyα, Hα and [O III], which originate from ionised regions around newly-formed stars; molecular emission lines such as carbon monoxide (CO), which traces the cold molecular gas content and generally correlates with the FIR luminosity (e.g. Gao & Solomon 2004; Kennicutt 1998; Kennicutt & Evans 2012).

Several mechanisms exist that can either suppress (quench) or enhance star formation in a galaxy. Quenching mechanisms generally serve to remove or heat up the cold gas in a galaxy, and can be driven by factors such as interactions with other galaxies or the surrounding environment (§1.3.1) or feedback from the central supermassive black hole (§1.2.5). Enhancing star formation involves replenishing the cold gas supply, which can occur via gas-rich mergers (§1.4) or via cold gas accretion through filaments (e.g. Kleiner et al. 2017).

The global star formation activity across the Universe is often quantified as the 'cosmic star formation rate density' (CSFRD), which is a measure of the stellar mass produced per unit time per unit volume at a given epoch. Many attempts have been made to constrain it across cosmic time; Figure 1.2 shows the culmination of several such efforts using UV and IR tracers of star formation activity (Madau & Dickinson 2014). A clear peak is seen in the CSFRD at $z \sim 2$, with declines in activity seen at higher and lower redshifts. This peak is commonly referred to as 'cosmic noon', and implies that the Universe was much more active

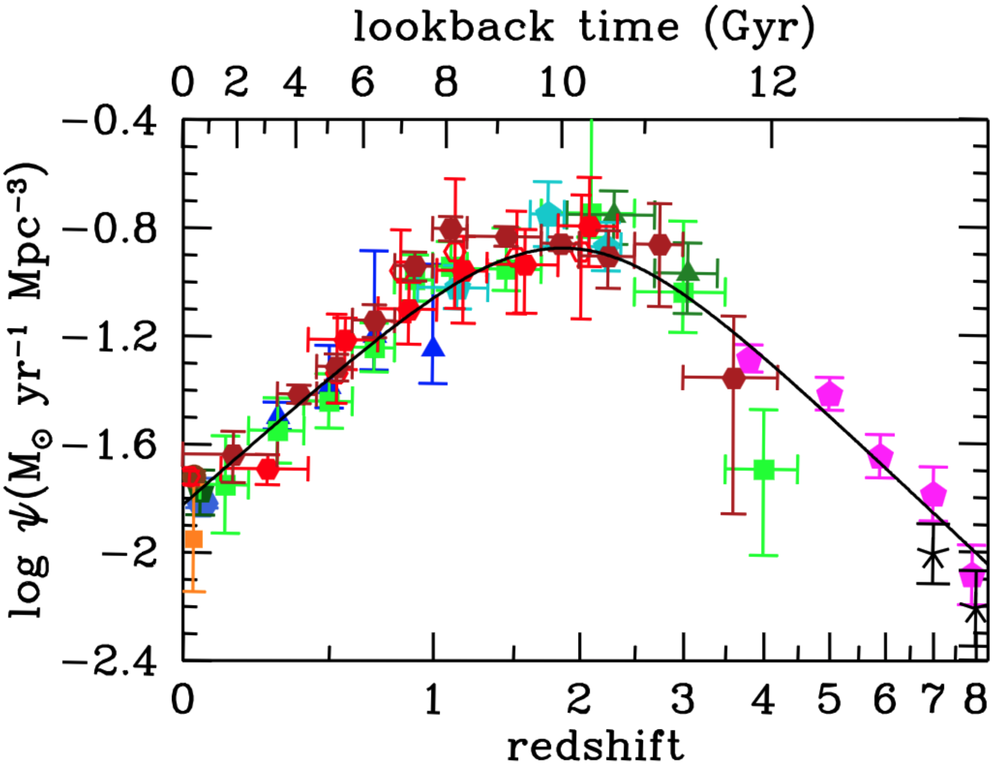

Figure 1.2: The evolution of the cosmic star formation rate density (CSFRD) of the Universe, measured using a combination of UV/optical and IR observations (see Madau & Dickinson 2014 and references therein). A clear peak in the CSFRD can be see at $z \sim 2$, in the epoch known as 'cosmic noon'. Figure from (Madau & Dickinson 2014).

in the past than it is today, with only ~25 percent of the total present-day stellar mass content being produced over the last 6 Gyr. Understanding the processes driving the observed evolution in the CSFRD remains a fundamental goal of modern astronomy.

1.2.5 Supermassive black holes & active galactic nuclei

Observational evidence suggests that at the core of almost every massive galaxy is a supermassive black hole (SMBH) with a mass of $M_\bullet \sim 10^{6-9}$ $\mathrm{M}_\odot$, where these masses are seen to correlate with the masses of the host galaxy (e.g. Ding et al. 2020; Kormendy & Ho 2013; Reines & Volonteri 2015). They emit no light themselves, having too strong a gravitational potential for even photons to escape within the Schwarzschild radius (Schwarzschild 1916). However, as matter falls toward a SMBH it forms an accretion disk, which loses energy in the form of radiation due to turbulence and friction.

A galaxy with an actively accreting and growing SMBH is known as having an ‘active galactic nucleus’ (AGN). AGN produce characteristic signatures in various parts of the spectrum ranging from radio to X-ray (e.g. Padovani et al. 2017). Radio emission is an important feature, originating from synchrotron radiation (e.g. Padovani 2017) resulting from interactions of relativistic particles with a strong magnetic field. AGN can vary greatly in radio luminosity, with the main distinction between radio-loud and radio-quiet populations being the presence of collimated radio ‘jets’ which can extend well beyond the host galaxy (e.g. Blandford et al. 2019).

Energy released from AGN (e.g. in the form of radiation, wind or jets) can impact the surrounding ISM and subsequently affect star formation, often resulting in the quenching of star formation by either preventing the gas from cooling or by removing it from the galaxy altogether. This is known as (negative) AGN feedback, and is often invoked as a means of explaining the observed deficit of massive galaxies with respect to massive dark matter halos (e.g. Bower et al. 2006, 2012). Negative AGN feedback can occur in two modes: the ‘quasar mode’ (also known as the ‘radiative mode’ or ‘wind mode’) and the ‘radio mode’ (also called the ‘kinetic mode’ or ‘maintenance mode’). Quasar mode feedback occurs in high-luminosity AGN where the black hole has reached its accretion rate limit such that radiation pressure begins to eject gas in the form of a wind (Silk & Rees 1998). It is more common at high redshifts, with models predicting a peak in their activity around $z \sim 2$ (Kormendy & Ho 2013). Meanwhile radio mode feedback is associated with lower-luminosity AGN, and occurs as a result of relativistic radio jets depositing kinetic energy into the surrounding gas and preventing it from cooling (e.g. Best et al. 2005; Kauffmann et al. 2008; Smolčić et al. 2009). Radio-mode AGN have lower accretion rates than quasar-mode AGN, and are seen to be more prevalent at lower redshifts, particularly in massive elliptical galaxies. Positive AGN feedback can also occur, by which star formation is enhanced as outflows from the AGN compress the molecular gas in the ISM; however, it has only been observed in a few instances (e.g. Cresci et al. 2015; Nesvadba et al. 2020; Shin et al. 2019).

1.2.6 Dark matter halo

Evidence from galaxy rotation curves implies that galaxies reside within vast halos of dark matter (Rubin et al. 1980; see also §1.1.1). These halos extend well beyond the baryonic matter of the galaxy (e.g. Somerville et al. 2018) and are generally ∼100–1000 times more massive than the stellar component (e.g. Behroozi et al. 2013).

Numerous efforts have been made to link the properties of a galaxy with those of the host dark matter halo, primarily through empirical models. Some of these models employ an approach known as 'abundance matching', by which the most massive galaxies are assumed to occupy the most massive dark matter halos. Early abundance matching models assumed one galaxy per dark matter halo (e.g. Colín et al. 1999; Kravtsov & Klypin 1999; Moustakas & Somerville 2002; Wechsler et al. 1998). However, dark matter halos can contain substructures known as subhalos, as a result of the accretion of smaller halos. More recent abundance matching techniques thus employ the *ansatz* that each halo and subhalo hosts a galaxy, with the same underlying assumption that more massive galaxies occupy more massive (sub)halos (e.g. Kravtsov et al. 2004; Tasitsiomi et al. 2004; Vale & Ostriker 2004).

Using techniques such as abundance matching it is possible to derive a stellar-to-halo mass relation (SHMR) from which one can determine the typical stellar mass of a galaxy occupying a dark matter halo of a given mass (e.g. Behroozi et al. 2013; Moster et al. 2010; Reddick et al. 2013). Figure 1.3 shows the empirically-derived SHMR from Behroozi et al. (2013), from which it can be seen that at all epochs ranging from $z = 0$ to $z = 8$ more massive dark matter halos tend to be dominated by more massive galaxies. The stellar-to-halo mass fraction shows a clear peak which shifts to lower masses at higher redshifts, showing that (a) there is a mismatch between the halo mass distribution and the stellar mass distribution throughout the Universe, and (b) that at a given epoch there is a maximum efficiency with which a galaxy can build its stellar mass in its dark matter halo. This latter feature is thought to be driven by feedback mechanisms such as supernovae and stellar winds at the low-mass end (e.g. Dekel & Silk 1986; Hopkins et al. 2012), and by AGN feedback at the high-mass end (e.g. Croton et al. 2006; Silk & Rees 1998; see also §1.2.5).

1.3 The evolution of clusters

1.3.1 Local galaxy clusters

Galaxy clusters are the largest gravitationally bound structures in the Universe today, having formed from some of the largest primordial density perturbations (§1.1.2). They contain anywhere from several tens to thousands of galaxies, within single virialised dark matter halos with masses $\sim10^{14-15}$ $M_\odot$ and diameters on the order of a few megaparsecs (Mpc). In addition to their dark matter halos and constituent galaxies, clusters also contain a hot plasma known as the intracluster medium (ICM), and a low-surface brightness component called the intracluster light (ICL) which is made up of stars that are gravitationally bound to the cluster halo rather than to individual galaxies. The ICM is visible when observed at X-ray wavelengths due to *bremsstrahlung* radiation from free electrons being deflected by the electric fields of charged particles in the ICM, and high-energy emission lines from heavy elements (e.g. Böhringer et al. 2001; Henry et al. 2006; Pacaud et al. 2016; Truemper 1993). The ICM can also be detected at millimetre wavelengths via a phenomenon known as the Sunyaev-Zel'dovich effect (SZ; Sunyaev & Zeldovich 1972), wherein photons from the CMB interact with electrons in the hot ICM and are scattered to higher energies through inverse Compton scattering (e.g. Bleem et al. 2015; Hasselfield et al. 2013; Planck Collaboration et al. 2016; Staniszewski et al. 2009; Williamson et al. 2011). Figure 1.4 shows a composite image of the cluster Abell 1689, with member galaxies visible in the foreground from optical *Hubble Space Telescope* (HST) imaging, while the ICM can be seen from *Chandra* X-ray observations as a bright, diffuse purple glow. While the dark matter halo cannot be directly detected, evidence of its presence

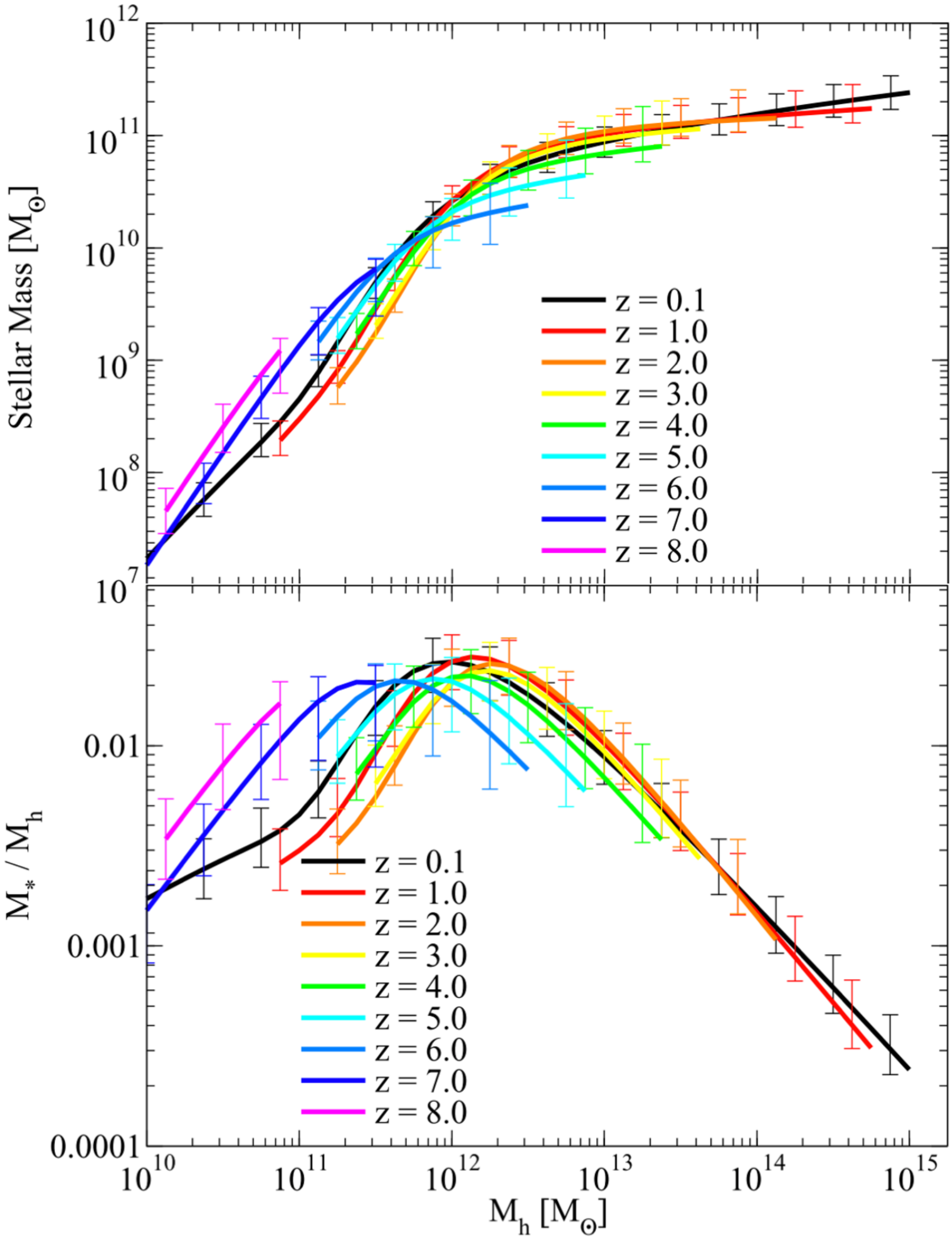

Figure 1.3: Evolution of stellar mass (top) and the stellar-to-halo mass ratio (bottom) as a function of halo mass, derived by Behroozi et al. (2013) for epochs ranging from $z = 0$ to $z = 8$. While the stellar masses show a monotonic increase with the host halo mass, the stellar-to-halo mass ratio shows a clear peak at each epoch, which is purported to be caused by feedback mechanisms at lower and higher masses. Figure adapted from Behroozi et al. (2013).

can be seen in the form of gravitationally lensed background galaxies, which appear as thin, elongated arcs away from the cluster centre. Gravitational lensing is a general relativistic effect whereby the strong gravitational potential of the dark matter halo 'bends' the path of the light emitted from the background galaxy; cluster halo masses can even be inferred via gravitational lensing (e.g. Hoekstra et al. 2013).

In the local Universe, galaxies follow a 'morphology-density relation', in which passive, early-type galaxies are preferentially found within regions with higher galaxy densities, while galaxies in the blank field (i.e. regions in which the galaxy density is average for its epoch) are generally star-forming late-types (Dressler 1980). Galaxy clusters in the local Universe are therefore dominated by passive, early-type galaxies. In a given cluster, the most massive of these galaxies is known as the 'brightest cluster galaxy' (BCG), and is generally found near the centre of the cluster as defined by the peak of its X-ray emission (e.g. Lin & Mohr 2004). BCGs tend to be more massive in more massive clusters, accumulating their mass predominantly via mergers (e.g. De Lucia & Blaizot 2007; Lin & Mohr 2004). They are also more likely to host radio-loud AGN than other galaxies with similar masses (e.g. Best et al. 2007; Von Der Linden et al. 2007).

The galaxies in local clusters have been observed to form a tight linear correlation in colour-magnitude space with very little intrinsic scatter known as the 'red sequence', by which brighter cluster members exhibit redder rest-frame UV-optical colours than their fainter counterparts (e.g. Bower et al. 1992; Visvanathan & Sandage 1977). The slope of the red sequence is thought to be driven by the mass-metallicity relation, in which more massive (and more luminous) galaxies are better at retaining the metal content in their ISM, which could otherwise be ejected via supernova feedback in shallower gravitational potential wells (Kodama et al. 1998). Meanwhile the minimal intrinsic scatter in the colours of red sequence galaxies is attributed to differences in the ages of their stellar populations (Bower et al. 1992; Jaffé et al. 2011).

The red sequence appears to have been in place in galaxy clusters even at redshifts as high as $z = 1.8$, implying that high formation redshifts ($z \gtrsim 2$) are required for the member galaxies in order to allow time for them to reach quiescence by these epochs (e.g. Ellis et al. 1997; Lidman et al. 2004; Mei et al.

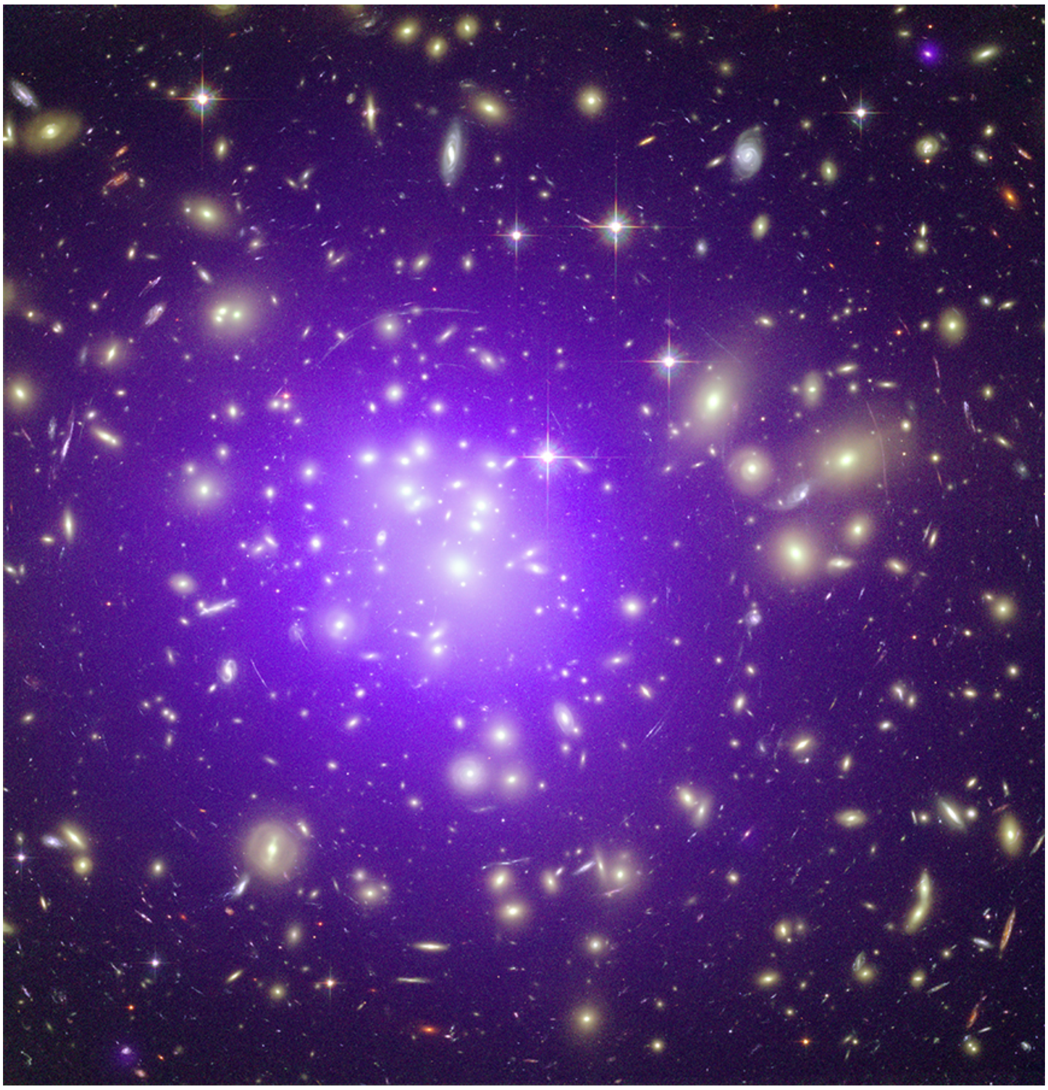

Figure 1.4: A composite X-ray (purple) and optical (yellow) image of the galaxy cluster Abell 1689 ($z = 0.18$). The image spans $3.2'$ along each side, corresponding to ~ 0.6 Mpc at the redshift of the cluster if one assumes a flat ΛCDM cosmology with $\Omega_{\mathrm{M}} = 0.315$, $\Omega_{\Lambda} = 0.685$ $H_0 = 67.4$ km s^{-1} (Planck Collaboration 2020). The hot ICM can clearly be seen via its X-ray emission, detected using the *Chandra* X-ray Observatory. A high density of early-type galaxies can be seen in the optical band, detected with the *Hubble Space Telescope*. Several gravitationally lensed background galaxies can also be seen in the form of long arcs in this band. The ICL is too faint to be visible in the optical imaging. Image credit: NASA/CXC/MIT (X-ray); NASA/STScI (Optical).

2009; Papovich et al. 2010; Snyder et al. 2012). There is evidence to suggest that the faint end of the red sequence evolves with cosmic time (at least out to $z \sim 1$), with clusters at higher redshift containing fewer faint red sequence galaxies (De Lucia et al. 2004, 2007; Gilbank et al. 2008; Martinet et al. 2015; Rudnick et al. 2009; Smail et al. 1998; Stott et al. 2007; Tanaka et al. 2005). At first glance this appears to contradict the hierarchical paradigm of structure formation by implying that high-mass galaxies in clusters are more evolved than their low-mass counterparts at these redshifts. However, this apparent 'antihierarchical' behaviour (often referred to as 'downsizing') may be explained if one considers that by the time the high-mass galaxies have assembled from the mergers of two (or more) progenitor galaxies, the stellar populations of these progenitors may already be old. The merger of these galaxies could therefore be gas-poor such that the merging process triggers little to no star formation activity, resulting in a massive early-type galaxy predated by its stellar content (e.g. De Lucia et al. 2006).

The build-up of the faint end of the red sequence is also accompanied by a decrease in the fraction of blue, star-forming galaxies in clusters as one moves to lower redshifts (e.g. Butcher & Oemler 1984; Gilbank et al. 2008). Possible explanations for this include galaxies being accreted onto the cluster and having their star formation suppressed (quenched) by interactions as they fall into the potential well (e.g. De Lucia et al. 2007; Stott et al. 2007, 2009).

Several possible mechanisms have been proposed for the quenching of star formation in clusters. 'Ram pressure stripping' is a mechanism by which a galaxy is stripped of its cold gas as it travels through the ICM (Gunn & Gott 1972), quickly depriving it of its fuel for star formation. 'Strangulation' can occur when the ICM cuts off the supply of cold gas into a galaxy, potentially by evaporating the hot gas halo (e.g. Peng et al. 2015). Galaxy-galaxy and galaxy-cluster interactions can also lead to quenching: tidal effects can disturb the gas in a galaxy to initially trigger a burst of star formation, which is then followed by quiescence as the gas is depleted (e.g. Byrd & Valtonen 1990; Moore et al. 1996). AGN feedback can also prevent intergalactic gas from cooling, thereby cutting off a source of star formation fuel for the host galaxy. Furthermore, simulations predict that it is possible for AGN feedback from the central galaxy in a cluster to suppress star formation in its satellites by heating the ICM (e.g. Dashyan et al. 2019). However, recent observational evidence of anisotropic quenching in galaxy clusters, in which galaxies along the minor axis of the BCG are less quenched than those along its major axis, has also inspired theories that AGN feedback can have an adverse effect on quenching by reducing the density of the ICM such that ram pressure stripping is less effective (e.g. Martín-Navarro et al. 2021; Stott 2022).

It is clear from what we know of galaxy clusters that environment plays an important role in shaping a galaxy's evolution, with denser environments having the tendency to accelerate the cessation of star formation. Understanding the formation history of galaxy clusters is therefore an important step in building a picture of galaxy evolution, especially of the most massive galaxies.

1.3.2 Protoclusters

Galaxy protoclusters (for a review, see Overzier 2016) are typically defined as high-redshift structures that will collapse and virialise to form a galaxy cluster by $z = 0$. Simulations show that in a ΛCDM universe, protoclusters form hierarchically at the highest-density regions of the matter distribution in the universe (the 'cosmic web'; Bond et al. 1996) at $z \sim 4$–6 (e.g. Baugh et al. 1998; Boylan-Kolchin et al. 2009; De Lucia & Blaizot 2007). As such, protoclusters are characterised by overdensities of galaxies relative to the average galaxy density in the coeval blank field. In contrast to their present-day descendants, galaxies in a protocluster are generally not bound to a single halo; they instead occupy large structures extended over megaparsec scales, with the main halo containing as little as 20 percent of the member galaxies (e.g. Chiang et al. 2013; Muldrew et al. 2015). Figure 1.5 shows the simulated growth of dark matter in a Coma-like galaxy cluster (i.e. a cluster with a present-day halo mass $\sim 10^{15}$ M$_\odot$) from the Millennium II simulation (Boylan-Kolchin et al. 2009). The overdensity of dark matter signifying the presence of the protocluster can be seen as early as $z \sim 6$, consisting of many small halos without a clear sign of a central halo until $z \sim 2$. The existence of significant overdensities such as this at $z \sim 6$ suggest that protoclusters should be detectable as early as ~ 1 Gyr after the Big Bang.

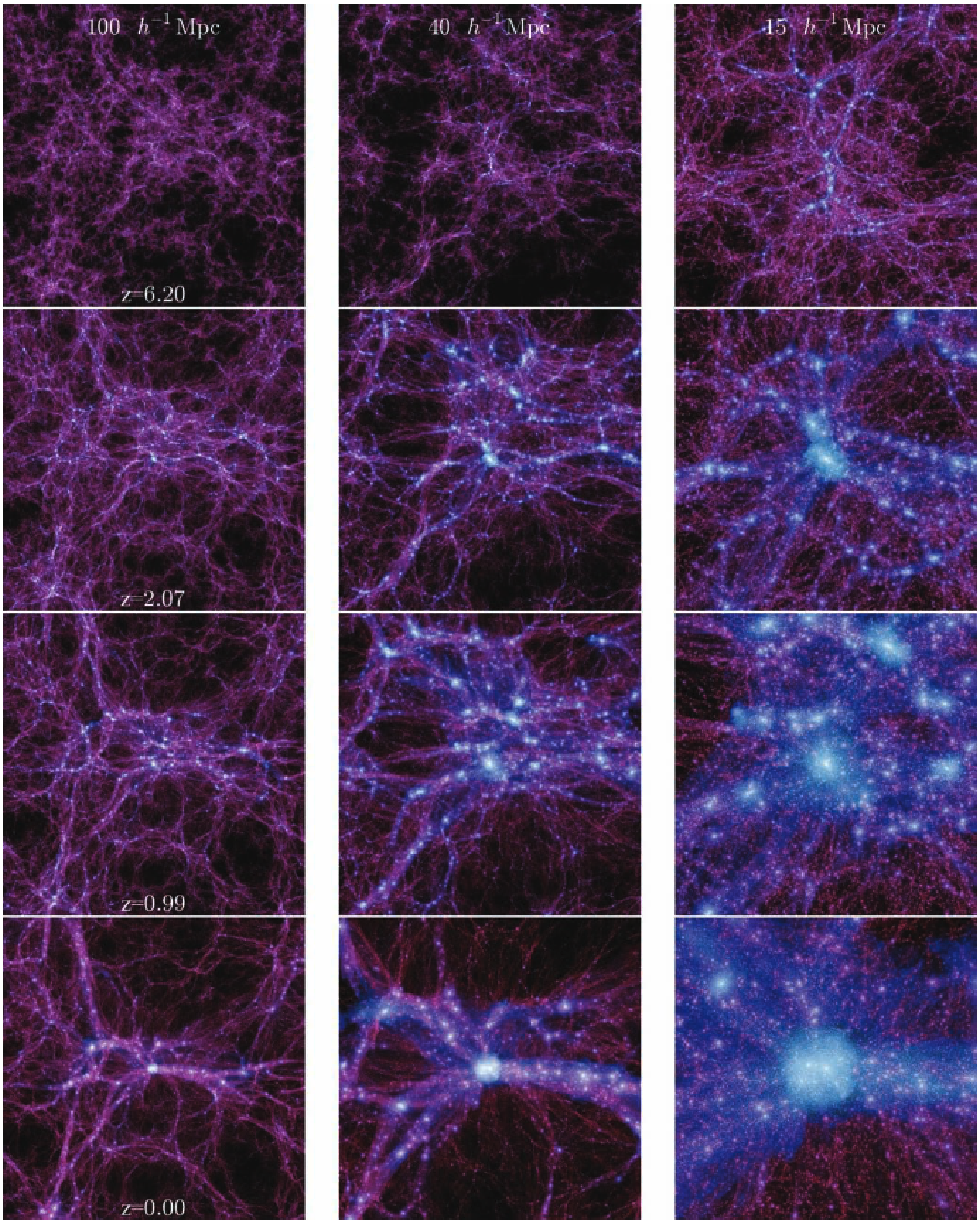

Figure 1.5: The evolutionary history of a Coma-like cluster in the Millennium II N-body simulation. Panels in each row show snapshots of the dark matter distribution at comoving scales of 100, 40, and 15 h^{-1} Mpc, with each row showing a different epoch (from top to bottom: $z = 6.20$, $z = 2.07$, $z = 0.99$ and $z = 0.00$). The large-scale overdensity that eventually evolves into the galaxy cluster can be seen as early as $z \sim 6$ spanning several tens of h^{-1} Mpc. Figure from Boylan-Kolchin et al. (2009).

The frontier of high-redshift cluster detection has been pushed to $z \sim 2$ by searching for their X-ray emission (e.g. Böhringer et al. 2001; Henry et al. 2006; Pacaud et al. 2016; Truemper 1993), their imprint on the cosmic microwave background at millimetre wavelengths via the SZ effect (e.g. Bleem et al. 2015; Hasselfield et al. 2013; Planck Collaboration et al. 2016; Staniszewski et al. 2009; Williamson et al. 2011), and high concentrations of passive early-type galaxies occupying a tight red sequence in colour-magnitude space (e.g. Gilbank et al. 2011; Gladders & Yee 2000, 2005; Muzzin et al. 2009; Wilson et al. 2009). However, these methods become impractical at higher redshifts due to the lack of a hot ICM and a well-defined red sequence.

Also in contrast with the clusters observed in the local Universe, protoclusters are expected to host mainly star-forming galaxies. Indeed, observations at high redshift hint towards a reversal of the morphology-density relation seen in the local Universe, with denser environments at $z \gtrsim 1$ hosting galaxies with higher SFRs than the blank field (e.g. Cooper et al. 2008; Elbaz et al. 2007). Consequently, the majority of protocluster surveys at $z \gtrsim 2$ resort to searching for overdensities of star-forming galaxies. Such searches depend on the existence of accurate redshift information across large cosmological volumes, and several protoclusters have been discovered serendipitously through large spectroscopic surveys (e.g. Cucciati et al. 2014; Lemaux et al. 2014; Steidel et al. 1998, 2000, 2005). In lieu of expensive large-scale spectroscopic observations, photometric techniques for identifying star-forming galaxies are often employed instead. These techniques include using narrowband photometry to search for strong emission lines such as Lyα or Hα (Hatch et al. 2011b; Hayashi et al. 2012; Koyama et al. 2013; Kuiper et al. 2011b; Palunas et al. 2004; Shimasaku et al. 2003; Tanaka et al. 2011; Venemans et al. 2002, 2005; Zheng et al. 2021; see also §1.5.1), or using pairs of broadband filters to search for galaxies with a Lyman break in their SEDs (e.g. Intema et al. 2006; Miley et al. 2004; Overzier et al. 2006; Toshikawa et al. 2016, 2018).

While protoclusters have been discovered through blind searches for galaxy overdensities, it is an inefficient way to identify them. A less cumbersome solution involves being able to predict where a protocluster might be, based on the assumed nature of its inhabitants. As will be discussed in §1.4, this requires that we are able to identify the progenitors of the massive elliptical galaxies observed in local galaxy clusters.

1.4 The evolution of massive galaxies

Massive galaxies in clusters have complex evolutionary histories driven by mergers of lower-mass progenitor galaxies, interactions with their surrounding environment, and feedback from AGN. Figure 1.6 illustrates one theory for the formation of massive ellipticals (Hopkins et al. 2008; Sanders et al. 1988). In this scenario, two (or more) disk galaxies of similar mass begin to cluster together due to gravitational attraction, until eventually their dark matter halos coalesce. Once within a single halo, interactions between the galaxies cause them to lose angular momentum and ultimately coalesce themselves. During this merger, gas flows into the centre of the resultant structure, triggering a burst of star formation while also fuelling the central black hole. As the black hole accretes rapidly it also ejects the remaining dust and gas from the galaxy (the 'quasar mode' of AGN feedback; §1.2.5), and the AGN dominates the emission from the galaxy. This quasar phase then fades since little matter is left to accrete onto the AGN, and the host galaxy rapidly reddens due to the lack of star formation fuel, resulting in a passive, early-type galaxy.

Searches for the progenitors of massive elliptical galaxies – and by proxy the progenitors of the galaxies in local clusters – can exploit the predictions laid out by this model. Indeed, searches for overdensities of galaxies around quasars at $z \gtrsim 2$ have resulted in the identification of several candidate protoclusters (e.g. Falder et al. 2011; Husband et al. 2013; Kashikawa et al. 2007; Kim et al. 2009; Matsuda et al. 2011; Morselli et al. 2014; Overzier et al. 2009; Stevens et al. 2010; Stiavelli et al. 2005; Wold et al. 2003), consistent with expectations that dense environments help fuel rapid accretion onto an AGN via mergers (e.g. Springel et al. 2005a). However, several other studies have found no significant overdensity around quasars in these epochs (e.g. Bañados et al. 2013; Simpson et al. 2014a), and recent spectroscopic works suggest that quasars reside in protoclusters in only ~ 10 percent of cases (e.g. Adams et al. 2015; Hennawi et al. 2015; Trainor

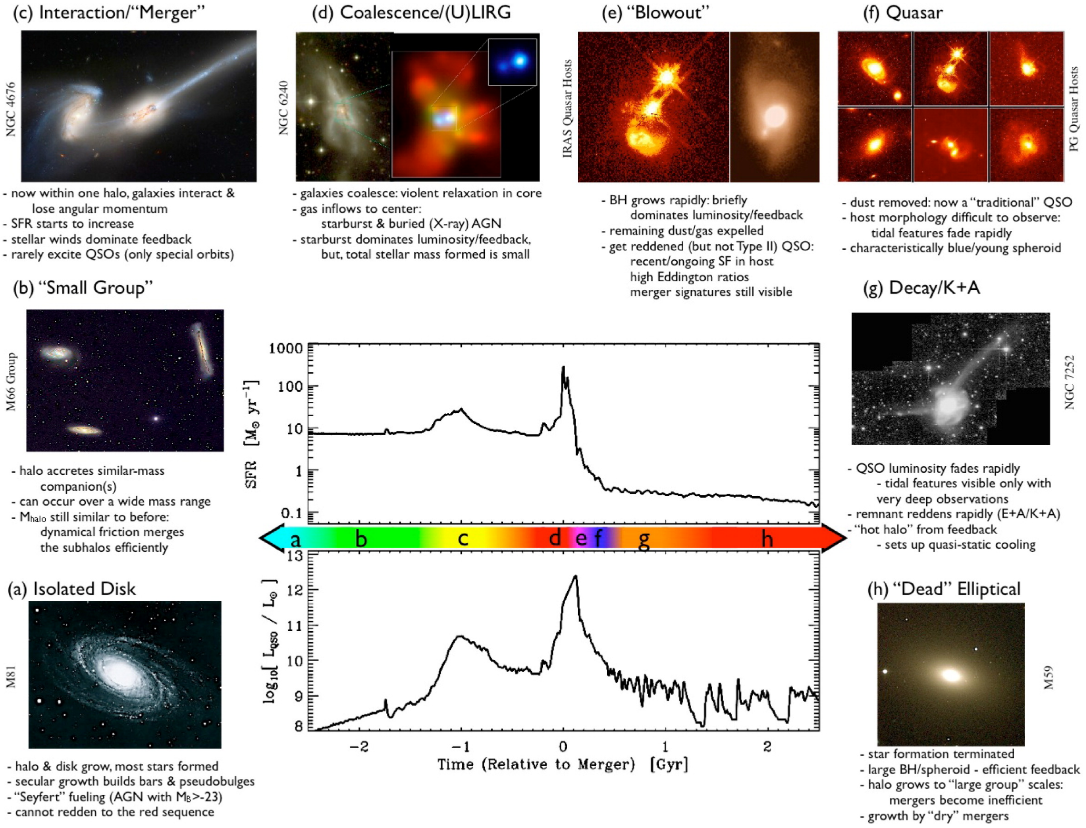

(c) Interaction/“Merger”

- now within one halo, galaxies interact & lose angular momentum
- SFR starts to increase
- stellar winds dominate feedback
- rarely excite QSOs (only special orbits)

(d) Coalescence/(U)LIRG

- galaxies coalesce: violent relaxation in core
- gas inflows to center:
    starburst & buried (X-ray) AGN
- starburst dominates luminosity/feedback,
    but, total stellar mass formed is small

(e) “Blowout”

- BH grows rapidly: briefly dominates luminosity/feedback
- remaining dust/gas expelled
- get reddened (but not Type II) QSO:
    recent/ongoing SF in host
    high Eddington ratios
    merger signatures still visible

(f) Quasar

- dust removed: now a “traditional” QSO
- host morphology difficult to observe:
    tidal features fade rapidly
- characteristically blue/young spheroid

(b) “Small Group”

- halo accretes similar-mass companion(s)
- can occur over a wide mass range
- M_{halo} still similar to before:
    dynamical friction merges the subhalos efficiently

(g) Decay/K+A

- QSO luminosity fades rapidly
    - tidal features visible only with very deep observations
- remnant reddens rapidly (E+A/K+A)
- “hot halo” from feedback
    - sets up quasi-static cooling

(a) Isolated Disk

- halo & disk grow, most stars formed
- secular growth builds bars & pseudobulges
- “Seyfert” fueling (AGN with M_B>-23)
- cannot redden to the red sequence

(h) “Dead” Elliptical

- star formation terminated
- large BH/spheroid - efficient feedback
- halo grows to “large group” scales:
    mergers become inefficient
- growth by “dry” mergers

Figure 1.6: A schematic diagram illustrating the proposed evolutionary path from isolated, star-forming disk galaxies to passive elliptical galaxies. The central plot shows the variation of star formation rate *(top)* and quasar luminosity *(bottom)* as one moves along the evolutionary sequence. Major mergers are seen to trigger an intense burst in both star formation and quasar activity. Figure from (Hopkins et al. 2008). Image credits: (a) NOAO/AURA/NSF; (b) REU program/NOAO/AURA/NSF; (c) NASA/STScI/ACS Science Team; (d) Optical (left): NASA/STScI/R. P. van der Marel & J. Gerssen; X-ray (right): NASA/CXC/MPE/S. Komossa et al.; (e) Left: J. Bahcall/M. Disney/NASA; Right: Gemini Observatory/NSF/University of Hawaii Institute for Astronomy; (f) J. Bahcall/M. Disney/NASA; (g) F. Schweizer (CIW/DTM); (h) NOAO/AURA/NSF.

& Steidel 2012), leaving some ambiguity about whether they can reliably trace high-density environments.

An alternative method of protocluster identification is by searching for signatures of starbursts (stage *d* in Figure 1.6) at high redshift. Searches for these galaxies at high redshift in the rest-frame optical/NIR are hindered by the vast amounts of dust present in their ISM. Instead, astronomers must turn to the submillimetre regime.

1.4.1 Submillimetre galaxies

Dust in galaxies reprocesses high-energy photons emitted by newly-formed stars and re-radiates them in the FIR (Hildebrand 1983; see also §1.2.3). The *Infrared Astronomical Satellite* (*IRAS*; Neugebauer et al. 1984) all-sky survey was the first to reveal that on average local galaxies emit approximately one third of their total luminosity in the IR regime (Soifer & Neugebauer 1991), while also unveiling that a minority are actually dominated by their emission at these wavelengths (see Sanders & Mirabel 1996 for a review). The most luminous of the *IRAS*-identified galaxies have FIR luminosities in excess of 10^{12} $L_{\odot}$ attributed to intense star formation ($\gtrsim$100 $M_{\odot}$ yr^{-1}) coupled with high dust content (e.g. Lutz et al. 1998); these are known as ultra-luminous infrared galaxies (ULIRGS).

The discovery of ULIRGS naturally led to questions about the dust content in galaxies at higher redshifts. Later the detection of a 'cosmic infrared background' (CIB) revealed that the Universe emits comparable energy densities at infrared/submillimetre wavelengths as it does in the UV/optical (Fixsen et al. 1998; Hauser et al. 1998; Puget et al. 1996). The implication of this is that approximately half of the total energy emitted by galaxies in the UV/optical is absorbed and re-radiated in the FIR by dust, and that much of this FIR emission must be coming from a population of galaxies that had previously escaped detection in optical/NIR surveys.

Blain & Longair (1993) predicted that submillimetre observations could be instrumental in unveiling this hidden population by exploiting the known shape of the dust component in existing galaxy SEDs. In the rest frame, the dust component exhibits a high peak in emission in the FIR, followed by a steep decline

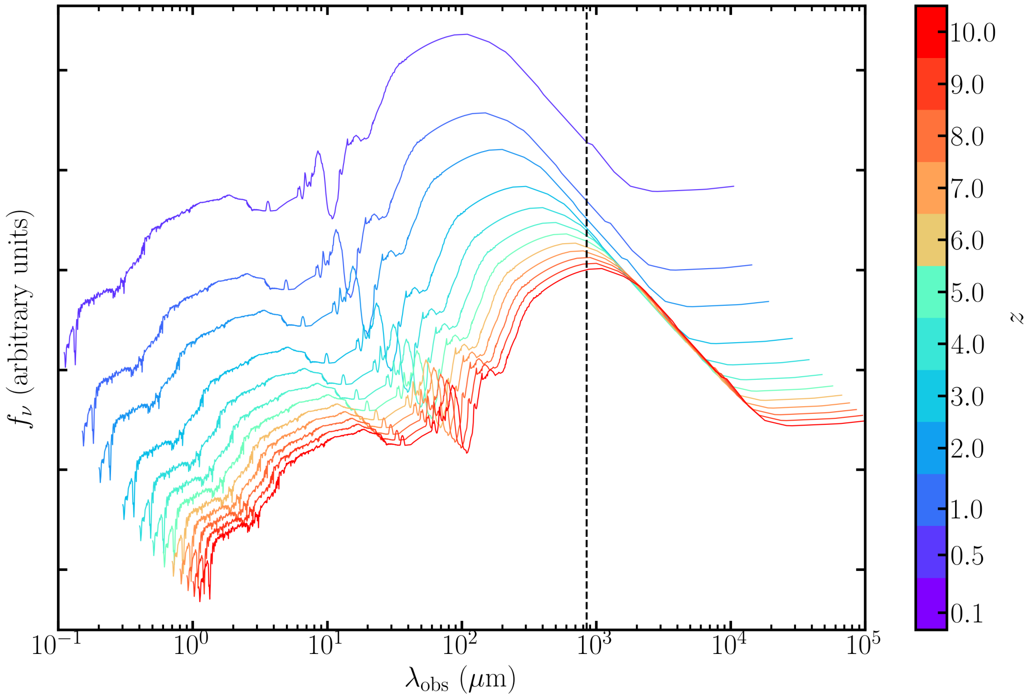

Figure 1.7: The SED of the nearby ULIRG Arp 220 (Silva et al. 1998) as it would be observed at the redshifts marked on the colourbar. The effect of the negative K-correction can be seen via the near-constant flux density at an observed wavelength of $\lambda_{\rm obs} \sim 850$ μm (marked by the vertical dashed line) for $z \sim 1$–10.

in the submillimetre regime. At higher redshifts however, the peak shifts longward into this regime and approximately negates the effect of cosmological dimming. This 'negative K-correction' ensures an almost constant flux at submillimeter wavelengths from $z \sim 1$ all the way to $z \sim 10$. Figure 1.7 shows an example of a ULIRG SED being progressively shifted from $z = 0.1$ to $z = 10$; one can see that at the highlighted observed wavelength of 850 μm there is little variation in the flux density at $z \sim 1$–10, due to the peak of the FIR emission shifting closer to this wavelength.

The first extragalactic submillimeter surveys conducted using the Submillimetre Common User Bolometer Array (SCUBA) on the James Clark Maxwell Telescope (JCMT) detected a significant population of 850 μm-selected galaxies at high redshift (Barger et al. 1998; Hughes et al. 1998; Lilly et al. 1999; Smail et al. 1997). The space density of these 'submillimetre galaxies' (SMGs) imply a strong evolution in the population size as one moves to higher redshifts, scaling with $\sim(1+z)^4$ (e.g. Blain et al. 1999; Smail et al. 1997).

Since their discovery much work has been undertaken to grasp the nature of SMGs. We now have a solid understanding of their key properties. Their typical rest-frame IR luminosities of $L_{\rm IR} \sim 10^{12\text{–}13}$ $\rm L_\odot$ are powered by intense star formation activity reaching SFRs of $\gtrsim$1000 $\rm M_\odot$ $\rm yr^{-1}$ (e.g. Chapman et al. 2005; Magnelli et al. 2012; Pope et al. 2006; Swinbank et al. 2014; Wardlow et al. 2011). They can host an AGN which can contribute to the IR luminosity via its accretion disk heating a surrounding dusty torus (e.g. Fritz et al. 2006), although this contribution is significantly overshadowed by the contribution from ongoing star formation (e.g. Alexander et al. 2005; Pope et al. 2008; Wang et al. 2013). They have high stellar masses of $M_* \sim 10^{10-11}$ $\rm M_\odot$ (e.g. Dudzevičiūtė et al. 2020; Hainline et al. 2011; Simpson et al. 2014b; da Cunha et al. 2015), dust masses of $\gtrsim$$10^8$ $\rm M_\odot$ (e.g. Dudzevičiūtė et al. 2020; Miettinen et al. 2017), and cold gas masses of $\sim$$10^{11}$ $\rm M_\odot$, but with gas depletion times of just a few hundred Myr (e.g. Birkin et al. 2021). They are predominantly located at $z \sim$ 1–3, with the peak of their redshift distribution occurring at $z \sim 2.5$ and a high-end tail extending out to $z \sim 6$ (e.g. Chapman et al. 2005; Dudzevičiūtė et al. 2020; Smail et al. 1997; Smolčić et al. 2012; Wardlow et al. 2011; Weiß et al. 2013). SMGs contribute up to $\sim$20 percent of the cosmic star-formation rate density at $z \sim 2$ (Barger et al. 2012; Chapman et al. 2005; Coppin et al. 2006; Swinbank et al. 2014; Wardlow et al. 2011).

The extreme properties of SMGs has long made them a good test of galaxy evolution models (e.g. Baugh et al. 2005; Béthermin et al. 2011; Davé et al. 2010; Hayward et al. 2013; Lacey et al. 2008, 2010; Narayanan et al. 2010, 2015; Niemi et al. 2012), yet questions remain about their evolution and role in the evolution of other galaxies. SMGs have similar properties to those expected of the progenitors of local massive elliptical galaxies, which formed most of their stars in short bursts at $z \gtrsim 2$ (Blakeslee et al. 2003; Ellis et al. 1997). Indeed, the dust emission from SMGs is typically compact, which is consistent with a scenario in which a gas-rich $z \gtrsim 2$ galaxy undergoes a compact starburst, leading to a compact quiescent galaxy, which eventually evolves into a local elliptical galaxy (Ikarashi et al. 2015; Simpson et al. 2015; Toft et al. 2014). Since local ellipticals are predominantly found in galaxy clusters (e.g. Dressler 1980) then if SMGs are indeed a progenitor phase in their formation, it is expected that SMGs should reside in early galaxy clusters, or ‘protoclusters’, at $z \gtrsim 2$.

Whether SMGs commonly inhabit protoclusters or protocluster-like environments is as yet uncertain. Several examples of SMGs residing in protoclusters have been documented (e.g. Casey et al. 2015; Daddi et al. 2009; Ivison et al. 2013; Walter et al. 2012), but these systems were selected for detailed follow-up because of prior evidence of high galaxy densities – i.e. they comprise a highly biased subset and therefore cannot be used to make inferences about the general SMG population. Clustering studies have been used to obtain statistical measurements indicative of the whole SMG population, and these suggest that on average SMGs at $z \sim 2.5$ reside in dark matter halos of mass $\sim 10^{13}$ $\mathrm{M}_{\odot}$ (e.g. Hickox et al. 2012; Wilkinson et al. 2017). This is marginally lower than expected for the progenitors of massive ellipticals, and implies that SMGs are instead more likely to evolve into 2–$3L^*$ galaxies in groups and small clusters. However, these halo mass measurements have typical uncertainties of ∼0.5 dex due to the difficulties associated with obtaining accurate photometric redshifts for SMGs (see §1.5.2). Furthermore, these clustering measurements relied on the statistical identification of optical/near-IR counterparts to submillimetre sources detected in single-dish surveys, which are incorrect in ∼30 percent of cases and incomplete in a further ∼30 percent (e.g. Hodge et al. 2013a). More recently, García-Vergara et al. (2020) and Stach et al. (2021) measured the clustering of SMGs which had been followed up interferometrically with the Atacama Large Millimetre/submillimeter Array (ALMA), with García-Vergara et al. (2020) finding lower halo masses than Stach et al. (2021) and both results being higher than measured by Wilkinson et al. (2017). Overall, the picture from clustering measurements is complex, and differing results from different studies may be methodological, due to sample selection or cosmic variance. Other ways of measuring the environments of SMGs are required. Statistical photometric redshifts have identified galaxy overdensities around ∼5–60 percent of SMGs (e.g. Davies et al. 2014; Smolčić et al. 2017a), but these are subject to significant selection biases (see Section 6 in Smolčić et al. 2017a), and few overdensities have been spectroscopically confirmed.

1.4.2 Brightest cluster galaxy progenitors

BCGs are special among the elliptical galaxy population. Their stellar populations are thought to have been in place since $z \sim 2$ (e.g. Stott et al. 2008), while their extremely high mass content is expected to assemble fairly late, with only half of their present-day masses locked into a single galaxy by $z \sim 0.5$ (De Lucia & Blaizot 2007). This late-stage mass build-up is therefore likely dominated by dry (gas-poor) mergers with quiescent galaxies, for which there is observational support in the fact that BCG stellar components extend over larger radii than expected for normal ellipticals with the same luminosities (e.g. Bernardi et al. 2007). Furthermore, as was mentioned in §1.3.1, BCGs are more likely to host radio-loud AGN than other elliptical galaxies of similar mass (e.g. Best et al. 2007; Von Der Linden et al. 2007).

High-redshift radio galaxies (HzRGs) are massive ($M_\star \gtrsim 10^{10.5}$ $\mathrm{M}_\odot$; Seymour et al. 2007) galaxies hosting radio-loud AGN (rest-frame $L_{500\ \mathrm{MHz}} >\ 10^{27}$ W Hz^{-1}; Miley & De Breuck 2008) at $z > 1$, and are a strong candidate for the progenitors of BCGs (Best et al. 1997; Miley & De Breuck 2008). In addition to their high stellar masses, they display signatures of high star formation activity (Dey et al. 1997) along with clumpy UV morphologies indicative of having formed through mergers (Dubinski 1998; Gao et al. 2004; Hilbert et al. 2016; Springel et al. 2005b), as expected of the progenitors of BCGs before dry mergers dominate their mass accretion. HzRGs are also frequently found to reside in protoclusters (e.g. Cooke et al. 2014; Hall et al. 2018; Hayashi et al. 2012; Kuiper et al. 2011a; Kurk et al. 2000; Venemans et al. 2002; Wylezalek et al. 2013), further supporting the theory that they will eventually evolve into BCGs.

However, whilst it is well-established that HzRGs trace galaxy overdensities, it is currently debated whether this is due to their typically high stellar masses, or whether interactions between the AGN activity and local environment leads to these observations (e.g. see discussion in Wylezalek et al. 2013). If the high masses of HzRGs is the driver behind their observed environment then one would expect to find radio-quiet galaxies with similar masses inhabiting similarly overdense environments, yet observational evidence suggests this may not be the case. For example, using *Spitzer* IRAC-selected galaxies Hatch et al. (2014) compared the environments of radio-loud AGN (including a sample of 208 HzRGs) from the CARLA survey (Wylezalek et al. 2013) with those of a radio-quiet control sample matched in stellar mass and redshift, finding that galaxies in the control sample reside in significantly less dense environments. This is further supported by simulations, in which HzRGs are seen to be hosted by more massive dark matter halos than radio-quiet galaxies with the same stellar mass, due to AGN feedback preventing the build-up of stellar mass in the HzRGs (e.g. Izquierdo-Villalba et al. 2018).

1.5 Observational probes of galaxy environments

1.5.1 Narrowband surveys

Identifying galaxies belonging to the same structure requires knowledge of their redshifts; otherwise interlopers in the foreground or background can easily be misconstrued as structure members. In an ideal world, one would obtain reliable spectroscopic redshifts for every galaxy in the sky and thus map the large scale structure of the Universe at all epochs. This is of course impractical, however, and more efficient alternatives are often sought out.

Narrowband photometric surveys present a highly economical alternative to large spectroscopic surveys. These surveys typically involve observing regions of the sky with a broadband (BB) filter and a narrowband (NB) filter whose wavelength coverage is also covered by the broadband filter. The underlying principle is that if a galaxy has a strong emission (absorption) line that has been redshifted into the narrowband filter, then the apparent magnitude measured in the NB filter, m_{NB}, will be significantly brighter (fainter) than that measured in the BB filter, m_{BB}. Since the wavelength coverage of the NB filter is small and there are only a few common strong emission (absorption) lines, this effectively narrows down the redshift of any galaxies exhibiting a significantly positive (negative) $\Delta m = m_{\mathrm{BB}} - m_{\mathrm{NB}}$ colour to a small selection of possibilities. This information can be used in conjunction with additional broadband photometry to derive high-precision photometric redshifts. Figure 1.8 shows an example of an emission line galaxy as seen in a narrowband image and a broadband image, as well as an image constructed by subtracting the broadband from the narrowband. As expected, the emission line galaxy leaves a clear signal in the subtracted data, while other galaxies around it disappear. This is due to the significant excess brightness generated in the narrowband by the presence of the strong emission line.

A common application for narrowband surveys is to identify star-forming galaxies via the presence of emission lines. These emission lines are typically one (or more) of either Lyα, Hα, [OII] or [OIII], as these are all generally bright emission lines originating from atoms which have recombined with electrons after being ionised by the intense UV radiation from hot, young stars. Hα, [OII] and [OIII] galaxies have been identified in several narrowband studies (e.g. Bayliss et al. 2011; Finkelstein et al. 2008; Gawiser et al. 2007; Guaita et al. 2010; Hayashi et al. 2018, 2020; Hu et al. 2010; Khostovan et al. 2015, 2020; Ly et al. 2007, 2011; Nilsson et al. 2009; Ouchi et al. 2008, 2010; Pirzkal et al. 2013; Ramakrishnan et al. 2023; Sobral et al. 2015), with some covering regions of sky spanning several deg^2.

Large studies of this nature can provide a measure of the field density of star-forming galaxies at certain epochs, although one must be wary of cosmic variance: since large-scale structure exists in the Universe, an observed region of sky may contain overdense and/or underdense regions and thus not be representative of the average density of the Universe. This effect can be mitigated by surveying a large enough area of sky, such that these variations in density effectively cancel each other out, as was the aim with surveys such as the High-z Emission Line Survey (HiZELS; Geach et al. 2008), which covers $\sim$2 deg^2 in the Cosmological Evolution Survey (COSMOS; Scoville et al. 2007) and SXDF Subaru-*XMM*-UKIDSS Ultra-Deep Survey (UDS; Lawrence et al. 2007) fields.

1.5.2 SMGs as environment tracers

While narrowband surveys are useful for targetting star-forming galaxies in the rest-frame optical/NIR, searching for overdensities via obscured star formation

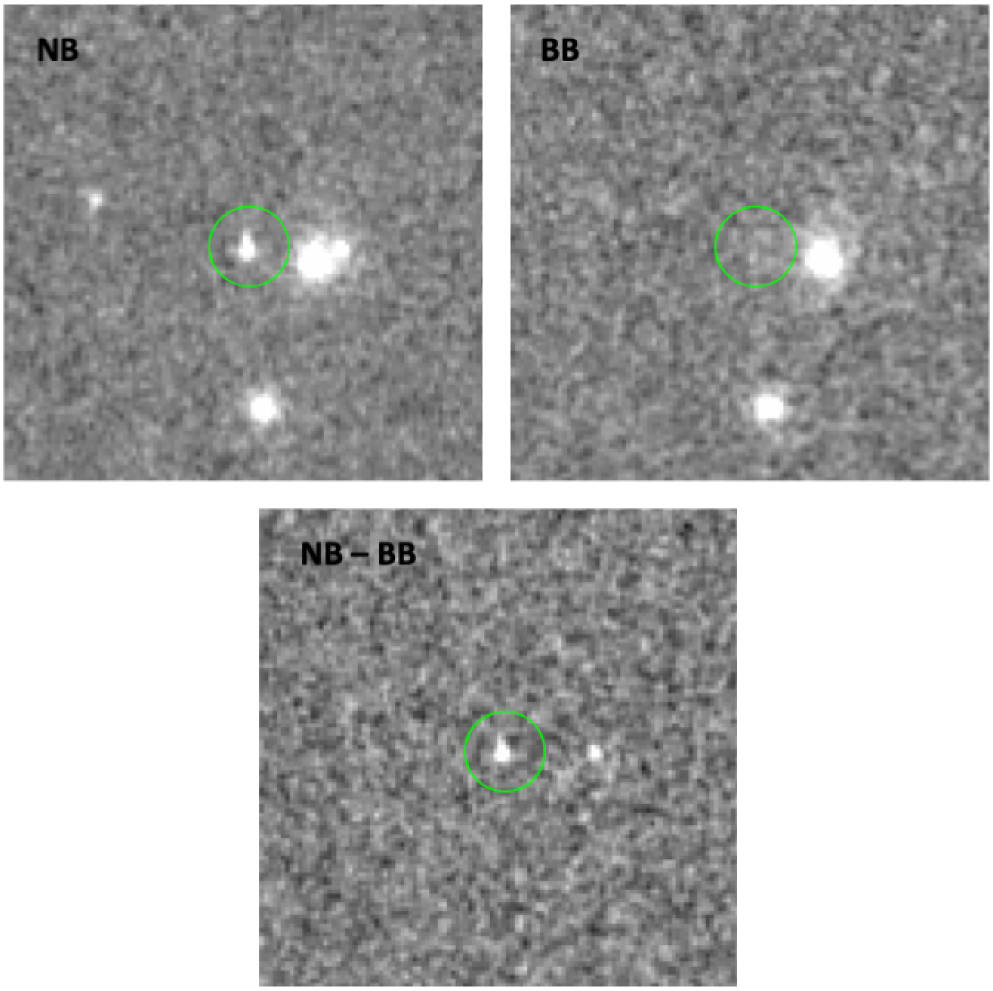

Figure 1.8: Example data used for the identification of emission line galaxies in Chapter 3. The top-left and top-right panels show cutouts from the narrowband (NB) and broadband (BB) images, respectively, centred on the position of an emission line galaxy (marked with a green circle). The bottom panel shows the result of subtracting the BB image data from the NB data. Each panel spans $12''$ on each side. Most of the other galaxies visible in the NB image are no longer visible, while the emission line galaxy still shows a clear signal in the subtracted data.

activity is another challenge entirely. Deep, wide-field surveys in the submillimetre are only possible using single-dish instruments and are therefore plagued by poor resolution, with typical angular resolutions $\gtrsim 10''$. This makes it extremely challenging to identify optical/NIR counterparts, which is further complicated by the fact that SMGs are often optically faint due to their high dust content and high redshifts. Moreover, spectroscopic redshifts are difficult to obtain for the same reason.

Statistical counterpart identification techniques have been developed which exploit correlations between the rest-frame FIR emission (i.e. the observed-frame submillimetre emission in SMGs) and either rest-frame MIR or radio emission. SMGs are typically luminous in both the rest-frame FIR and MIR regimes simultaneously due to their dust content (Elbaz et al. 2002); this correlation can then be used to identify the most likely MIR counterpart near an SMG with a given FIR luminosity (e.g. Biggs et al. 2011; Chapin et al. 2009; Ivison et al. 2004, 2007; Pope et al. 2006). Similarly the radio luminosity of a galaxy is tightly correlated with its FIR luminosity (Condon 1992), such that high-resolution radio interferometry can be used to identify the most likely radio counterpart to an SMG (e.g. Biggs et al. 2011; Chapin et al. 2009; Ivison et al. 2002, 2005, 2007). The low surface density of radio- and MIR-selected galaxies reduces the probability of chance association with the SMG. Reliable counterparts cannot always be identified however, either because they simply are not detected in the MIR and/or radio, or because the probability of any potential counterparts being associated with the SMG by chance is deemed too high.

Submillimetre interferometers such as ALMA remove the need for statistical counterpart identification by being able to spatially resolve SMGs even to sub-arcsecond scales. Furthermore, spectroscopic redshifts can be obtained via the detection of emission lines originating from the ISM that occur in the rest-frame FIR, such as rotational transition lines from carbon monoxide (CO), or fine-structure transitions of singly-ionised carbon ([CII]) or nitrogen ([NII]). However, interferometers are limited by small fields of view, and single-dish instruments remain the most efficient means of surveying large areas in the submillimetre.

Even in lieu of spectroscopic or photometric redshifts, wide-field submillimetre surveys can at least provide a measure of the surface density of SMGs on the sky, and constraints on the average density have been obtained via several such studies (e.g. Casey et al. 2013; Geach et al. 2017; Simpson et al. 2019). Comparisons of the SMG density in a given region of sky with these blank-field estimates can be used to identify the positions of candidate protoclusters: if a structure exists that is overdense with SMGs then it will show up as an excess in the SMG surface density relative to the field. This signal will likely be smoothed by the presence of SMGs in the foreground and/or background of the structure and therefore harder to detect than if one were comparing volumetric densities (e.g. Rigby et al. 2014). Nevertheless, single-dish submillimetre surveys can still be instrumental in narrowing down the search for protoclusters via their dust-obscured star formation activity.

1.6 This thesis

This thesis focuses on furthering our understanding of how massive galaxies in clusters have evolved across cosmic time, by probing the environments of their suspected progenitors at high redshift. Our investigation begins with the use of narrowband observations to search for overdensities of star-forming galaxies in the vicinities of known SMGs, and subsequently infer whether SMGs typically reside in protoclusters. Chapter 2 describes the data used to conduct this investigation, and outlines the bespoke data reduction pipeline written for the calibration of these data. In Chapter 3 we use the resultant catalogue of multiband photometry to identify candidate companion galaxies for each target SMG and deduce the nature of their environments. We then turn our investigation to the most massive radio-quiet galaxies at high redshift to determine if they, like their HzRG counterparts, reside in the most massive dark matter halos at their respective epochs. Chapter 4 describes how we use archival data from the COSMOS field to search for overdensities of SMGs in the environments of a large sample of these galaxies at $z = 1$–3, and discusses the implications for their evolution. Our final conclusions are presented in Chapter 5, along with possible avenues for further investigation.

Throughout this thesis we assume a flat ΛCDM cosmology with $\Omega_{\rm M} = 0.315$, $\Omega_\Lambda = 0.685$ and $H_0 = 67.4$ km s^{-1} Mpc^{-1} (Planck Collaboration 2020). Physical scales with this cosmology are 0.495 Mpc arcmin^{-1} at $z = 1$ and 0.473 Mpc arcmin^{-1} at $z = 3$. All magnitudes are presented in the AB system, where a 1 μJy source has a magnitude of 23.9 (Oke & Gunn 1983).

Chapter 2

NB-ALESS: observations, data reduction and catalogue production

Abstract

Narrowband photometric studies are an efficient tool for surveying large areas of sky in search of galaxies with strong emission/absorption lines. We present our own narrowband study (NB-ALESS), conducted in the Extended *Chandra* Deep Field South (ECDFS) using narrowband and broadband photometry from VLT/HAWK-I. Using a bespoke data reduction pipeline written in PYTHON, we calibrate the raw HAWK-I data and extract photometry from the resultant images, alongside archival broadband images of the ECDFS. A catalogue is produced containing UV-to-MIR photometry for a total of 3929 sources detected in the narrowband filter, which is then used in Chapter 3 to achieve the science goals of NB-ALESS.

2.1 Introduction

NB-ALESS is a narrowband photometric survey with the goal of identifying companion star-forming galaxies for a sample of spectroscopically-confirmed SMGs. By measuring the volume density of companions we aim to test the hypothesis that SMGs are the progenitors of local massive elliptical galaxies in clusters by looking for signatures of protocluster-like environments. The scientific analyses and results of this study are presented in Chapter 3. In this chapter I discuss the observations, the steps involved in creating high-quality narrowband and broadband images, and the production of final catalogues containing new VLT/HAWK-I photometry supplemented with photometry from archival imaging.

The process of converting the raw data from a telescope into images from which robust scientific analysis can be made is non-trivial. One might naïvely expect that the value measured at each pixel on a detector is directly proportional to the amount of light hitting the pixel, but in reality the pixel values consist of contributions from multiple sources. Data reduction is the process of identifying and removing the unwanted contributions, so that the only signal that remains is purely from astronomical sources, or as close to it as possible.

For this study we use data acquired using the High Acuity Wide field K-band Imager (HAWK-I; Casali et al. 2006; Kissler-Patig et al. 2008; Pirard et al. 2004; Siebenmorgen et al. 2011) on the VLT, which is operated by the European Southern Observatory (ESO). While ESO provides pre-made data reduction pipelines for the majority of the instruments at the VLT – including HAWK-I – we opted to write our own dedicated pipeline in Python, so that we could have full control and flexibility with the data reduction process, shaping the pipeline to suit the specific needs of our study.

This chapter is structured as follows: in §2.2 I briefly describe the HAWK-I instrument and the motivation behind its use in this study; §2.3 outlines the selection of target SMGs and the observing strategy; in §2.4 I summarise the steps carried out by our bespoke data reduction pipeline to get from the raw HAWK-I data to science-ready final images; §2.5 outlines the process of identifying sources in the final images and extracting their photometry; §2.6 describes the procedure used to supplement our HAWK-I photometry using archival data; in §2.7 I summarise the final catalogues and how it will be used for the scientific analyses discussed in Chapter 3.

2.2 HAWK-I

HAWK-I is a wide-field near-IR imager with 10 available photometric filters spanning a wavelength range of 0.85–2.5 μm. These filters include four broadband filters (Y, J, H, K_s) and six narrowband filters (NB1060, NB1190, CH_4, NB2090, H_2, Brγ), whose transmission curves are shown in Figure 2.1. Two filter wheels are available (each with six slots) so that light can be passed through two filters if desired. The detector mosaic consists of four Hawaii-2RG chips, each with dimensions of 2048×2048 pixels. The total field of view is $7.5' \times 7.5'$, excluding a cross-shaped $15''$ gap between the chips (see Figure 2.2).

Since 2018 HAWK-I has also included an adaptive optics (AO) system, called the 'GRound layer Adaptive optics system Assisted by Lasers' (GRAAL; Arsenault et al. 2008; Paufique et al. 2010). AO is a technique by which atmospheric disturbance is measured and corrected in real time, for example using a deformable mirror. This can significantly improve the resolution in observations taken by a telescope and consequently reduce the exposure time required to reach a given depth. A bright guide star is required in order to measure wavefront distortions, but AO systems can use lasers to generate a bright reference source in the atmosphere to minimise requirements on the natural guide star. GRAAL uses laser guide stars (LGS) and has an LGS-only mode, which enables some AO correction at any sky position accessible to HAWK-I.

The motivation for using HAWK-I for this study is threefold. Firstly, the Brγ filter ($\lambda_c = 2.165$ μm; $\Delta\lambda = 0.030$ μm) is well-suited for detecting the Hα and [OIII]λ5007 emission lines at redshifts of $z = 2.299 \pm 0.023$ and $z = 3.324 \pm 0.060$, respectively, and its alignment with the K_s filter ($\lambda_c = 2.146$ μm; $\Delta\lambda = 0.324$ μm) allow for easy identification of these emission lines using the narrowband technique. Secondly, the wide field of view, which corresponds to physical scales of $\sim$3.8 Mpc$\times$3.8 Mpc (3.4 Mpc$\times$3.4 Mpc) at $z \sim 2.3$ (3.3), is large enough to cover an appreciable fraction of a protocluster at these redshifts (e.g.

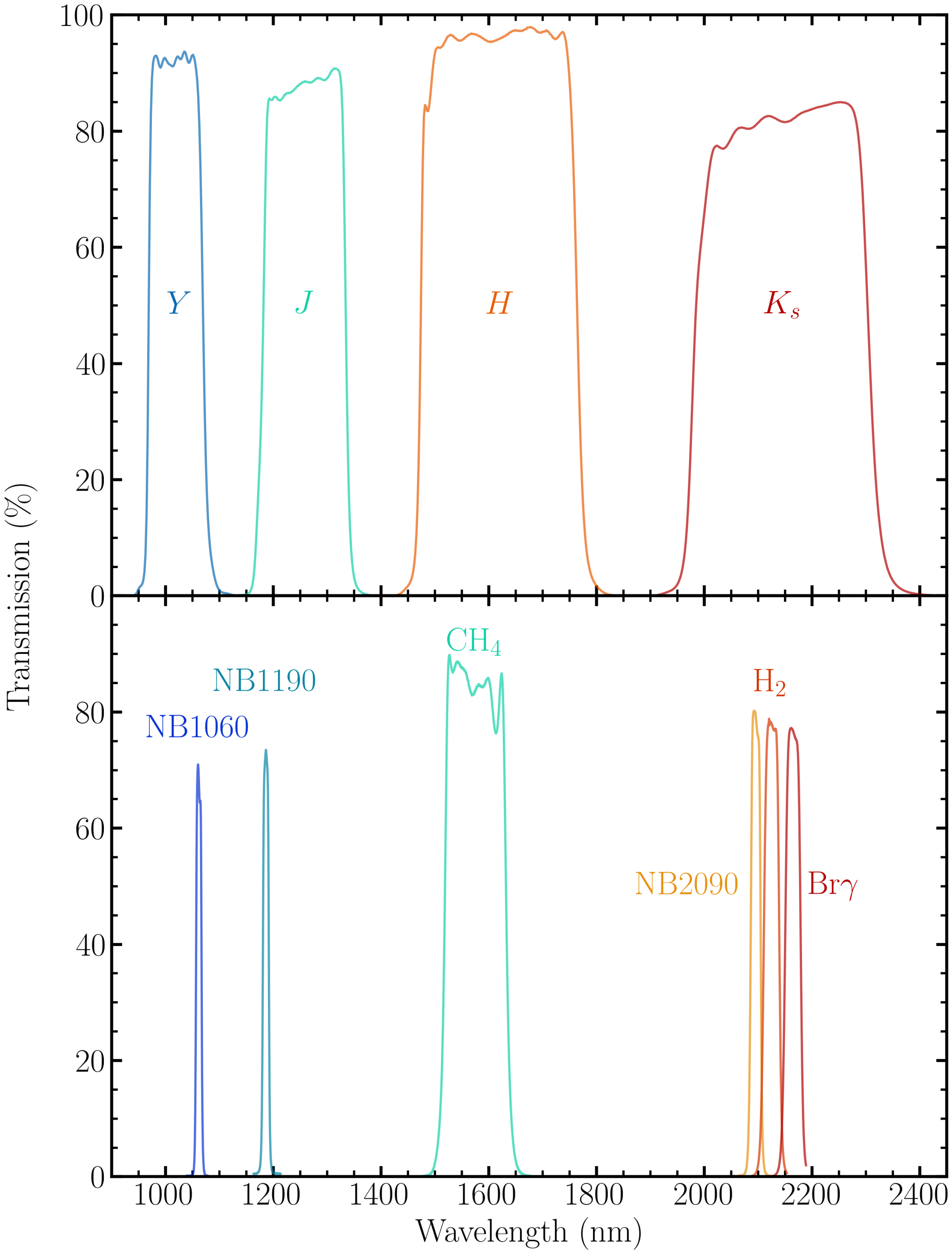

Figure 2.1: Transmission curves of the 10 available HAWK-I filters.

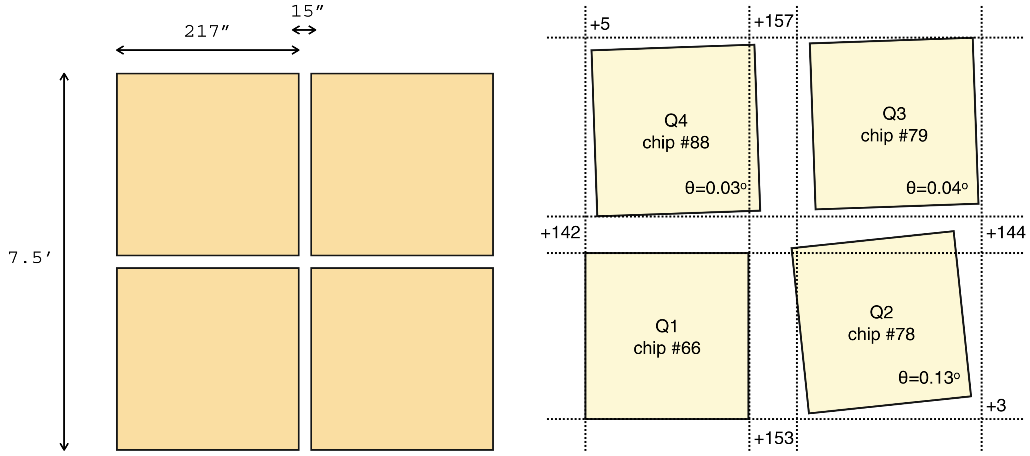

Figure 2.2: Schematics showing the arrangement of the four HAWK-I detectors. *Left:* The HAWK-I field of view on the sky, with the 15″ gap between detectors shown. *Right:* Relative orientation of each detector, with average gap sizes labelled in pixels. Note that the rotation of each detector has been exaggerated for visualisation purposes. Figure from Kissler-Patig et al. (2008).

Chiang et al. 2013; Muldrew et al. 2015; Yajima et al. 2022; see also Figure 2.3). Finally, the improved seeing afforded by GRAAL makes HAWK-I an especially economical tool for obtaining deep observations. In short, HAWK-I was chosen as its wide-field imaging capabilities and photometric filters are synergistic with conducting economical narrowband surveys of protocluster environments at $z \sim 2.3$ and 3.3.

2.3 Observations and sample selection

2.3.1 Sample selection

The blank-field LESS survey observed 0.5×0.5 degrees in ECDFS with APEX/LABOCA and detected 126 sources at $>3.7\sigma$ at 870 μm (Weiß et al. 2009). Each of these sources was followed-up with ALMA to yield the 131 ALESS sources described in Hodge et al. (2013a), divided into a main catalogue of 99 SMGs and a supplementary catalogue of 32 SMGs. The SMGs in the main catalogue all lie within the ALMA primary beam full width at half-maximum (FWHM) of the highest-

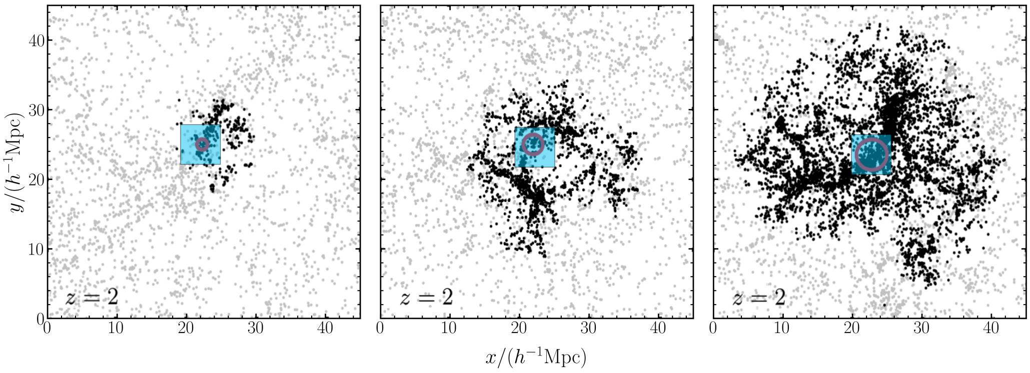

Figure 2.3: Spatial extents of simulated protoclusters at $z = 2$ whose present-day descendants have predicted halo masses of $10^{14.0}$ h^{-1} $\mathrm{M}_\odot$ *(left)*, $10^{14.8}$ h^{-1} $\mathrm{M}_\odot$ *(middle)*, and $10^{15.4}$ h^{-1} $\mathrm{M}_\odot$ *(right)*. Black dots represent protocluster member galaxies, while grey dots symbolise galaxies that are not associated with the structure. The blue square in each panel shows the approximate area that would be covered by a single HAWK-I pointing, which covers an appreciable fraction of the protocluster in all cases. This figure has been adapted from Muldrew et al. (2015).

quality maps, while those in the supplementary catalogue were either extracted from outside the primary beam or from lower-quality maps (Hodge et al. 2013a).

Spectroscopic redshifts are provided for 52 of the 131 ALESS SMGs in Danielson et al. (2017). Targets for this study were selected from ALESS if their spectroscopic redshifts are such that the Hα or [OIII]λ5007 emission lines are shifted into the wavelength coverage of the HAWK-I Brγ filter; this requires that the SMGs are located at $z = 2.299 \pm 0.023$ or $z = 3.324 \pm 0.060$. Of the 52 ALMA-identified SMGs with spectroscopic redshifts from Danielson et al. (2017), five (ALESS 6.1, 75.2, 87.1, 102.1, and 112.1) have spectroscopic redshifts within the desired range for Hα. A sixth SMG (ALESS 5.1) has a CO-derived spectroscopic redshift of $z = 3.303$ (Birkin et al. 2021), which places [OIII] in the Brγ filter coverage.

These six SMGs were the proposed targets for four HAWK-I pointings (PID: 0103.A-0668). The six SMGs are selected purely based on their spectroscopic redshifts, with no consideration of their environments. Of the four pointings, only two were observed during the service-mode observations and the choice of pointings was made by ESO observers (i.e. without bias as to environment). The two observed pointings contain three of the six proposed targets: ALESS 5.1,

Table 2.1: Details of the target SMGs.

SMG	z_{spec}	S_{870} [mJy][a]	mag K_s[b]	Target line[c]
ALESS 5.1	3.303[d]	7.8 ± 0.7	19.79 ± 0.01	[OIII]λ5007
ALESS 75.2	2.294[e]	5.0 ± 1.2	20.67 ± 0.01	Hα
ALESS 102.1	2.296[f]	3.1 ± 0.5	21.07 ± 0.08	Hα

[a] Primary-beam-corrected ALMA 870 μm flux densities from Hodge et al. (2013a).

[b] K_S-band magnitude from Simpson et al. (2014b).

[c] The emission line that is redshifted into the HAWK-I Brγ filter at the SMG redshift (see §2.3.1) and used to identify companion galaxies.

[d] Obtained via detection of the CO(4–3) and [CII] emission lines (Birkin et al. 2020).

[e] Based on Hα+[NII] and [SII] detections (Danielson et al. 2017).

[f] Determined using a combination of Lyα, [CIII] and continuum measurements (Danielson et al. 2017).

ALESS 75.2, and ALESS 102.1, whose spectroscopic redshifts are $z = 3.303$, 2.294, and 2.296, respectively. Details of these three SMGs are provided in Table 2.1. A total of 16 other ALESS SMGs lie within the two HAWK-I pointings, but these are not considered in this study as their redshifts are such that no bright emission lines are expected in the narrowband filter.

2.3.2 Observing strategy

Each pointing was imaged using HAWK-I in the K_s ($\lambda_c = 2.146$ μm; $\Delta\lambda = 0.324$ μm) and Brγ ($\lambda_c = 2.165$ μm; $\Delta\lambda = 0.030$ μm) filters. The FWHM, $\Delta\lambda$, of the Brγ filter is equivalent to $\Delta z = 0.046$ (0.060) or $\Delta v = 6500$ km s^{-1} (7600 km s^{-1}) at $z \sim 2.3$ (3.3). All three observing blocks (OBs) for the pointing containing ALESS 5.1 and 75.2 (hereafter P5_75) were executed on 2019 August 21, while the OBs for the pointing containing ALESS 102.1 (hereafter P102) were split among three separate nights from 2019 August 21 to 2020 January 01. The total exposure times for P5_75 (P102) were 7.2 ks (6.6 ks) and 900 s (660 s) in the Brγ and K_s filters, respectively. Individual exposures of 120 s (Brγ) and

30 s (K_s) were taken using the 'HAWKI img obs AutoJitter' template, with five random dither positions within a $20''$ box for each filter in each OB. Each pointing covers a $7.5' \times 7.5'$ area, except for the cross-shaped gap of width $15''$ between the detector's four arrays (see Figure 2.2). Using HAWK-I's GRAAL system we achieved point spread functions (PSFs) of $\sim 0.4''$ in Brγ and $\sim 0.3''$ in K_s (see Table 2.2).

2.4 PfHAWKI: a Python-based data reduction pipeline for HAWK-I

In order to be able to achieve the intended science goals for the observations captured by HAWK-I, the raw data need to go through the process of data reduction. To this end, we develop a dedicated pipeline written in PYTHON, PfHAWKI, to perform all the steps necessary to create high-quality final images ready for source extraction. This pipeline is based on PfHiZELS (Sobral et al. 2009), with modifications to optimise it for our HAWK-I data.

The pipeline processes can be broadly split into the following steps:

1. *Book-keeping:* the organisation of files included in the raw data downloaded from the ESO archive.

2. *Dark subtraction and flat-fielding:* calibration frames are used to remove artifacts introduced by the detectors from the science frames.

3. *Creation of stacked images:* all calibrated science frames for a given pointing and filter are astrometrically calibrated and combined into one.

4. *Final calibration:* astrometry is finalised and stacked images are photometrically calibrated, ready for source extraction and measurement.

The following subsections explore these steps in more detail.

2.4.1 Book-keeping

Data downloaded from the ESO archive are all of Flexible Image Transport System (FITS) type. FITS files consist of header-data units (HDUs), which in turn contain a 'header unit' and an optional 'data unit'. A single FITS file can contain multiple HDUs, the first of which is known as the 'primary HDU' while subsequent HDUs are referred to as 'extensions'. A data unit contains an N-dimensional array of values, and the accompanying header unit contains metadata to aid with interpreting the data. HAWK-I data are presented in multi-extension FITS files (MEF) with four extensions, one for each of the four HAWK-I detector chips.

Before the pipeline can begin processing the data, all the relevant files need to be sorted into the correct locations. Since observations are grouped into hour-long 'observing blocks' (OBs), and different OBs for a given pointing do not necessarily take place on the same night and are thus subject to variable conditions, the pipeline is designed to initially consider each OB separately. It is only when creating the final images that data from all relevant OBs are considered together. As such, the pipeline requires that the data be downloaded for each OB separately and stored in separate directories, all within a parent directory dedicated to the pointing being observed. Furthermore, files associated with each filter must be grouped separately into subdirectories within the OB directory.

Once the files are downloaded and sorted according to pointing, OB and filter, the pipeline automates the rest of the sorting process. It begins by cycling through each file and retrieving relevant metadata from the primary HDU, including the pointing name, exposure time, date of observations, which filters were in the primary and secondary filter wheel slots (the latter being irrelevant for these data as only one filter was used at a time), the pixel scale (i.e. the number of arcseconds subtended by the length of a pixel), the original file name, and the observation type (either 'science', or a type of calibration frame, such as 'dark' or 'flat'; see §2.4.2). Headers and data for each individual quadrant are then retrieved and saved to separate single-extension FITS files, with the headers updated to include the metadata retrieved from the primary HDU.

Each quadrant is designated a letter to use as a prefix when saving the files: 'w', 'x', 'y' and 'z' are used to denote Q1, Q2, Q3 and Q4, respectively. Within each filter directory, separate subdirectories are made for each quadrant and the files sorted into the relevant ones. The final directory structure therefore obeys the following hierarchy:

- Pointing
    - OB
        - Filter
            - Quadrant

2.4.2 Dark subtraction and flat-fielding

With the science frames and corresponding calibration frames sorted into the relevant directories, we can begin reducing the data. This is done by first calibrating each individual science frame.

Dark subtraction is the process by which the 'dark current' is removed from astronomical observations. This dark current arises from the thermal motion of electrons in the detector, which can generate signal in a pixel even without photons hitting it. To account for this problem, 'dark frames' are produced around the same time as the observations. These have the same exposure times as the science frames but are taken with the shutter closed so that any signal is purely from the thermal motion of electrons.

Within each quadrant subdirectory, the pipeline identifies all science and dark frames with the same exposure time. The selected dark frames are then median-combined: all frames are used to obtain a distribution of values for each pixel, and a new 'master dark' frame is produced containing the medians of these distributions (Figure 2.4). The master dark frame is then subtracted from all science frames in the same directory with the same exposure time.

Next, the dark-subtracted frames need to be flat-fielded. *Flat-fielding* accounts for the non-uniformity in the response of the detector to light, which can arise from vignetting (dimming of an image toward the corners of an image), the presence of dust on the optical elements, or inherent pixel-to-pixel variation in sensitivity. Removing this non-uniformity requires images taken with uniform illumination, using the same filter as for the science frames. These images are

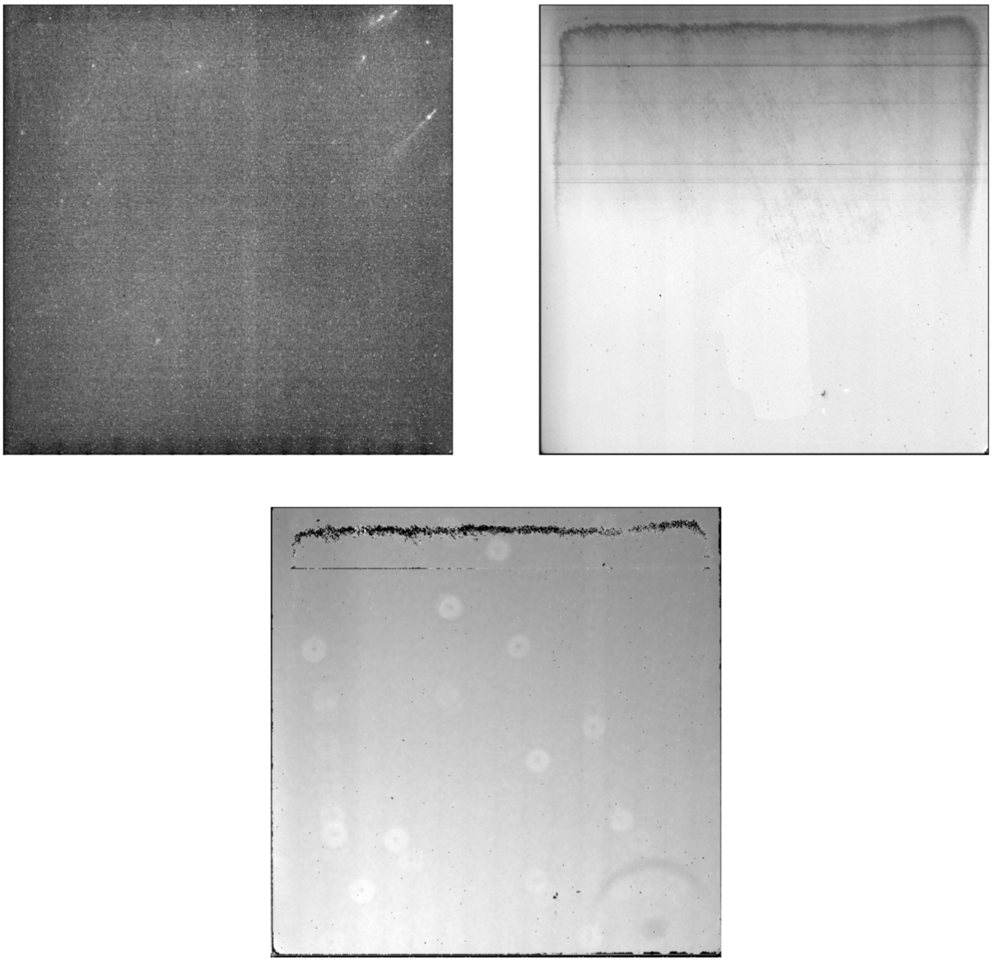

Figure 2.4: Examples of a dark frame *(top-left)*, a twilight flat *(top-right)*, and a 'self-flat' frame *(bottom)*. (See main text for explanations of each.) Note that the brightness of each frame has been scaled for visualisation purposes; the apparent brightness of each pixel does not necessarily correspond to the same value across all three frames.

known as ‘flats’, and are typically obtained by pointing the telescope at the sky during twilight, or at the inside of the dome. For our HAWK-I observations, twilight flats were taken (Figure 2.4).

The pipeline identifies all flats in each quadrant subdirectory, which are already known to have been taken with the same filter due to the way in which the files have been organised (§2.4.1). Since these frames are also susceptible to dark current, dark subtraction is performed on each flat as outlined above. The dark-subtracted flats are median combined to produce a ‘master flat’, which is normalised such that the median of all pixels in the master flat is equal to one. Each science frame is then divided by the master flat.

Some artifacts still remained in the science frames even after flat-fielding – for example, so called optical ‘ghosts’ were sighted due to the telescope being out of focus and causing the secondary mirror to be visible as doughnut-shaped bright regions (Figure 2.5). A second-pass flat-fielding is thus required, which we refer to as *self-flatting*. This process relies on the fact that the HAWK-I observations have been dithered, meaning that the pointing is shifted slightly between taking individual exposures. The result is that sources are not situated at exactly the same pixels in all frames, which allows for fixed-pattern noise/artifacts (e.g hot pixels) to be identified and removed.

Firstly, the source extraction software SExtractor (Bertin & Arnouts 1996) is used to identify sources in each science frame. SExtractor produces segmentation maps for each frame, which contain arrays with the same dimensions as the science frames, where pixels corresponding to extracted sources are assigned positive integers (pixels belonging to the same source are given the same integer) while all other pixels are set to zero. The pipeline converts these into masks wherein source positions are now set to zero while all other pixels are set to one. It is perhaps prudent to discuss at this stage some of the key SExtractor parameters. The first two of these parameters are labelled DETECT_MINAREA and DETECT_THRESH, where the former determines the minimum number of contiguous pixels that need to be above some threshold set by the latter in order for a source to be detected. By default DETECT_THRESH is interpreted by SExtractor as a scaling factor for the background RMS noise: for example a DETECT_THRESH of 3 means that a pixel must be at least 3× the RMS noise in order to be considered part of a prospective source. The third parameter is BACK_SIZE, which pertains to how SExtractor measures the background level: it divides the image into a grid with cells whose size is set by BACK_SIZE, and estimates the local background in each mesh of the grid using a combination of σ-clipping and mode estimation (see Bertin & Arnouts 1996). We found that a DETECT_MINAREA of 8 pixels, a DETECT_THRESH of 2.0, and a BACK_SIZE of 20 were appropriate for creating the segmentation maps used for self-flatting our data.

Secondly, the pipeline cycles through each science frame and retrieves the data from all other science frames in the same directory, along with their corresponding source masks. Each of these other science frames is then normalised by dividing by its median pixel value, and they are then all median-combined while using the masks to exclude pixels at source positions from the calculation of the medians. This results in a bespoke master flat for each science frame (Figure 2.4), by which they are then divided to get the final reduced frames.

Figure 2.5 shows an example science frame undergoing the above steps. The contrast between the raw data and the processed frame is dramatic, highlighting the importance of data reduction. However, it is evident that some features may still remain even after the self-flatting stage: for example, a bright white artifact can be seen at the top of the self-flatted frame in Figure 2.5. Pixels in this region have values of $+\infty$, which is a side-effect of SExtractor detecting 'sources' at these positions in every science frame when producing the segmentation maps, resulting in a divide-by-zero occurring when the science frame is divided by its bespoke master self-flat. While prevalent in many of the frames, it is not an issue for our study, as these features are filtered out in the creation of final stacks (§2.4.3).

2.4.3 Creation of stacked images

With the individual science frames all reduced, the next step is to create one final image per quadrant per filter per pointing, ultimately by median-combining the reduced frames. This process is known as 'stacking' or 'coadding', and serves to increase the signal-to-noise ratio (SNR) above what is achieved in any of the individual science frames. This is because the noise in each frame is random

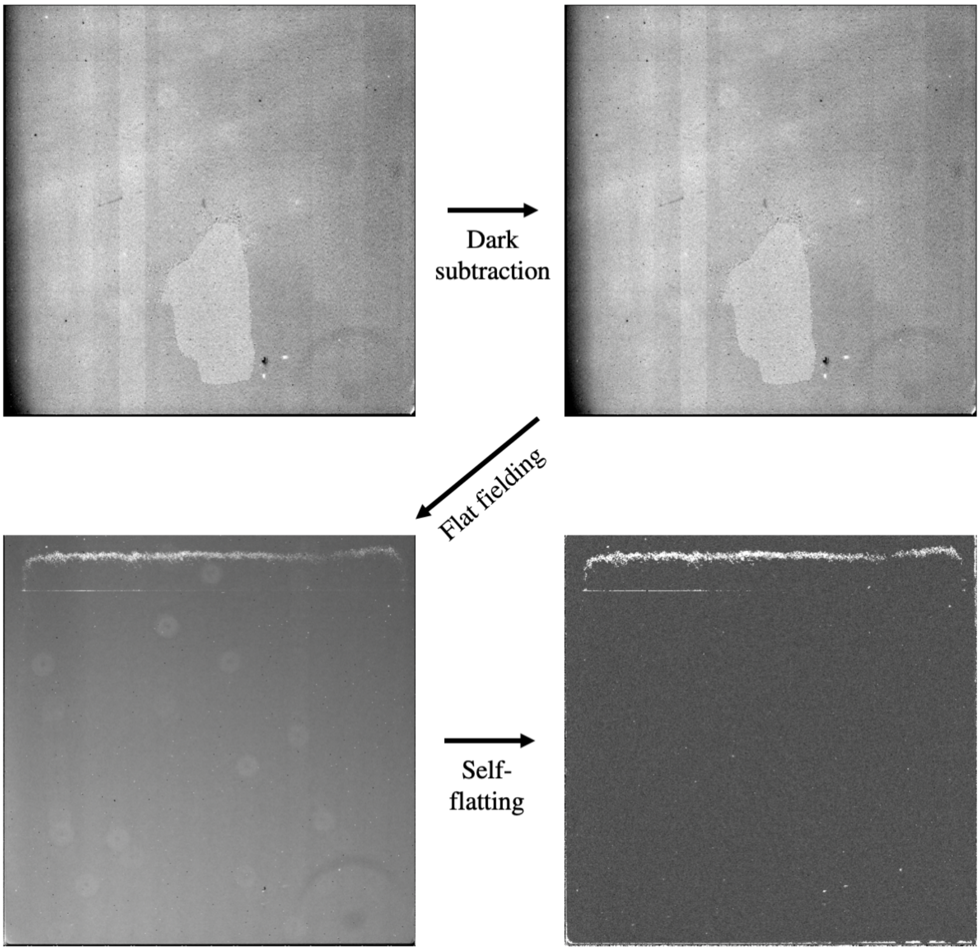

Figure 2.5: A schematic showing a science frame (a 120 s exposure taken with the Brγ filter) from Q1 of the detector, following each stage of the data reduction process. The top-left shows the raw science frame. The top-right shows the frame after dark subtraction, where the change is so small as to seem indistinguishable from the raw frame. In the bottom left is the result of flat-fielding, where several artifacts can still be seen such as bright rings. Most of these features are no longer present in the self-flatted frame at the bottom-right, where the background brightness is also much more uniform and astronomical sources are visible.

and Poissonian, while sources remain at the same position on the sky. Therefore once the frames are stacked, real objects should have approximately the same pixel values while the noise gets averaged out, resulting in a SNR that scales proportionally to the square root of the combined exposure time.

However, before the frames can be stacked their astrometry needs to be calibrated; due to dithering, one cannot simply median-combine the science frames since sources will not be at the same pixel locations in all of them. Furthermore, the astrometry of the final image needs to be calibrated to previous studies of the same regions so that the final catalogues can be cross-matched between bands and compared with existing multiwavelength data.

The astrometry of each individual frame is calibrated by mapping each pixel to the celestial sphere. This is done using SCAMP (Bertin 2006), which requires as input a catalogue containing the uncalibrated astrometric information of sources extracted directly from the science frame, and a reference catalogue containing the coordinates of sources for which the astrometry is already known from some previous data. The latter requires an image with calibrated astrometry. For this we used K_s-band images from the MUltiwavelength Survey by Yale-Chile (MUSYC; Gawiser et al. 2006a; Taylor et al. 2009) and the Taiwan ECDFS NIR Survey (TENIS; Hsieh et al. 2012) as these covered the same regions of sky as our observations. Different reference images were required for each pointing because while TENIS is deeper and has higher resolution, roughly a quarter of the P102 field of view lies outside of the TENIS coverage.

Once a reference image is provided, we run SEXTRACTOR to identify sources in each science frame and the reference image, and save their coordinates to catalogues with the appropriate formatting for SCAMP, which is then run in order to determine the astrometric solution. SCAMP outputs the solution to a '.head' file with the same name as the science frame being calibrated, where this file contains metadata – similar to that found in a FITS header – describing the corrected astrometry.

Once the astrometric solution is calculated, modified versions of each science frame with the corrected astrometry are created. This is done by feeding the SCAMP outputs into SWARP (Bertin 2010), which is designed to resample and/or coadd FITS images. SWARP begins by performing a background subtraction on each frame, implementing the same technique as SExtractor to estimate the background (Bertin & Arnouts 1996; see also §2.4.2). It then resamples the frame by projecting the original grid of pixels onto a new grid defined by the corrected astrometry information contained in the scamp output. New pixel values are calculated via interpolation, for which we use the 'bilinear' option. This interpolates pixel values using a pyramidal response function with a FWHM of 1 pixel, and gives the best results in terms of image depth for our data.

Finally, SWarp coadds the frames, calculating either the median or mean value for each pixel on the resampled grid. We choose not to provide weight-maps for each image since all science frames in a given filter have the same exposure time and thus approximately equal depths; instead we opt for an unweighted median coaddition. Figure 2.6 shows a side-by-side comparison of a single reduced science frame for Q1 taken using a 120 s exposure in the Brγ filter, and the final image obtained by median-combining 60 similar exposures. The resultant increase in depth is clearly visible, and the artifacts that still remained in the single frame are minimised by stacking.

Achieving a good astrometric solution requires some degree of fine tuning with regards to the SExtractor settings used to create the input catalogues for scamp. Ideally each extracted catalogue would feature a large number of bright sources spread across the entire coverage of the science frame being calibrated, as this allows scamp to more reliably match sources between images. Ensuring each frame produces such a catalogue is not always trivial however, as a high detection threshold can leave too few sources to sufficiently constrain the astrometry across the whole science frame. Conversely, lowering the threshold can result in the detection of faint, poorly centroided sources, or sources that are unmatched in the reference catalogue, which can confuse the fitting procedure that scamp uses. This in turn can result in poor depth in the final stacks, or manifest as visible distortions, particularly at the edges and corners of the image.

In order to generate catalogues containing a sufficient number of widely-distributed sources in all frames we first use Python to median combine the frames that are taken at the same dither position (typically 2-4 exposures) to create 'dither-grouped coadds' (DGCs). scamp and SWarp are not required for this since sources will be located at the same pixel positions in these frames.

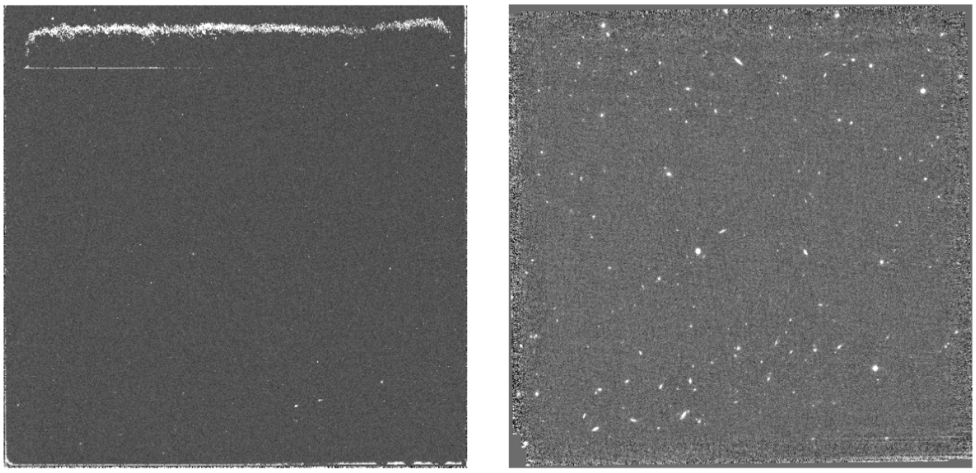

Figure 2.6: A side-by-side comparison of a single calibrated science frame *(left)* with the final stacked image in the same filter and quadrant *(right)*. The depth of the latter is significantly improved relative to the former, such that many more astronomical sources become visible. Noisy regions at the edges show where fewer of the science frames overlap due to the telescope dithering. The white artifact seen in the single science frame is no longer visible in the stack as median-combining the frames effectively ignores these values.

Catalogues are then obtained from each DGC with SExtractor, run with a moderately high detection threshold of 4.0 (a DETECT_MINAREA of 8 pixels is used at all stages of this process). In this way we obtain catalogues containing real astronomical sources which would have lower SNRs in the individual science frames without having to use a lower detection threshold. The catalogues from each DGC are then visually inspected alongside the reference catalogue and, by looking at the source positions in both the catalogue and the images, any dubious sources or sources that were likely to confuse SCAMP are removed.

SExtractor is then run on the individual frames with a lower detection threshold, which identifies as many real sources as possible, but also includes spurious objects. To remove the spurious objects the pipeline cross-matches this low-threshold catalogue with the catalogue extracted from its corresponding DGC to create a robust, deep catalogue with sources widely distributed across the frame. This is fed into SCAMP along with the reference catalogue so that it can finally determine the astrometric solution for each science frame.

2.4.4 Final calibrations

With the final stacks created for each quadrant of each pointing in each filter, a final astrometric recalibration is performed to ensure that sources with existing astrometric information from prior studies have consistent astrometry in the stacks. As with the individual frames, this is done using a combination of SExtractor, SCAMP and SWarp. However, since the stacks generally reach a greater depth than any individual frame, the process is simplified greatly by the ability to run SExtractor with a relatively high SNR threshold while still detecting enough sources to sufficiently constrain the astrometric solution. We therefore run SExtractor with a detection threshold of 4.0 and feed the resultant catalogues (along with the same reference catalogues as before) directly into SCAMP with no additional fine-tuning. SWarp is then run to resample the image and map it to the corrected astrometry.

Finally, the photometry is calibrated by determining and scaling the photometric zeropoint (ZP) of each image. This calibration is necessary to ensure that the photometry extracted from the final images is physical and consistent with existing photometry. Moreover, in order to conduct narrowband studies like the one performed in Chapter 3, the broadband and narrowband photometry need to have the same ZP.

To calibrate the ZP of each image (treating the stacks for each quadrant separately), SExtractor is first run using a detection threshold of 3.0, capturing the majority of bright sources and minimal interlopers. The resultant catalogue contains photometry as measured in bespoke apertures which SExtractor determines for each source according to its light profile (see Bertin & Arnouts 1996). When running SExtractor at this stage, we use 'MAG_ZEROPOINT' = 0 such that the uncalibrated magnitudes (m) measured by SExtractor are a direct conversion from the photon counts:

$$m = -2.5 \log_{10}(\text{counts}). \tag{2.1}$$

The catalogue is then cross-matched with a reference catalogue containing broadband photometry in the same (or equivalent) photometric bands. Since the pointings observed for our study lie within the ECDFS region of the sky, the MUSYC (Gawiser et al. 2006a; Taylor et al. 2009) K_s-band catalogue is used for photometric calibration. Once provided with this reference catalogue, PfHAWKI cross-matches it with the output from SExtractor using a matching radius of $1''$.

The next objective is to identify bright stars in the final stacks, so that these can be used to calibrate the ZP. This is done by selecting all sources whose apparent magnitudes in the reference catalogue are within a range defined by the user, which requires some fine tuning: if the range extends too bright (i.e. lower apparent magnitudes) then some of the selected stars will saturate the detector and thus produce unreliable photometry. If sources that are too faint are selected then the photometry will be affected by noise and scatter. As a representative example, we found that a range of 16 to 20 mag was suitable for K_s-band observations (see Figure 2.7). We additionally remove any sources for which SExtractor measures the FWHM of the light profile to be $> 1''$, as these sources are not point-like and therefore unlikely to be stars.

Once suitable calibration sources are identified, the difference between their magnitudes in the reference catalogue and the SExtractor-derived values, Δm, is calculated. An iterated 2σ clip is then performed on Δm to remove any outliers that might negatively impact the accuracy of the ZP estimation, and the measured ZP is the median value of Δm for the remaining sources. The image ZP is then recalibrated to a common value of 30 for all final stacks by multiplying each pixel value by a factor determined with the following equation:

$$f_{\mathrm{new}} = 10^{0.4(30-\mathrm{ZP})} f_{\mathrm{old}}, \tag{2.2}$$

where f_{old} and f_{new} are the old and new pixel values, respectively.

Figure 2.7 shows example colour-magnitude diagrams for sources detected (using a SNR threshold of 3) in the Brγ stacks for each quadrant in one of our HAWK-I pointings, P5_75. The colour along the y-axis is equivalent to Δm, where m_{AUTO} is the apparent Brγ magnitude measured by SExtractor in the stacks. Note that even though the Brγ images are being calibrated here, the SExtractor-derived magnitudes are still being compared with K_s magnitudes from MUSYC. This comparison is still valid because the Brγ filter is centred close to the middle of the K_s filter (Figure 2.1), and bright stars are not expected to have strong emission or absorption lines at these wavelengths, such that their K_s and Brγ AB magnitudes are expected to be approximately equal. Sources ultimately used for the ZP estimation are highlighted, and the final ZP estimate is shown with a dashed line.

2.5 Source extraction

Once all the steps implemented by PfHAWKI have been completed, the final stacks are ready for source identification and photometric measurements. However, even in the final stacks there are some regions which are unreliable and masked for these purposes. These regions are typically contaminated by light from a nearby bright star, or have a high noise level, as is the case at the edges of the image where fewer frames overlap due to dithering.

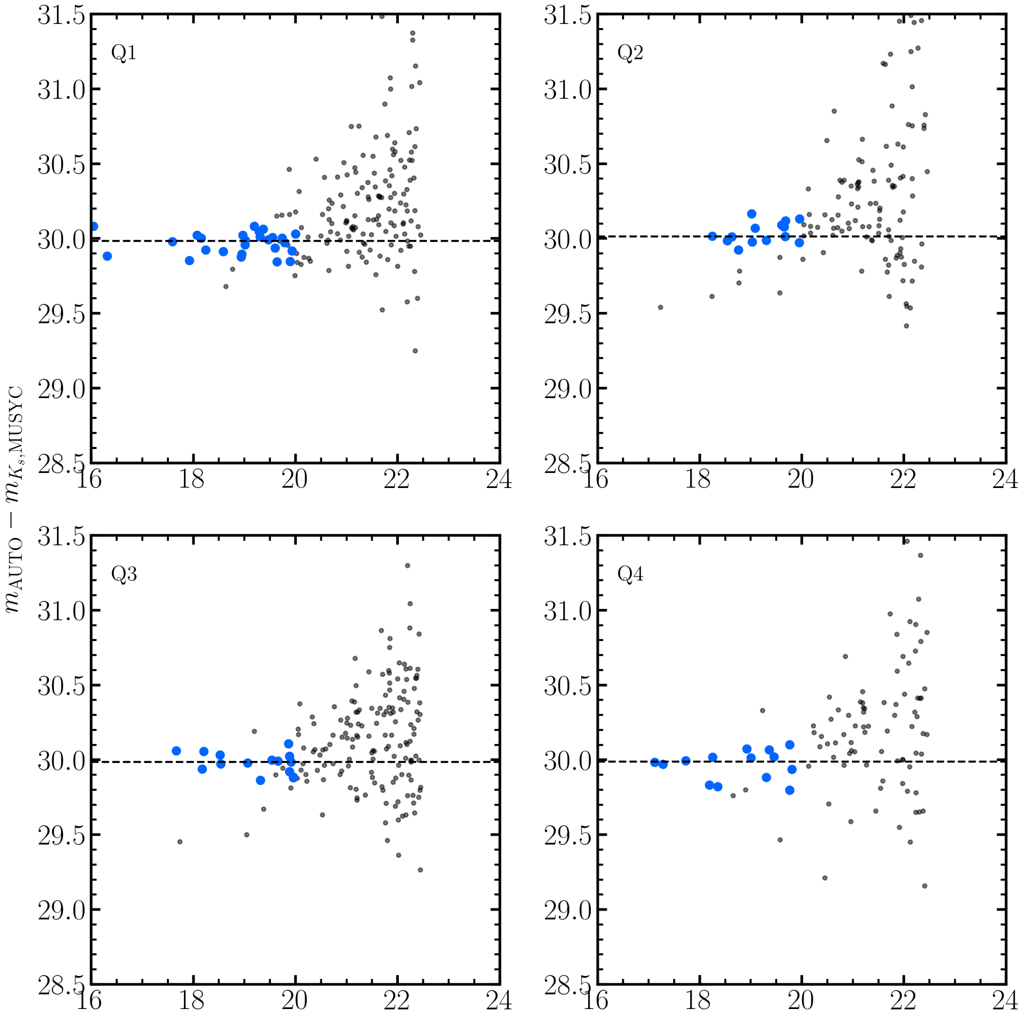

Figure 2.7: Example of the zero-point calibration process, applied to the final Brγ stacks for each quadrant in P5_75. Grey dots show all sources with Brγ detections in the quadrant above a detection threshold of 3; blue circles show the subset of these sources that meet the selection criteria (see text). Dashed lines show the median colour for the highlighted sources, which is used as an estimate of the image ZP.

To avoid extracting photometry in such regions, masks are created in PYTHON for each image, where these are FITS files containing data with the same dimensions as the image in question. The data consist of 1s at every pixel except those belonging to the undesired regions. These can then be provided to SEXTRACTOR as additional input, from which it will infer that sources should not be extracted from these regions.

Source detection and photometry were then conducted (on each quadrant individually) by running SEXTRACTOR in 'dual-image mode'; the stacked Brγ images were used to identify the positions of sources, and then photometry was extracted at these positions in both the Brγ and K_s images to ensure that any difference between the measured Brγ and K_s photometry is a purely intrinsic property of the sources and not caused by positional offsets. Using a DETECT_THRESH of 1.6 and DETECT_MINAREA of 10 pixels, we detected a total of 2175 sources in P5_75 and 1754 in P102. Apertures with a diameter of $1.25''$ were used, as this was large enough to contain the majority of the flux for all detected sources while minimising the amount of additional background noise captured. The positions of these sources are marked with green circles on Figure 2.8, which shows the final stacks for each of the two observed HAWK-I pointings in the Brγ filter, with all four quadrants aligned according to their relative positions. It can also be seen from this figure which regions were masked and ignored for source extraction, especially at the edges of each quadrant.

The apparent magnitudes of each source are calculated by SEXTRACTOR from the counts measured in each aperture using:

$$m = -2.5 \log_{10}(\text{counts}) + \text{ZP}, \tag{2.3}$$

where we know ZP to be 30 mag (see §2.4.4). Limiting magnitudes at the 3σ level are measured by placing 5000 apertures with a diameter of $1.25''$ across each image, avoiding the positions of extracted sources with the help of segmentation maps produced by SEXTRACTOR. First, the median of the counts measured in the 5000 apertures is calculated and subtracted from all of them. A 3σ clip is then performed on the resultant distribution of counts. The standard deviation

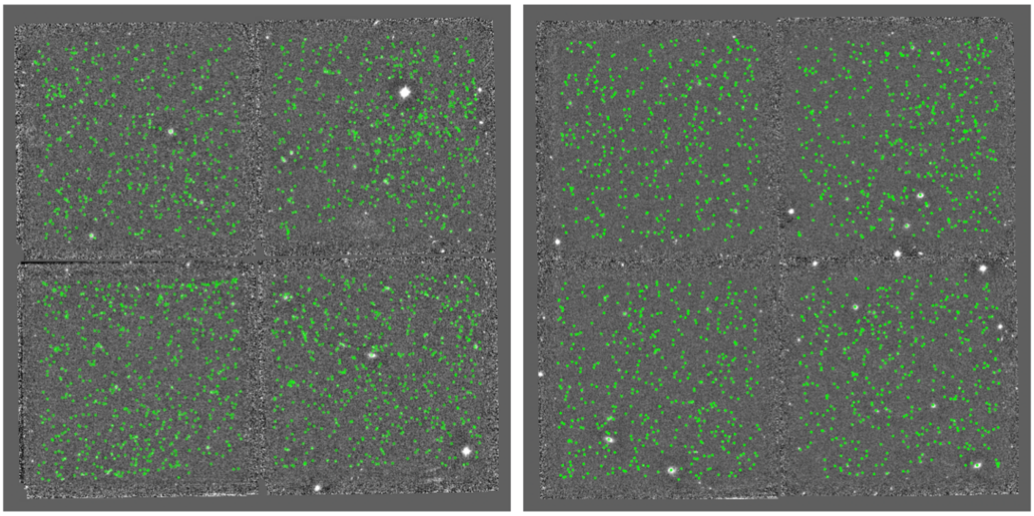

Figure 2.8: Final Brγ stacks for all four quadrants in each of the two HAWK-I pointings observed for NB-ALESS, P5_75 (left) and P102 (right). Positions of detected sources are highlighted with green circles.

of the remaining aperture counts is then taken to be the rms noise. Values corresponding to the 99.73 percentile are used to estimate the 3σ limiting magnitudes via Equation 2.3. These are provided for each filter and each HAWK-I detector chip in Table 2.2.

Corrections are applied to the $1.25''$ aperture magnitudes, $m_{\rm APER}$, by comparing with the magnitudes calculated by SExtractor using adaptively scaled apertures that match the light profile of each source, $m_{\rm AUTO}$. In each pointing in each filter, the median value of $\Delta m = m_{\rm AUTO} - m_{\rm APER}$ is calculated for bright, point-like sources (selected using a magnitude cut of $16.0 < m_{\rm AUTO} < 19.5$ mag), which is then added to the $1.25''$ aperture magnitudes for all sources. The values of these corrections are provided in Table 2.3. The uncertainty in the correction is estimated by generating 10000 $m_{\rm APER}$ and $m_{\rm AUTO}$ values for each source used in its estimation, where these values are randomly drawn from Gaussian distributions with means equal to their $m_{\rm APER}$ and $m_{\rm AUTO}$ values, and widths equal to the 1σ uncertainties in each of these quantities measured by SExtractor. The aperture correction is calculated for each of these 10000 magnitude pairings and the standard deviation of the resultant distribution is used as the uncertainty in

---

[1] Quadrants are assigned the same labels as in Casali et al. (2006).

Table 2.2: Limiting 3σ AB magnitudes and resolution for each stacked image. Limiting magnitudes are measured using $1.25''$ apertures. Due to variation in the four HAWK-I detector chips, each quadrant[1] is considered separately.

Pointing	Quadrant	$m_{\rm lim}^{3\sigma}$		PSF ($''$)	
		Brγ	K_s	Brγ	K_s
P5_75	Q1	24.29	24.01	0.28	0.27
	Q2	24.19	24.27	0.27	0.27
	Q3	24.30	24.19	0.35	0.26
	Q4	24.22	24.27	0.32	0.26
P102	Q1	24.09	23.85	0.38	0.30
	Q2	24.08	24.00	0.37	0.30
	Q3	24.19	24.01	0.44	0.30
	Q4	24.11	24.09	0.41	0.29

Table 2.3: Magnitude corrections, c_m, applied to the photometry measured in fixed $1.25''$ apertures.

Pointing	Filter	c_m
P5_75	Brγ	-0.027 ± 0.002
	K_s	-0.027 ± 0.002
P102	Brγ	-0.122 ± 0.002
	K_s	-0.061 ± 0.002

the correction. Uncertainties in the corrected magnitudes are then derived by adding the SExtractor-derived uncertainty in $m_{\rm APER}$ and the uncertainty in the aperture correction in quadrature.

2.6 Ancillary photometry

So that we may ultimately fit SEDs for the galaxies in our sample (§3.2.2), we also extract fixed-aperture photometry at their HAWK-I Brγ positions in images spanning the UV to MIR. These images were sourced from the MUSYC 2010 Public Data Release (Cardamone et al. 2010) and TENIS (Hsieh et al. 2012). The MUSYC dataset consists of $UU_{38}BVRI$ broadband images from the Wide Field Imager (WFI) on the MPG/ESO 2.2m telescope (Hildebrandt et al. 2006); 5000 Å narrowband and z' broadband imaging from the Mosaic-II camera on the CTIO Blanco 4m telescope (Gawiser et al. 2006a,b), with JK_s broadband imaging from the Infrared Sideport Imager on the same telescope (Taylor et al. 2009); 18 medium-band (IA427, IA445, IA464, IA484, IA505, IA527, IA550, IA574, IA598, IA624, IA651, IA679, IA709, IA738, IA767, IA797, IA827, IA856) images taken with the Subaru telescope's Suprime-Cam (Cardamone et al. 2010); *Spitzer*/IRAC images at 3.6, 4.5, 5.8 and 8.0 μm (Cardamone et al. 2010; Damen et al. 2011)[1].

Each image is astrometrically calibrated using SCAMP (Bertin 2006) and SWARP (Bertin 2010) to match the astrometry of our HAWK-I images, and then photometrically recalibrated so that all images have a zeropoint magnitude of 30.0 mag. Photometry is extracted in fixed apertures using the PHOTUTILS PYTHON package (Bradley et al. 2022); apertures of diameter $2.0''$ are used for all images except those from *Spitzer*/IRAC, for which we use apertures of diameter $3.8''$ due to the larger point spread function (PSF). Aperture corrections are determined for each filter by measuring the median difference between the magnitudes measured in these apertures and those measured in adaptively scaled apertures with SEXTRACTOR for bright point sources. Final corrections are applied to each filter to account for Galactic attenuation, using values from Cardamone et al. (2010) and Hsieh et al. (2012).

2.7 Conclusions

We have developed a bespoke data reduction pipeline for HAWK-I observations dedicated to conducting a narrowband survey of SMG environments. Beginning with the raw science and calibration frames provided by ESO, this pipeline dark subtracts and flat-fields each science frame and stacks them to produce high-quality final images with 3σ limiting magnitudes ranging from 24.08–24.30 (23.85–24.27) mag in the Brγ (K_s) filter. Significant care is taken when calibrating the astrometry and photometry at the relevant stages.

The final catalogue produced in this Chapter contains the astrometry (RA and Dec.), the UV-to-MIR photometry (total magnitudes and corresponding un-

---

[1] H-band data are also available but our pointings are not covered.

certainties) extracted from our reduced HAWK-I data and from archival images, and unique IDs for all 3929 sources detected in the narrowband images. This catalogue is now ready for application of the narrowband technique to identify emission-line galaxies, and for the fitting of SEDs to derive properties such photometric redshift, star formation rate and stellar mass. As will be demonstrated in Chapter 3, this is the first step towards identifying galaxies in the environments of the SMGs that are the targets of NB-ALESS.

Chapter 3

NB-ALESS: an unbiased study of SMG environments measured with narrowband imaging

Abstract

Submillimetre galaxies (SMGs) are some of the most extreme star-forming environments in the Universe, whose place in the universal framework of galaxy evolution is as yet uncertain. It has been hypothesised that SMGs are progenitors of local early-type galaxies, which would imply that SMGs should reside in galaxy cluster progenitors at high redshift. We test this hypothesis and explore SMG environments using a narrowband VLT/HAWK-I study of Hα and [OIII] emitters around an unbiased sample of three ALMA-identified and spectroscopically-confirmed SMGs at $z \sim 2.3$ and $z \sim 3.3$. The target SMGs were selected based only on spectroscopic redshift and with no consideration of their surroundings. We compare with blank-field observations at similar epochs, and find that two of the three SMGs (ALESS 75.1 and ALESS 5.1 at $z \sim 2.3$ and $z \sim 3.3$, respectively) reside in environments that are overdense on the $\sim$ 4 Mpc scale of the HAWK-I field of view with overdensity parameters of $\delta_g = 2.6^{+1.4}_{-1.2}$ and $4.0^{+15}_{-3.2}$, respectively. On this scale the environment of ALESS 102.1 is consistent with the blank field, having $\delta_g = 0.2^{+0.6}_{-0.5}$, but on smaller scales ($\sim$ 1.6 Mpc) the environment of ALESS 102.1 is also significantly overdense. These results are consistent with two of the three SMGs being in spatially-extended, high-redshift overdensities, as expected of the progenitors of local early-type galaxies, with the remaining target being in an evolving smaller galaxy group. The total masses of the overdensities are estimated to be $\log(M_h/\mathrm{M}_\odot) = 12.4$–14.3, 12.7–14.4, and 12.4–14.4 for ALESS 5.1, 75.2 and 102.1, respectively, leading to present-day masses of $\log(M_{h,z=0}/\mathrm{M}_\odot) = 13.9$–16.6, 13.6–15.8, and 13.0–15.9. For ALESS 5.1 and 75.2 these values are similar to high-redshift protoclusters identified with other methods

and are broadly consistent with the progenitors of Fornax- or Coma-like clusters. The region around ALESS 102.1 also has the potential to evolve into a cluster of similar mass, however its mass is uncertain and it may instead evolve into a present-day galaxy group.

3.1 Introduction

As was discussed in §1.4.1, the question of whether SMGs are the progenitors of massive elliptical galaxies in clusters remains uncertain. While SMGs have been found to reside in protoclusters (as expected of these progenitors), these are not necessarily representative of the general SMG population since these systems were selected for detailed follow-up based on prior evidence of galaxy overdensities (e.g. Casey et al. 2015; Daddi et al. 2009; Ivison et al. 2013; Walter et al. 2012). Meanwhile clustering studies present a complex and inconclusive picture due to large uncertainties and methodological differences between studies (e.g. García-Vergara et al. 2020; Hickox et al. 2012; Stach et al. 2021; Wilkinson et al. 2017). Furthermore they can only provide information for the SMG population as a whole; the nature of individual SMG environments is not explored.

The objective of NB-ALESS is to obtain targeted observations exploring the environments of individual SMGs and determine if these environments are consistent with the progenitors of galaxy clusters. By targeting individual SMGs which were selected based only on their spectroscopic redshifts and with no prior knowledge of their environments, we aim to determine the nature of a 'typical' SMG while avoiding the biases of previous studies. In Chapter 2 we described the VLT/HAWK-I observations undertaken for this narrowband photometric survey, as well as the steps taken to calibrate the data and combine them with archival data to produce a catalogue of UV-to-MIR photometry for all sources detected in the HAWK-I data. We now use that photometry to identify galaxies sharing the same environments as our target SMGs and determine the nature of these environments.

The structure of this Chapter is as follows: §3.2 describes the methodology used to identify galaxies associated with each target SMG; in §3.3 we explore the properties of each SMG environment; our conclusions are presented in §3.4.

3.2 Mapping the SMG environments

3.2.1 Emission line galaxy selection

Star-forming galaxies at the same redshifts as our target SMGs ($z \sim 2.295 \pm 0.023$ for ALESS 75.2 and ALESS 102.1; $z \sim 3.324 \pm 0.030$ for ALESS 5.1) have emission lines that are redshifted into the narrow wavelength coverage of the Brγ filter. Since the Brγ filter is near the centre of the K_s transmission a galaxy without line emission at these wavelengths will have a (K_s–Brγ) colour of zero. However, due to the narrow width of the Brγ filter relative to the K_s filter, galaxies with redshifts that place an emission line in the narrow Brγ filter will have a (K_s–Brγ) colour that is significantly greater than zero. We employ the same methodology as previous narrowband surveys (e.g. Geach et al. 2008; Moorwood et al. 2000; Sobral et al. 2013) to identify line-emitting galaxies. This methodology uses two parameters to select sources with a significant, physically-driven narrowband excess, as opposed to an excess due to random noise.

The first of these parameters, Σ, quantifies the significance of the narrowband excess compared to the expected random scatter for a source with zero (K_s–Brγ) colour (Bunker et al. 1995). Σ is given by:

$$\Sigma = \frac{1 - 10^{-0.4(\mathrm{BB}-\mathrm{NB})}}{10^{-0.4(\mathrm{ZP}-\mathrm{NB})}\sqrt{\mathrm{rms}_{\mathrm{NB}}^2 + \mathrm{rms}_{\mathrm{BB}}^2}}\,, \tag{3.1}$$

where NB and BB are the apparent magnitudes in the narrowband (Brγ) and broadband (K_s) filters, respectively; ZP is the zeropoint magnitude of the narrowband images; $\mathrm{rms}_{\mathrm{NB}}$ and $\mathrm{rms}_{\mathrm{BB}}$ are the rms counts in $1.25''$ apertures for the individual narrowband and broadband quadrants, respectively. We require candidate line-emitters have $\Sigma > 3$, which is consistent with previous narrowband studies (e.g. Bunker et al. 1995; Sobral et al. 2013); see Figures 3.1 and 3.2. Note that this Σ does not correspond directly to signal-to-noise (SNR) in the Brγ filter, but is a separate quantity based on counts; $\Sigma > 3$ implicitly excludes sources with SNR $\lesssim 8$ in Brγ (for details see e.g. Sobral et al. 2009).

In addition to having $\Sigma > 3$, line emitters are required to have an observed equivalent width (EW) > 50Å. The EW is calculated for each source using:

$$\mathrm{EW} = \Delta\lambda_{\mathrm{Br}\gamma} \frac{f_{\mathrm{Br}\gamma} - f_{K_s}}{f_{K_s} - f_{\mathrm{Br}\gamma}(\Delta\lambda_{\mathrm{Br}\gamma}/\Delta\lambda_{K_s})}\,, \tag{3.2}$$

where $\Delta\lambda_{\mathrm{Br}\gamma}$ and $\Delta\lambda_{K_s}$ are the widths of the two filters and $f_{\mathrm{Br}\gamma}$ and f_{K_s} are the flux densities of the source in each filter. The 50 Å lower limit on EW for a source to be selected as a line emitter was chosen to lie above the 3σ scatter in (K_s–Brγ) colours for bright (Br$\gamma < 19.5$ mag) sources in both pointings (Figures 3.1 and 3.2).

Before applying the selection criteria, we first account for sources that are detected with $\geq 3\sigma$ significance in the Brγ filter but $<3\sigma$ in K_s. We classify these sources as non-detections in K_s, and replace their aperture magnitudes with the relevant 3σ limiting magnitude (see Table 2.2). However, several of these non-detections have counterparts in the S14 catalogue (within a $1''$ matching radius) and thus have K_s magnitudes from either TENIS (Hsieh et al. 2012), archival HAWK-I observations (Zibetti et al., in prep.), or MUSYC (Taylor et al. 2009). For these sources, we replace our HAWK-I K_s photometry with values from one of these surveys, preferentially using TENIS photometry as it is the deepest of the three; if no TENIS photometry is available then we opt for the archival HAWK-I values, using MUSYC only when no photometry exists for either of the other two, as it has the poorest depth and seeing of the three.

Using the $\Sigma > 3$ and EW > 50 Å selection criteria, 81 and 80 candidate line emitters are identified in P5_75 and P102, respectively (Figures 3.1 and 3.2). Of these candidates, 30 are K_s non-detections with no K_s photometry in the S14 catalogue, and thus Σ and EW are calculated by assuming that their K_s magnitudes are equal to the 3σ limiting magnitudes of our data. Since this can only provide a lower limit for the (K_s–Brγ) colour and thereby underestimate Σ for these sources, we do include these sources in our sample of candidate line emitters.

Finally, we visually inspect all 161 candidates line emitters, removing stars and image artefacts. The final sample consists of 79 and 68 candidate line emitters in P5_75 and P102, respectively (147 sources in total).

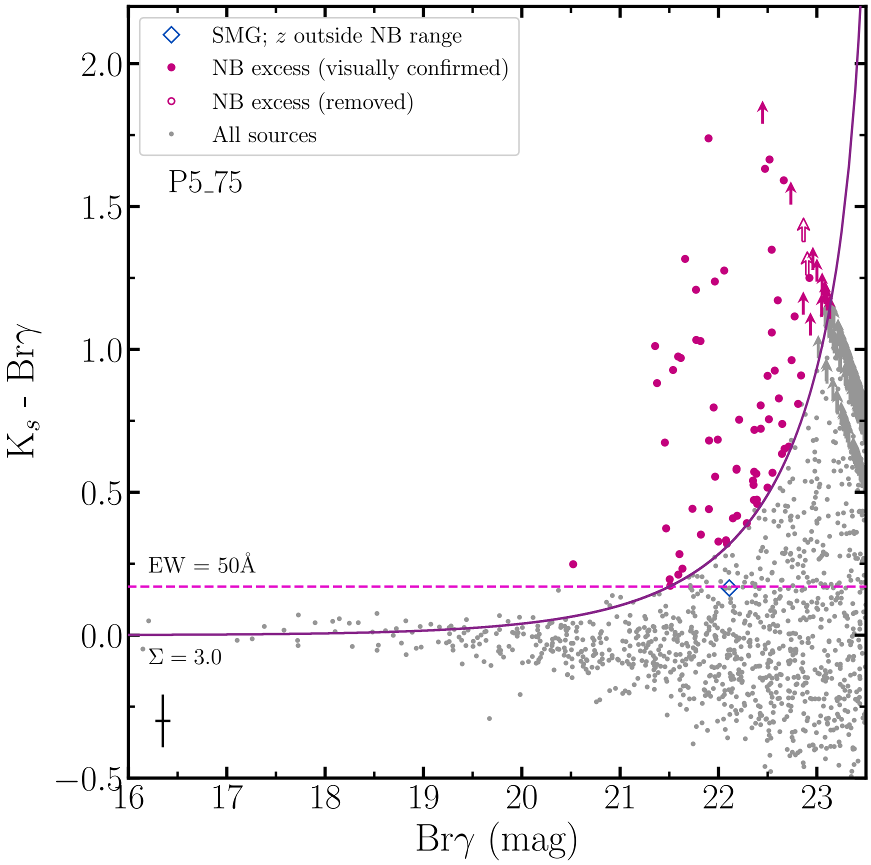

Figure 3.1: Colour-magnitude diagrams demonstrating the criteria described in §3.2.1 for the selection of candidate narrowband emitters in the field containing ALESS 5.1 & 75.2 (P5_75). All sources detected in the Brγ observations are shown and sources identified as narrowband emitters are highlighted. Open symbols represent candidate narrowband emitters which were removed from the sample following visual checks. Sources that are detected in Brγ but are undetected in our K_s data and have no K_s photometry in S14 are shown as lower limits. The $\Sigma = 3$ curve for the average properties and the observed-frame equivalent width cut for the field are shown. ALESS SMGs with counterparts in our HAWK-I data are highlighted. Several ALESS SMGs within the field of view (including the two target SMGs, ALESS 5.1 and 75.2) are not detected and are therefore not shown. The black cross in the bottom left corner shows the mean uncertainties in colour and Brγ magnitude. Note that the thick grey bands towards the right of the figure are the result of several overlapping arrow symbols, caused by a high density of K_s non-detections in this part of the colour-magnitude space.

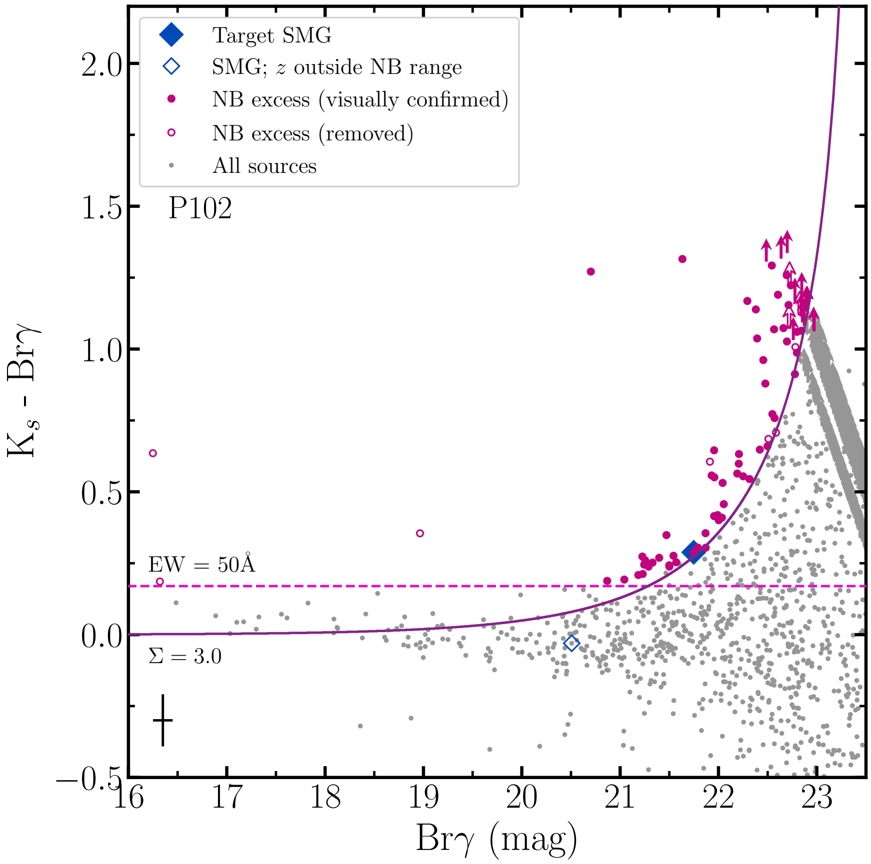

Figure 3.2: The same as Figure 3.1 but for the pointing containing ALESS 102.1 (P102). Note that in this pointing the target SMG is detected in the HAWK-I data and is therefore highlighted.

3.2.2 Identifying line emitters associated with the SMGs

Narrowband excess alone is not sufficient to identify star-forming galaxies in the same environments as our target SMGs; such an excess could be caused by a number of possible bright emission lines at different redshifts (e.g. Figure 3.4). We therefore use the wealth of available multi-band photometric data covering our pointings to estimate photometric redshifts for the narrowband emitters in our sample. The S14 catalogue contains photometric redshift estimates for sources across the ECDFS, however after cross-matching with our data (using a matching radius of $1''$), a significant fraction (>30 percent) of the line emitters identified in §3.2.1 do not have broadband counterparts in this catalogue and thus lack any redshift information. We therefore use the multiband photometry obtained in Chapter 2 to perform our own spectral energy distribution (SED) fitting using EAZY-PY[1], an updated version of the photometric redshift code EAZY (Brammer et al. 2008) written in PYTHON.

EAZY-PY operates using a χ^2-minimisation procedure in which linear superpositions of template SEDs are tested at different redshifts to find an optimal fit to the observed fluxes (Brammer et al. 2008). In keeping with other recent studies which implement EAZY-PY (e.g. Finkelstein et al. 2022; Stevans et al. 2021), we use the "tweak_fsps_QSF_12_v3" set of 12 template SEDs, which cover a wide range of galaxy types and utilise a Chabrier (2003) initial mass function (IMF) and a Kriek & Conroy (2013) dust attenuation law while assuming solar metallicity. An advantage of these templates is that they are inclusive of emission lines, such that a narrowband excess can provide a relatively tight constraint on the redshift.

We also make use of spectroscopic redshifts in the ECDFS from studies whose areas overlap with our pointings, obtained from publicly-available composite catalogues[2,3] (Silverman et al. 2010). The spectroscopic redshifts used are from the VIMOS VLT Deep Survey (VVDS; Le Fèvre et al. 2005); the GOODS/VIMOS survey (Balestra et al. 2010; Popesso et al. 2009); the Extended *Chandra* Deep

---

[1] `https://github.com/gbrammer/eazy-py`

[2] `https://www.eso.org/sci/activities/garching/projects/goods/MasterSpectroscopy.html`

[3] `http://member.ipmu.jp/john.silverman/CDFS_vlt.html`

Field-South Survey (Silverman et al. 2010); and Treister et al. (2009). Additionally we utilise the results of the spectroscopic study conducted as part of ALESS by Danielson et al. (2017). Using a matching radius of 1.5″, we cross-match our data with these catalogues. This gives spectroscopic redshifts for 163 (∼4.1 percent) of the 3929 sources detected in our HAWK-I imaging, including nine for which photometric redshifts could not be estimated due to insufficient photometry. Seven of the 163 sources with spectroscopic redshifts are emission line galaxies selected in §3.2.1; the spectroscopic redshifts for these sources are used for our analyses. We compare the photometric and spectroscopic redshifts for our HAWK-I sources in Figure 3.3. There is strong agreement between the photometric and spectroscopic redshifts, which is quantified using the normalised median absolute deviation (NMAD) of Δz:

$$\sigma_{\mathrm{NMAD}} = 1.48 \times \mathrm{median}\left(\left|\frac{\Delta z - \mathrm{median}(\Delta z)}{1 + z_{\mathrm{spec}}}\right|\right) , \tag{3.3}$$

where z_{spec} is the spectroscopic redshift and $\Delta z = z_{\mathrm{spec}} - z_{\mathrm{phot}}$, with z_{phot} being the photometric redshift. We obtain $\sigma_{\mathrm{NMAD}} = 0.062$ when considering all 152 HAWK-I detections with photometric and spectroscopic redshifts.

Only five (∼3.4 percent) of the emission line galaxies have neither spectroscopic nor photometric redshifts, the latter being due to a lack of photometry with sufficient depth. Figure 3.4 shows the redshifts of the remaining 142 emission line galaxies, compared with the significance of their narrowband excess (Σ; Equation 3.1). Peaks in the redshift distribution are visible at $z \sim 2.3$ (both pointings) and $z \sim 3.3$ (P5_75 only), as expected of Hα and [O III] in the environments of the target SMGs. We select as Hα ([O III]) emitters any galaxies for which $2.23 < z < 2.37$ ($3.23 < z < 3.41$), where these redshift ranges correspond to 3× the FWHM of the Brγ filter when Hα ([O III]) has redshifted to the centre. We represent these selection criteria with shaded regions in Figure 3.4; the highlighted galaxies are henceforth assumed to be Hα and [O III] emitters at similar redshifts as the target SMGs. We identify 44 Hα emitters and 4 [O III] emitters in P5_75, and in P102 there are 11 Hα emitters ([O III] emitters in P102 are not further considered because there is no SMG at $z \sim 3.3$ in this pointing). Table

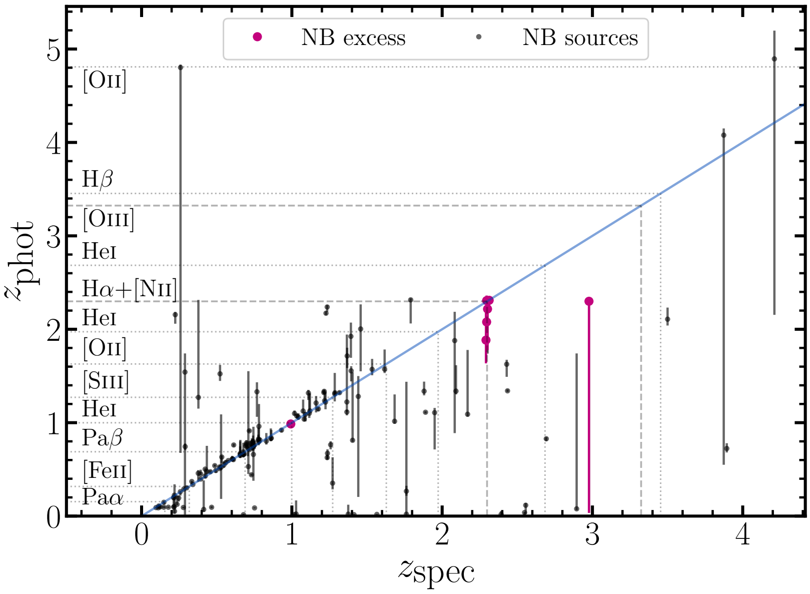

Figure 3.3: Photometric redshifts from EAZY-PY (Brammer et al. 2008) compared to spectroscopic redshifts for all sources detected in HAWK-I Brγ with archival spectroscopic redshifts (from Balestra et al. 2010; Danielson et al. 2017; Le Fèvre et al. 2005; Popesso et al. 2009; Silverman et al. 2010; Treister et al. 2009). Galaxies included in our final sample of candidate line emitters (see §3.2.1) are highlighted. The redshifts at which common extragalactic emission lines enter the Brγ filter are shown using horizontal and vertical lines; dashed lines highlight Hα and [OIII], which are the emission lines of interest in this study. The diagonal line shows a one-to-one correspondence; the scatter is low and the majority of sources have photometric redshifts that are consistent with their spectroscopic redshifts. The NMAD (Equation 3.3) is 0.062, indicating good agreement between our photometric redshifts and the archival spectroscopic redshifts.

3.1 summarises the results of each step in the sample selection.

To identify any AGN in the sample we use a $1''$ matching radius to locate counterparts in the Lehmer et al. (2005) *Chandra* point source catalogue. None of the [OIII] emitters and only one of the Hα emitters (2.3%) is an X-ray luminous AGN, which is consistent with the rate of X-ray AGN in blank-field surveys of Hα emitters at the same redshift (e.g. $1.8 \pm 1.3\%$ in Calhau et al. 2017). Since the AGN fraction is the same as in field surveys then this galaxy is kept in our sample to enable a fair like-for-like comparison between the SMG fields and blank field Hα emitters.

Figure 3.5 shows the distributions of emission line galaxies across the HAWK-I pointings, with Hα and [OIII] emitters highlighted. For all three target SMGs, the companion galaxies are spread across the entire field of view and therefore span several physical Mpc. This is consistent with expectations from simulations (e.g. Chiang et al. 2013; Muldrew et al. 2015; Yajima et al. 2022, see also §3.3.3), in which protoclusters are seen to extend over several Mpc, such that the entire structure is unlikely to be captured by a single HAWK-I pointing. We also note the presence of a dense clump of seven Hα emitters (three of which are spectroscopically confirmed at $z \sim 2.3$) in the northeast of P5_75, which coincides with a photometrically-identified Lyα blob at $z \sim 2.3$ (CDFS-LAB03; Yang et al. 2010). This is discussed further in §3.3.3.

Of the three SMGs targeted, only ALESS 102.1 is identified as an Hα (or [OIII]) emitter in our data. Danielson et al. (2017) did not identify ALESS 102.1 as an Hα emitter in their spectroscopy, because the wavelength coverage with VLT/FORS2 and VLT/VIMOS does not cover Hα at $z \sim 2.3$. The original spectroscopic redshift for ALESS 5.1 is from CO(4-3) (Birkin et al. 2020) and no emission lines were observed in Keck/DEIMOS, Keck/MOSFIRE or VLT/XSHOOTER observations (Danielson et al. 2017); this is likely because the redshifted [OIII] line clashes with a bright OH$^-$ sky line for this source (Ramsay et al. 1992). For ALESS 75.2 the original spectroscopic redshift was measured, in part, thanks to a faint Hα line detected in Keck/MOSFIRE observations (Danielson et al. 2017), which is below the detection limit of our data.

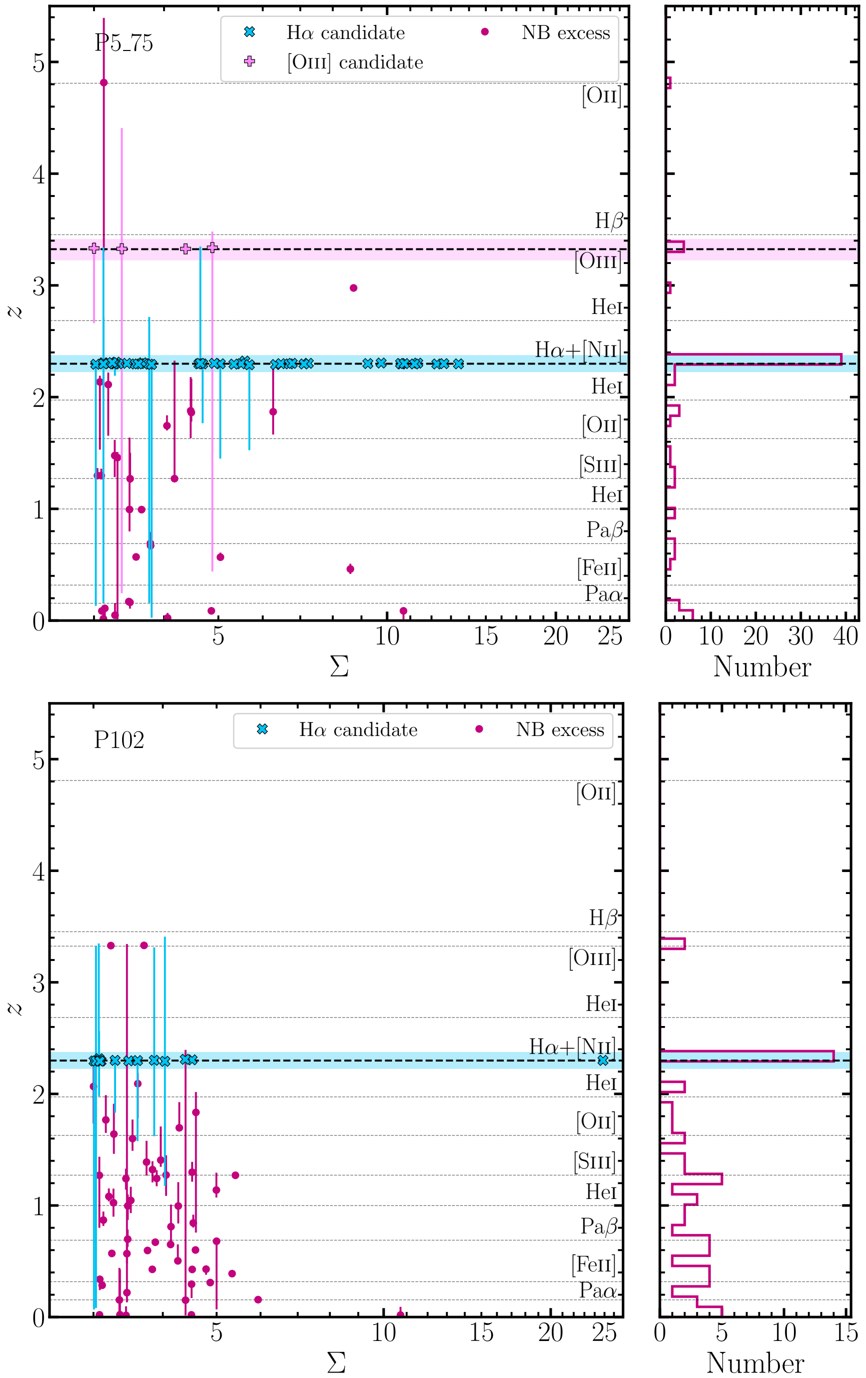

Figure 3.4: The distributions of redshifts for the emission line galaxies in P5_75 *(top)* and P102 *(bottom)* compared with their emission-line significance, Σ. Photometric redshifts are computed using EAZY-PY (Brammer et al. 2008), with archival spectroscopic redshifts included where available (§3.2.2). Hα and [OIII] emitters are highlighted, and shaded regions show the redshift ranges used to select them. Peaks in the redshift distributions at these redshifts may be driven by overdensities of these line emitters. Horizontal dashed lines show the redshifts at which other common extragalactic emission lines enter the Brγ filter.

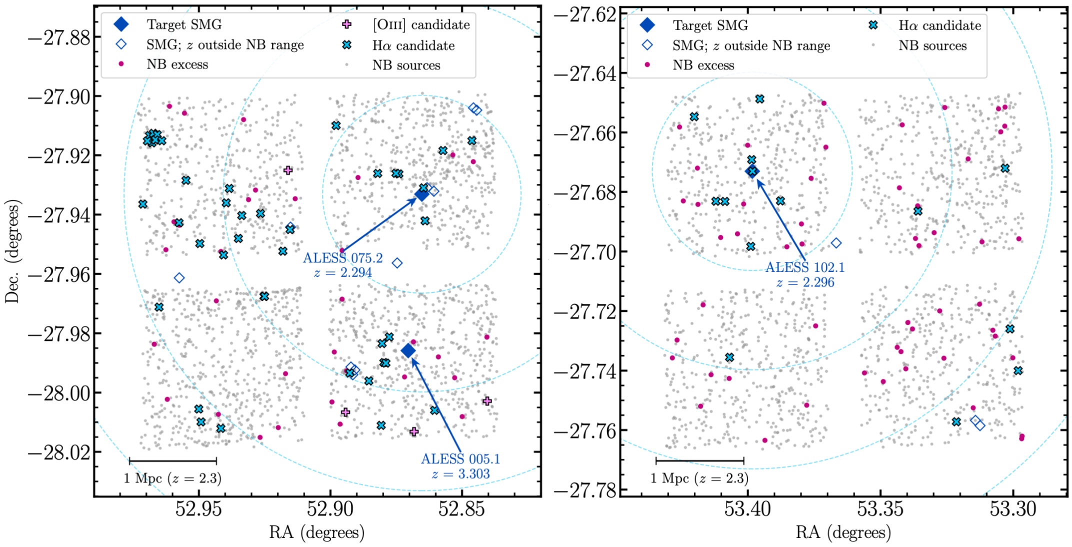

Figure 3.5: Spatial distribution of the emission line galaxies and the other Brγ detections in the pointings P5_75 *(left)* and P102 *(right)*. Also shown are the positions of the target SMGs and other ALESS SMGs in these areas, although the redshifts of the non-target SMGs are either unknown or outside the ranges that would place the Hα or [OIII] emission lines in the Brγ filter (Birkin et al. 2020; Danielson et al. 2017). Hα and [OIII] candidates are indicated. While P102 does contain [OIII] candidates, they are not shown here because there are no ALESS SMGs at $z \sim 3.3$ in this pointing. For all three SMGs, the candidate companion galaxies are distributed across the entire HAWK-I field of view, corresponding to physical spans of a few Mpc, as expected from protoluster simulations (e.g. Chiang et al. 2013; Muldrew et al. 2015; Yajima et al. 2022). Dashed circles show the boundaries of annuli used to measure radial trends in the density of companion galaxies (§3.3.3).

Table 3.1: Summary of the sample at each stage of the selection process described in §3.2.1 and §3.2.2.

	Number per pointing		
	P5_75	P102	Total
Brγ detections	2175	1754	3929
Line emitter candidates (initial)	81	80	161
Line emitter candidates (confirmed)	79	68	147
Hα candidates	44	11	55
[OIII] candidates	4	2	6

3.3 The nature of SMG environments

3.3.1 Measuring luminosity functions

In order to quantify whether the SMGs reside in significant overdensities of Hα or [OIII] emitters, a comparison to the blank field needs to be drawn. The High Redshift (z) Emission Line Survey (HiZELS; Geach et al. 2008) is a large narrowband survey of emission line galaxies, including Hα emitters at $z = 2.23$ (Sobral et al. 2013) and [OIII] emitters at $z = 3.24$ (Khostovan et al. 2015) in COSMOS. The HiZELS results are therefore representative of Hα and [OIII] emitters in regions of average density at redshifts similar to those of our target SMGs, and we use their luminosity functions as a blank-field sample for comparison with our results.

To construct luminosity functions for our Hα and [OIII] emitters we bin them according to line luminosities, making corrections to the observed number counts in each bin to account for completeness, contamination from other emission lines, dust attenuation, and the shape of the narrowband filter profile. Each of these steps is described in more detail below.

3.3.1.1 Survey volumes

Approximating the Brγ filter profile as a top-hat function with width equal to the FWHM of the filter ($\Delta\lambda = 0.030$ μm), the Hα emission line should be detectable from $z_{\rm min} = 2.276$ to $z_{\rm max} = 2.322$, corresponding to a comoving volume per square degree of 5.86×10^5 cMpc^3 deg^{-2}. The redshift range within which [OIII] can be detected extends from $z_{\rm min} = 3.294$ to $z_{\rm max} = 3.354$, which gives 1.04×10^6 cMpc^3 deg^{-2}. Accounting for the high-noise regions that were masked prior to source detection (see §2.5) and the gaps between the HAWK-I detector chips, the surveyed areas in P5_75 and P102 are 0.0117 and 0.0118 deg^2, respectively. The volumes probed are therefore: 6859 cMpc^3 for Hα in P5_75; 6891 cMpc^3 for Hα in P102; 12180 cMpc^3 for [OIII] in P5_75; 12230 cMpc^3 for [OIII] in P102. In §3.3.1.6 we correct the derived luminosity functions to account for the fact that the Brγ filter is not a perfect top-hat function, which leads to the volume probed being slightly different for sources with different luminosities.

3.3.1.2 Completeness correction

It is possible that real galaxies with weak emission lines were missed in our selection process (§3.2.1) despite actually meeting the selection criteria: the sample is incomplete at low emission line fluxes. We correct for this using the method employed by Sobral et al. (2013), applying it separately for each quadrant of each pointing due to the variation in depth between detector chips (see Table 2.2). For each emission line (Hα and [O III]), we select sources that failed to meet the emission line galaxy selection criteria (i.e. sources for which EW < 50 Å and/or $\Sigma < 3$) with redshifts within the range used to identify the targeted emission line (see §3.2.2). Due to the size of these samples, we generate $\sim$1000 mock galaxies by randomly varying the K_s and Brγ magnitudes of the selected galaxies according to their uncertainties and placing them at random positions within their quadrant, removing any sources for which these changes result in them being classed as a line emitter. We then artificially inject line flux to each galaxy in this bolstered sample of non-line emitters, beginning with $10^{-22}\,\mathrm{erg\,s^{-1}\,cm^{-2}}$ and incrementally increasing it by 0.05 dex. Line fluxes are calculated as

$$F_{\mathrm{line}} = \Delta\lambda_{\mathrm{Br}\gamma}\frac{f_{\mathrm{Br}\gamma} - f_{K_s}}{1 - (\Delta\lambda_{\mathrm{Br}\gamma}/\Delta\lambda_{K_s})}\,, \tag{3.4}$$

where $f_{\mathrm{Br}\gamma}$ and f_{K_s} are the Brγ and K_s flux densities, respectively, in units of erg s^{-1} cm^{-2} Å^{-1}. With each increment of injected line flux, we recalculate the EW and Σ and reapply the line emitter selection criteria to determine the catalogue completeness as a function of line flux. This is used to estimate the completeness corrections for our luminosity functions. The uncertainty in the completeness at a given line flux is estimated by regenerating the mock galaxies 1000 times and measuring the standard deviation in the completeness across all iterations.

3.3.1.3 Removing [N II] contamination

The Hα emission line lies in between a doublet of [N II] lines at rest-frame wavelengths of 6548 Å and 6583 Å, which will contribute to the measured Brγ flux density and therefore affect the observed EW and emission line flux. Using spectroscopic data taken with Subaru/FMOS and Keck/MOSFIRE, Sobral et al.

(2015) observed an anti-correlation between the [NII]λ6583-to-Hα line flux ratio and the rest-frame EW ($\mathrm{EW_{rest}} = \mathrm{EW}/(1+z)$) for the H$\alpha$ emitters in HiZELS, deriving the following empirical relation:

$$\frac{F_{[\mathrm{N\,II}]}}{F_{\mathrm{H}\alpha}} = -0.296 \times \log_{10}(\mathrm{EW}_{\mathrm{rest,H}\alpha+\mathrm{N\,II}}) + 0.8\,. \tag{3.5}$$

We adopt this relation to apply corrections to the line fluxes of all Hα emitters in our sample, resulting in a median decrease of 11^{+9}_{-5} percent in emission line flux.

3.3.1.4 Relative contributions from [OIII]λ5007, [OIII]λ4959 and Hβ

Thus far only the [OIII]λ5007 emisson line has been considered in the discussion of [OIII] emitters at $z \sim 3.3$. However, this line is part of a doublet, with its counterpart residing at a rest-frame wavelength of 4959 Å, and there is a narrow range of redshifts (z = 3.336–3.344) in which both lines can contribute to a galaxy's Brγ flux. Furthermore, while the Hβ emission line is sufficiently separated from the [OIII] doublet to avoid contaminating the measured [OIII] line flux, it is still close enough such that there is the potential for Hβ emitters to be misidentified as [OIII] emitters (see Figure 3.4). Therefore, rather than try and separate our sample into [OIII]λ5007, [OIII]λ4959 and Hβ emitters, we present a combined [OIII]+Hβ luminosity function; this also allows for a consistent comparison with the blank-field [OIII]+Hβ luminosity function from Khostovan et al. (2015).

We do however take into account the results of Sobral et al. (2015) when estimating the total volumes probed by the Brγ filter in the search for [OIII] emitters: using spectroscopy, Sobral et al. (2015) find that for HiZELS ~50 percent of photometrically-selected [OIII]+Hβ emitters at $z \sim 1.4$ are [OIII]λ5007, ~27 percent are [OIII]λ4959, ~16 percent are Hβ, with the remaining ~7 percent being simultaneous detections of [OIII]λ5007 and [OIII]λ4959. Based on these results, Sobral et al. (2015) then add to the total volume probed (i.e. the volume probed if searching for [OIII]λ5007 emitters) 16 percent of the volume that would be probed had their search been for Hβ, and 25 percent of the volume had they been searching for [OIII]λ4959. We thus apply similar corrections to our total volume probed for [OIII]λ5007 emitters.

3.3.1.5 Corrections for dust attenuation

Dust in star-forming galaxies reprocesses light emitted in the rest-frame UV and optical, and can therefore reduce the amount of Hα and [OIII] flux observed. In order to estimate the intrinsic brightness of the emission lines (i.e. their integrated luminosities), one has to correct for the effect of dust attenuation. For an attenuation of $A_{\rm line}$ (mag) at the emission line wavelength, the conversion from line flux to intrinsic line luminosity is

$$L_{\rm line} = 4\pi D_{\rm L}^2 F_{\rm line} \times 10^{0.4A_{\rm line}}\,, \tag{3.6}$$

where $D_{\rm L}$ is the luminosity distance. We follow Sobral et al. (2013) and assume an attenuation at the Hα wavelength of $A_{\rm H\alpha} = 1$ mag, which is based on previous HiZELS studies (Garn et al. 2010; Sobral et al. 2012). Khostovan et al. (2015) do not correct for dust attenuation when plotting their luminosity functions, so we also leave our [OIII]+Hβ luminosities uncorrected to ensure a consistent comparison. Khostovan et al. (2015) later go on to calculate the dust-corrected star formation rates (SFRs) of their galaxies, where they then assume an attenuation of $A_{\rm [OIII]+H\beta} = 1.35$ mag, derived by assuming $A_{\rm H\alpha} = 1$ mag and using a Calzetti et al. (2000) dust attenuation curve. We thus adopt the same correction when calculating our own SFRs (see §3.3.4).

3.3.1.6 Filter profile volume corrections

The comoving volumes used for our luminosity functions (§3.3.1.1) are calculated by approximating the Brγ filter as a top-hat filter with width equal to the Brγ FWHM. Since the filter profile is not a top-hat in reality, this introduces two main effects which need to be accounted for when estimating the galaxy number densities. Firstly, bright emitters whose line falls near the edges of the Brγ filter will suffer a significant loss of line flux and thus appear to be fainter than they really are. This produces an overall bias towards faint sources in our sample. Secondly, any faint emitters close to the filter edges might be missed from our sample, and are therefore only detectable over a narrower redshift range (and thus a smaller volume) than their bright counterparts.

To correct for these effects, we follow the method used by Sobral et al. (2013) and Khostovan et al. (2015), as first proposed in Sobral et al. (2009). An initial fit is performed to the uncorrected[1] data using a Schechter function (Schechter 1976):

$$\Phi(L)dL = \ln(10)\Phi^* \left(\frac{L}{L^*}\right)^{\alpha+1} e^{-(L/L^*)} d\log L\,, \tag{3.7}$$

where $\Phi(L)$ is the number density at luminosity L, Φ^* is the normalisation of the luminosity function, L^* is the characteristic luminosity, and α is the slope at the faint end of the luminosity function, where the power-law component dominates. We then generate a mock sample of 10^5 fake sources with a luminosity distribution that is weighted by the uncorrected Schechter function. These sources are randomly assigned redshifts with a uniform distribution across the whole possible Brγ coverage. They are then convolved through the Brγ filter profile such that their luminosities decrease according to their assigned redshift (i.e. according to the position of the redshifted emission line in the filter profile) and rebinned using the same luminosity bins as for the uncorrected data. Comparing the resultant distribution to the input distribution reveals that the number of bright sources is underestimated relative to the fainter sources, as expected. The real data are corrected using the ratio of these distributions.

3.3.1.7 Fitting Schechter functions

Finally, we perform fits to the corrected data using a Schechter function of the form given in Equation 3.7. The faintest bins (open symbols in Figures 3.6 and 3.7) are excluded from each fit due to their low completeness. For the Hα emitters, we take 'low completeness' to mean that the low-luminosity edge of the bin lies below the 30 percent completeness limit. The line luminosities of all [OIII]+Hβ emitters lie above the 90 percent completeness threshold; we therefore do not exclude any from the fit.

Due to the small number of bins left available for fitting, it is impossible to reliably constrain all three free parameters of the Schechter function simultane-

---

[1] 'Uncorrected' only in terms of the filter profile correction; the results have already been corrected for line completeness and dust attenuation by this stage.

ously. For the Hα luminosity functions, we therefore fix the faint-end slope, α, to the value of -1.59 obtained by Sobral et al. (2013) at $z = 2.23$. For the [O III]+Hβ emitters, we only have one available bin and thus fix both α and $\log(L^*/\mathrm{erg\ s}^{-1})$ to the values for the $z = 3.24$ sample of [O III]+Hβ from Khostovan et al. (2015), which are -1.60 and 42.83, respectively. Thus our [O III]+Hβ luminosity function is effectively a renormalised version of the Khostovan et al. (2015) result, with Φ^* being the only free parameter. In addition to the Hα luminosity functions of the individual pointings, we also construct fits to the combined sample of Hα emitters from both SMG fields, as this provides a more general view of SMGs at $z \sim 2.3$ with improved statistics.

The best-fit parameters for each luminosity function are summarised in Table 3.2. Uncertainties are estimated for each free parameter by randomly perturbing the bin heights according to their uncertainties and then recalculating the fit, and repeating this process until 10^5 fits have been made. The 1σ confidence interval for each parameter is then estimated using the 16th and 84th percentiles of the best-fit values.

3.3.2 Analysing luminosity functions

We next use the luminosity functions to assess whether the targeted SMGs reside in overdensities of star-forming galaxies. Figures 3.6 and 3.7 compare the observed luminosity functions from the SMG fields to those from the blank field surveys of Sobral et al. (2013) and Khostovan et al. (2015). The environments of ALESS 75.2 and ALESS 5.1 both show signs of being overdense relative to the field at their respective epochs, with most bins lying significantly above the blank field luminosity functions. Conversely the environment of ALESS 102.1 is broadly consistent with the blank field luminosity function. An overdensity remains when the Hα emitters from both SMG fields at $z \sim 2.3$ are combined, implying that on average SMGs at this epoch reside in overdense, protocluster-like environments, which is qualitatively consistent with clustering results (e.g. García-Vergara et al. 2020; Hickox et al. 2012; Stach et al. 2021; Wilkinson et al. 2017). The contrast between the individual Hα luminosity functions suggests that there is significant

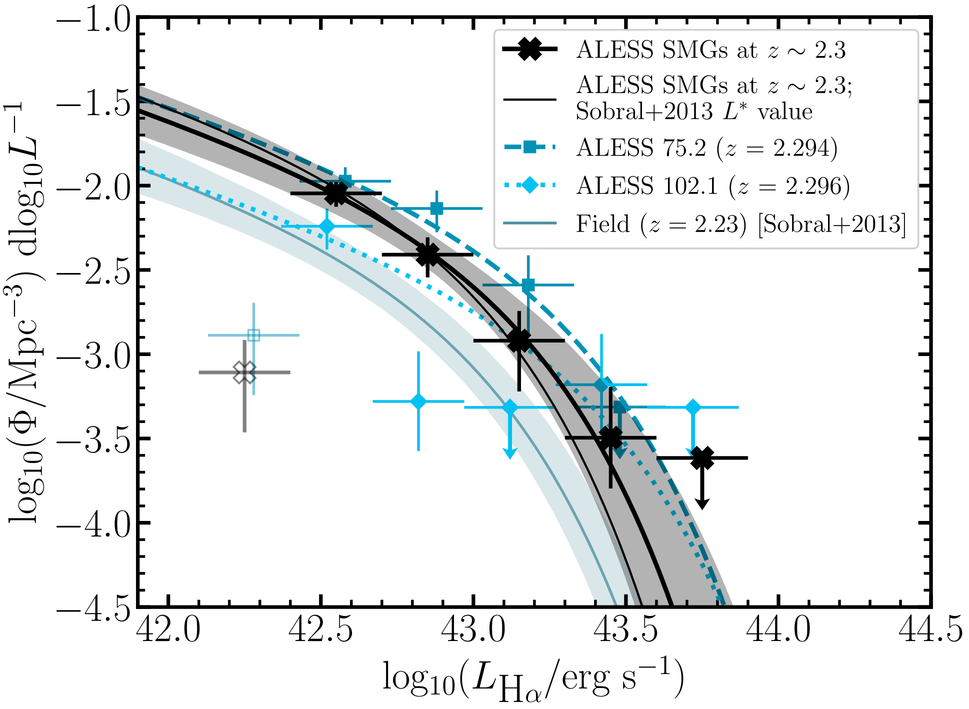

Figure 3.6: Luminosity functions of Hα emitters identified around the two target SMGs at $z \sim 2.3$. Open symbols represent bins that are highly incomplete and are thus excluded from the fits (see §3.3.1.7). The data are compared with a luminosity function from a blank field study of Hα emitters at a similar redshift (Sobral et al. 2013), which is highlighted with a coloured solid curve. Shaded regions represent the 1σ uncertainties on each luminosity function. For our Hα luminosity functions the faint-end slope is fixed to the value from the corresponding blank-field luminosity function ($\alpha = -1.59$; Sobral et al. 2013) and dashed and dotted curves show the fitted Schechter functions for the environments of ALESS 75.2 and ALESS 102.1, respectively. The thick, solid black curve shows the Schechter function obtained by fitting to the data for our combined sample of Hα emitters at $z \sim 2.3$ (black data points); the grey shaded region shows the 1σ confidence region for this fit. The thin black line shows another Schechter function obtained by fitting to the black data points, but with L^* fixed to the blank-field value of $\log(L^*/\mathrm{erg\ s}^{-1}) = 42.87$ (Sobral et al. 2013). Comparison with the blank-field luminosity function reveals that ALESS 75.2 and 102.1 reside in environments with overdensity parameters of $\delta_g = 2.6^{+1.4}_{-1.2}$ and $0.2^{+0.6}_{-0.5}$, respectively. On average, the SMGs at $z \sim 2.3$ reside in environments with galaxy overdensities of $\delta_g = 1.5^{+1.0}_{-0.8}$.

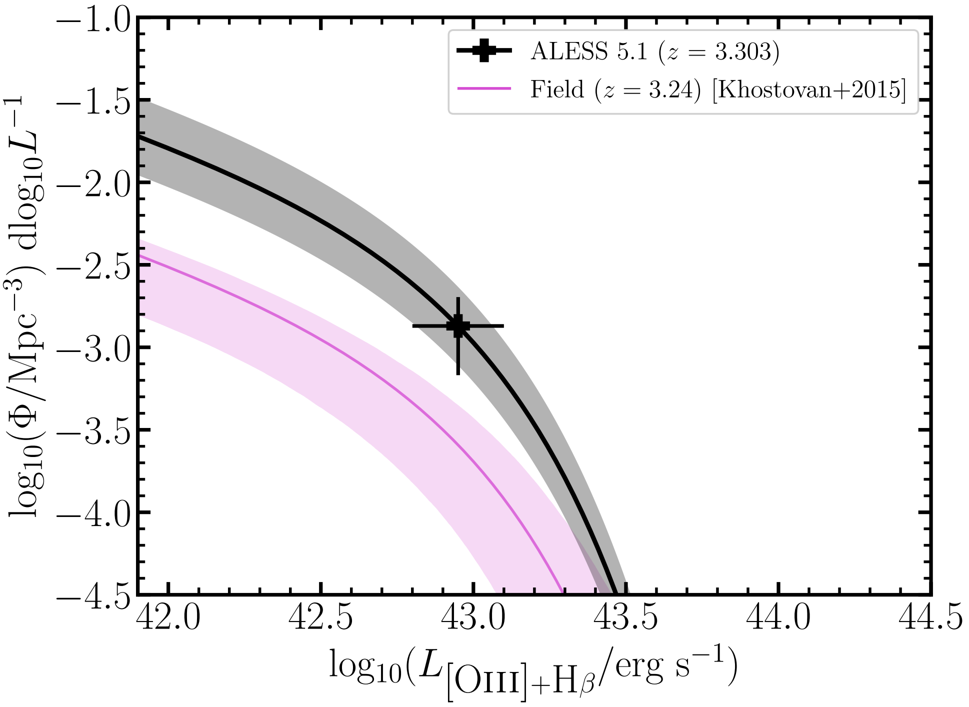

Figure 3.7: Luminosity function for [OIII]+Hβ emitters identified around ALESS 5.1 ($z = 3.303$), compared with a luminosity function for [OIII]+Hβ emitters in the approximately coeval blank field (Khostovan et al. 2015). The thick solid black curve and grey shaded region shows the result of scaling up the blank-field luminosity function to fit to the single bin of [OIII] emitters from the environment of ALESS 5.1. The overdensity parameter for this environment is $\delta_g = 4.0^{+15}_{-3.2}$, as calculated by comparing the observed data with the blank-field luminosity function.

variation across SMG environments, although observations of additional SMGs are required to confirm and quantify the field-to-field variation.

To quantitatively compare the SMG field and blank field luminosity functions we consider the parameters of the Schechter function fits (§3.3.1.7). The parameters of Schechter function fitting are often correlated, so in Figure 3.8 we show the uncertainties of the luminosity function parameters in the L^*–Φ^* plane (as described in §3.3.1.7 the faint-end slope, α, is fixed), comparing our SMG fields with the blank fields at similar redshifts. In all the SMG fields the fit parameters are offset from those from blank-fields, although for the ALESS 102.1 region the offset is only at the $\sim 1\sigma$ level. For the SMGs at $z \sim 2.3$ these separations are driven by a higher L^*, and, in the case of ALESS 75.2, by a larger Φ^*, which implies that this environment is preferentially overdense in bright line emitters compared to the blank field.

We quantify the galaxy overdensity in each sample of Hα and [OIII]+Hβ emitters in two ways. Firstly, we calculate the ratio of the Φ^* from the best fit Schechter function to those from the relevant blank-field luminosity functions, $\Phi^*/\Phi^*_{\rm field}$. This ratio tells us how much higher the 'knee' of each SMG-field luminosity function is relative to the blank-field. These ratios are presented in Table 3.2. The value for the [OIII]+Hβ luminosity function suggests that the environment of ALESS 5.1 at $z \sim 3.3$ is $5.3^{+2.5}_{-1.7}$ times as dense as the field. However, for the Hα emitters at $z \sim 2.3$, L^* is also a free parameter in the Schechter fits, and the L^*–Φ^* correlation means that we must first refit the data with L^* fixed to the $z \sim 2.3$ blank-field value from Sobral et al. (2013) (i.e. $\log(L^*/{\rm erg\ s^{-1}}) = 42.83$). These fits give $\Phi^*/\Phi^*_{\rm field}$ values of $3.6^{+0.6}_{-0.6}$ and $1.7^{+0.3}_{-0.3}$ for the ALESS 75.2 and ALESS 102.1 fields, respectively. The combined sample of Hα emitters from both SMG environments suggests that the average SMG environment at $z \sim 2.3$ is $2.6^{+0.4}_{-0.4}$ times more dense than the blank field at this epoch.

To derive a more representative estimate of the galaxy overdensity in each environment, we also estimate the number of Hα or [OIII]+Hβ emitters that one would expect to find in a blank field with the volumes probed by our observations. To do this, we integrate the field luminosity functions across the luminosity range covered by our data, excluding low completeness bins; i.e. we integrate across the ranges $42.4 \leq \log(L^*_{\rm H\alpha}/{\rm erg\ s^{-1}}) < 43.6$ and $42.8 \leq \log(L^*_{\rm [OIII]+H\beta}/{\rm erg\ s^{-1}}) < 43.1$

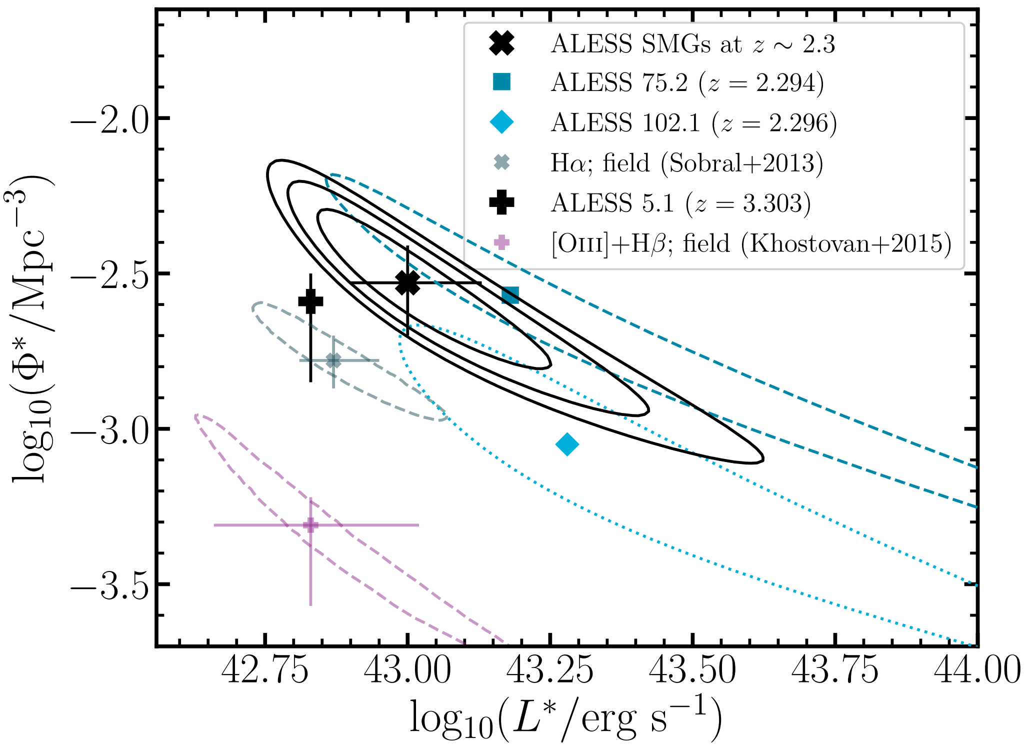

Figure 3.8: Contours showing the correlated uncertainties on the Schechter parameter fits to the luminosity functions shown in Figures 3.6 and 3.7. For all the SMG fields, the faint-end slope, α, is fixed to match the blank-field luminosity functions from Sobral et al. (2013) and Khostovan et al. (2015). Single contours are at the 1σ level; the combined $z \sim 2.3$ data has 1, 2 and 3σ contours shown. For ALESS 5.1, only the 1σ error bars are shown as L^* is fixed. All of the luminosity functions around SMGs are separated from the corresponding blank-field luminosity functions in L^*–Φ^* space, although for ALESS 102.1 this is only at the $\sim 1\sigma$ level. Increases in L^* relative to the blank-field, as seen for both SMGs at $z \sim 2.3$ (and for their combined luminosity function), imply that their environments may preferentially harbour brighter galaxies than those in the field.

and multiply by the volumes probed in each HAWK-I pointing to estimate the expected number counts in an equivalent blank field, N_{field}. Since these field galaxies would have contributed to the observed number counts, we quantify the galaxy overdensity in each environment using

$$\delta_g = \frac{N_{\text{total}} - N_{\text{field}}}{N_{\text{field}}} \tag{3.8}$$

where N_{total} is the sum of the counts in our complete bins. Uncertainties in N_{total} are determined by adding in quadrature the uncertainties in the bin heights. For N_{field} the uncertainties are estimated by randomly permuting the blank-field Schechter parameters within their uncertainties prior to integrating, then repeating the process 10^5 times and using the 16th and 84th percentiles of the resultant number counts to define the 1σ confidence interval.

The values of δ_g for each sample of Hα and [O III]+Hβ emitters are summarised in Table 3.2 along with the significance of this overdensity, σ_δ. Based on these values, the environments of ALESS 5.1, 75.2, and 102.1 are overdense by factors of $4.0^{+15}_{-3.2}$ ($1.3\sigma_\delta$), $2.6^{+1.4}_{-1.2}$ ($2.3\sigma_\delta$), and $0.2^{+0.6}_{-0.5}$ ($0.5\sigma_\delta$), respectively. If the samples of Hα emitters from both pointings are considered as one, then the SMG environments at $z \sim 2.3$ are overdense by a factor of $1.5^{+1.0}_{-0.8}$ ($1.9\sigma_\delta$) on average. The above uncertainties do not account for cosmic variance, which could cause a factor ~ 2 difference in number counts, as based on the Hα emitters in two equal depth HAWK-I pointings in COSMOS and UDS (Sobral et al. 2013). Including cosmic variance in our calculations does not change our overall conclusions that the ALESS 5.1, ALESS 75.2 and the combined $z \sim 2.3$ SMG fields are overdense.

While P102 as a whole is not overdense, the majority of the Hα emitters in this pointing are contained within the same quadrant as the SMG, as can be seen in Figure 3.5 (see also §3.3.3). We therefore recalculate δ_g for this SMG environment, this time considering only the volume probed within that quadrant (1722 cMpc^3), finding $\delta_g = 3.8^{+2.4}_{-1.8}(2.1\sigma)$ in this area, which suggests that ALESS 102.1 actually does reside in an overdense environment with a physical scale of ~1.6 Mpc. This high concentration of galaxies surrounding the SMG could be indicative of structure formation on smaller scales than those of protoclusters and it is possible that ALESS 102.1 resides in a protogroup (e.g. Diener et al. 2013). We discuss the spatial distribution of companion galaxies in each SMG environment in more detail in §3.3.3.

The question remains as to whether the target SMGs reside in protoclusters, which will evolve into bound clusters by the present day. To learn more, we compare the overdensities in the SMG fields with previous studies of protoclusters. However, protoclusters exhibit a wide range of galaxy overdensities; a 'typical' value of δ_g is not well-defined, though we highlight here structures at similar redshifts to our target SMGs. For example, $\delta_g = 2.5$ for the $z = 1.99$ protocluster in the GOODS-N field (Chapman et al. 2009). The protoclusters 4C 10.48 ($z = 2.35$) and 4C 23.56 ($z = 2.48$), which were both identified using narrowband selection of Hα emitters around luminous radio galaxies, were found to have overdensities of $\delta_g = 11^{+2}_{-2}$ and $\delta_g = 4.3^{+5.3}_{-2.6}$, respectively (Hatch et al. 2011b; Tanaka et al. 2011). The protocluster Cl J0227-0421 at $z = 3.29$ is overdense by a factor of $\delta_g = 10.5 \pm 2.8$ (Lemaux et al. 2014). Two protoclusters in the COSMOS field at $z = 2.10$ and $z = 2.47$ were found to have overdensities of $\delta_g \sim 8$ and $\delta_g \sim 3.3$, respectively (Chiang et al. 2017; Yuan et al. 2014). Zheng et al. (2021) confirm overdensities of Hα emitters in two protocluster candidates, BOSS1244 and BOSS1542, with overdensity factors of $\delta_g = 5.6 \pm 0.3$ and $\delta_g = 4.9 \pm 0.3$, respectively. Comparing δ_g for these protoclusters with our values, we posit that the environments of our target SMGs are consistent with being protoclusters, albeit at the lower-density end. For the remainder of the analyses we assume that members of these overdensities will form larger structures by $z = 0$, although we caution that the significance of these overdensities is relatively low (1.3–2.3σ_δ) and thus it is uncertain whether they will coalesce by $z \sim 0$ (e.g. Angulo et al. 2012; Chiang et al. 2013; Overzier et al. 2009).

Table 3.2: Summary of the best-fit Schechter parameters for companion galaxies in the environments of the target SMGs, along with comparisons to the blank field at similar redshifts. In all cases, the faint-end slope of the luminosity function, α, is fixed to the value from the relevant blank-field luminosity function and, where indicated, the characteristic luminosity, L^*, is also fixed to the blank-field values. The values of $\Phi^*_{\rm field}$ are taken from the relevant blank-field Schechter functions. All blank-field parameters are from (Sobral et al. 2013) and (Khostovan et al. 2015).

SMG environment	$\log(L^*/\rm erg\ s^{-1})$	$\log(\Phi^*/\rm Mpc^{-3})^a$	$\log(\Phi^*_{{\rm fixed}\,L^*}/\rm Mpc^{-3})^b$	$\Phi^*/\Phi^{*}_{\rm field}{}^a$	$\Phi^*_{{\rm fixed}\,L^*}/\Phi^*_{\rm field}{}^b$	$\delta_g{}^c$	$\sigma_\delta{}^d$
ALESS 75.2	$43.18^{+0.42}_{-0.28}$	$-2.57^{+0.29}_{-0.39}$	$-2.22^{+0.05}_{-0.09}$	$1.62^{+1.05}_{-0.80}$	$3.63^{+0.58}_{-0.59}$	$2.61^{+1.42}_{-1.15}$	2.3
ALESS 102.1	$43.28^{+0.50}_{-0.28}$	$-3.05^{+0.17}_{-0.42}$	$-2.55^{+0.08}_{-0.12}$	$0.54^{+0.22}_{-0.23}$	$1.70^{+0.30}_{-0.32}$	$0.21^{+0.55}_{-0.45}$ [e]	0.5 [e]
SMGs at $z \sim 2.3$	$43.00^{+0.12}_{-0.10}$	$-2.53^{+0.12}_{-0.17}$	$-2.36^{+0.04}_{-0.08}$	$1.78^{+0.41}_{-0.43}$	$2.63^{+0.41}_{-0.42}$	$1.51^{+0.98}_{-0.80}$	1.9
ALESS 5.1	42.83 (fixed)	–	$-2.61^{+0.09}_{-0.26}$	–	$5.25^{+2.49}_{-1.70}$	$4.03^{+14.9}_{-3.2}$	1.3

[a] Φ^* as measured when both Φ^* and L^* are free parameters (α is always fixed to the blank-field values).

[b] $\Phi^*_{{\rm fixed}\,L^*}$ is obtained by fitting a Schechter function to the data with both L^* and α fixed to the blank-field values. The values of L^* are taken from the relevant blank-field Schechter functions.

[c] Galaxy overdensity, $\delta_g = (N_{\rm total}/N_{\rm field}) - 1$; see §3.3.2.

[d] Significance of the galaxy overdensity, δ_g.

[e] ALESS 102.1 has $\delta_g = 3.8^{+2.4}_{-1.8}$ (i.e. $\sigma_\delta = 2.1$) when considering only the HAWK-I quadrant containing the SMG (§3.3.2).

3.3.3 Spatial distribution of line emitters

In order to investigate the role of environment in shaping the evolution of SMGs, and to assess whether the target SMGs reside in special regions within their surrounding structures, we next explore the spatial distributions of coeval line emitters across our HAWK-I pointings. Due to the small size of the [OIII] emitter sample, we limit this part of the analysis to the Hα emitters around ALESS 75.2 and 102.1. Figure 3.9 compares the surface density of Hα emitters as measured in annuli centred on each target SMG (where the density calculations account for masked and unobserved regions by assuming the density is the same as in the observed regions) with the surface densities one would expect based on the blank-field luminosity function from Sobral et al. (2013). The annuli have inner and outer radii increasing in increments of $2'$, and are represented by dashed circles in Figure 3.5. Note that these large annuli are necessary due to the sample sizes, but make it difficult to probe the protocluster structures in detail. We therefore also show in Figure 3.10 the result of smoothing the distributions of Hα emitters in P5_75 (left) and P102 (right) using a 2D Gaussian kernel with width corresponding to 0.5 Mpc at $z \sim 2.3$. This method of visualisation clarifies where the SMGs lie in relation to any density peaks and can highlight any substructures. For simplicity we assume that there are no Hα emitters in the unobserved region between the detector chips, or in regions of the image that have been masked, and thus the densities shown in these regions are potentially underestimated.

For ALESS 102.1, there is a noticeable decrease in the surface density of Hα emitters as a function of radial distance from the SMG, with the innermost bin in Figure 3.9 being significantly overdense relative to the field despite the environment not being overdense as a whole (see also §3.3.2). This is also clear from Figure 3.10, which shows that the SMG lies $\sim 20''$ from a $\sim 3.25'$ (~ 1.6 Mpc) density peak. Furthermore, Figure 3.5 demonstrates that the innermost $2.0'$ annulus contains more than half of the Hα emitters detected across the P102 pointing. Figure 3.10 includes a panel showing the location of the SMGs and our Hα emitter density maps in the context of the overdensity of Lyα emitters (LAEs) mapped by Yang et al. (2010). This shows that the small-scale overdensity around

ALESS 102.1 is in a broader underdense region, and it is therefore unlikely to be a condensed infalling knot within a larger structure.

In the case of ALESS 75.2 we show two results in Figure 3.9: one where we include all Hα emitters in the pointing (open squares), and one where we exclude the dense clump of Hα emitters in the north-east (filled squares; see §3.2.2). In both cases, there is no significant trend in the Hα surface density as a function of separation from the SMG, although it does show signs of decreasing at the outermost radii if the dense north-easterly clump is excluded. This lack of trend implies that ALESS 75.2 does not reside in a particularly special region of the structure, and/or the structure extends beyond the HAWK-I field of view. The latter hypothesis is supported by the comparison of the Hα emitter overdensity with that of the LAEs from Yang et al. (2010) (Figure 3.10, right), which shows that the whole structure around ALESS 75.2 is within a larger region of LAE overdensity. This suggests that the Hα emitter structure likely spans a physical distance $\gtrsim 3.5\,\mathrm{Mpc}$ at $z \sim 2.3$, which is consistent with the simulations of e.g. Muldrew et al. (2015), in which protoclusters are expected to extend over $\gtrsim 10\,\mathrm{Mpc}$ at $z \sim 2$. The Yang et al. (2010) structure in this region includes the Lyα blob CDFS-LAB03, which coincides with seven Hα emitters (see also §3.2.2). The overall picture is consistent with previous findings, in which Lyα blobs are found to be associated with massive dark matter halos and filamentary large-scale structures (e.g. Geach et al. 2016; Umehata et al. 2019).

3.3.4 SMG companions: SFRs and stellar masses

In this section we investigate the dust-corrected star formation rates (SFR) and stellar masses ($M_\star$) of the individual galaxies around each target SMG, to determine whether they lie on the main sequence of star formation at their epochs. This correlation between SFR and $M_\star$ has been observed out to $z \sim 6$ (e.g. Brinchmann et al. 2004; Daddi et al. 2007; Elbaz et al. 2007; González et al. 2010; Schreiber et al. 2015; Scoville et al. 2017; Speagle et al. 2014) and galaxies significantly above the main sequence are usually considered to be short-lived starbursts, whereas those significantly below the main sequence are typically quenched. The position of galaxies relative to the main sequence provides insights into their evolutionary

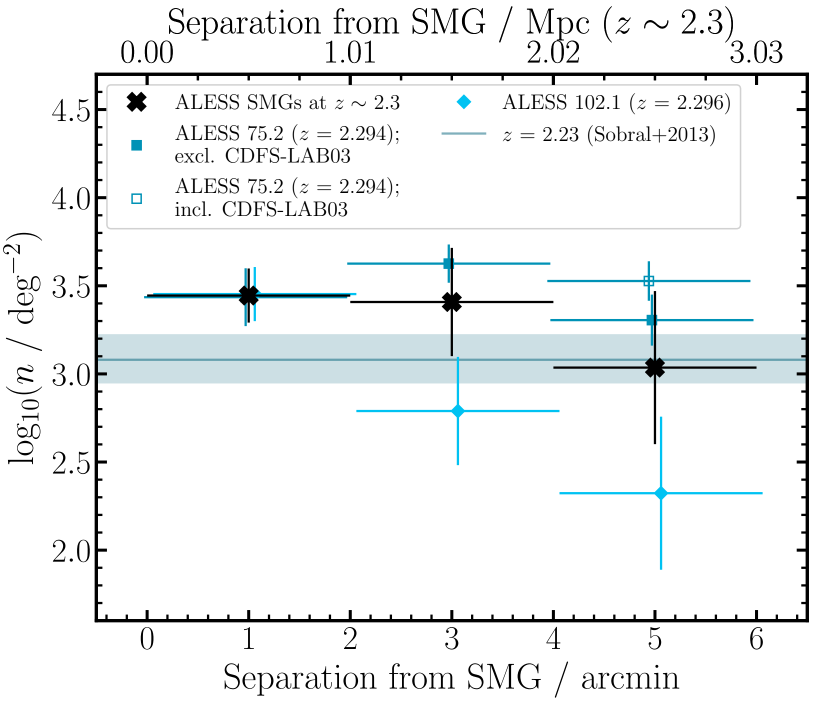

Figure 3.9: Surface density of Hα emitters measured in 2.0′ annuli centred on the two target SMGs at $z \sim 2.3$ and compared with expected values from the blank-field Hα luminosity function (horizontal line and shaded region; Sobral et al. 2013). The shape of the field and positions of the SMGs means that coverage is incomplete with data for 74% (81%) of the inner, 36% (31%) of the middle, and 26% (27%) of the outer annuli for P5_75 (P102). Open symbols show the values calculated if the dense clump of Hα emitters in the northeast of P5_75 (see §3.2.2) is included. Both $z \sim 2.3$ SMGs have high densities of Hα emitters in the central ~ 1 Mpc. For ALESS 102.1 the density falls with increasing separation from the SMG, though no significant trend exists for ALESS 75.2. The existence of a significant overdensity within $\sim$2′ of ALESS 102.1 with no evidence of further extension suggests it may reside in an early galaxy group, while ALESS 75.2 appears to reside in a larger structure that extends beyond the HAWK-I coverage.

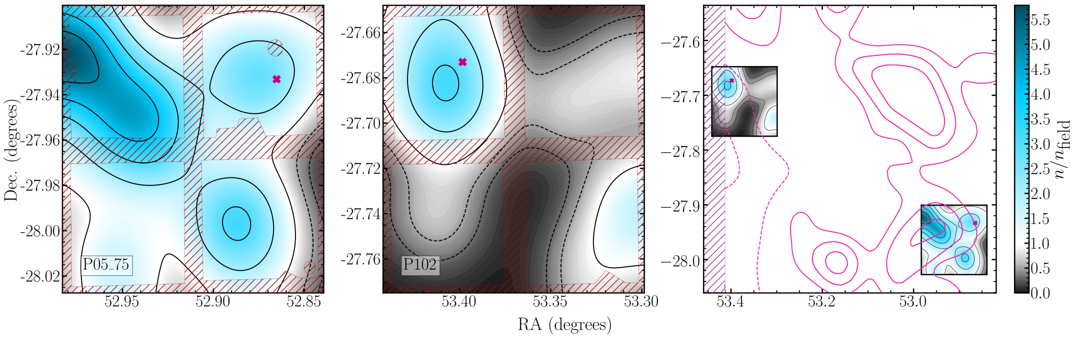

Figure 3.10: Maps showing the variation of surface overdensity, $n/n_{\rm field}$, of Hα emitters across the P5_75 *(left)* and P102 *(middle)* fields, and in the context of Lyα emitter (LAE) density at $z \sim 2.3$ in the wider ECDFS *(right)*. The maps are smoothed using a 2D Gaussian kernel with a width of 0.5 Mpc. Contour levels are $n/n_{\rm field} = 0.25, 0.5, 1$ and increasing in intervals of 1 thereafter; dashed lines represent underdensities. Crosses mark the positions of the target SMGs, ALESS 75.2 and ALESS 102.1, and hatching indicates regions outside our HAWK-I coverage (including chip-gaps) or that are masked (e.g. due to the presence of a bright star). Note that the smoothing implicitly assumes that no Hα emitters reside in these regions, such that the densities here are conservative lower limits. Both SMGs are in/near Hα density peaks, although ALESS 75.2 is not in the highest density region in P5_75. The rightmost panel shows the Hα overdensities in the two SMG fields compared to the wider LAE density measured in the whole ECDFS (Yang et al. 2010); LAE contour levels are at $n/n_{\rm field} = 0.3, 0.5, 1, 2$ and 3. The region of highest Hα density in P5_75 corresponds to strong overdensity of LAEs, which contains the Lyα blob CDFS-LAB03 (Yang et al. 2010, see §3.2.2) and there is an overall correlation between the Hα and LAE overdensities in this region. Conversely, despite being in a small region of localised Hα overdensity, ALESS 102.1 is in a region that is underdense in LAEs on the scales probed by Yang et al. (2010).

state and can be used to infer the role of any environmentally-driven mechanisms enhancing or inhibiting star formation activity.

We obtain stellar masses and SFRs for our galaxies by using the SED fitting code, MAGPHYS (da Cunha et al. 2008), to fit SEDs to the same fixed-aperture photometry used to derive photometric redshifts in §3.2.2. Figure 3.11 compares the relationship between SFR and stellar mass for the Hα and [OIII]+Hβ emitters that are SMG companions with the main-sequence at similar epochs using the prescription from Speagle et al. (2014). These galaxies generally scatter about the main sequence at their respective epochs, following a similar trend of increasing SFR with increasing stellar mass. We thus find no significant evidence of enhanced star formation in these SMG environments. This is contrary to some previous studies in which enhanced SFRs have been found in overdense environments at $z \gtrsim 1$ (e.g. Cooper et al. 2008; Elbaz et al. 2007; Lemaux et al. 2022), however it is consistent with several other studies in which no environmentally-driven SFR enhancement is observed at high redshift (e.g. Darvish et al. 2016; Scoville et al. 2013; Zavala et al. 2019).

In addition to the MAGPHYS-derived SFRs, we also calculate the dust-corrected star formation rates for the Hα emitters using the scaling relation from Kennicutt (1998), modified for a Chabrier (2003) IMF:

$$\mathrm{SFR}(\mathrm{M}_{\odot}\ \mathrm{yr}^{-1}) = 5.16 \times 10^{-42} L_{\mathrm{H}\alpha}\ (\mathrm{erg\ s}^{-1})\,, \tag{3.9}$$

where the Hα line flux has been corrected for contamination by the nearby [NII] doublet (see §3.3.1.3) and we assume a dust attenuation of $A_{\mathrm{H}\alpha} = 1$ mag (§3.3.1.5). For the [OIII]+Hβ emitters we assume an attenuation of $A_{[\mathrm{OIII}]+\mathrm{H}\beta} = 1.35$ mag following Khostovan et al. (2015) and use the relation between SFR and $L_{[\mathrm{OIII}]+\mathrm{H}\beta}$ from Osterbrock & Ferland (2006), similarly modified for a Chabrier (2003) IMF:

$$\mathrm{SFR}(\mathrm{M}_{\odot}\ \mathrm{yr}^{-1}) = 4.80 \times 10^{-42} L_{[\mathrm{OIII}]+\mathrm{H}\beta}\ (\mathrm{erg\ s}^{-1})\,. \tag{3.10}$$

The bottom panel of Figure 3.11 shows how the ratio of the MAGPHYS-derived and line-derived SFR estimates varies with stellar mass. Also shown is the Hα

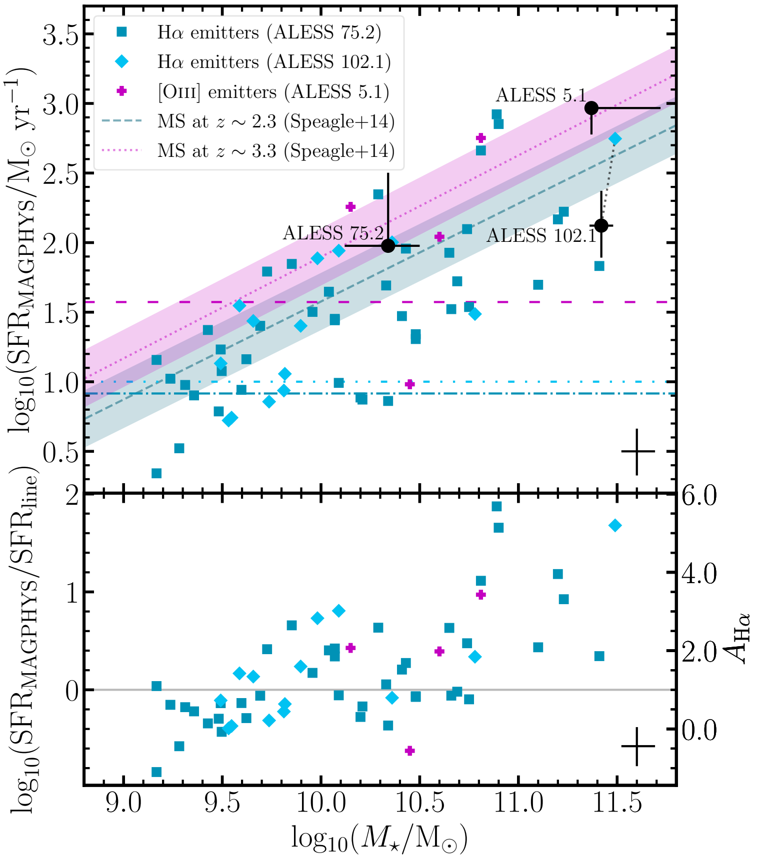

Figure 3.11: *(Top)* MAGPHYS-derived SFR vs stellar mass for the Hα and [OIII] emitters identified in this study, compared with the z∼2.3 and z∼3.3 main sequence (shaded regions represent 0.2 dex scatter; Speagle et al. 2014). The target SMGs are also shown, with masses and SFRs from Danielson et al. (2017) and Birkin et al. (2021) (black points; ALESS 102.1 is connected with a black dotted line to the counterpart Hα emitter identified from our data; discussed in §3.3.4) Dashed, dot-dashed, and dot-dot-dashed horizontal lines correspond to the minimum SFR sensitivity of our survey in the environments of ALESS 5.1, 75.2, and 102.1, respectively, based on estimates using the line luminosities (Equation 3.9). The galaxies generally follow the main sequence for their respective epochs, with some scatter in all three SMG environments. *(Bottom)* Ratio of MAGPHYS-derived SFRs to the SFRs derived from line luminosities using fixed dust Hα ([OIII]) dust attenuations of 1.0 (1.35) mag, plotted as a function of stellar mass. The right-hand axis shows the corresponding dust attenuation required to make the line luminosity-derived SFR match the MAGPHYS-derived SFR for Hα emitters, $A_{\mathrm{H}\alpha}$ (Equation 3.11). (Analogous values for [OIII] emitters, $A_{[\mathrm{OIII}]}$, can be obtained by adding 0.14.) The observed correlation suggests that assuming a constant dust attenuation for all Hα/[OIII] emitters results in underestimated SFRs at high stellar masses; such an approximation should therefore be used with caution. The black cross in the bottom-right of each panel shows the mean parameter uncertainties.

dust attenuation required for the SFR derived from Equation 3.9, $\mathrm{SFR}_{\mathrm{H}\alpha}$, to agree with the MAGPHYS-derived value, $\mathrm{SFR}_{\text{MAGPHYS}}$, as given by:

$$A_{\mathrm{H}\alpha} = 2.5\log_{10}\left(\frac{\mathrm{SFR}_{\text{MAGPHYS}}}{\mathrm{SFR}_{\mathrm{H}\alpha}}\right) + 0.4\,. \tag{3.11}$$

An analagous equation for $A_{[\mathrm{O\,III}]+\mathrm{H}\beta}$ can be obtained by adding 0.14 mag. It is evident that as one moves to higher stellar mass, the assumption that $A_{\mathrm{H}\alpha}$ ($A_{[\mathrm{O\,III}]+\mathrm{H}\beta}$) = 1.0 (1.35) mag results in underestimated SFRs compared with the results from SED fitting. We therefore caution that while such an assumption may be suitable for galaxies with low-to-average stellar mass, it becomes less reliable for high-mass galaxies.

We also include the SMGs themselves in Figure 3.11, with the SFRs and stellar masses for these calculated by Danielson et al. (2017) and Birkin et al. (2021) using MAGPHYS. As expected for sources selected due to their infrared-brightness, the SMGs are among the most actively star-forming galaxies in the observed fields. ALESS 5.1 and ALESS 102.1 are also some of the most massive galaxies in these regions, which suggests that if they are in protoclusters then the SMGs themselves may be brightest cluster galaxy (BCG) progenitors, i.e. proto-BCGs. Conversely, ALESS 75.2 has a lower mass which is not exceptional for its environment, and which points towards it being more likely to evolve into a normal cluster member. This is consistent with the spatial analysis of Hα emitters and LAEs (§3.3.3), which showed that ALESS 75.2 is offset from the densest regions of this field.

Since ALESS 102.1 has a counterpart Hα emitter in our sample, we also compare our MAGPHYS-derived SFR and stellar mass with those derived by Danielson et al. (2017). Our stellar mass of $\log(M_\star/\mathrm{M}_\odot) = 11.49^{+0.18}_{-0.05}$ is in good agreement with their value of $\log(M_\star/\mathrm{M}_\odot) = 11.42^{+0.06}_{-0.06}$. Conversely, our SFR of $\log(\mathrm{SFR}/\mathrm{M}_\odot\mathrm{yr}^{-1}) = 2.75^{+0.22}_{-0.25}$ is significantly higher than their estimate of $\log(\mathrm{SFR}/\mathrm{M}_\odot\mathrm{yr}^{-1}) = 2.12^{+0.25}_{-0.23}$. This is likely due to the inclusion of FIR and radio photometry in their SED fitting which are absent from our own fit; the dust component (and thus the SFR) is better constrained in the Danielson et al. (2017) SED fit. We therefore opt to use their values of SFR and stellar mass for this galaxy instead of our own.

3.3.5 Stellar mass functions

We next construct the stellar mass functions of the galaxies around each SMG and compare these with the blank field. The stellar mass functions are derived following a similar procedure as for the luminosity functions (see §3.3.1), minus the corrections that are only relevant to luminosity functions (dust attenuation, line flux contamination, filter profile corrections). Completeness corrections were applied to each mass bin according to the completeness values estimated in §3.3.1.2 based on the emission line fluxes. We then fit Schechter functions to the data:

$$\Phi_{\mathrm{M}}(M_\star)dM_\star = \ln(10)\Phi^*_{\mathrm{M}}\left(\frac{M_\star}{M^*_\star}\right)^{\alpha_{\mathrm{M}}+1} e^{-(M_\star/M^*_\star)}d\log M_\star\,, \tag{3.12}$$

where $\Phi_{\mathrm{M}}(M_\star)$ is the number density at stellar mass $M_\star$, Φ^*_{M} is the normalisation of the stellar mass function, $M^*_\star$ is the characteristic stellar mass, and α_{M} is the slope at the faint end of the stellar mass function. Mass bins that are less than 50 percent complete are excluded from the fitting procedure. As with the luminosity functions, we also fix the faint-end slope α_{M} to the values derived for blank-field stellar mass functions by Sobral et al. (2014) and Khostovan et al. (2016) (i.e. $\alpha_{\mathrm{M}} = -1.37$ and $\alpha_{\mathrm{M}} = -1.3$ for the for the Hα and [OIII]+Hβ emitters, respectively). For [OIII]+Hβ emitters we also fix the characteristic stellar mass, $M^*_\star$, to the blank-field value of $\log(M^*_\star/\mathrm{M}_\odot) = 10.96$ (Khostovan et al. 2016).

The stellar mass functions are presented in Figures 3.12 and 3.13, with the parameters in Table 3.3. Uncertainties in each parameter are estimated following the same procedure as for those of the luminosity functions (see §3.3.1.7) and the correlation between the parameters and their uncertainties are shown in Figure 3.14, which demonstrates that at the upper limit the characteristic stellar mass, $M^*_\star$, is poorly constrained for all of our samples except the Hα emitters around ALESS 75.2. However, the lower limit is sufficient to show that in the $z \sim 2.3$ SMG regions the characteristic stellar mass is significantly higher than the $z \sim 2.3$ field, which suggests that the stellar mass build-up in SMG companion galaxies is further advanced than the coeval field (e.g. Muzzin et al. 2013). Due

Table 3.3: Summary of the best-fit stellar mass function parameters for the companion galaxies in the environments of the target SMGs. In all cases, the faint-end slope of the stellar mass function, α_{M}, is fixed to the value from the relevant blank-field stellar mass function (Khostovan et al. 2016; Sobral et al. 2014). Where indicated, the characteristic stellar mass, $M_\star^*$, is also fixed to the blank-field value from Khostovan et al. (2016).

SMG environment	$\log(M_\star^*/\mathrm{M}_\odot)$	$\log(\Phi_{\mathrm{M}}^*/\mathrm{Mpc}^{-3})$
ALESS 75.2	$11.69^{+0.41}_{-0.15}$	$-3.37^{+0.09}_{-0.25}$
ALESS 102.1	$12.08^{+0.52}_{-0.59}$	$-4.01^{+0.23}_{-0.41}$
SMGs at $z \sim 2.3$	$11.85^{+0.30}_{-0.34}$	$-3.64^{+0.16}_{-0.18}$
ALESS 5.1	10.96 (fixed)	$-3.73^{+0.08}_{-0.08}$

to our selection of Hα emitters, the galaxies have non-negligible star-formation rates (though many are below the main sequence; §3.3.4). Observations using a local galaxy density estimator suggest that local environment has minimal effect on the stellar mass function of star-forming or quiescent galaxies at $z = 1.5$–2 (Papovich et al. 2018). However, there is evidence of protocluster environments being skewed towards containing galaxies with higher masses than the field (e.g. Cooke et al. 2014), consistent with our results.

3.3.6 Dark matter halos

We next estimate the total halo masses of the SMG environments in order to place them within the context of existing protoclusters and trace their likely evolution. Since these overdensities are unvirialised and lack a detectable intracluster medium, the classic methods for weighing galaxy clusters cannot be used. Instead, we use two methods that have been used in protocluster studies, though the underlying assumptions required can lead to significant uncertainties, as discussed in the following subsections. The first method is detailed in §3.3.6.1 and uses the stellar-to-halo mass relation (SHMR) to estimate the high-redshift mass of the clusters (hereafter SHMR method) and evolve it to the local Universe using the Millennium and Millennium-II simulations (Fakhouri et al. 2010; McBride et al. 2009). The second method follows Steidel et al. (1998) and assumes the region of interest is a homogeneous sphere undergoing spherical collapse and uses

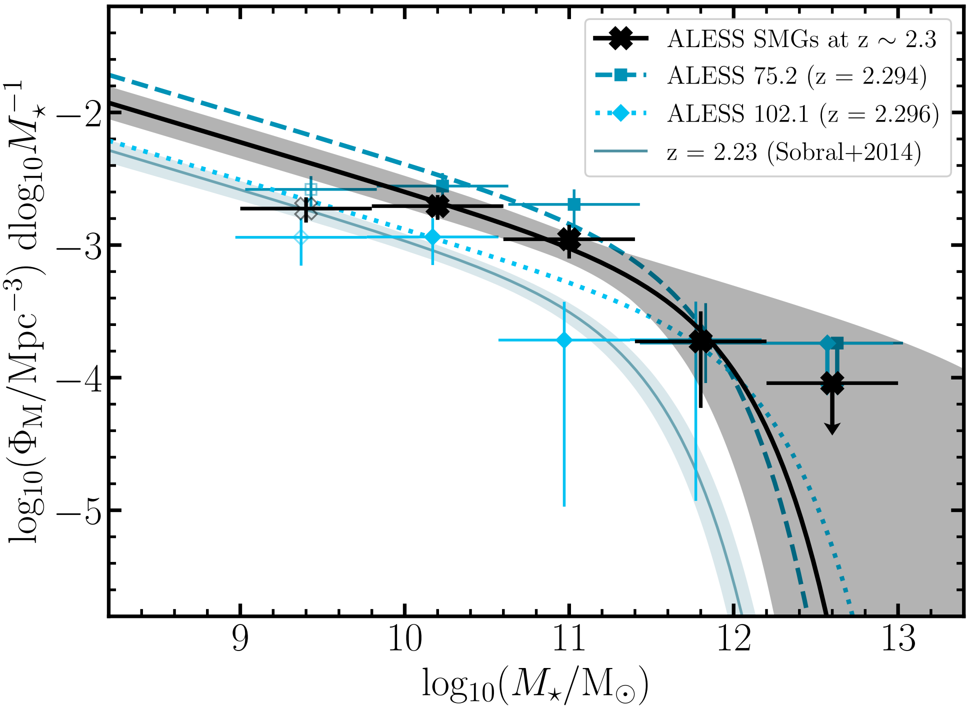

Figure 3.12: Stellar mass functions for the Hα emitters identified in this study. The data are compared with a blank-field study of Hα emitters at a similar redshift (Sobral et al. 2014) and shaded regions represent 1σ uncertainties. For each of our stellar mass functions, we fix the faint-end slope to the blank-field value of $\alpha_{\rm M} = -1.37$ (Sobral et al. 2014). The upper limit of $M_\star^*$ is poorly constrained (see also Figure 3.14), which leads to large uncertainties at the high mass end. There are offsets between the blank-field stellar mass functions and those around our SMGs in all targeted SMG regions; these are quantified in Figure 3.14 and Table 3.3.

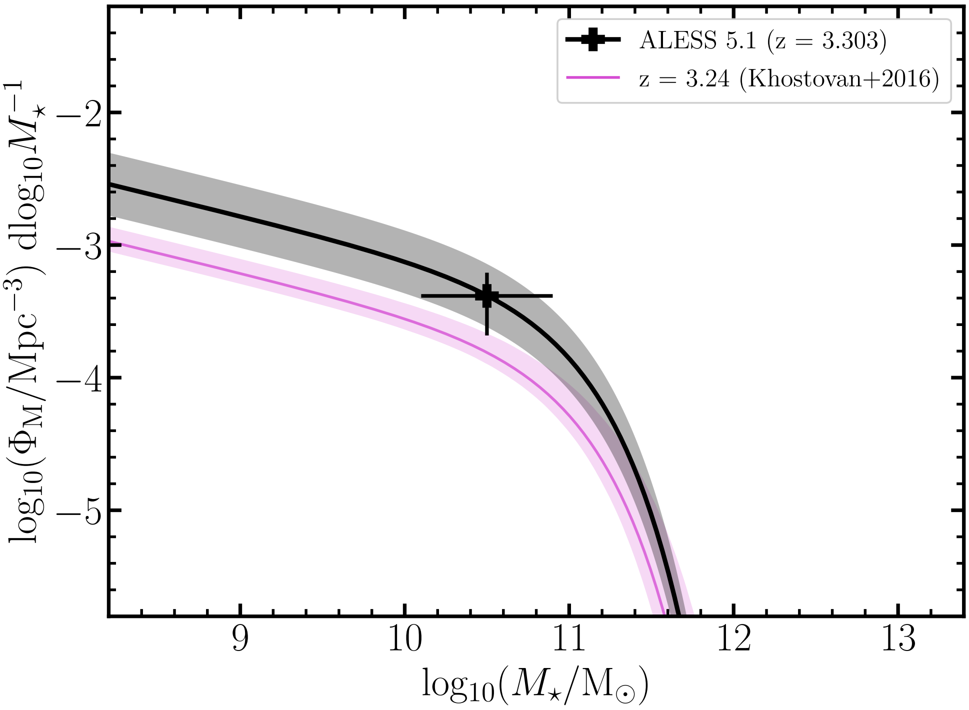

Figure 3.13: Stellar mass function for [Oiii]+Hβ emitters identified around ALESS 5.1 ($z = 3.303$), compared with a stellar mass function for [Oiii]+Hβ emitters in the blank field at a similar epoch (Khostovan et al. 2016). We fix both the faint-end slope and the characteristic stellar mass to the blank-field values of $\alpha_\mathrm{M} = -1.3$ and $\log(M_\star^*/\mathrm{M}_\odot) = 10.96$, respectively (Khostovan et al. 2016), such that the thick solid black curve and grey shaded region effectively shows the result of scaling up the blank-field stellar mass function to fit to the single bin of [Oiii]+Hβ emitters from the environment of ALESS 5.1. As with the Hα stellar mass functions, the resultant offset is quantified in Figure 3.14 and Table 3.3.

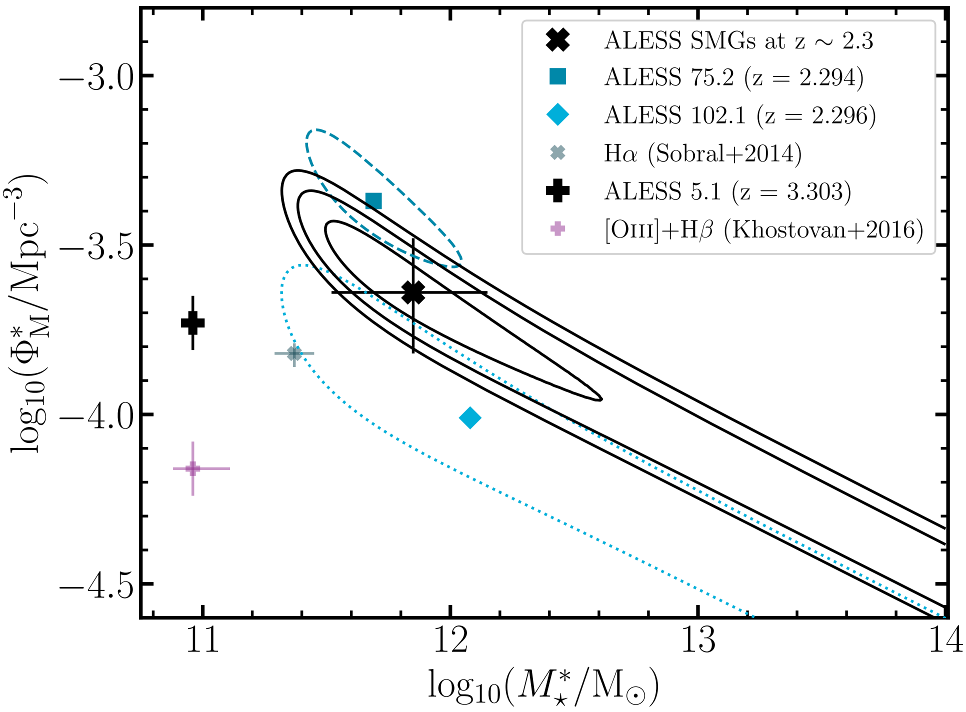

Figure 3.14: Contours showing the correlated uncertainties on the Schechter fit parameters for the stellar mass functions shown in Figures 3.12 and 3.13. In all cases, the faint-end slope, α_M, is fixed to match the blank-field stellar mass functions (Khostovan et al. 2016; Sobral et al. 2014), and for ALESS 5.1 $M^*_\star$ is also fixed. Symbols and contours have the same meaning as in Figure 3.8. For the Hα emitters at $z \sim 2.3$ the characteristic stellar mass, $M^*_\star$, is effectively a lower limit due to the correlation with Φ^*_M; this can also be seen in Figure 3.12. The offset between $M^*_\star$ for field Hα emitters (Sobral et al. 2014) and the galaxies around $z \sim$ 2.3 SMGs indicates that there is an excess of high-mass galaxies around the SMGs, and this is likely partially responsible for the overdensity around ALESS 75.2.

the overdensity parameter to estimate the $z = 0$ descendant mass, which we trace back to high-redshift using the Millennium and Millenium-II simulations. This is referred to as the spherical collapse model (SCM) method and detailed in §3.3.6.2. In §3.3.6.3 we discuss the evolution of the SMG environments compared with other systems and previous measurements.

3.3.6.1 The SHMR method for deriving halo masses

The SHMR method for estimating protocluster masses involves identifying the most massive galaxy in the structure and converting its stellar mass to a halo mass, and taking this to be the halo mass of the whole structure. This method has been employed in recent protocluster studies (e.g. Calvi et al. 2021; Ito et al. 2023; Long et al. 2020; Sillassen et al. 2022) and implicitly assumes that all member galaxies occupy a single halo at the observed redshift of the structure, which may not be the case if some of the galaxies are still infalling. Nevertheless, we deem this assumption preferable to the commonly-used alternative of estimating the halo masses of each individual galaxy and summing them together (e.g. Calvi et al. 2021; Long et al. 2020), which risks 'double-counting' overlapping dark matter halos to produce an overestimate of the structure halo mass.

We estimate halo masses for each target SMG and their candidate companion galaxies using the SHMR from Behroozi et al. (2013). We use the relation as defined at $z = 2$ for galaxies in the environments of ALESS 75.2 and 102.1, and at $z = 3$ for galaxies in the environment of ALESS 5.1. For the SMGs themselves we use the stellar masses from the literature (Birkin et al. 2021; Danielson et al. 2017, see also §3.3.4). Some of our galaxies have stellar masses which lie above the range at which the SHMR is defined and for these we use the stellar-to-halo mass ratio for the largest halo mass at which the relation is defined (see Figure 1.3) to convert the stellar mass to a halo mass. This affects only two Hα emitters from P5_75, along with one from P102 which we have identified as a counterpart to ALESS 102.1 (see §3.3.4 and Figure 3.11). None of the [OIII] emitters have stellar masses above the range for which the SHMR is defined at $z \sim 3$, but ALESS 5.1 does lie above this range. Uncertainties on individual galaxy halo masses are estimated based on the stellar mass uncertainties and the uncertainties in the SHMR derived by Behroozi et al. (2013).

We derive halo masses of $\log(M_h/\mathrm{M}_\odot) = 11.45$–$14.46$ for individual Hα and [Oiii] emitters, with medians of $\log(M_h/\mathrm{M}_\odot) = 12.20, 11.92, 11.74$ for galaxies in the environments of ALESS 5.1, 75.2 and 102.1, respectively. The halo masses of the corresponding SMGs are $\log(M_h/\mathrm{M}_\odot) = 13.94^{+0.38}_{-0.21}, 12.02^{+0.08}_{-0.25}, 14.39^{+0.03}_{-0.37}$. ALESS 5.1 and 102.1 are both the most massive galaxies in their respective environments; we therefore adopt their halo masses as the total masses of the potential structures at the observed redshifts. ALESS 75.2 is not the dominant galaxy in its environment, being surpassed in stellar (and halo) mass by ∼40 percent of its companion Hα emitters. The most massive of these is a spectroscopically confirmed member (Balestra et al. 2010; Popesso et al. 2009) located in the Hα emitter density peak associated with the Lyα blob CDFS-LAB03 (see Figure 3.10), with a halo mass of $\log(M_h/\mathrm{M}_\odot) = 14.38^{+0.01}_{-0.40}$. We thus assume this is the total mass of the surrounding structure. Since high-redshift radio galaxies are commonly found in protocluster cores (e.g. Cooke et al. 2014; Hayashi et al. 2012; Kuiper et al. 2011b; Kurk et al. 2000; Venemans et al. 2002; Wylezalek et al. 2013), we search for radio counterparts for this galaxy in the second data release from the Very Large Array 1.4 GHz survey of the ECDFS (Miller et al. 2013), for which the typical sensitivity is 7.4 μJy per $2.8'' \times 1.6''$ beam. We find no counterparts within $30''$ of this Hα emitter and thus rule it out as being a high-redshift radio galaxy.

The total halo masses at the observed redshift obtained using the SHMR method are thus $\log(M_h/\mathrm{M}_\odot) = 13.94^{+0.38}_{-0.21}, 14.38^{+0.01}_{-0.40}, 14.39^{+0.03}_{-0.37}$ for the environments of ALESS 5.1, 75.2, and 102.1, respectively. The upper limits from these masses are represented by the upper bounds on Figure 3.15 (the lower bounds are derived in §3.3.6.2), which compares the halo masses of the SMG environments with previously-studied galaxy clusters and protoclusters.

To assess whether these SMG environments are true protoclusters, we evolve the masses derived from the SHMR method to the present day masses and compare with known galaxy clusters in the local Universe. This is done using the redshift-dependent formula for the mean mass accretion rate derived from the results of the Millennium and Millennium-II simulations (Fakhouri et al. 2010; McBride et al. 2009):

$$\begin{aligned}\langle \dot{M} \rangle_{\text{mean}} = 46.1\text{M}_{\odot}\text{yr}^{-1} \left(\frac{M_z}{10^{12}\text{M}_{\odot}} \right) (1 + 1.11z) \\ \times \sqrt{\Omega_{m,0}(1+z)^3 + \Omega_{\Lambda,0}}\,,\end{aligned} \tag{3.13}$$

where M_z is the halo mass of the structure at its observed redshift, and $\Omega_{m,0}$ and $\Omega_{\Lambda,0}$ are the present-day density parameters for matter and the cosmological constant according to our assumed cosmology (Planck Collaboration 2020).

For each overdensity we begin with the total halo masses estimated using the SHMR method and apply Equation 3.13 to incrementally add mass in small time steps until the present day is reached. The present-day masses obtained with this method are $\log(M_{z=0}/\text{M}_{\odot}) = 15.93^{+0.62}_{-0.33}, 15.81^{+0.01}_{-0.55}, 15.82^{+0.04}_{-0.50}$ for the overdensities containing ALESS 5.1, ALESS 75.2, and ALESS 102.1, respectively. These masses suggest that these structures would all evolve into some of the most massive clusters in the Universe, rivalling that of the Coma cluster (e.g. Gavazzi et al. 2009; Ho et al. 2022) and other massive clusters at $z \lesssim 1$ such as those in the CLASH survey (Merten et al. 2015; Postman et al. 2012). However, given the rarity of such massive structures seen in the local Universe, we posit that the identification of progenitor structures around all three of our target SMGs is due to systematics in the calculation, rather than a real occurrence. One possible source of systematic error is that the mean mass accretion rate given by Equation 3.13 is poorly constrained for halos with masses of $\log(M_h/\text{M}_{\odot}) \gtrsim 14$ beyond $z \sim 0.5$; using this equation to trace the evolution of halos already above this mass at $z \sim 2.3$ or 3.3 may therefore provide an inaccurate result. Furthermore, this equation alone does not account for the diversity of evolutionary paths that real dark matter halos undergo, being the mean result for many halos in the Millennium simulation. With these caveats in mind, we take the upper bound of the 1–σ confidence interval for each halo mass as upper limits and the evolutionary track connecting the upper limit at the SMG redshift to the corresponding value at $z = 0$ as the upper limit on the evolving mass of the structures. This upper limit on the halo mass at the SMG redshift and the evolution to the present day is shown in Figure 3.15 as the upper edge of the shaded region for each SMG.

3.3.6.2 The SCM method for deriving halo masses

An alternate method for estimating the present-day mass of each SMG environment is obtained following Steidel et al. (1998), which approximates each SMG environment as a homogeneous sphere undergoing spherical collapse. In this case the total present-day mass is given by:

$$M_{z=0} = \bar{\rho} V (1 + \delta_m)\,, \tag{3.14}$$

where $\bar{\rho}$ is the mean comoving matter density of the Universe, δ_m is the dark matter mass overdensity, and V is the comoving volume of the structure. We refer to this method as the spherical collapse model (SCM) method.

The volumes probed by each pointing (as calculated in §3.3.1.1) are calculated using the FWHM of the Brγ filter, and thus correspond to velocity dispersions of $\sigma_v \sim 6500$ (7600) km s^{-1} at $z \sim 2.3$ (3.3). These values are significantly larger than those typically measured for protoclusters at similar redshifts, which tend to be around 300–1000 km s^{-1} (e.g. Lemaux et al. 2014; Toshikawa et al. 2016, 2020; Yuan et al. 2014). To avoid significantly overestimating the present-day masses we therefore assume a velocity dispersion of $\sigma_v = 600 \pm 50$ km s^{-1} based on the values collated by Toshikawa et al. (2020) for 34 protoclusters at $z = 2$–6. Using this velocity dispersion and the area covered by each pointing (or the area covered by just the quadrant containing the SMG in the case of ALESS 102.1) gives comoving volumes of $V = 660 \pm 60, 620 \pm 60, 160 \pm 10$ cMpc^3 for the overdensities containing ALESS 5.1, 75.2, and 102.1, respectively.

The dark matter mass overdensity is linked to the observed galaxy overdensity, δ_g, via

$$\delta_m = \delta_g / b\,, \tag{3.15}$$

where b is the bias parameter. To estimate the bias parameters for Hα emitters at $z \sim 2.3$, we make use of the relationship between b and $L_{\mathrm{H}\alpha}$ derived by Cochrane et al. (2017) at $z = 2.23$. Following a similar method to that of Stott et al.

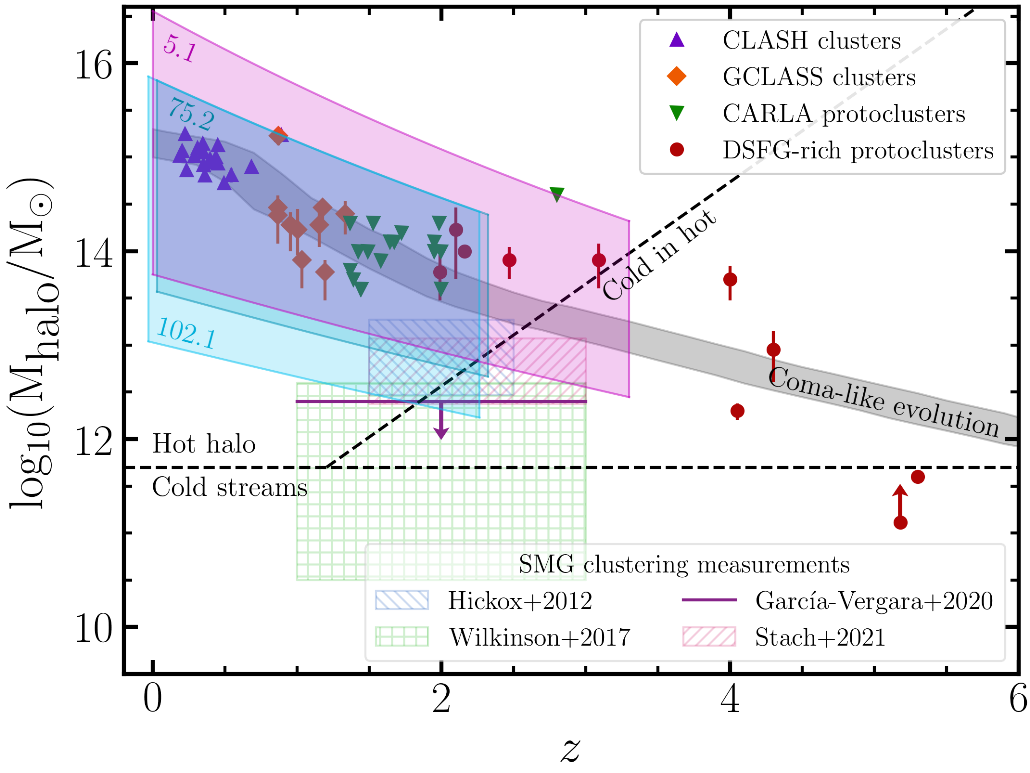

Figure 3.15: A comparison of protocluster halo masses across cosmic time. Two mass estimates are obtained for each SMG environment at both the observed redshift of the potential structure and at $z = 0$, using the methods described in §3.3.6. The evolutionary paths of these halos across cosmic time are estimated using the redshift-dependent mean mass accretion rate formula derived from the Millennium simulations (Fakhouri et al. 2010; McBride et al. 2009). The coloured shaded regions show the possible mass ranges and evolution for each of our target SMG environments, and are labelled with the ALESS ID of the inhabiting SMG. The upper bounds of these mass ranges correspond to the masses estimated using the stellar-to-halo mass relations from Behroozi et al. (2013), while the lower bounds are derived by assuming a spherical collapse model (see text for details). The grey shaded region shows the expected evolution of a Coma-like cluster (Chiang et al. 2013) and coloured symbols show samples of clusters and protocluster from CLASH, GCLASS and CARLA, and protoclusters targeted due to their richness in DSFGs, as detailed in §3.3.6.3. We include regions showing measurements of SMG halo masses obtained from clustering studies (García-Vergara et al. 2020; Hickox et al. 2012; Stach et al. 2021; Wilkinson et al. 2017) and mark the borders between different gas regimes (Dekel & Birnboim 2006). All three SMGs reside in environments consistent with protoclusters, with the possible exception of ALESS 102.1 which may reside in a protogroup instead. The lower bounds of our mass estimates are broadly consistent with the masses obtained from SMG clustering studies, while the upper bounds imply these structures may evolve into Coma-like structures or larger.

(2020), we fit a straight line to this relation and estimate b at the mean value of $L_{\mathrm{H}\alpha}$ for each SMG environment. This gives $b_{\mathrm{H}\alpha} = 2.9^{+0.2}_{-0.1}$ and $2.8^{+0.2}_{-0.3}$ for the candidate companions of ALESS 75.2 and 102.1, respectively. For the [Oiii] emitters, we first convert from $L_{[\mathrm{O\,III}]+\mathrm{H}\beta}$ to SFR using Equation 3.10, then from SFR to $L_{\mathrm{H}\alpha}$ using Equation 3.9. We then assume that the relationship between b and $L_{\mathrm{H}\alpha}$ undergoes little evolution between $z \sim 2.3$ and $z \sim 3.3$ such that the same relationship can be used here. This gives $b_{[\mathrm{O\,III}]} = 3.2^{+0.1}_{-0.1}$ for the companions of ALESS 5.1.

Using the above values of b and V along with the δ_g values calculated in §3.3.2, we obtain present-day halo masses of $\log(M_{z=0}/\mathrm{M}_{\odot}) = 14.08^{+0.25}_{-0.33}, 13.68^{+0.10}_{-0.11}, 13.18^{+0.12}_{-0.14}$ for the environments of ALESS 5.1, ALESS 75.2, and ALESS 102.1, respectively. Contrary to the previous present-day mass estimates, these masses are more akin to those of galaxy groups than galaxy clusters (e.g. Han et al. 2015; Man et al. 2019) with the possible exception of the ALESS 5.1 environment, which could evolve into a 'Fornax-like' cluster by $z = 0$ (e.g. Chiang et al. 2013).

The significant disparity between the present-day halo mass estimates from the SCM method compared with the SHMR method likely arises from the assumptions and uncertainties in the calculations. In particular, the comoving volume V is highly uncertain due to the width of the narrowband filter, and the assumed velocity dispersions (and associated uncertainties) may be underestimates. Indeed, several protoclusters have been found to have velocity dispersions $\gtrsim$1000 km s^{-1} (e.g. Kuiper et al. 2011a; Lemaux et al. 2018; Ouchi et al. 2005; Toshikawa et al. 2016), where these high values are typically attributed to a multi-component nature: these protoclusters may in fact be undergoing a merger of two (or more) halos at the time of observation. We cannot rule out this possibility for the SMG environments studied here; as such, the mass estimates derived with the spherical collapse model may be underestimates. Nevertheless we proceed with these estimates and adopt the lower bound of the 1–σ confidence intervals as lower limits for the present-day halo masses. Thus, the present-day halo mass estimates from the two methods gives a range of plausible evolutionary pathways for the SMG environments as shown on Figure 3.15.

Table 3.4: Halo mass estimates for each SMG environment.

SMG environment	$\log(M_h^{\rm SHMR}/{\rm M}_\odot)^a$	$\log(M_{h,0}^{\rm SHMR}/{\rm M}_\odot)^b$	$\log(M_h^{\rm SCM}/{\rm M}_\odot)^c$	$\log(M_{h,0}^{\rm SCM}/{\rm M}_\odot)^d$
ALESS 5.1	$13.94^{+0.38}_{-0.21}$	$15.93^{+0.62}_{-0.33}$	$12.68^{+0.18}_{-0.24}$	$14.08^{+0.25}_{-0.33}$
ALESS 75.2	$14.38^{+0.01}_{-0.40}$	$15.81^{+0.01}_{-0.55}$	$12.75^{+0.08}_{-0.09}$	$13.68^{+0.10}_{-0.11}$
ALESS 102.1	$14.39^{+0.03}_{-0.37}$	$15.82^{+0.04}_{-0.50}$	$12.35^{+0.10}_{-0.12}$	$13.18^{+0.12}_{-0.14}$

[a] Halo mass derived using the SHMR method (§3.3.6.1) at the redshift of the SMG (i.e. $z \sim 2.3$ for ALESS 75.2 and ALESS 102.1, and $z \sim 3.3$ for ALESS 5.1).

[b] Halo mass derived using the SHMR method and evolved to $z = 0$ using Equation 3.13.

[c] Halo mass derived using the SCM method and traced back to the SMG redshift using Equation 3.13 (§3.3.6.2).

[d] Descendant halo mass at $z = 0$ derived using the SCM method (§3.3.6.2).

We can also use the present-day halo mass estimates from the SCM method in combination with Equation 3.13 to trace the evolution of the SMG environments back in time to their observed redshifts, thereby obtaining a second estimate of the total mass at these redshifts. These masses are $\log(M_h/\mathrm{M}_\odot) = 12.68^{+0.18}_{-0.24}, 12.75^{+0.08}_{-0.09}, 12.35^{+0.10}_{-0.12}$ for the potential structures around ALESS 5.1, ALESS 75.2, and ALESS 102.1, respectively. This calculation provides an evolutionary track that connects the lower halo mass limit at the SMG redshift to the corresponding value at $z = 0$, and this is what defines the bottom edge of each shaded region in Figure 3.15.

3.3.6.3 Halo masses and evolution

The halo mass estimates of each SMG environment are summarised in Table 3.4, and Figure 3.15 compares the SMG halo masses and their evolution with previously-studied galaxy clusters and protoclusters. As described in §3.3.6.1 and §3.3.6.2, the upper and lower bounds shown for the SMG halos are derived from the upper limit from the SHMR method and lower limits from the SCM method, respectively. Thus, this covers the full range of reasonable halo masses and evolution for ALESS 5.1, ALESS 75.2, and ALESS 102.1. In Figure 3.15 these are compared with clusters from the Cluster Lensing And Supernova Survey with Hubble (CLASH; Merten et al. 2015; Postman et al. 2012); clusters from the Gemini Cluster Astrophysics Spectroscopic Survey (GCLASS; Muzzin et al. 2012; van der Burg et al. 2014); clusters and protoclusters from the Clusters Around Radio-Loud AGN program (CARLA; Mei et al. 2023; Wylezalek et al. 2013). We also show the halo masses calculated by Casey (2016) for overdense structures known to be rich in dusty star-forming galaxies (DSFGs), including: the GOODS-N protocluster at $z = 1.99$ (Blain et al. 2004; Chapman et al. 2009); the COSMOS protoclusters at $z = 2.10$ (Yuan et al. 2014) and $z = 2.47$ (Casey et al. 2015; Chiang et al. 2015; Diener et al. 2015); the ‘Spiderweb’ protocluster, MRC 1138-256, at $z = 2.16$ (Kuiper et al. 2011a; Kurk et al. 2000); the SSA 22 protocluster at $z = 3.09$ (Hayashino et al. 2004; Lehmer et al. 2009; Steidel et al. 1998; Tamura et al. 2009; Umehata et al. 2015); the GN20 overdensity at $z = 4.05$ (Daddi et al. 2009; Hodge et al. 2013b); the HDF 850.1 overdensity at $z = 5.18$

(Walter et al. 2012); the AzTEC-3 overdensity at $z = 5.30$ (Capak et al. 2011). In this sample of DSFG-rich protoclusters we additionally include the halo masses of the DRC at $z = 4$ (Long et al. 2020) and the SPT 2349-56 protocluster at $z = 4.3$ (Hill et al. 2020; Miller et al. 2018). Figure 3.15 shows that the potential structures surrounding our target SMGs are consistent with being protoclusters at their respective epochs.

Both the present-day masses and the high-redshift masses obtained using the SCM method (§3.3.6.2) are significantly lower than those obtained via the SHMR method (§3.3.6.1), and generally lower than the masses of protoclusters at similar redshifts (see Figure 3.15). Instead the SCM masses are more consistent with the results of SMG clustering studies (e.g. García-Vergara et al. 2020; Hickox et al. 2012; Stach et al. 2021; Wilkinson et al. 2017, see Figure 3.15), which generally agree that SMGs reside in halos with $\log(M_h/\mathrm{M}_\odot) \lesssim 13$ at $z = 1$–3. In particular García-Vergara et al. (2020) derive upper limits on the halo masses of SMGs at these redshifts based on their 870 μm flux densities, S_{870}, and find that brighter SMGs tend to occupy more massive halos, with only the brightest ($S_{870} \gtrsim 6$ mJy) being likely to evolve into massive local elliptical galaxies. Their results appear consistent with the masses derived here: ALESS 5.1 is the only target SMG above this 6 mJy threshold (Table 2.1), and based on our mass estimates is the most likely to reside in a cluster by $z = 0$ (albeit with large uncertainties). Conversely ALESS 102.1 is the faintest of the three SMGs at 870 μm, and based on the SCM method appears to be more likely to reside in a protogroup than a protocluster.

Figure 3.15 also includes the approximate boundaries separating different gas regimes, as proposed by Dekel & Birnboim (2006): in halos for which $\log(M_h/\mathrm{M}_\odot) \lesssim 12$, inflowing gas is predominantly cold and enables the growth of galaxies; in halos above this mass threshold, these gas inflows are shock-heated resulting in strangulation of the galaxy within. However, if these massive halos still fall below some other, redshift-dependent mass threshold (as marked by the 'cold in hot' boundary in Figure 3.15), then penetrating cold gas may still be sustaining galaxy growth. At $z \sim 2.3$ this mass threshold is $\log(M_h/\mathrm{M}_\odot) \sim 12.9$, while at $z = 3.3$ it is $\log(M_h/\mathrm{M}_\odot) \sim 14.0$.

Based on our mass estimates, the environment of ALESS 5.1 is likely in the 'cold in hot' category at its observed redshift: while the threshold mass is within the 1σ confidence interval for the SHMR-derived halo mass, the SCM-derived mass is significantly below the threshold. It is therefore probable that galaxies in the environment of ALESS 5.1 are undergoing growth sustained by penetrating cold gas inflows. Conversely galaxies in the environment of ALESS 75.2 are more likely to be undergoing strangulation due to shock-heating in the halo at the observed redshift; the SHMR-derived halo mass lies significantly above the limit for 'cold in hot' gas inflows, and while the SCM-derived mass is $>1\sigma$ below the limit we caution that the uncertainties on this mass are likely underestimated. Finally, the two mass estimates for the environment of ALESS 102.1 at its observed redshift are separated from the 'cold in hot' threshold mass by $\gtrsim 4\sigma$ on either side; we thus do not conclude anything about the gas regime in this environment.

3.4 Conclusions

We have conducted a wide-field narrowband survey of star-forming galaxies in the environments of three SMGs at $z \sim 2.3$ and $z \sim 3.3$ to determine whether these SMGs reside in protocluster-like environments. By studying individual SMGs selecting based only on their spectroscopic redshifts we have measured 'typical' SMG environments. Our main conclusions are as follows:

- Using HAWK-I Brγ and K_s photometry, we identified a total of 147 candidate emission line galaxies in the two HAWK-I pointings containing the three target SMGs. Having extracted photometry from archival UV-to-MIR broadband images, we performed SED fitting with EAZY-PY to obtain photometric redshifts for these galaxies and identified 44, 11, and 4 companion galaxies to the SMGs ALESS 75.2 ($z_{\rm spec} = 2.294$), ALESS 102.1 ($z_{\rm spec} = 2.296$), and ALESS 5.1 ($z_{\rm spec} = 3.303$), respectively.

- By constructing luminosity functions for each SMG environment and comparing with blank-field luminosity functions from the literature at similar redshifts, we measure overdensity parameters of $\delta_g = 4.0^{+14.9}_{-3.2}$, $2.6^{+1.4}_{-1.2}$, and $0.2^{+0.6}_{-0.5}$ across the whole ~ 4 Mpc HAWK-I field of view for ALESS 5.1, 75.2, and 102.1, respectively. Whilst ALESS 102.1 is not overdense on these large scales, it does sit in a ~ 1 Mpc region with $\delta_g = 3.8^{+2.4}_{-1.8}$.

- We considered the spatial distribution of companion Hα emitters in the environments of the two SMGs at $z \sim 2.3$ (ALESS 75.2 and 102.1) by measuring their density in annuli around the SMGs and by constructing overdensity maps. For ALESS 75.2 the companion galaxies are spread out across the entire HAWK-I field of view, spanning a few Mpc. This is consistent with simulations, in which protoclusters are seen to extend over several Mpc at $z \sim$ 2–3. The SMG resides near a possible density peak of Hα emitters, although a greater peak is seen a few arcminutes eastward which appears to be associated with a previously discovered Lyα blob (Yang et al. 2010). The overdensity around ALESS 102.1 is smaller ($\sim$ 1 Mpc) and could instead evolve into a galaxy group locally.

- Stellar masses and SFRs were obtained for the companion galaxies in each SMG environment by performing SED fitting with MAGPHYS. The galaxies are generally scattered about the star-forming main sequence at their respective epochs, with no evidence of enhanced star formation activity in either environment.

- Two methods were used to estimate the total halo mass of each SMG environment, which provided upper and lower bounds on the halo masses at the observed redshifts and evolving to the present day. At $z \sim 2.3$ ALESS 75.2 and 102.1 occupy potential structures with masses of $\log(M_h/\mathrm{M}_\odot) = 12.7$–14.4, and 12.4–14.4, respectively. These are expected to evolve into corresponding structures with $\log(M_h/\mathrm{M}_\odot) = 13.6$–15.8 and 13.0–15.9 at $z = 0$. For ALESS 5.1 at $z \sim 3.3$ the halo mass is $\log(M_h/\mathrm{M}_\odot) = 12.4$–14.3, which grows to 13.9–16.6 at the present day. Whilst these estimates are uncertain, they suggest that ALESS 5.1 and 75.2 likely reside in protoclusters, while ALESS 102.1 resides in either a protocluster or a protogroup.

With this study we have demonstrated the efficacy of narrowband surveys as a means of searching for galaxy overdensities around SMGs selected without bias towards particular environments. Future followup with larger samples of SMGs and/or spectroscopic confirmation of companion galaxies would confirm the nature of the overdensities that we have detected, and resolved analyses (e.g.

with ALMA and/or JWST) will further reveal how the member galaxies evolve (see §5.3).

Chapter 4

The Radio Galaxy Environment Reference Survey (RAGERS): a submillimetre study of the environments of massive radio-quiet galaxies at $z = 1$–3

Abstract

Measuring the environments of massive galaxies at high redshift represents an important part of understanding galaxy evolution and the conditions that gave rise to the distribution of matter we see in the Universe today. While high-z radio galaxies (HzRGs) and quasars tend to reside in protocluster-like environments, the environments of their radio-quiet counterparts are relatively unexplored, particularly in the submillimetre regime, which traces dust-obscured star formation. In this study we search for 850 μm-selected submillimetre galaxies in the environments of massive ($M_\star > 10^{11}$ M$_\odot$), radio-quiet ($L_{500\ \mathrm{MHz}} \lesssim 10^{25}$ W Hz^{-1}) galaxies at $z \sim 1$–3 in COSMOS. By constructing number counts in circular regions of radius $1'$–$6'$ and comparing with blank-field measurements, we find no significant overdensities of SMGs around massive radio-quiet galaxies at any of these scales, despite being sensitive to overdensities of $\delta \sim 0.4$. To probe deeper than the catalogue we also examine the distribution of peaks in the SCUBA-2 SNR map, which reveals only tentative signs of any difference in the SMG densities of the radio-quiet galaxy environments compared to the blank field, and only on smaller scales ($1'$ radii, corresponding to ~ 0.5 Mpc) and higher SNR thresholds. We conclude that massive, radio-quiet galaxies at high redshift are typically in environments with $\delta \lesssim 0.4$. These environments are either consistent in their SMG density with the blank field, or contain only weak overdensities spanning small (sub-Mpc) physical scales. The contrast between our results and studies of HzRGs with similar stellar masses and redshifts suggests there is interaction and feedback between the wide-field environment and radio AGN activity at high redshift.

4.1 Introduction

Given their known tendency to reside in protoclusters, HzRGs are a strong contender for the progenitors of BCGs (see §1.4.2). These only comprise a fraction of the high-mass population at high redshift however, and the evolution of similarly massive radio-quiet (RQ) counterparts has been relatively unexplored. It is therefore uncertain whether the overdense environments of HzRGs are purely a consequence of their high stellar masses (galaxies with higher stellar mass do tend to occupy more massive dark matter halos; see §1.2.6), or if their radio-loudness is also intrinsically linked to this type of environment. This latter scenario could lead to a selection bias by which radio-loud AGN are easier to observe in overdense environments. Observations are yet to disentangle these possibilities however: some studies have found a positive trend between galaxy density and radio power, thereby vindicating this suspicion of a selection bias (e.g. Falder et al. 2010); meanwhile others have found no such trend (e.g. Karouzos et al. 2014) or even a negative trend (e.g. Donoso et al. 2010). Dedicated investigations of the environments of massive RQ galaxies at high redshift are needed in order to truly determine whether stellar mass, AGN activity, or both are related to the density of the surrounding environment.

Studies of galaxy environments at high redshift have predominantly involved identifying overdensities of galaxies selected in the rest-frame UV to optical, e.g. via Lyα or Hα emission (e.g. Kurk et al. 2000; Shimakawa et al. 2018; Venemans et al. 2007), or through the Lyman or Balmer/4000 Å breaks (e.g. Hatch et al. 2011a; Kajisawa et al. 2006; Uchiyama et al. 2022). Such studies implicitly omit the population of dusty star-forming galaxies (DSFGs) now known to be a significant contributor to the total star-formation rate density at these redshifts (e.g. Barger et al. 2012; Coppin et al. 2006; Swinbank et al. 2014). These DSFGs are highly obscured in the rest-frame UV-to-optical due to the high abundance of dust, instead being most luminous in the far-infrared/submillimetre (with the brightest of these galaxies being labelled ‘submillimetre galaxies’, or SMGs). A complete picture of protocluster formation thus also requires dedicated far-IR/submillimetre studies. For a review of cluster evolution in the infrared see Alberts & Noble 2022.

Far-IR and submillimetre observations of known high-redshift protoclusters have confirmed overdensities of SMGs in these structures (e.g. Blain et al. 2004; Matsuda et al. 2011; Tamura et al. 2009), and simulations confirm that SMGs can trace overdensities (e.g. Davé et al. 2010). However, there is still debate as to whether SMGs as a population typically reside in protoclusters, or whether they may simply be effective as tracers of such structures (e.g. Calvi et al. 2023; Casey 2016; Miller et al. 2015, see also Chapter 3). Far-IR and submillimetre surveys targeting HzRGs have identified dust-obscured emission for the HzRGs themselves, as well as identifying nearby populations of SMGs, in excess of the numbers expected in the field (e.g. Greve et al. 2007; Ivison et al. 2000; Rigby et al. 2014; Stevens et al. 2003, 2010). However, there is a dearth of similar studies of high mass, high redshift, but radio-quiet galaxies. Rigby et al. (2014) found a hint of a correlation between radio power and the overdensity of nearby *Herschel*-detected galaxies, though they only probe down to radio luminosities of $L_{500\mathrm{MHz}} \sim 10^{28.5}$ W and it is not a statistically significant finding. This work, along with similar low-significance results at shorter wavelengths (e.g. Galametz et al. 2012), provides a hint that radio-quiet galaxies may have fewer (submillimetre) companions than HzRGs, which suggests the potential for different evolutionary pathways in these populations.

The RAdio Galaxy Environment Reference Survey (RAGERS; Greve et al., in prep.) is a JMCT/SCUBA-2 Large Program with the aim of mapping the submillimetre environments of 27 powerful HzRGs at $1 < z < 3.5$ and comparing them to the environments of a radio-quiet control sample that has been matched in stellar mass and redshift. In this Chapter we measure the environments of this control sample using archival SCUBA-2 data, and compare the SMG densities with blank field expectations to assess whether these environments are overdense.

This Chapter is structured as follows: in §4.2 we describe our sample selection; §4.3 details the method used to measure the submillimetre environments of our sample; §4.4 and §4.5 contain our key results and subsequent discussion; we present our conclusions in §4.6.

4.2 Data

The aim of this study is to measure the density of SMGs around a large sample of massive, RQ galaxies, where these RQ galaxies have similar redshifts and stellar masses to the radio-loud (RL) galaxies targeted by RAGERS. The 27 HzRGs in the RAGERS sample are approximately uniformly distributed at $z = 1$–3.5 and were selected from the *Herschel* Radio Galaxy Evolution Project (HeRGÉ) (De Breuck et al. 2010; Seymour et al. 2007, 2012). In terms of stellar mass and radio luminosity the RAGERS targets are representative of typical HzRGs at $z = 1$–3.5 (Greve et al. in prep), and thus by selecting RQ analogues to the RAGERS galaxies our study is broadly applicable and representative of RQ galaxies in comparison to the whole HzRG population at these redshifts.

In order to select appropriate RQ galaxies and study their submillimetre environments, we require: (1) High-quality redshifts and stellar masses for all RQ galaxies for comparison with the RL sample; (2) RQ galaxies must reside in areas with contiguous, deep submillimetre coverage to enable identification of companion SMGs; and (3) The targets must have been observed in the radio, to enable the exclusion of radio-loud galaxies from our study.

We therefore choose the COSMOS field as the location for our study, due to the wide area, deep radio and submillimetre data, and extensive optical and NIR photometry and spectroscopy. The COSMOS2020 catalogue (Weaver et al. 2022) contains UV-to-NIR photometry covering the entire $2\,\mathrm{deg}^2$ of the COSMOS field, as well as high-quality photometric redshifts and galaxy properties (such as stellar masses) derived from spectral energy distribution (SED) fitting. The VLA-COSMOS survey adds extensive radio coverage at 1.4 and 3 GHz (Schinnerer et al. 2004; Smolčić et al. 2017b), and SCUBA-2 submillimetre observations at 850μm are provided by S2COSMOS (Simpson et al. 2019, henceforth S19). S2COSMOS reaches a median noise level of $\sigma_{850\ \mu\mathrm{m}} = 1.2$ mJy beam^{-1} over the deepest 1.6 deg^2 of the survey (the ‘MAIN’ region), though there is an additional 1 deg^2 SUPP region with shallower data (median $\sigma_{850\ \mu\mathrm{m}} = 1.7$ mJy beam^{-1}), which we exclude from our analyses (see Figure 4.1). Combining the data from these three studies enables the effective identification of RQ analogues for the RAGERS RL galaxies and measurement of their submillimetre environments.

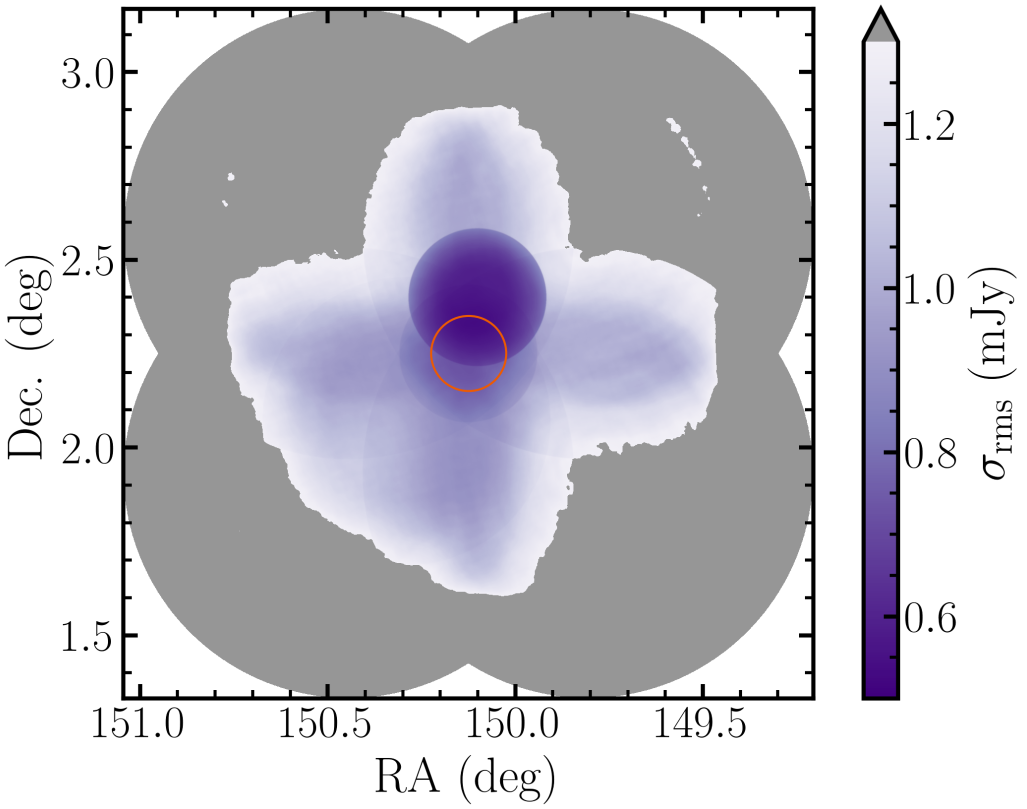

Figure 4.1: Map showing the 1σ sensitivity, $\sigma_{\rm rms}$, of the S2COSMOS observations at 850 μm. All regions for which $\sigma_{\rm rms} > 1.3$ mJy have been greyed out such that only the area considered in this study is highlighted. The orange circle at the centre of the map has a radius of $6'$ and thus represents the largest aperture that we use to search for SMGs around a given galaxy in our sample (see §4.3.2). The disconnected regions in which $\sigma_{\rm rms} \leq 1.3$ mJy that are visible to the north-west and north-east are not considered in this study.

4.2.1 Sample selection

In order to study RQ galaxies that are analogues of the RAGERS HzRGs, we require a sample of RQ galaxies with similar stellar masses and redshifts to RAGERS sources. By comparing the environments of RQ galaxies with similar stellar masses and redshifts to those of HzRGs, we ensure that any observed difference between their environments is linked to the AGN activity and radio-loudness of the galaxy. We therefore select RQ galaxies from COSMOS2020 (Weaver et al. 2022) that have stellar masses and redshifts within $\Delta \log(M_{\star}/\mathrm{M}_{\odot}) = \pm 0.05$ and $\Delta z = \pm 0.1$ of a RAGERS HzRG, respectively (Figure 4.2). The sizes of the redshift and stellar mass intervals were chosen such that each RAGERS HzRG has at least 10 RQ analogues in the final sample. Of the 27 RAGERS RL galaxies, nine have only have upper limits on their stellar masses (due to AGN contamination in the photometry) and are therefore excluded, and the remainder of this study focuses on RQ analogues to the remaining 18 HzRGs in RAGERS.

Having selected COSMOS2020 sources with similar stellar masses and redshifts to RAGERS galaxies, we next identify and remove candidate RL galaxies using VLA-COSMOS (Smolčić et al. 2017c), which contains all 3 GHz sources that are detected at $>5\sigma$ (median σ = 2.3 mJy beam^{-1}) and have counterparts at optical, near-infrared, mid-infrared, or X-ray wavelengths. Sources in VLA-COSMOS are flagged as either moderate-to-high radiative luminosity AGN (HLAGN), low-to-moderate radiative luminosity AGN (MLAGN), or star-forming galaxies (SFGs) according to their multiwavelength properties (see Smolčić et al. 2017c for details). Using a matching radius of $1''$ we cross-match the COSMOS2020 catalogue with the optical/NIR/MIR counterpart positions listed in the VLA-COSMOS catalogue and exclude any sources flagged as HLAGN or MLAGN from our sample. We also remove any sources that have multiple radio components and sources with a probability >20 percent of being falsely matched to their optical/NIR/MIR counterpart in VLA-COSMOS.

Finally, we use the sensitivity map from S2COSMOS (Simpson et al. 2019; see Figure 4.1) to select sources with the deepest 850 μm coverage, where the depth is $\sigma_{\mathrm{rms}} < 1.3$ mJy beam^{-1}. Our study probes the environments of RQ galaxies out to $6'$, so we therefore also require that the deep SCUBA-2 coverage extends at least 6′ radius around each RQ galaxy, and we exclude sources that are close to the edge of the deep SCUBA-2 regions.

The final sample consists of the 1128 galaxies that remain after applying all of these selection criteria. Of the 1128 galaxies there are between 11 and 185 RQ analogues (median 51) for each of the 18 RAGERS HzRGs. The stellar masses and redshifts of this sample of RQ galaxies, compared with the HzRGs from RAGERS and the whole COSMOS2020 catalogue are shown in Figure 4.2.

4.3 Calculating number counts

4.3.1 Method

In order to probe the environments of RQ galaxies we measure the 850 μm number counts in apertures around the target galaxies. Number counts quantify the surface density of sources as a function of their submillimetre flux density; as such they provide a direct measure of source abundance and environment. Number counts are particularly useful for submillimetre data as they do not require cross matching to other wavelengths or obtaining redshifts, both of which are challenging and biased for SMGs due to the large beam sizes of single-dish surveys and the faintness of these dusty, high-redshift galaxies at optical and near-IR wavelengths (e.g. see Casey et al. 2014 for a review). In this study we measure both the differential (dN/dS [mJy deg^{-2}]) and cumulative ($N(>S)$ [deg^{-2}]) number counts around the RQ galaxies and the blank field. We use both differential and cumulative counts because of the different strengths and weaknesses of the two measurements: differential counts have the advantage that the measurements in each bin are relatively independent of each other, but cumulative counts contain more sources in the fainter bins and therefore have smaller uncertainties.

Constructing number counts requires knowledge of the survey completeness as a function of observed flux. In S19 this was derived using simulations to map the variation in completeness with deboosted 850 μm flux density and local rms noise level. We reproduce the completeness map from Figure 6b of S19 using the following procedure: first, the completeness contours from the figure are used to

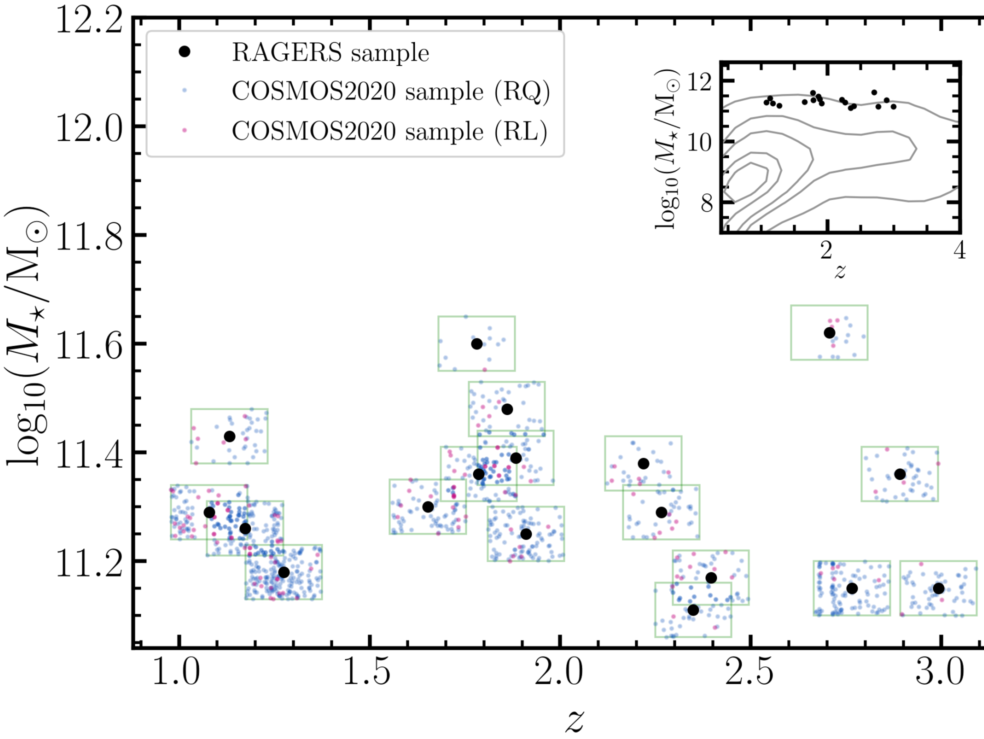

Figure 4.2: Distribution of the RAGERS radio-loud galaxies (black circles) in stellar mass and redshift, with green boxes to show the selection criteria for identifying radio-quiet analogues used in this study. Coloured dots show all galaxies from COSMOS2020 (Weaver et al. 2022) with redshifts and stellar masses that satisfy the selection criteria, and also reside in a region with a local rms noise of $\lesssim$1.3 mJy beam^{-1} in the 850 μm map from S2COSMOS (Simpson et al. 2019). Pink dots show the subset of these galaxies that are flagged as MLAGN or HLAGN in VLA-COSMOS (Smolčić et al. 2017c), while blue dots show galaxies which do not have this flag and thus make it into the final sample of RQ analogues. The inset panel shows the stellar masses and redshifts of RAGERS HzRGs overlaid on contours marking the 10th, 30th, 50th, 70th and 90th percentiles of galaxies in the entire COSMOS2020 catalogue, demonstrating that HzRGs (and thus our RQ analogues) have high stellar masses for their redshifts.

obtain values of deboosted flux density and local rms corresponding to 10, 30, 50, 70, and 90 percent completeness, which are then mapped to a uniformly spaced grid of flux density and rms values. A 2D interpolator is then used to estimate the completeness in the gaps between these curves on the grid. To estimate curves of constant completeness for completenesses <10 and >90 percent, which aren't quantified in the S19 figure, we consider each row in the grid (corresponding to a constant rms) individually to examine the completeness as a function of flux density at a given rms. We then use a Fermi-Dirac-like[1] function to fit to the known data from the S19 figure (i.e. the flux densities at 10, 30, 50, 70, and 90 percent completeness), and use the fit to extrapolate to completenesses <10 and >90 percent. By mapping these to the grid and interpolating, we obtain the completeness as a 2D function of deboosted flux density and local rms. Further details and figures outlining this procedure can be found in Appendix A.1.

To test the accuracy of the derived completeness function, we recreate the S2COSMOS number counts and compare our results with those in S19. Following S19, we create 10^4 realisations of the S2COSMOS catalogue, where each version is generated by randomly drawing (deboosted) flux density values for each source based on their uncertainties as quoted in the original catalogue. Completeness corrections are then calculated for each randomly drawn flux density using the completeness function derived previously, along with the local rms provided for each source in the original catalogue. Differential and cumulative number counts are constructed for each realisation of the catalogue using the same binning as S19, and the median of the resultant distribution for each bin determines the bin height. Uncertainties are derived by considering both the 16th–84th percentile ranges of these distributions and Poissonian uncertainties. Figure 4.3 compares the number counts from S19 with our reconstruction. After applying our completeness corrections, we find good agreement for all bins above 3 mJy, with any discrepancies (which reach a maximum of $\sim$ 10 percent) being within the uncertainties. For bins fainter than 3 mJy the discrepancies range from $\sim$ 4–20

---

[1] While true Fermi-Dirac functions describe the distribution of fermion energy states in a quantum system, its shape is similar to the characteristic S-shape of a completeness curve when plotted as a function of flux density (see e.g. Figure 8 of Geach et al. 2017), hence the choice to use a similar function here.

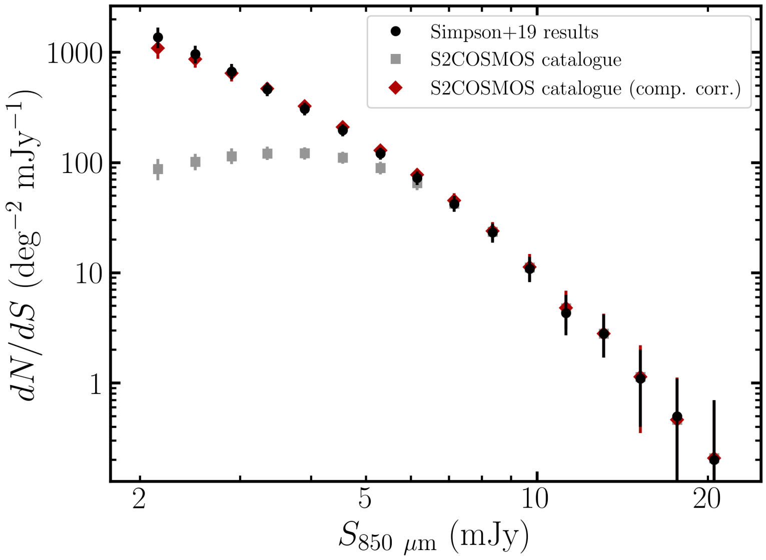

Figure 4.3: Comparison of the submillimetre number counts in S2COSMOS as measured in Simpson et al. (2019) (black) and from the catalogue; the grey points show the result of directly binning the sources in the S2COSMOS catalogue by their deboosted 850 μm flux densities, while the red points show the result of applying completeness corrections using the function shown in Figure A.2.

percent. While this is still within the uncertainties, we note that the completeness corrections at these flux densities are heavily dependent on the extrapolated completeness function and therefore may not be reliable. These bins are also potentially impacted by the absence of sources below the faint end of the catalogue limit. We therefore exclude any bins fainter than 3 mJy in subsequent analyses. We further test this method by fitting Schechter functions (§4.4.1) to the reproduced S2COSMOS counts and verify that the derived parameters are comparable to those presented in S19.

4.3.2 Application for this study

Number counts are next derived for the environments of the RQ galaxies selected in §4.2 by considering one RQ analogue for each RAGERS HzRG at a time and using the method described in §4.3.1. The galaxies are randomly chosen but with the proviso that the same galaxy cannot be selected as an analogue for multiple

HzRGs, as would otherwise be possible for HzRGs with similar stellar masses and redshifts (see Figure 4.2). We then identify submillimeter sources in S2COSMOS that lie within apertures of radius R centred on each RQ galaxy. To assess the scale of any overdensities and examine whether the choice of radius affects the results we construct four versions of the number counts using radii of $1'$, $2'$, $4'$, and $6'$. These radii correspond to physical scales of $\sim$0.5–3 Mpc at the redshifts probed by this study. An aperture with $R = 6'$ covers approximately three percent of the S2COSMOS region probed by this study (see Figure 4.1). Consequently, the mean area considered when simultaneously measuring the environments of 18 randomly-selected RQ galaxies is ~ 42 percent of the S2COSMOS area (note that some of the apertures are likely to overlap). We therefore do not consider larger apertures so that we avoid sampling the majority of S2COSMOS.

For each of the 10^4 realisations of the S2COSMOS catalogue, the selected submillimeter sources are binned by their randomly drawn deboosted flux densities and each source is weighted by the reciprocal of the completeness corresponding to its local rms noise and deboosted flux density. For the differential number counts, the weighted counts in each bin are divided by the product of the bin width (ΔS) and the combined area of the apertures used to survey the RQ galaxy environments ($A_{\rm tot}$); for the cumulative number counts, each bin is just divided by $A_{\rm tot}$. Each aperture is treated independently – i.e. any overlap between apertures is ignored, and sources within the overlapping area are multiply counted – such that $A_{\rm tot}$ is simply the sum of each aperture's area.

The random selection of RQ galaxies is repeated 1000 times and number counts constructed for all 10^4 realisations of the catalogue each time, such that each bin ultimately has a distribution of 18×10^7 values associated with it. The width of this distribution encapsulates the uncertainties from both the source flux densities and the stochasticity in the selection of RQ analogues for each iteration. The final bin heights are then taken to be the medians of these distributions and the bin uncertainties incorporate both the 16th–84th percentile ranges in the distributions and Poissonian uncertainties.

To interpret the submillimetre number counts around RQ galaxies we require a measure of the number counts in the blank field. For this we use the MAIN sample from S2COSMOS ($A_{\rm tot} = 1.6$ deg^2) and apply the method described in

§4.3.1, using binning that matches the number counts for our RQ galaxies to ensure a direct like-for-like comparison. In generating the blank-field counts all 10^4 realisations of the catalogue are used and we have verified that our results are consistent with those from S19, where S19 showed that COSMOS is similarly dense at 850μm as other blank fields.

4.4 Results

4.4.1 The environments of massive RQ galaxies

The differential and cumulative number counts calculated in §4.3 for the RQ galaxy environments are presented in Figure 4.4. Results are shown separately for the four different search radii of $1'$, $2'$, $4'$, and $6'$, alongside the blank-field results constructed from the MAIN S2COSMOS sample. The combined number counts for all the RQ analogues are highlighted and it is these that we use for the remainder of our analyses. We also show the number counts around the RQ analogues of each RAGERS HzRG to demonstrate the scatter between fields, though the small numbers involved mean that uncertainties on these subsets are significant. When considering the whole sample, there is qualitatively no significant difference between the number counts of the blank field and the RQ environment, regardless of the spatial scale considered.

To quantitatively determine whether the environments of RQ galaxies have different submillimetre number counts we fit them with Schechter functions (Schechter 1976). Differential number counts are typically parametrised using Schechter functions of the form

$$\frac{dN}{dS} = \frac{N_0}{S_0}\left(\frac{S}{S_0}\right)^{-\gamma} \exp\left(-\frac{S}{S_0}\right) \tag{4.1}$$

where N_0 and S_0 determine surface density and flux density at the 'knee' of the Schechter function, respectively, and γ is the slope of the function at the faint end. By integrating Equation 4.1 the same parameters are used to define a function

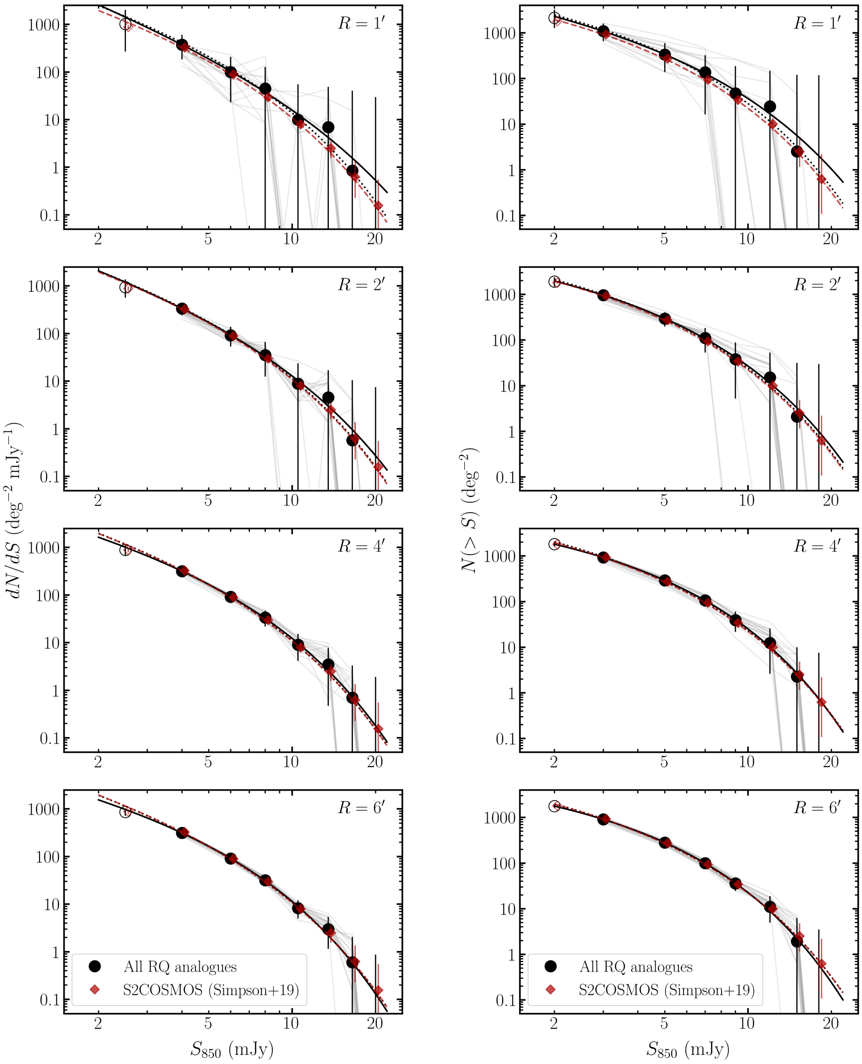

Figure 4.4: Differential *(left)* and cumulative *(right)* 850 μm number counts comparing the regions around RQ galaxies with the blank field. Each row shows the measurements and Schechter function fits using a different radius to search for candidate submillimetre companions (black points), as indicated in the top-right corner of each panel (*top to bottom:* $1'$, $2'$, $4'$, $6'$). Red diamonds and dashed lines represent the blank field and show the number counts and corresponding fits for the entire MAIN region of the S2COSMOS field, created using the method described in §4.3 and catalogue from S19. Grey lines show the results for the RQ analogues of each individual RAGERS HzRG and give an indication of the scatter between different RQ galaxy regions (though the small number statistics means that uncertainties are significant). Solid black lines show the best-fit Schechter functions for the combined datasets when all parameters are allowed to vary, and dotted black lines show the fits when N_0 is the only free parameter (i.e. S_0 and γ are fixed to the blank field values; see §4.4.1). Bins with flux density < 3 mJy are marked with open symbols and excluded from the fitting due to low completeness. There is no significant difference between the submillimetre environments of the RQ sample and the blank field at any of these scales.

to fit the cumulative counts:

$$N(>S') = \int_{S'}^{\infty} \frac{dN}{dS} dS = N_0 \Gamma(-\gamma + 1, \frac{S'}{S_0}) \tag{4.2}$$

where Γ represents the upper incomplete gamma function.

The best-fit parameters for the functions described by Equations 4.1 and 4.2 are measured for both the blank field and the RQ environment number counts using a Markov Chain Monte Carlo (MCMC) fitting procedure. Bins with flux density < 3 mJy are excluded from the fitting due to low completeness. The S_0, N_0 and γ measured for each region are summarised in Figure 4.5 (including the correlations between parameters) and Table 4.1, and the corresponding best-fit functions are shown on the number counts in Figure 4.4.

As shown by Figure 4.5, at all scales examined ($1' - 6'$) there is no significant difference between the best-fit parameters in regions close to RQ galaxies and the blank-field. The significant overlap, even at the 1σ level indicates that there is no significant overdensity of 850 μm-selected SMGs in the environments of RQ galaxies.

Due to the sizeable uncertainties in our number counts and in fitting three-parameter Schechter functions, we also test for significant differences in the N_0 parameter when S_0 and γ are both fixed to the blank-field values, i.e. for $S_0 =$ 3.1 (3.0) mJy and $\gamma = 1.6$ (1.5) for the differential (cumulative) number counts. Since the N_0 parameter scales the number density of submillimetre sources (i.e. the y-axis on Figure 4.4) a value of N_0 significantly above the blank-field value would imply an overdense environment. However, even with the added constraints of a single parameter fit (and the resulting smaller uncertainties), we still find no significant difference between the blank-field and the environments of the RQ analogues (see Table 4.1). These results are in contrast to the environments of HzRGs, which have been found to contain overdensities of submillimetre sources (e.g. Greve et al. 2007; Ivison et al. 2000; Rigby et al. 2014; Stevens et al. 2003, 2010).

Table 4.1: Best-fit Schechter parameters for the differential and cumulative number counts, obtained from MCMC fitting. The values quoted are the medians of the posterior distributions for each parameter obtained through MCMC fitting, with 1σ uncertainties defined by the 16th and 84th percentiles.

Region [a]	N_0 [b] (deg^{-2})	S_0 [b] (mJy)	γ [b]	$N_{0,\mathrm{fixed}}$ [c] (deg^{-2})
Differential counts				
$1'$	5700^{+5700}_{-3600}	$3.1^{+1.5}_{-1.2}$	$2.2^{+2.1}_{-1.6}$	6700^{+2900}_{-2300}
$2'$	5500^{+5200}_{-3100}	$3.0^{+1.5}_{-1.1}$	$1.8^{+1.3}_{-1.3}$	5600^{+1300}_{-1200}
$4'$	4900^{+3100}_{-2300}	$2.9^{+1.6}_{-1.0}$	$1.5^{+0.8}_{-1.0}$	5330^{+630}_{-610}
$6'$	5100^{+2200}_{-2100}	$2.8^{+1.4}_{-0.8}$	$1.4^{+0.8}_{-0.9}$	5220^{+450}_{-440}
S2COSMOS	5300^{+1600}_{-2200}	$3.1^{+1.1}_{-0.8}$	$1.6^{+0.6}_{-0.7}$	—
Cumulative counts				
$1'$	5000^{+5900}_{-3600}	$3.2^{+1.9}_{-1.2}$	$2.1^{+1.8}_{-1.5}$	6600^{+2300}_{-1900}
$2'$	4800^{+4800}_{-3000}	$3.0^{+2.0}_{-1.1}$	$1.7^{+1.1}_{-1.3}$	5610^{+1000}_{-940}
$4'$	4500^{+2300}_{-2100}	$2.9^{+1.6}_{-0.9}$	$1.4^{+0.9}_{-1.0}$	5420^{+500}_{-480}
$6'$	4800^{+1600}_{-1700}	$2.7^{+1.2}_{-0.7}$	$1.2^{+0.8}_{-0.9}$	5260^{+360}_{-350}
S2COSMOS	5100^{+1000}_{-1500}	$3.0^{+0.8}_{-0.6}$	$1.5^{+0.5}_{-0.6}$	—

[a] Region studied, where numbers give the radius of a circular area around RQ galaxies as described in §4.4.1, and S2COSMOS is the blank field.
[b] Parameters of the best-fit Schechter function when all three parameters are allowed to vary.
[c] $N_{0,\mathrm{fixed}}$ is the measured N_0 when S_0 and γ are fixed to the blank-field values (§4.4.1).

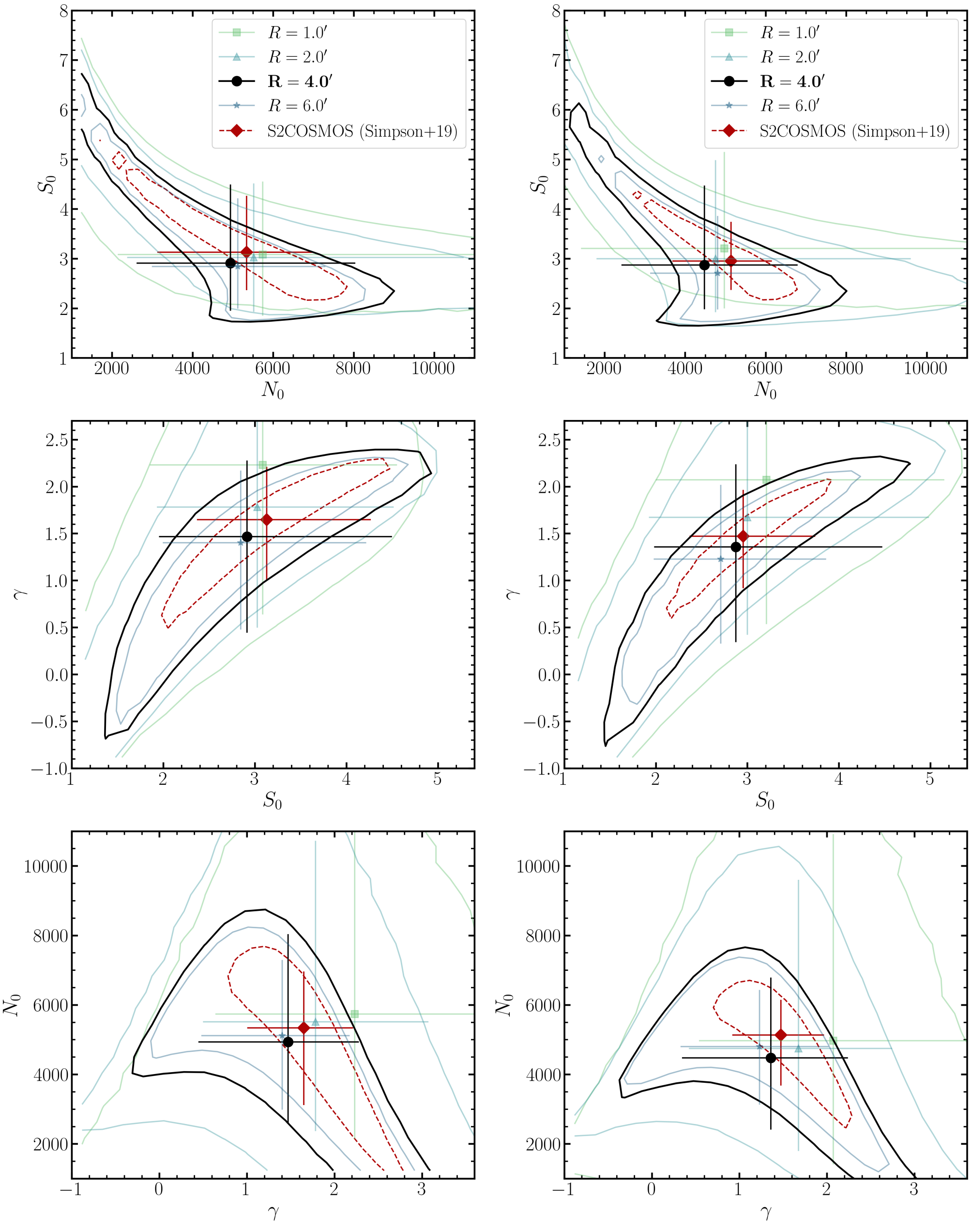

Figure 4.5: Contours representing the 1σ confidence regions for the parameters of the Schechter functions fitted to the differential *(left)* and cumulative *(right)* number counts. Data points and error bars show the medians and 16th–84th percentile ranges on each individual parameter. Black circles and thick contours represent the fits to the RQ analogue number counts when a $4'$ radius is used; squares, upward triangles and downward triangles are used for radii of $1'$, $2'$ and $6'$, respectively. Red diamonds and dashed contours show the results for the blank-field, based on the MAIN sample of S2COSMOS. There is significant overlap between the measurements at all radii and with the blank-field results, demonstrating that there is no significant difference between the $1'$–$6'$ scale environments of our RQ analogues and the blank field.

4.4.2 The environments of radio AGN in COSMOS

When selecting the RQ sample we excluded any galaxies that had been flagged as ‘MLAGN’ or ‘HLAGN’ in the VLA-COSMOS catalogue (Smolčić et al. 2017c; pink dots in Figure 4.2), so as to minimise any contamination by radio-loud sources (§4.2.1). We are therefore able to repeat the construction of the number counts, but in environments around galaxies with AGN and radio emission. This sample consists of 148 galaxies, with a median of 6 matched in mass and redshift to each of the 18 considered RAGERS HzRGs.

Note that these VLA-COSMOS AGN are not necessarily ‘radio loud’. HzRGs have rest-frame 500 MHz radio luminosities of $L_{500\mathrm{MHz}} > 10^{27}$ W Hz^{-1} (Miley & De Breuck 2008) and this is also the lower limit of radio luminosity for RAGERS galaxies. In VLA-COSMOS, Smolčić et al. (2017c) select MLAGN and HLAGN using several multiwavelength criteria, so to see how they compare with HzRGs we extrapolate the rest-frame 500 MHz luminosities for each MLAGN and HLAGN by using the observed-frame 1.4 GHz and 3 GHz luminosities from VLA-COSMOS to calculate the spectral index, α_s, of the radio SED[1]. This spectral index is defined via

$$S_\nu \propto \nu^{\alpha_s} \tag{4.3}$$

where S_ν is the flux density at frequency ν. Only two of the 148 MLAGN/HLAGN analogues to the RAGERS galaxies have $L_{500\mathrm{MHz}} > 10^{27}$ W Hz^{-1}; the median $L_{500\mathrm{MHz}}$ is $10^{24.2}$ W Hz^{-1}. The majority of these galaxies (146/148=99%) are therefore not true HzRGs and have significantly fainter radio luminosities than the RAGERS sample. This MLAGN/HLAGN sample probes an intermediate regime between HzRGs and our RQ sample.

We repeat the construction of the number counts and Schechter function fitting within 1′, 2′, 4′ and 6′ of galaxies in this MLAGN/HLAGN sample and find no significant difference with respect to either the blank field or the RQ environment number counts (Figures 4.6 and 4.7). Whilst at odds with studies of SMGs around HzRGs (e.g. Greve et al. 2007; Ivison et al. 2000; Rigby et al. 2014;

---

[1] For galaxies where only 3 GHz luminosities were measured, Smolčić et al. (2017c) assume a spectral index $\alpha_s = -0.7$ to estimate the 1.4 GHz luminosities.

Stevens et al. 2003, 2010) this result is likely due to the MLAGN/HLAGN sample not being traditional radio-loud galaxies, and instead having radio emission that is more similar to RQ galaxies.

4.4.3 Sensitivity to overdensities

In order to interpret the significance of the apparent similarity between the environments of the RQ analogues and the blank field, the next step is to determine the strength of overdensity that is required for a signal to be detected using our analyses. To address this question we measure the counts from randomly drawn samples of mock submillimetre sources, increasing the sample size (i.e. equivalent of N_0) to find the minimum number of sources required to measure number counts that are significantly different to those of the blank-field.

The procedure is as follows, and is repeated for each of the four spatial scales studied ($1'$, $2'$, $4'$ and $6'$). Firstly, each bin centre (or lower bin edge in the case of cumulative counts) is assigned a probability of selection based on the shape of the best-fit blank-field Schechter function (§4.4.1). An initial number of simulated galaxies, $N_{\rm gal}$, is generated based on these probabilities and each simulated galaxy is assigned flux density uncertainties that match the median values of real S2COSMOS sources in the relevant flux bin. As with the calculation of the real number counts (§4.3) we then create 10^4 realisations of the simulated catalogue and the entire process – from randomly choosing $N_{\rm gal}$ flux densities onwards – is repeated 1000 times for each $N_{\rm gal}$, such that each bin has a distribution of 10^7 possible counts associated with it. The number counts in each bin are then the medians of these values, and the uncertainties account for both Poissonian uncertainties and the 16th–84th percentile ranges.

A Schechter function of the form described by Equation 4.1 (or its integral described by Equation 4.2 for the cumulative counts) is fitted to the resultant number counts by fixing S_0 and γ to the blank-field values and scaling N_0, as was done for the real RQ galaxies (§4.4.1). We then define the quantity ϕ, to

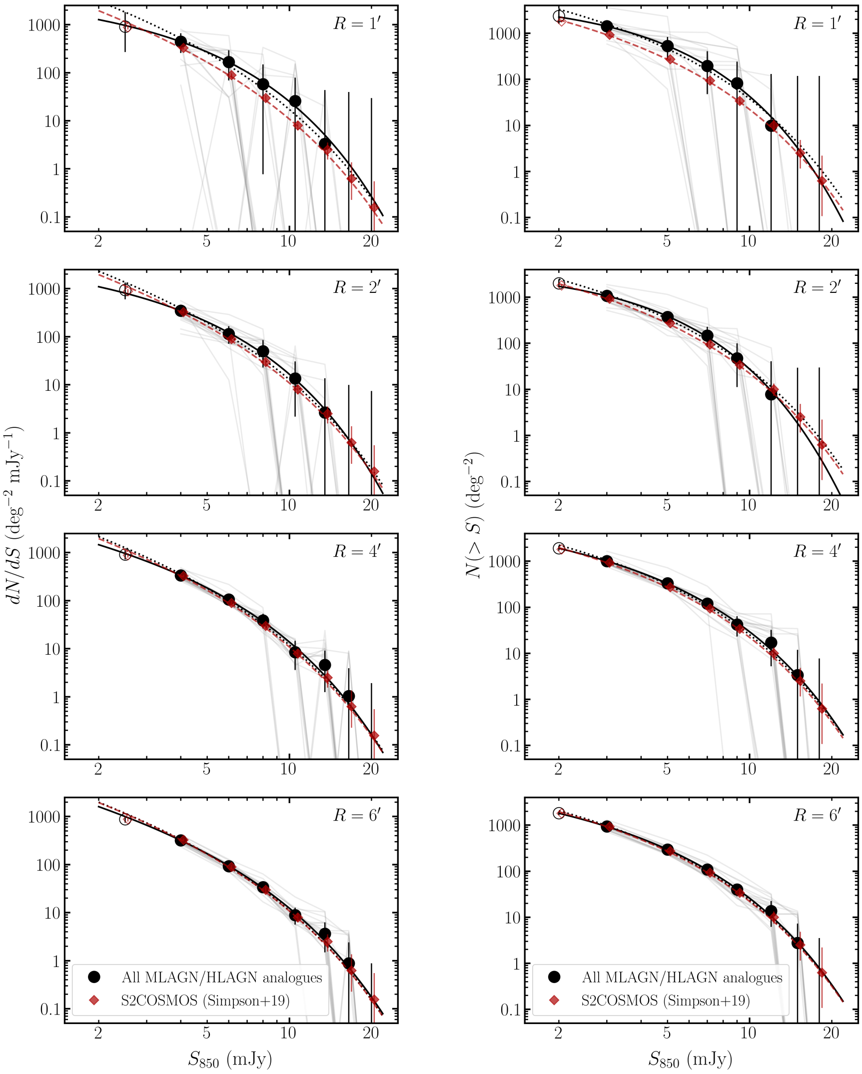

Figure 4.6: As Figure 4.4 but for regions around MLAGN and HLAGN in COSMOS. As with galaxies in our RQ sample, there is no evidence for an overdensity of submillimetre sources around these systems.

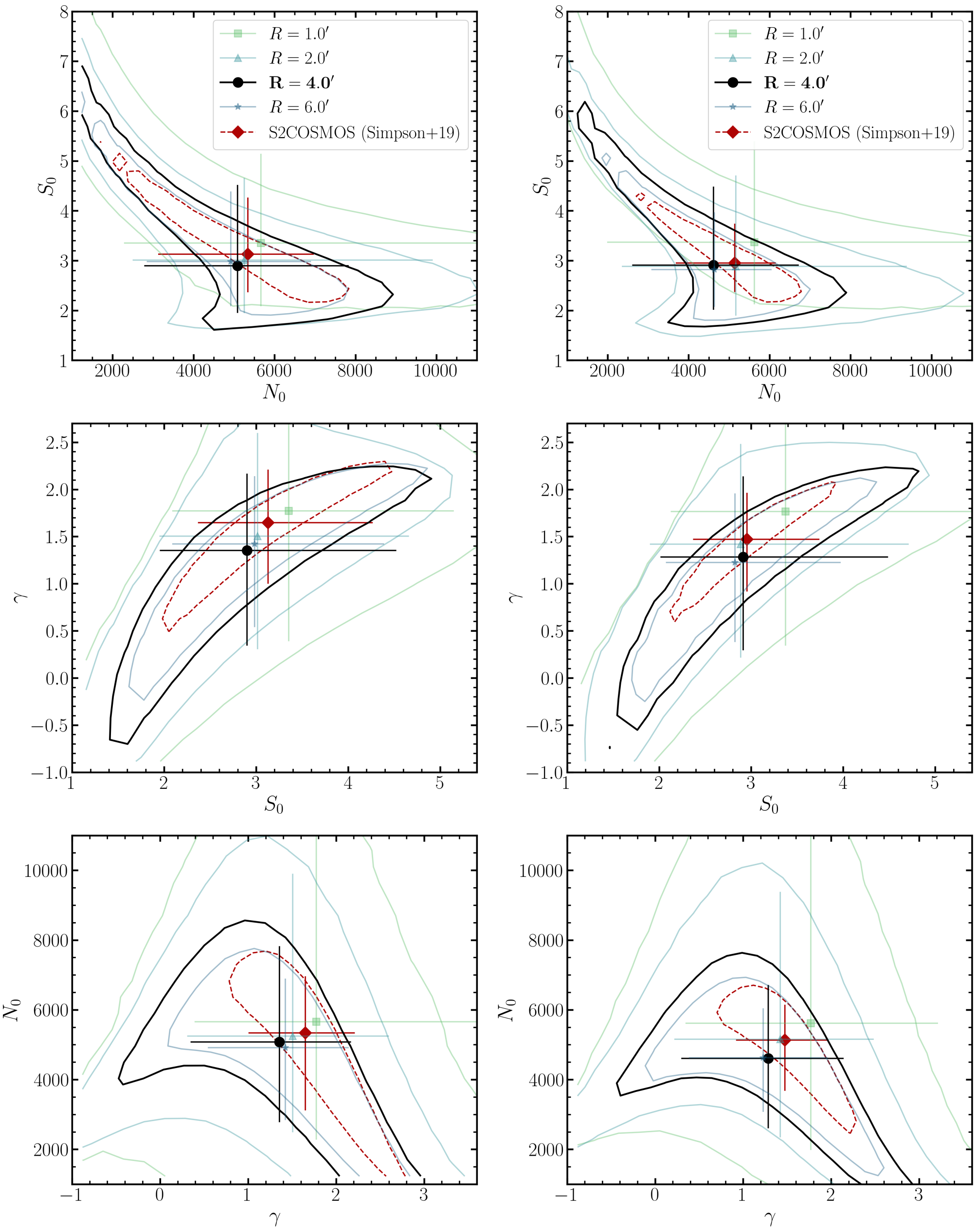

Figure 4.7: As Figure 4.5 but for regions around MLAGN and HLAGN in COSMOS. As with the RQ galaxies, there is significant overlap between the measurements at all radii and with the blank-field results; there is no significant difference between the 1′–6′ scale environments of these MLAGN/HLAGN and the blank field.

parametrise the relative measured density of the simulated number counts, as:

$$\phi = \frac{N_0^{\rm fit}}{N_0^{\rm bf}} - 1, \tag{4.4}$$

where $N_0^{\rm fit}$ is the best-fit value to the simulated number counts and $N_0^{\rm bf}$ is the blank-field value. Thus, $\phi = 0$ indicates the number counts that are identical to those of the blank field. The significance of an overdensity in the simulated number counts is given by the ratio of ϕ to its 1σ uncertainty. If this ratio is greater than unity, then the overdensity has a significance of $>1\sigma$. This procedure is repeated until the value of $N_{\rm gal}$ converges on the minimum number of galaxies required for a 1σ overdensity to be detected, which is parametrised as $N_{\rm gal}^{\rm min}$.

To translate $N_{\rm gal}^{\rm min}$ into terminology more commonly used in protocluster studies, we calculate the overdensity parameter, δ, which for a given dataset is defined via:

$$\delta = \frac{N_{\rm gal}^{\rm data}}{N_{\rm gal}^{\rm bf}} - 1, \tag{4.5}$$

where $N_{\rm gal}^{\rm data}$ is the number of galaxies in the data and $N_{\rm gal}^{\rm bf}$ is the number of galaxies in the blank field across the same flux density range and area as the dataset. To find the minimum overdensity to which our method is sensitive, we substitute $N_{\rm gal}^{\rm data}$ for $N_{\rm gal}^{\rm min}$, and calculate $N_{\rm gal}^{\rm bf}$ by summing all bins > 3 mJy in the blank-field number counts and multiplying by the simulated area (and by the bin widths in the case of the differential number counts). This analysis shows that our study of differential submillimetre number counts is sensitive to overdensities with $\delta \gtrsim 1.2$, 0.93, 0.86, and 0.85 for radii of $1'$, $2'$, $4'$, and $6'$, respectively. For the cumulative counts, we are sensitive to $\delta \gtrsim 0.47$, 0.40, 0.38, and 0.37 for $1'$, $2'$, $4'$, and $6'$ radii. Thus, the lack of detections in any of our samples suggests that RQ galaxies are in regions with $\delta \lesssim 0.4$ at submillimetre wavelengths.

For comparison, Rigby et al. (2014) found values of δ ranging from -0.27–0.9 for 500 μm-selected sources in known protoclusters around HzRGs at $z \sim 2$–4, using a search radius of $3.5'$. Meanwhile, protoclusters known to be rich in SMGs can have δ values of ∼10–100 (Casey 2016). Thus, overdensities commensurate with those around HzRGs would have been detected by our study of submillimetre number counts around RQ galaxies, and the absence of the detection of a significant overdensity requires that RQ galaxies at $z = 1$–3 are in less overdense environments than HzRGs of similar masses. The implication of this finding is discussed further in §4.5.

4.4.4 Density of faint sources

Single-dish submillimetre surveys (including S2COSMOS) are affected by confusion and high backgrounds: much of the 'noise' in the maps is from a background of faint sources. By studying the statistics of noise peaks in the maps we can therefore probe the distribution of galaxies that are below the flux limit of the catalogue (e.g. Glenn et al. 2010; Viero et al. 2013).

We next investigate the environments of the RQ analogues using the S2COSMOS signal-to-noise (SNR) map to track whether there is an overdensity of faint submillimetre sources in these regions. SNR peaks are identified in the map using the PYTHON package PHOTUTILS (Bradley et al. 2022) with detection thresholds from 1.5–4, and the surface density of these peaks within $1'$, $2'$, $4'$, and $6'$ of each RQ analogue is calculated. The blank-field density is estimated (for each aperture radius) by randomly placing 10^4 apertures across the SNR map and repeating the calculation.

We compare the blank-field and RQ galaxy environments by comparing the surface density distributions between the regions around RQ galaxies and the blank field, as shown in Figures 4.8 and 4.9 for the $\mathrm{SNR} > 1.5$ and $\mathrm{SNR} > 4$ detections, respectively. To quantitatively compare the statistics of SNR peaks in the blank field and near RQ galaxies we perform a two-sample Kolmogorov-Smirnov (KS) test on the resultant distributions.

For SNR detection thresholds < 2.5 (e.g. Figure 4.8) the KS test shows that there is no significant difference from the blank-field distributions at any radii ($p > 0.11$, and typically $p > 0.4$). For the higher SNR thresholds (e.g. Figure 4.9), where a larger fraction of the SNR peaks are likely real sources, the p-values exhibit a trend such that at the largest radii the distributions of source density between the blank-field and RQ galaxies are likely drawn from the same distribution, but they start to show hints of a different distribution at the smallest radii. The most significant result is in the $1'$ radii search for SNR > 4 peaks in the map (i.e. the closest analogue to using the S2COSMOS catalogue directly), where $p = 7 \times 10^{-6}$, corresponding to a $\sim$4.5σ confidence that the distribution between RQ environments and the blank-field are different at this scale and SNR limit. The KS test significance drops to $\sim$2.5σ at $2'$ ($p = 0.025$) and is even lower at larger radii and smaller SNR thresholds. If this result is confirmed then it suggests that RQ galaxies may be marginally overdense at small scales ($\sim 1'$, which corresponds to $\sim$ 0.5 Mpc at $z \sim 2$) for faint sources at submillimetre wavelengths. We caution however that these differences could be driven by small number statistics, as there are few objects within these small radii.

4.5 Discussion

In this study we used number counts to show that massive RQ galaxies at $z = 1$–3 reside in regions that have similar submillimetre source density to blank-field regions. The RQ galaxies have $\delta \lesssim 0.4$, though our constraints are marginally stronger on larger scales (up to $\sim$ 3 Mpc) and weaker on smaller scales (down to to $\sim$ 0.5 Mpc; §4.4.3). Similarly, our study of peaks in the 850 μm SNR map found that the regions around massive RQ galaxies are mostly consistent with being drawn from the same distribution as blank-field regions, although there is a hint of some overdensity on $< 1'$ ($\sim$ 0.5 Mpc) scales.

The sample of RQ galaxies analysed was selected to match known HzRGs in stellar mass and redshift (§4.2), and it is known that HzRGs are found in regions that are overdense in the submillimetre, though there is significant field-to-field variation with $-0.27 < \delta < 0.9$ at 500 μm (e.g. De Breuck et al. 2004; Rigby et al. 2014, Greve et al. in prep.). Therefore, our results suggest that there is difference between the submillimetre environments around similarly massive RQ and RL galaxies at $z \sim$ 1–3. This implies either the AGN or the radio emission has direct impact on the environment and star-formation activity in galaxies around HzRGs, or the HzRGs themselves are preferentially located in overdense regions, including regions with a lot of star-formation in submillimetre sources.

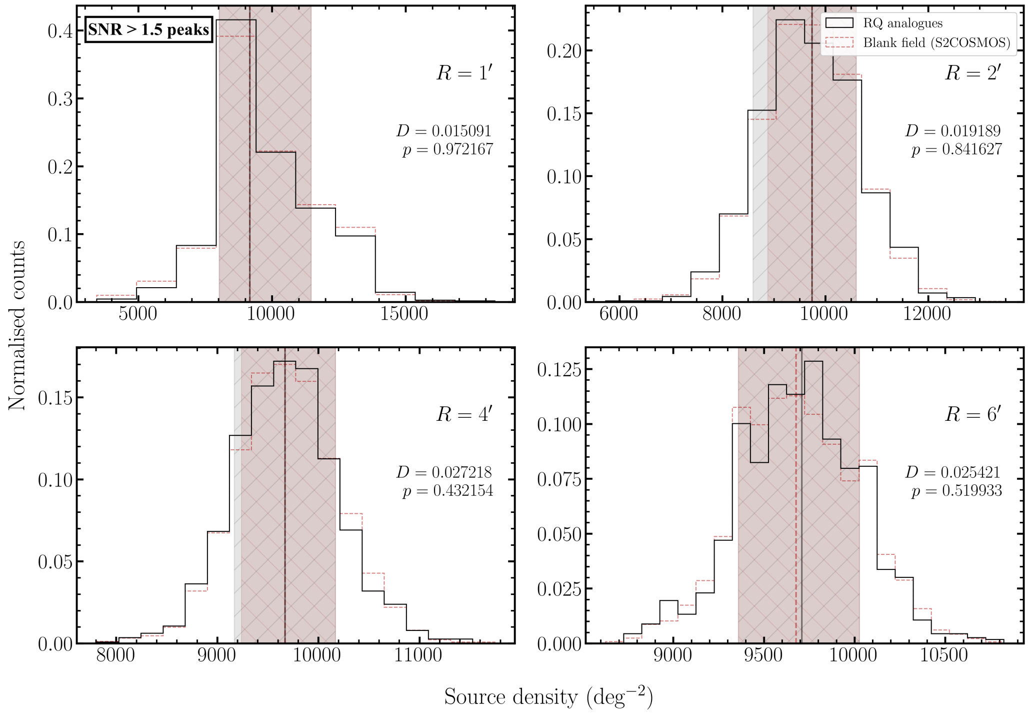

Figure 4.8: Distribution of the density of submillimetre peaks with SNR > 1.5 around RQ galaxies compared with the blank field. The histograms compare regions of radius $R = 1'$, $2'$, $4'$and $6'$ (as labelled) around RQ galaxies with the equivalent blank field area. Vertical lines and shaded regions show the median and 16th–84th percentiles of the distributions, which significantly overlap in most panels. Results from two-sample KS-tests (p and D) are printed on the right of each panel and show that for the SNR > 1.5 peaks in all four cases the regions around RQ galaxies are consistent with being drawn from the same distribution as the blank-field. As discussed in §4.4.4 the results are similar for all radii tested at this SNR threshold.

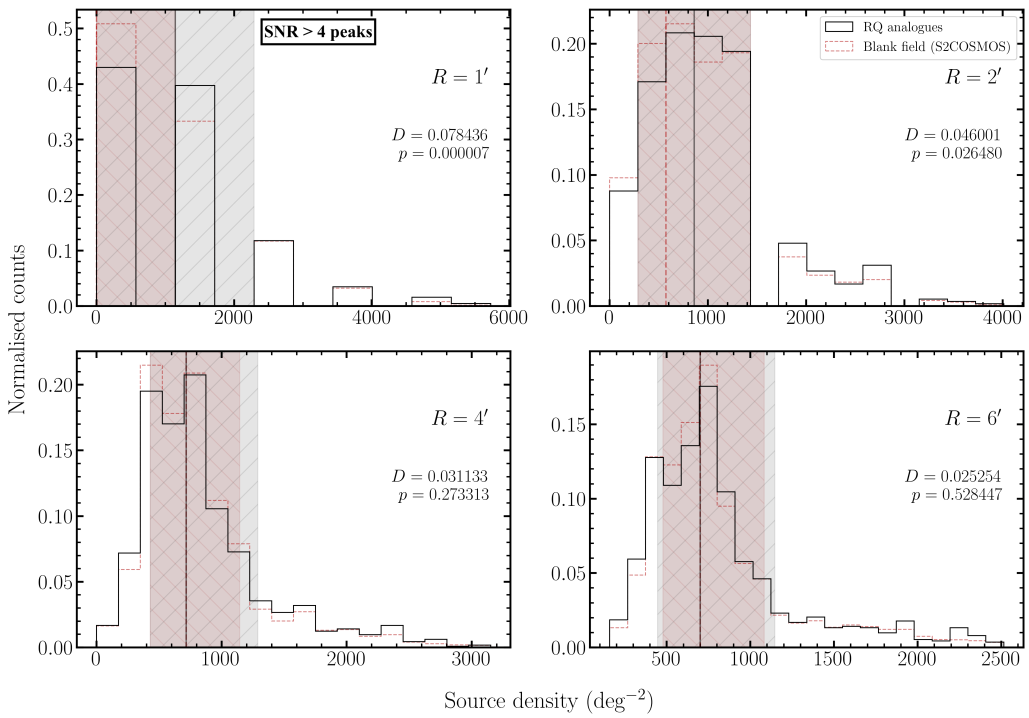

Figure 4.9: The same as Figure 4.8 but for submillimetre peaks with SNR > 4.0. With this stricter SNR threshold there is a hint of overdensity at the smallest scales, but this could be driven by small number statistics, and the results at larger scales are consistent with the blank field.

We also investigated the number counts in regions around galaxies with radio emission and classified as MLAGN or HLAGN by Smolčić et al. (2017c) and find no significant overdensities around these galaxies. These radio galaxies have significantly lower radio luminosity than 'classic' HzRGs, and this non-detection also suggests that they reside in environments for which $\delta \lesssim 0.4$.

Overall, our results are consistent with a picture similar to those discussed by Wylezalek et al. (2013), in which regions of higher galaxy density impact the production of jets and radio emission from AGN. For example, galaxy mergers in overdensities may increase the spin of black holes, which makes them more able to power radio jets (e.g. Sikora et al. 2007; Wilson & Colbert 1995). Another possibility in which the intergalactic medium (IGM) impacts the production of AGN radio emission is the jet confinement theory, which proposes radio synchrotron emission may be brightened by interaction with a denser IGM (Barthel & Arnaud 1996). Our study of the SNR peaks in the SCUBA-2 map suggested that massive RQ galaxies may be in small overdensities on $\lesssim 0.5$ Mpc scales (§4.4.4). If this result is found to be robust (e.g. in studies of larger samples, or deeper data) then it cannot be caused by interaction of radio jets with the IGM (since large-scale jets are not present in RQ galaxies). Instead such a result would suggest that some of the observed overdensity around these RQ galaxies and their RL counterparts is due to their high stellar masses predisposing them to occupy high-density environments, but with HzRGs being most likely to be present in the most massive halos due to galaxy mergers or interaction with the IGM.

4.6 Conclusions

We have conducted a search for 850 μm-selected SMGs in the environments of massive, radio-quiet galaxies at $z \sim 1$–3 in the COSMOS field. The sample of RQ galaxies was selected to match the stellar masses and redshifts of HzRGs so our results can be compared with studies of HzRGs. Our main conclusions are as follows:

- Using data from the S2COSMOS catalogue (Simpson et al. 2019) we constructed number counts in the regions of the RQ galaxies and compared these with the blank-field to determine whether massive, $z \sim$ 1–3 RQ galaxies typically reside in overdense regions, as is expected of their radio-loud counterparts. No significant difference is detected between the number counts for the environments of the RQ galaxies and those for the blank field. This result remains when examining regions from $1'$ to $6'$ scales and using both differential and cumulative number counts. It also holds both for completely free Schechter function fits and when fixing S_0 and γ to the blank-field values to pinpoint any difference in N_0.

- We tested the sensitivity of our analyses to identifying SMG overdensities by using simulated number counts, and found that we can detect overdensities with $\delta \gtrsim 0.4$. This threshold is sufficient to identify many known protoclusters, though there is significant variation between fields, particularly at submillimetre wavelengths.

- A similar examination of the submillimetre number counts around galaxies detected in the radio and classified as MLAGN or HLAGN by Smolčić et al. (2017c) found that these sources are also in environments that are statistically indistinguishable (i.e. $\delta \lesssim 0.4$ using our method) from the blank-field. These galaxies have some radio emission, but they are not HzRGs and have median rest-frame 500 MHz luminosity that is nearly three orders of magnitude fainter than HzRGs.

- To probe faint sources not individually detected in the S2COSMOS catalogue we also investigated the distribution of SNR peaks in the 850 μm map and used KS tests to search for differences between the region around massive, $z \sim$ 1–3 RQ galaxies and the blank field. We test detection thresholds of SNR > 1.5 up to SNR > 4 (similar to the S2COSMOS catalogue) and regions of $1'$ to $6'$ radius, finding that the density of submillimetre peaks around RQ galaxies is consistent with the blank field in most cases. For the higher SNR cuts and the smaller radii the KS test p statistic is smallest, and suggests that there may be some weak overdensities around RQ galaxies when compared to the field.

Thus, our analyses suggest that massive RQ galaxies at high redshift do not typically reside in substantial SMG overdensities. This is at odds with previous studies of HzRGs (e.g. Rigby et al. 2014) and suggests that the mechanisms powering RL galaxies have some interaction with the wider environment. Future RAGERS papers will compare these findings in detail with results for the RL sample (Greve et al. in prep.) and with expectations from simulations (Vijayan et al. in prep.) and further explore the role of environment in regulating AGN activity.

Chapter 5

Conclusions & Future Work

In this thesis I have presented observational studies of high-redshift galaxy environments, with the aim of improving our constraints on how massive galaxies and clusters evolve through cosmic time. Here I summarise the main findings of these studies and discuss possible approaches for continuing research in this area.

5.1 NB-ALESS

With the NB-ALESS study presented in Chapters 2 and 3, we set out to determine the nature of 'typical' SMG environments using a wide-field narrowband survey with VLT/HAWK-I. The three target SMGs (ALESS 5.1, ALESS 75.2 and ALESS 102.1) were selected based only on their spectroscopic redshifts ($z_{\rm spec}$ = 3.303, 2.294 and 2.296, respectively) so as to minimise any biases towards environment. We began by writing a dedicated data reduction pipeline in PYTHON for the processing of our HAWK-I data, and collating the reduced narrowband (Brγ) and broadband (K_s) images with archival UV-to-MIR broadband images covering the same regions of sky. The HAWK-I photometry was then used to identify star-forming galaxies through the presence of strong emission lines, and SED fitting was used to constrain their redshifts and identify candidate Hα/[OIII] emitters in the environments of each SMG. From a catalogue of

3929 sources detected in the Brγ images, we found 4, 44, and 11 companions to ALESS 5.1, 75.2 and 102.1, respectively.

We compared luminosity functions and density maps for the SMG environments with expected results from the coeval blank field, and found that all three target SMGs reside in overdense environments, as expected of the progenitors of local massive elliptical galaxies. The final estimates for the overdensity parameters were $\delta_g = 4.0^{+14.9}_{-3.2}$, $2.6^{+1.4}_{-1.2}$, and $3.8^{+2.4}_{-1.8}$ for the environments of ALESS 5.1, 75.2 and 102.1, respectively. The candidate companions for ALESS 5.1 and 75.2 are distributed across the whole HAWK-I field of view and thus have physical scales in excess of ∼4 Mpc × 4 Mpc, as expected of protoclusters at these epochs. Meanwhile the overdensity around ALESS 102.1 spans only ∼ 1/4 of the field of view, corresponding to a physical scale of ∼1 Mpc × 1 Mpc.

A true protocluster must evolve into a galaxy cluster before $z = 0$ (e.g. Overzier 2016). We thus estimated the total halo mass of each SMG environment and predicted their evolution between their observed redshifts and the present day. We obtained present-day halo masses of $\log(M_h/\mathrm{M}_\odot) = 13.9$–16.6, 13.6–15.8, and 13.0–15.9 for the environments of ALESS 5.1, 75.2 and 102.1, respectively. These masses suggest that the former two likely reside in protoclusters, while the third resides in either a protocluster or a protogroup, which is consistent with the spatial extent of these overdensities. The results of this study are consistent with SMGs being the progenitors of the massive elliptical galaxies found in local galaxy clusters.

5.2 RAGERS

In Chapter 4 we used 850 μm observations from S2COSMOS (Simpson et al. 2019) to measure the densities of SMGs in the environments of a large sample of massive RQ galaxies at $z \sim 1$–3, where this sample was selected to match the stellar masses and redshifts of HzRGs in RAGERS. The aim of this study was to determine whether these galaxies tend to reside in protoclusters like their HzRG counterparts, and from this infer whether the density of the surrounding environment is linked with stellar mass alone, or if other factors such as AGN feedback also play a role in determining the nature of the environment.

By comparing SMG number counts in the regions surrounding the RQ galaxies with blank-field number counts constructed using the whole S2COSMOS field, we found no sign that these RQ galaxies reside in environments that are overdense with SMGs, despite being sensitive to overdensities with $\delta \gtrsim 0.4$. This result holds regardless of the size of the examined regions, for which radii ranging from $1'$ to $6'$ were tested. We also extended the search to SNR thresholds below the cut-off used for the S2COSMOS catalogue, by measuring the densities of SNR peaks in the 850 μm map and performing KS tests to compare the distribution with that of the blank field. SNR thresholds ranging from 1.5–4 were tested with regions of radius $1'$ to $6'$. The results of these KS tests also imply that the environments of RQ galaxies are consistent with the blank field, although signatures of possible weak overdensities were seen in the smaller regions when SNR thresholds of $\sim$4 were used.

Overall the results of this study imply that massive RQ galaxies do not tend to reside in significant SMG overdensities, unlike HzRGs of similar mass and redshift. This in turn suggests that massive RQ galaxies reside in less massive dark matter halos than their radio-loud counterparts and are thus less likely to evolve into present-day BCGs; the mechanisms powering the radio emission in HzRGs is therefore likely linked to the density of the surrounding environment.

5.3 Future Work

5.3.1 NB-ALESS

With the NB-ALESS study presented in Chapters 2 and 3 we identified candidate companion galaxies for three spectroscopically-confirmed SMGs. An obvious first step in taking this further would be to perform the study on the three SMGs that were proposed for NB-ALESS but were not observed. This would double our current sample size and take us one step closer to understanding the environments of ‘typical’ SMGs.

However, the potential for narrowband studies does not end with these SMGs. The methodology could easily be extended to a larger sample of SMGs, as long as they have spectroscopic redshifts at which a strong emission line would shift into an existing narrowband filter. Many SMGs have been identified in other large surveys such as AS2UDS (Stach et al. 2019) and AS2COSMOS (Simpson et al. 2020), several of which have been spectroscopically confirmed (Chen et al. 2022; Dudzevičiūtė et al. 2020). These studies therefore need not be limited to HAWK-I; other wide-field NIR imagers with narrowband filters exist, enabling searches for star-forming galaxies similarly close to the peak of the SMG redshift distribution. For example, the Multi-Object InfraRed Camera and Spectrograph (MOIRCS) on the Subaru telescope has a field of view of $4' \times 7'$ and 11 narrowband filters, with which Hα ([O III]) emitters could be identified at redshifts of ~ 1.4–2.5 (2.1–3.6). Similarly the Espectrógrafo Multiobjeto Infra-Rojo (EMIR) instrument on the Gran Telescopio Canarias (GTC) offers a $6.67' \times 6.67'$ field of view with six NIR narrowband filters, allowing for Hα ([O III]) surveys at redshifts of ~ 1.5–2.4 (2.3–3.5). The high ends of these redshift ranges would probe similar epochs to those already covered by NB-ALESS, but surveys at $z \sim 1.5$ would explore the low end of the SMG redshift distribution (see §1.4.1) and determine whether high galaxy densities are conducive to SMG formation after cosmic noon.

With the recent advent of the *James Webb Space Telescope* (JWST), the question of whether it could be used for the science goals of NB-ALESS naturally springs to mind. While the field of view of its Near Infrared Camera (NIRCam) instrument is smaller than that of HAWK-I (consisting of two $2.2' \times 2.2'$ fields separated by a $44''$ gap) it is still large enough to cover a significant portion of the expected extent of a protocluster. Moreover, it can detect the Hα emission line out to much higher redshifts than ground-based instruments, which are limited to $z \sim 2.5$ due to high levels of absorption at these wavelengths by the Earth's atmosphere. Using the reddest of the available narrowband filters on NIRCam, one could potentially conduct narrowband surveys of Hα-emitters out to $z \sim 6.2$ and thus probe the environments of SMGs at the high end of their redshift distribution, thereby determining whether their apparent tendency to reside in overdense environments holds out to ~ 1 Gyr after the Big Bang. If so then these surveys could be used to identify some of the earliest protoclusters (see §1.3.2).

As with any narrowband photometric survey, NB-ALESS only goes so far in constraining the redshifts of emission-line galaxies: due to both the width of the Brγ filter (corresponding to $\Delta v \sim 6500$ km s^{-1} at $z = 2.3$) and the limitations of photometric redshifts, there remains some uncertainty as to whether the galaxies identified as companions to the target SMGs actually share the same structure in reality. Obtaining spectroscopic follow-up for these candidates to precisely measure their redshifts will significantly reduce this uncertainty and consequently result in better constraints on the total masses of each potential structure.

Multi-object spectrographs are prime tools to carry out such a task due to their ability to collect spectra for multiple sources within a single pointing. The K-band Multi Object Spectrograph (KMOS) on the VLT is especially well-suited for follow-up of our candidate protocluster members. As a K-band spectrograph it can be used to detect the very Hα or [OIII] emission lines that are suspected to be causing the excess brightness in the Brγ filter for these sources, with a spectral resolution that would enable us to measure a galaxy's velocity to $\Delta v \sim 100$ km s^{-1} at $z = 2.3$ and $z = 3.3$. It has 24 configurable arms corresponding to as many integral field units (IFUs), which can be positioned across a patrol field $7.2'$ in diameter, meaning that several candidate protocluster members can be chosen as simultaneous targets across almost the entire HAWK-I pointing. The integral field spectroscopy adds further appeal, as spatially-resolved spectra in this wavelength regime would allow for the kinematics of the ionised gas to be measured in each target, revealing information about their structures and allowing for properties such as dynamical masses to be estimated for each. The kinematics of the gas can also be used to infer recent or ongoing merger activity, for example if the rotational velocities deviate significantly from the ordered disk structure expected of 'typical' star-forming galaxies at these epochs (e.g. Förster Schreiber et al. 2018; Molina et al. 2017).

One unanswered question is how much obscured star formation activity is occurring in each of the ALESS SMG environments. We assume a level of dust extinction in each candidate member galaxy, and even derive a separate estimate of the dust extinction via SED fitting, but the dearth of deep photometry in the FIR/submillimetre for these galaxies leaves the true values largely unconstrained. Furthermore, there might exist some galaxies that are so dust-obscured as to be undetected by our NB-ALESS observations which were also not bright enough to be detected in the submillimetre regime by LESS. Without accurate knowledge of the dust-obscured star formation we only partly uncover the nature of these environments. Interferometric follow-up of member galaxies, for example with ALMA Bands 6 or 7, would enable better constraints on their rest-frame FIR luminosities and in turn on their obscured star-formation activity. Moreover, certain emission lines originating from the cold molecular gas in these galaxies will be observable with ALMA: for example at $z \sim 2.3$ the CO(3-2) emission line shifts into the coverage of ALMA's Band 3, thereby providing another means of precisely constraining their redshifts.

While narrowband studies are effective at identifying galaxies within narrow redshift ranges, they are not a requirement for high-quality photometric redshifts. With the wealth of photometry available in regions of sky such as the COSMOS field, the photometric redshifts in the COSMOS2020 catalogue (Weaver et al. 2022) could be used to map the environments of SMGs without the need for additional dedicated narrowband observations. In lieu of reliable photometric redshifts one could instead turn to dropout techniques by using colours in certain filter combinations to identify the presence of sharp 'breaks' in a galaxy's SED: a galaxy for which this break is redshifted to lie between a given pair of filters will exhibit a significant colour. The Lyman break (which occurs at a rest-frame wavelength of 912 Å) could be used to identify star-forming galaxies, particularly at $z \gtrsim 3$ when the break begins to shift redward of the U filter. One could potentially also exploit the Balmer/4000 Å break to search for passive galaxies in SMG environments. While this is an interesting line of investigation at any redshift and could be used to identify companion galaxies which would otherwise be missed using Lyman break or emission line searches, it may be especially prudent at the low end of the SMG redshift distribution, when the first evolved clusters have begun to emerge (e.g. Bleem et al. 2015; Böhringer et al. 2001; Gilbank et al. 2011; Gladders & Yee 2000, 2005; Hasselfield et al. 2013; Henry et al. 2006; Muzzin et al. 2009; Pacaud et al. 2016; Planck Collaboration et al. 2016; Staniszewski et al. 2009; Truemper 1993; Williamson et al. 2011; Wilson et al. 2009) and the cosmic star formation rate density has begun to decline (Madau & Dickinson 2014). Through these various techniques the environments of SMGs could be explored across their full redshift distribution, unveiling the nature of these environments and their evolution across cosmic time.

A serendipitous by-product of the NB-ALESS study was the discovery of a small-scale overdensity of seven Hα emitters in the environment of ALESS 75.2 which coincides with the position of a previously detected Lyα blob (LAB; Yang et al. 2010). Three of these Hα emitters are spectroscopically confirmed, so obtaining spectroscopic redshifts for the remaining four candidates will confirm both their membership of the environment of ALESS 75.2 and their physical association with this LAB. The apparent association between these Hα emitters and the LAB raises the question of how the Lyα emission from the blob is powered. Optical/NIR spectroscopy in conjunction with deep submillimetre observations has the potential to provide the answer. The deep submillimetre photometry would serve to measure the obscured star formation activity in the system as discussed previously. Meanwhile the relative contributions from star formation and AGN could be disentangled using the optical/NIR spectroscopy, for example via the construction of BPT diagrams (Baldwin et al. 1981), provided one could obtain spectroscopic coverage sufficient to detect the Hα, the [NII] doublet, and the [OIII]+Hβ complex; such a feat could be accomplished for galaxies at $z \sim 2.3$ with spectrographs such as VLT/XSHOOTER.

5.3.2 RAGERS

We note that the non-detection of any SMG overdensities in the environments of massive radio-quiet galaxies in Chapter 4 does not rule out the possibility of these galaxies residing in protoclusters, as such environments are not necessarily SMG-rich. A complementary study tracing the density of optical/NIR-selected galaxies (such as those in the COSMOS2020 catalogue; Weaver et al. 2022) would reveal whether these environments are truly consistent with the blank-field, or actually rich with galaxies while not hosting large populations of SMGs.

We also cannot entirely rule out that the massive RQ galaxies in our sample do not reside in overdensities of SMGs, given that our analyses of the SNR peaks in the SCUBA-2 map implied the possibility of small overdensities on $\lesssim 0.5$ Mpc scales. Larger samples and/or deeper data are required in order to determine whether this result is robust. Doing so would allow us to better determine the relevance of stellar mass and radio luminosity to the density of the surrounding environment: if robust, this result implies that overdensities around massive galaxies at high redshift must be at least partly driven by their stellar mass, even if radio-loud galaxies are more predisposed to high-density environments than their radio-quiet counterparts.

So far we have compared the results of this study with results for other HzRGs in the literature (e.g. Rigby et al. 2014; Wylezalek et al. 2013) to draw our conclusions about the differences between their environments and the environments of massive radio-quiet galaxies. However, a fairer test would be to compare with the HzRGs to which these radio-quiet galaxies were matched in stellar mass and redshift. This is precisely the aim of RAGERS, and work towards measuring the SMG density in these HzRG environments using new SCUBA-2 observations is ongoing (Greve et al., in prep.). Since radio luminosity should then be the only factor separating the radio-loud and radio-quiet samples, any differences observed in their environments must be linked with this property.

Simulations are also essential for understanding the role of AGN feedback in shaping the evolution of a galaxy and the surrounding environment. Work is currently under way in RAGERS making use of the SHARK semi-analytic model (Lagos et al. 2018); detailed analyses of the submillimetre environments of simulated HzRGs and coeval radio-quiet galaxies of similar mass will be presented in Vijayan et al. (in prep). Initial examination appears to contradict the results of our observational study, as even massive radio-quiet galaxies are found to reside in significant SMG overdensities in the simulation, albeit less significant than the HzRGs. Further investigation – both observationally and via simulations – is required in order to reconcile these findings.

5.3.3 Future submillimetre facilities

Submillimetre studies using single-dish observations – such as the study described in Chapter 4 – are subject to the limitations of current single-dish facilities. Poor resolution ($\gtrsim$10$''$ beam size) inhibits the ability to reliably identify counterparts in other parts of the spectrum while also raising the sensitivity floor due to confusion noise. Furthermore, since counterparts in the UV/optical/NIR are often faint and thus undetected by surveys in these regimes, these cannot always be used to obtain spectroscopic redshifts for SMGs identified via single-dish surveys. Submillimetre spectroscopy provides a solution in principle, e.g. through detection of CO emission lines or FIR fine-structure lines such as [Cii] or [Nii], but in practice current spectrometers in this regime lack the sensitivity, multiplexing, and/or bandwidth to efficiently search for these emission lines in large samples of SMGs with unknown redshifts.

In order to overcome these limitations we need a larger submillimetre facility with a wide field of view, multiple wavebands and highly multiplexed spectroscopy. This would enable direct measurement of dust SEDs for large numbers of objects and spectroscopy for significant samples. One proposal is the Atacama Large Aperture Sub-mm/mm Telescope (AtLAST; Klaassen et al. 2020; Ramasawmy et al. 2022), which would be a 50 m single-dish submillimetre telescope. The expected resolution ($\sim 1.8''$ at 450 μm), field of view (~ 2 deg^2), mapping speeds, sensitivity and broad spectral coverage of AtLAST are all synergistic with conducting wide-field submillimetre surveys with both imaging and spectroscopic components. The sensitivity of AtLAST is such that even 'normal' star-forming galaxies are expected to be detectable via their submillimetre emission, even out to high redshifts. The ability to efficiently detect galaxies via their submillimetre emission across large fields of view and search wide spectral ranges for submillimetre emission lines will revolutionise our understanding of galaxy environments via their obscured star formation activity. For example, the environments of bright SMGs could be traced directly in the far IR, rather than requiring optical/NIR follow-up for less active companions, such as we did in Chapter 3.

Similarly, the study presented in Chapter 4 is limited by the lack of spectroscopic information available for the SMGs. Future large submillimeter surveys such as those proposed for AtLAST (e.g. Dannerbauer et al. 2019; Geach et al. 2019) would ultimately allow us to identify true companions to these RQ galaxies and conclusively determine whether they reside in SMG overdensities (see Appendix A.2).

Appendix A

Appendices

A.1 Reconstructing the S2COSMOS completeness function

In §4.3.1 we describe how we use Figure 6b from Simpson et al. (2019) to reproduce the completeness function used to construct their 850 μm number counts. Figure A.1 shows the completeness as a function of 850 μm flux density (S_{850}) at fixed values of the local rms (σ). Between completenesses of 10 and 90 percent these functions are obtained by interpolating between the contours at 10, 30, 50, 70 and 90 percent completeness shown in Figure 6b of Simpson et al. (2019). Fermi-Dirac-like functions are then used to extrapolate the completeness as a function of 850 μm flux density to values below 10 percent and above 90 percent at each value of the local rms. These functions have the form

$$f_{\mathrm{FD}}(S_{850}) = \frac{1}{e^{A(B-S_{850})} + 1} \tag{A.1}$$

where A and B are free parameters determined by fitting to the known data points at 10, 30, 50, 70 and 90 percent completeness.

Figure A.2 shows the result of mapping the 1D functions onto a 2D grid, with local rms forming the second axis of the grid. The result is a 2D map showing the

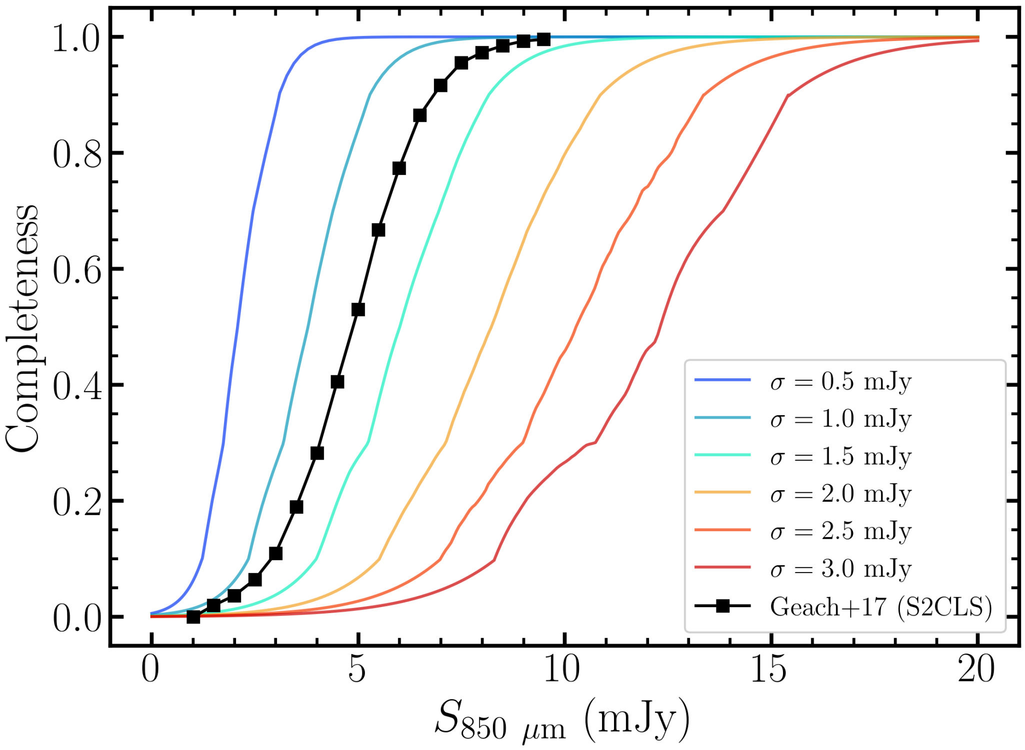

Figure A.1: Completeness as a function of deboosted 850 μm flux density, at fixed values of rms. Black points show the results for the COSMOS field from S2CLS Geach et al. (2017). The overall shape of the Geach et al. (2017) completeness function is similar to those of our derived functions, suggesting that the method used to construct them is reliable.

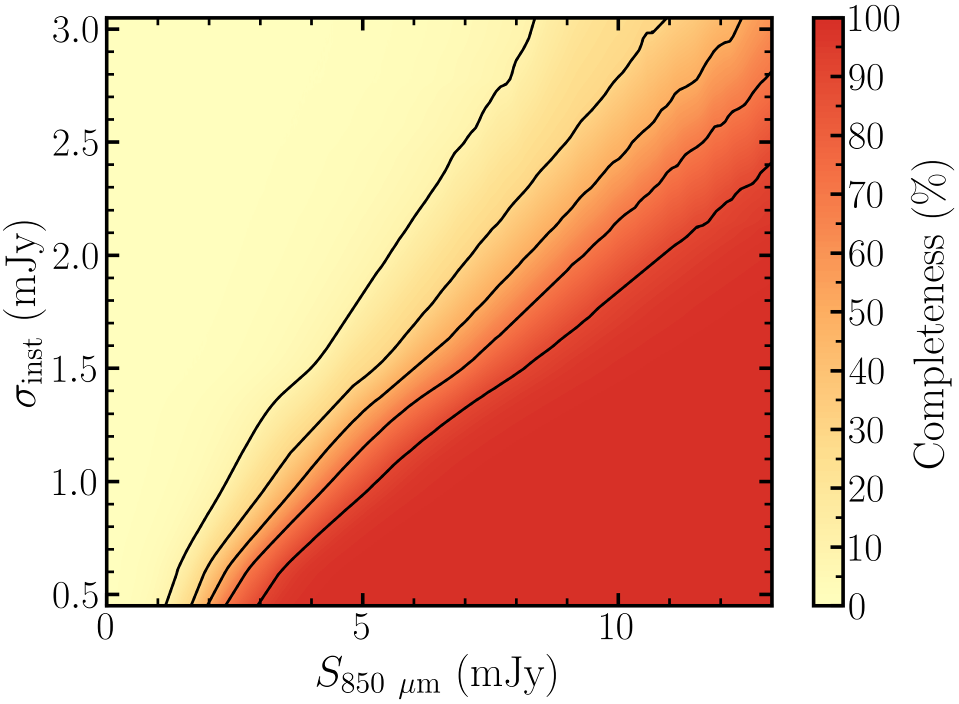

Figure A.2: Completeness as a function of local RMS noise and deboosted 850 μm flux density, recreated from Simpson et al. (2019) using the S2COSMOS catalogue. The black curves show lines of constant completeness at values of (from left to right) 10, 30, 50, 70, and 90 percent.

completeness as a function of both 850 μm flux density and local rms, which is then applied to sources in the S2COSMOS catalogue when constructing number counts.

A.2 AtLAST: a science use case

AtLAST Science Use Case

Project Details

Title: Measuring galaxy environments and their role in galaxy evolution across cosmic time

Principal Investigator: Thomas Cornish, Lancaster University, t.cornish@lancaster.ac.uk

Co-authors: Dr Julie Wardlow, Joanna Ramasawmy

Time request:

Expected Observing Bands

Frequency Coverage (GHz)	Spectral line (heterodyne/IFU/MOS/other)	Continuum (multi-chroic/single band)	Other (please specify)
84-116 (B3)	MOS	single-band	
125-163 (B4)	MOS	single-band	
163-211 (B5)		single-band	
211-275 (B6)		single-band	
275-373 (B7)		single-band	
385-500 (B8)		single-band	
602-720 (B9)		single-band	
787-950 (B10)		single-band	
950+			
Other (please specify)	(B3 & B4 required; additional bands useful.)	(Selection of 4+ single-bands required, ideally including at least 1 of B9 or B10.)	

Observing mode

☑ Normal
☐ Fixed schedule
☐ Time-critical override
☐ Collaborative & Coordinated
☐ Other

AtLAST Science Use Case

Details: This science case uses wide-area survey-type observations, which are suitable for normal observing mode.

Comments on observing strategy

Multi-band continuum and low-resolution spectroscopic observations will be used to conduct a blind survey of ∼1000 square degrees of sky. Continuum observations will be used for measuring the submillimetre emission from tens of thousands of galaxies and determine their dust properties. Meanwhile the broad-band low-resolution spectroscopy will be used to search for spectral features stemming from the cool ISM, such as bright CO lines and atomic fine-structure lines, enabling the determination of redshifts and measurement of the environments of the galaxies.

Polarisation products required

☐ XX
☐ YY
☐ XY
☐ YX
☐ Stokes I
☐ Stokes Q
☐ Stokes U
☐ Stokes V

Scientific Description

The link between a galaxy's evolution and its surrounding environment has long been recognised: locally, denser environments such as galaxy clusters are typically dominated by passive early-type galaxies, while the low-density blank field hosts a greater proportion of star-forming late-type galaxies [1]. The elliptical galaxies in clusters are thought to have formed most of their stars in short bursts at $z \gtrsim 2$ [2, 3] in contrast to the field where most of the activity occurs at $z < 1$ [4]. For given distant galaxy populations, determining their local environment enables us to infer their history and predict their eventual fate, making galaxy environments a crucial component in understanding galaxy evolution. Furthermore, by combining environmental, dust, and gas measurements across a wide range of redshifts, stellar masses, and star-formation rates, it is possible to disentangle the role of environment on galaxy evolution and there is significant potential for identifying fundamental relationships between these parameters that could be used in place of intensive observations in future studies.

Mapping a galaxy's environment, however, is not trivial: ultimately it requires precise redshift measurements for the majority of nearby galaxies, which in turn requires a wealth of photometric data for reliable fitting of spectral energy distributions (SEDs), and/or spectroscopic detections of emission/absorption features. Moreover, large-area observations are required to map large scale structures at $z \gtrsim 1$; for example, a single typical galaxy protocluster at $z \sim 2$ is expected to extend over several Mpc, requiring a field of view in excess of ~ 4 arcmin^2 to cover [5].

Large imaging surveys, particularly those with dedicated spectroscopic components, such as the Sloan Digital Sky Survey (SDSS [6]), thus provide an excellent framework for studying the role of environment in galaxy evolution. The combination of wide-area broadband imaging and follow-up spectroscopic observations have enabled the detailed study of huge samples of galaxies (e.g. [7, 8]) and their environments (e.g. [9, 10]). However, such studies are currently limited to the rest-frame UV and optical, and as such are highly susceptible to dust attenuation leading to optically faint dusty galaxies being easily missed. They are also limited to $z \lesssim 1$ and are only capable of tracing the ionised gas content in these galaxies. In order to understand the environments of dusty galaxies, high-redshift galaxies, and the interplay between environment and molecular gas content in galaxies a multi-band, photometric and spectroscopic, wide-area survey in the submillimetre is required.

AtLAST will make it possible to conduct an 'SDSS-like' survey, with both continuum and spectroscopic components, in the submillimetre regime and thus significantly enhance our understanding of galaxy evolution and environment. Photometrically probing the peak of thermal dust emission and combining with submillimetre spectroscopy leads to direct measurements of redshift, obscured star-formation rates, star-formation efficiencies, molecular gas content, and dust-to-gas ratios. Furthermore, an unconfused, untargeted, wide-field survey would enable analyses of the environments of all galaxies, including the dusty and high-redshift systems that can't be sufficiently studied in the optical and near-IR. Mapping the 3D distribution of galaxies of different types (mass, star-formation rate, morphology etc) will then enable measurements of local correlations, from which a picture can be built of galaxy evolution within a variety of environments across cosmic time.

AtLAST Science Use Case

Target specifications

Type of observation:

- ☐ Individual pointings per object
- ☐ Individual fields-of-view with multiple objects
- ☑ Survey
- ☐ Other

Details: This science case uses an 'SDSS-like' ~ 1000 deg^2 photometirc and spectroscopic extragalactic survey data.

Number of targets: ~ 1000 deg^2 survey

Multiple epochs/repeated observations? No

Rapidly changing sky position? No

Time critical? No

Required integration depth, and/or estimated time:

Average peak flux density per target: N/A

Range of peak flux densities: From 10s of μJy/beam to ~ 100 mJy/beam in the continuum, depending on band.

Expected polarised flux density: N/A

Observational Setup

Central frequencies (GHz): Spectral scan across all of B3 & B4 at minimum. Scans across other bands will improve the science by giving more reliable redshifts, extension to higher redshift, and a wider range of observed emission lines, with more overlap between systems at different redshifts. Main targets will be $z \sim 1$–4.5.

Continuum photometry in at least four bands, ideally with at least one of B9 or B10 (to constrain the SED peak).

Total bandwidth (GHz): As wide as possible.

Spectral resolution (kHz): For spectroscopic component $\lesssim 50\mathrm{kms}^{-1}$; i.e. ~ 15 MHz depending on band. For photometric component whole bands is sufficient.

Temporal resolution (if required): N/A

Comments: N/A

AtLAST Science Use Case

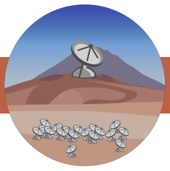

Imaging considerations – CONTINUUM

Please indicate the specifications for instrumentation required for your science goals. For proposed instrumentation, see our SPIE paper [11, section 5.1] and for recent example specification see e.g. TolTEC [12]

The primary imaging requirements are: (1) wide-field coverage (hundreds of square degrees), (2) at least four band photometry, sufficient for measuring SEDs in galaxies down to SFR ~ 5 M$_\odot$yr^{-1} at $z \sim 2$ (i.e. down to $M^* \sim 10^9$ M$_\odot$ on the $z \sim 2$ SFR-M^* "main-sequence"), and (3) resolution sufficient to identify individual galaxies (i.e $\lesssim 1''$). For observational feasibility this likely means a large field-of-view, multichroic instrument (i.e. AtLAST Cam).

Required angular resolution: $\lesssim 1''$

Mapped image size: ~ 1000 deg^2

Largest required angular scales: $\lesssim 5''$

Number of output channels: 1 per band. At least four band output, including at least one of B9 or B10 (more bands will improve measurement precision though).

Output bandwidth: 84–950 GHz

Required rms: Of order 10μJy/beam in Band 7; deeper in lower frequency bands and can be shallower in higher frequency bands.

Dynamic range within image: Typical sources will range from a few tens of μJy/beam to a few tens of mJy/beam: so a factor of ~ 1000 in dynamic range.

Absolute flux scale calibration (if relevant):

☐ 1 – 3%
☐ 5%
☑ 10%
☐ 20 – 50%
☐ N/A

Relative flux scale calibration (if relevant):

☐ 1 – 3%
☑ 5%
☐ 10%
☐ 20 – 50%
☐ N/A

Comments: N/A

AtLAST Science Use Case

Imaging considerations – SPECTRAL

Please indicate the specifications for instrumentation required for your science goals. For proposed instrumentation, see our SPIE paper [11, section 5.1]. Instruments may include, but are not constrained to, multiplexed heterodyne [see, eg 13], wideband IFU [see, eg 14], ultra wideband heterodyne and multi-object spectrograph.

This science requires measuring redshifts and line luminosities for as many galaxies as possible across the area of the survey. Thus, the study requires wide-band (all of Band 3 and Band 4 at minimum), multiplexed data. Since the main goals are detection and line flux measurement, low spectral resolution is acceptable.

Type of instrument (example types of instruments):

☐ highly multiplexed heterodyne [see, eg 13]
☐ Wideband IFU [see, eg 14]
☐ Ultra wideband heterodyne
☑ Multi Object Spectrograph
☐ Other (specified below)

Required angular resolution: Ideally $\lesssim 1''$, but up to $\sim 5''$ would be manageable with extra data processing.

Mapped image size: Survey ~ 1000 deg^2

Fully Sampled or MOS: MOS

Number of image channels: N/A

Number of pixels: N/A

Channel width: $\lesssim 50$ km s^{-1}

Output bandwidth: 84–163 GHz at minimum. Additional bandwidth (in other bands) will improve the science.

Required rms (Jy/beam or K): To attain CO detections of the faintest sources detected in the continuum requires rms ~ 10 μJy/beam, although this could be binned over several spectral resolution elements (expected linewidths $\gtrsim 100$ kms^{-1}).

Dynamic range within image: A factor ~ 1000

Absolute flux scale calibration (if relevant):

☐ 1 – 3%
☐ 5%
☐ 10%
☑ 20 – 50%
☐ N/A

Relative flux scale calibration (if relevant):

☐ 1 – 3%
☐ 5%
☑ 10%
☐ 20 – 50%
☐ N/A

Required baseline stability:

Is a contiguous bandwidth required? If so, over what frequency range? Yes. 84–163 GHz (B3 & B4) at minimum. Additional bandwidth (in other bands) will improve the science.

Comments: N/A

AtLAST Science Use Case

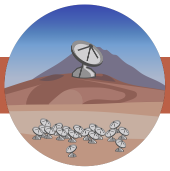

Critical telescope specifications for your science

Which of the telescope specifications are most important to this project? If you could change one parameter by 10%, which would have the most significant impact? Why are we unable to do this science with existing facilities?

The most crucial specifications are:

- wide area coverage (~ 1000 deg^2),
- multi-band photometry deep enough to be sensitive to $M^* \sim 10^9 \mathrm{M}_\odot$ "main-sequence" galaxies, which have $SFR \sim 5\ M_\odot \mathrm{yr}^{-1}$ at $z \sim 2$, and spatial resolution sufficient to separate galaxies,
- sensitive broadband spectroscopy to measure the redshifts of as many galaxies as possible. To reach the faintest-continuum detected sources this requires rms $\lesssim 10\ \mu$Jy/beam.

10%-level changes to the areal coverage, spatial resolution, or photometric depth, are likely to have minimal effect on the overall scientific success of this project, although they will impact the scope (i.e. how broadly results can be measured/applied) and the robustness/statistical significance of the conclusions.

Continual spectral coverage in both Band 3 and Band 4 are required for the science, and loss of some of that coverage would have an outsized impact on the science as it would result in many galaxies having unknown or significantly uncertain redshifts (e.g. no lines would be detected, or only a single line). Increasing the spectral coverage (i.e. in to B5+) will significantly improve the science as it will confirm uncertain low SNR redshifts and provide additional measures of the cool ISM in the galaxies.

Data analysis

Processing considerations: N/A

Data products: FITS images and cubes are the minimal requirements. Ultimately, catalogues of sources and spectroscopic features from the images and cubes will be needed, and matched between bands/datasets.

Data product fidelity: Astrometry should be stable enough for cross-matching between catalogues and datasets (including to optical/near-IR data): so $\lesssim 0.5''$. Photometry will be used for SED fitting, so calibrated at the 10% level, although with more stability between bands. The spectroscopic requirements are to measure redshifts and line luminosities, and therefore likely to be significantly less stringent than most programs.

Other considerations

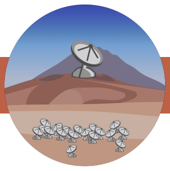

References

[1] A. Dressler. Galaxy morphology in rich clusters: implications for the formation and evolution of galaxies. *The Astrophysical Journal*, 236:351–365, March 1980. doi: 10.1086/157753.

[2] Richard S. Ellis, Ian Smail, Alan Dressler, Warrick J. Couch, Jr. Oemler, Augustus, Harvey Butcher, and Ray M. Sharples. The Homogeneity of Spheroidal Populations in Distant Clusters. *The Astrophysical Journal*, 483(2):582–596, July 1997. doi: 10.1086/304261.

[3] John P. Blakeslee, Marijn Franx, Marc Postman, Piero Rosati, Brad P. Holden, G. D. Illingworth, H. C. Ford, N. J. G. Cross, C. Gronwall, N. Benítez, R. J. Bouwens, T. J. Broadhurst, M. Clampin, R. Demarco, D. A. Golimowski, G. F. Hartig, L. Infante, A. R. Martel, G. K. Miley, F. Menanteau, G. R. Meurer, M. Sirianni, and R. L. White. Advanced Camera for Surveys Photometry of the Cluster RDCS 1252.9-2927: The Color-Magnitude Relation at z = 1.24. *The Astrophysical Journal, Letters*, 596(2):L143–L146, October 2003. doi: 10.1086/379234.

[4] S. J. Lilly, L. Tresse, F. Hammer, David Crampton, and O. Le Fevre. The Canada-France Redshift Survey. VI. Evolution of the Galaxy Luminosity Function to Z approximately 1. *The Astrophysical Journal*, 455: 108, December 1995. doi: 10.1086/176560.

[5] Stuart I. Muldrew, Nina A. Hatch, and Elizabeth A. Cooke. What are protoclusters? - Defining high-redshift galaxy clusters and protoclusters. *Monthly Notices of the Royal Astronomical Society*, 452(3): 2528–2539, September 2015. doi: 10.1093/mnras/stv1449.

[6] Donald G. York, J. Adelman, Jr. Anderson, John E., Scott F. Anderson, James Annis, Neta A. Bahcall, J. A. Bakken, Robert Barkhouser, Steven Bastian, Eileen Berman, William N. Boroski, Steve Bracker, Charlie Briegel, John W. Briggs, J. Brinkmann, Robert Brunner, Scott Burles, Larry Carey, Michael A. Carr, Francisco J. Castander, Bing Chen, Patrick L. Colestock, A. J. Connolly, J. H. Crocker, István Csabai, Paul C. Czarapata, John Eric Davis, Mamoru Doi, Tom Dombeck, Daniel Eisenstein, Nancy Ellman, Brian R. Elms, Michael L. Evans, Xiaohui Fan, Glenn R. Federwitz, Larry Fiscelli, Scott Friedman, Joshua A. Frieman, Masataka Fukugita, Bruce Gillespie, James E. Gunn, Vijay K. Gurbani, Ernst de Haas, Merle Haldeman, Frederick H. Harris, J. Hayes, Timothy M. Heckman, G. S. Hennessy, Robert B. Hindsley, Scott Holm, Donald J. Holmgren, Chi-hao Huang, Charles Hull, Don Husby, Shin-Ichi Ichikawa, Takashi Ichikawa, Željko Ivezić, Stephen Kent, Rita S. J. Kim, E. Kinney, Mark Klaene, A. N. Kleinman, S. Kleinman, G. R. Knapp, John Korienek, Richard G. Kron, Peter Z. Kunszt, D. Q. Lamb, B. Lee, R. French Leger, Siriluk Limmongkol, Carl Lindenmeyer, Daniel C. Long, Craig Loomis, Jon Loveday, Rich Lucinio, Robert H. Lupton, Bryan MacKinnon, Edward J. Mannery, P. M. Mantsch, Bruce Margon, Peregrine McGehee, Timothy A. McKay, Avery Meiksin, Aronne Merelli, David G. Monet, Jeffrey A. Munn, Vijay K. Narayanan, Thomas Nash, Eric Neilsen, Rich Neswold, Heidi Jo Newberg, R. C. Nichol, Tom Nicinski, Mario Nonino, Norio Okada, Sadanori Okamura, Jeremiah P. Ostriker, Russell Owen, A. George Pauls, John Peoples, R. L. Peterson, Donald Petravick, Jeffrey R. Pier, Adrian Pope, Ruth Pordes, Angela Prosapio, Ron Rechenmacher, Thomas R. Quinn, Gordon T. Richards, Michael W. Richmond, Claudio H. Rivetta, Constance M. Rockosi, Kurt Ruthmansdorfer, Dale Sandford, David J. Schlegel, Donald P. Schneider, Maki Sekiguchi, Gary Sergey, Kazuhiro Shimasaku, Walter A. Siegmund, Stephen Smee, J. Allyn Smith, S. Snedden, R. Stone, Chris Stoughton, Michael A. Strauss, Christopher Stubbs, Mark SubbaRao, Alexander S. Szalay, Istvan Szapudi, Gyula P. Szokoly, Anirudda R. Thakar, Christy Tremonti, Douglas L. Tucker, Alan Uomoto, Dan Vanden Berk, Michael S. Vogeley, Patrick Waddell, Shu-i. Wang, Masaru Watanabe, David H. Weinberg, Brian Yanny, Naoki Yasuda, and SDSS Collaboration. The Sloan Digital Sky Survey: Technical Summary. *The Astronomical Journal*, 120(3):1579–1587, September 2000. doi: 10.1086/301513.

[7] J. Brinchmann, S. Charlot, S. D. M. White, C. Tremonti, G. Kauffmann, T. Heckman, and J. Brinkmann. The physical properties of star-forming galaxies in the low-redshift Universe. *Monthly Notices of the Royal Astronomical Society*, 351(4):1151–1179, July 2004. doi: 10.1111/j.1365-2966.2004.07881.x.

[8] Guinevere Kauffmann, Timothy M. Heckman, Simon D. M. White, Stéphane Charlot, Christy Tremonti, Jarle Brinchmann, Gustavo Bruzual, Eric W. Peng, Mark Seibert, Mariangela Bernardi, Michael Blanton, Jon Brinkmann, Francisco Castander, Istvan Csábai, Masataka Fukugita, Zeljko Ivezic, Jeffrey A. Munn, Robert C. Nichol, Nikhil Padmanabhan, Aniruddha R. Thakar, David H. Weinberg, and Donald York. Stellar masses and star formation histories for 10^5 galaxies from the Sloan Digital Sky Survey. *Monthly Notices of the Royal Astronomical Society*, 341(1):33–53, May 2003. doi: 10.1046/j.1365-8711.2003.06291.x.

[9] I. K. Baldry, M. L. Balogh, R. G. Bower, K. Glazebrook, R. C. Nichol, S. P. Bamford, and T. Budavari. Galaxy bimodality versus stellar mass and environment. *Monthly Notices of the Royal Astronomical Society*, 373(2):469–483, December 2006. doi: 10.1111/j.1365-2966.2006.11081.x.

[10] Ying-jie Peng, Simon J. Lilly, Katarina Kovač, Micol Bolzonella, Lucia Pozzetti, Alvio Renzini, Gianni Zamorani, Olivier Ilbert, Christian Knobel, Angela Iovino, Christian Maier, Olga Cucciati, Lidia Tasca, C. Marcella Carollo, John Silverman, Pawel Kampczyk, Loic de Ravel, David Sanders, Nicholas Scoville, Thierry Contini, Vincenzo Mainieri, Marco Scodeggio, Jean-Paul Kneib, Olivier Le Fèvre, Sandro Bardelli, Angela Bongiorno, Karina Caputi, Graziano Coppa, Sylvain de la Torre, Paolo Franzetti, Bianca Garilli, Fabrice Lamareille, Jean-Francois Le Borgne, Vincent Le Brun, Marco Mignoli, Enrique Perez Montero, Roser Pello, Elena Ricciardelli, Masayuki Tanaka, Laurence Tresse, Daniela Vergani, Niraj Welikala, Elena Zucca, Pascal Oesch, Ummi Abbas, Luke Barnes, Rongmon Bordoloi, Dario Bottini, Alberto Cappi, Paolo Cassata, Andrea Cimatti, Marco Fumana, Gunther Hasinger, Anton Koekemoer, Alexei Leauthaud, Dario Maccagni, Christian Marinoni, Henry McCracken, Pierdomenico Memeo, Baptiste Meneux, Preethi Nair, Cristiano Porciani, Valentina Presotto, and Roberto Scaramella. Mass and Environment as Drivers of Galaxy Evolution in SDSS and zCOSMOS and the Origin of the Schechter Function. *The Astrophysical Journal*, 721(1):193–221, September 2010. doi: 10.1088/0004-637X/721/1/193.

[11] Pamela D. Klaassen, Tony K. Mroczkowski, Claudia Cicone, Evanthia Hatziminaoglou, Sabrina Sartori, Carlos De Breuck, Sean Bryan, Simon R. Dicker, Carlos Duran, Chris Groppi, Hans Kaercher, Ryohei Kawabe, Kotaro Kohno, and James Geach. The Atacama Large Aperture Submillimeter Telescope (AtLAST). In *Society of Photo-Optical Instrumentation Engineers (SPIE) Conference Series*, volume 11445 of *Society of Photo-Optical Instrumentation Engineers (SPIE) Conference Series*, page 114452F, December 2020. doi: 10.1117/12.2561315.

[12] Sean Bryan, Jason Austermann, Daniel Ferrusca, Philip Mauskopf, Jeff McMahon, Alfredo Montaña, Sara Simon, Giles Novak, David Sánchez-Argüelles, and Grant Wilson. Optical design of the TolTEC millimeter-wave camera. In Jonas Zmuidzinas and Jian-Rong Gao, editors, *Millimeter, Submillimeter, and Far-Infrared Detectors and Instrumentation for Astronomy IX*, volume 10708 of *Society of Photo-Optical Instrumentation Engineers (SPIE) Conference Series*, page 107080J, July 2018. doi: 10.1117/12.2314130.

[13] Christopher Groppi, Andrey Baryshev, Urs Graf, Martina Wiedner, Pamela Klaassen, and Tony Mroczkowski. First Generation Heterodyne Instrumentation Concepts for the Atacama Large Aperture Submillimeter Telescope. *arXiv e-prints*, art. arXiv:1907.03479, July 2019.

[14] Sean Bryan, James Aguirre, George Che, Simon Doyle, Daniel Flanigan, Christopher Groppi, Bradley Johnson, Glenn Jones, Philip Mauskopf, Heather McCarrick, Alessandro Monfardini, and Tony Mroczkowski. WSPEC: A Waveguide Filter-Bank Focal Plane Array Spectrometer for Millimeter Wave Astronomy and Cosmology. *Journal of Low Temperature Physics*, 184(1-2):114–122, July 2016. doi: 10.1007/s10909-015-1396-5.

References

Adams S. M., Martini P., Croxall K. V., Overzier R. A., Silverman J. D., 2015, MNRAS, 448, 1335

Alberts S., Noble A., 2022, Universe, 8, 554

Alexander D. M., Bauer F. E., Chapman S. C., Smail I., Blain A. W., Brandt W. N., Ivison R. J., 2005, ApJ, 632, 736

Angulo R. E., Springel V., White S. D. M., Cole S., Jenkins A., Baugh C. M., Frenk C. S., 2012, MNRAS, 425, 2722

Arsenault R., et al., 2008, in Hubin N., Max C. E., Wizinowich P. L., eds, Society of Photo-Optical Instrumentation Engineers (SPIE) Conference Series Vol. 7015, Adaptive Optics Systems. p. 701524, doi:10.1117/12.790359

Bañados E., Venemans B., Walter F., Kurk J., Overzier R., Ouchi M., 2013, ApJ, 773, 178

Baldwin J. A., Phillips M. M., Terlevich R., 1981, The Publications of the Astronomical Society of the Pacific, 93, 5

Balestra I., et al., 2010, A&A, 512, A12

Bardeen J. M., Steinhardt P. J., Turner M. S., 1983, Physical Review D, 28, 679

Barger A. J., Cowie L. L., Sanders D. B., Fulton E., Taniguchi Y., Sato Y., Kawara K., Okuda H., 1998, Nature, 394, 248

Barger A. J., Wang W. H., Cowie L. L., Owen F. N., Chen C. C., Williams J. P., 2012, ApJ, 761, 89

Barlow M. J., et al., 2010, A&A, 518, L138

Barthel P. D., Arnaud K. A., 1996, MNRAS, 283, L45

Baugh C. M., Cole S., Frenk C. S., Lacey C. G., 1998, ApJ, 498, 504

Baugh C. M., Lacey C. G., Frenk C. S., Granato G. L., Silva L., Bressan A., Benson A. J., Cole S., 2005, MNRAS, 356, 1191

Bayliss K. D., McMahon R. G., Venemans B. P., Ryan-Weber E. V., Lewis J. R., 2011, MNRAS, 413, 2883

Behroozi P. S., Wechsler R. H., Conroy C., 2013, ApJ, 770, 57

Bernardi M., Hyde J. B., Sheth R. K., Miller C. J., Nichol R. C., 2007, AJ, 133, 1741

Bertin E., 2006, in Gabriel C., Arviset C., Ponz D., Enrique S., eds, Astronomical Society of the Pacific Conference Series Vol. 351, Astronomical Data Analysis Software and Systems XV. p. 112

Bertin E., 2010, SWarp: Resampling and Co-adding FITS Images Together (ascl:1010.068)

Bertin E., Arnouts S., 1996, AAPS, 117, 393

Best P., Longair M., Rottgering H., 1997, in da Costa L. N., Renzini A., eds, Galaxy Scaling Relations: Origins, Evolution and Applications. p. 232 (`arXiv:astro-ph/9703055`), doi:10.48550/arXiv.astro-ph/9703055

Best P. N., Kauffmann G., Heckman T. M., Brinchmann J., Charlot S., Ivezić Ž., White S. D. M., 2005, MNRAS, 362, 25

Best P. N., von der Linden A., Kauffmann G., Heckman T. M., Kaiser C. R., 2007, MNRAS, 379, 894

Béthermin M., Dole H., Lagache G., Le Borgne D., Penin A., 2011, A&A, 529, A4

Bianchi S., 2013, A&A, 552, A89

Biggs A. D., et al., 2011, MNRAS, 413, 2314

Birkin J. E., et al., 2020, arXiv e-prints, p. arXiv:2009.03341

Birkin J. E., et al., 2021, MNRAS, 501, 3926

Blain A. W., Longair M. S., 1993, MNRAS, 264, 509

Blain A. W., Smail I., Ivison R. J., Kneib J. P., 1999, MNRAS, 302, 632

Blain A. W., Smail I., Ivison R. J., Kneib J. P., Frayer D. T., 2002, Physics Reports, 369, 111

Blain A. W., Chapman S. C., Smail I., Ivison R., 2004, ApJ, 611, 725

Blakeslee J. P., et al., 2003, ApJL, 596, L143

Blandford R., Meier D., Readhead A., 2019, Annual Review of Astron and Astrophys, 57, 467

Bleem L. E., et al., 2015, ApJS, 216, 27

Böhringer H., et al., 2001, A&A, 369, 826

Bolatto A. D., Wolfire M., Leroy A. K., 2013, Annual Review of Astron and Astrophys, 51, 207

Bond J. R., Kofman L., Pogosyan D., 1996, Nature, 380, 603

Bower R. G., Lucey J. R., Ellis R. S., 1992, MNRAS, 254, 601

Bower R. G., Benson A. J., Malbon R., Helly J. C., Frenk C. S., Baugh C. M., Cole S., Lacey C. G., 2006, MNRAS, 370, 645

Bower R. G., Benson A. J., Crain R. A., 2012, MNRAS, 422, 2816

Boylan-Kolchin M., Springel V., White S. D. M., Jenkins A., Lemson G., 2009, MNRAS, 398, 1150

Bradley L., et al., 2022, astropy/photutils:, doi:10.5281/zenodo.6385735, `https://doi.org/10.5281/zenodo.6385735`

Brammer G. B., van Dokkum P. G., Coppi P., 2008, ApJ, 686, 1503

Brinchmann J., Charlot S., White S. D. M., Tremonti C., Kauffmann G., Heckman T., Brinkmann J., 2004, MNRAS, 351, 1151

Bunker A. J., Warren S. J., Hewett P. C., Clements D. L., 1995, MNRAS, 273, 513

Butcher H., Oemler A. J., 1984, ApJ, 285, 426

Byrd G., Valtonen M., 1990, ApJ, 350, 89

Calhau J., Sobral D., Stroe A., Best P., Smail I., Lehmer B., Harrison C., Thomson A., 2017, MNRAS, 464, 303

Calvi R., Vulcani B., Poggianti B. M., Moretti A., Fritz J., Fasano G., 2018, MNRAS, 481, 3456

Calvi R., Dannerbauer H., Arrabal Haro P., Rodríguez Espinosa J. M., Muñoz-Tuñón C., Pérez González P. G., Geier S., 2021, MNRAS, 502, 4558

Calvi R., Castignani G., Dannerbauer H., 2023, arXiv e-prints, p. arXiv:2302.10323

Calzetti D., Armus L., Bohlin R. C., Kinney A. L., Koornneef J., Storchi-Bergmann T., 2000, ApJ, 533, 682

Capak P. L., et al., 2011, Nature, 470, 233

Cardamone C. N., et al., 2010, ApJS, 189, 270

Casali M., et al., 2006, in McLean I. S., Iye M., eds, Society of Photo-Optical Instrumentation Engineers (SPIE) Conference Series Vol. 6269, Society of Photo-Optical Instrumentation Engineers (SPIE) Conference Series. p. 62690W, doi:10.1117/12.670150

Casey C. M., 2016, ApJ, 824, 36

Casey C. M., et al., 2013, MNRAS, 436, 1919

Casey C. M., Narayanan D., Cooray A., 2014, Physics Reports, 541, 45

Casey C. M., et al., 2015, ApJL, 808, L33

Cazaux S., Minissale M., Dulieu F., Hocuk S., 2016, A&A, 585, A55

Chabrier G., 2003, The Publications of the Astronomical Society of the Pacific, 115, 763

Chapin E. L., et al., 2009, MNRAS, 398, 1793

Chapman S. C., et al., 2005, ApJ, 622, 772

Chapman S. C., Blain A., Ibata R., Ivison R. J., Smail I., Morrison G., 2009, ApJ, 691, 560

Chen C.-C., et al., 2022, ApJ, 929, 159

Chiang Y.-K., Overzier R., Gebhardt K., 2013, ApJ, 779, 127

Chiang Y.-K., et al., 2015, ApJ, 808, 37

Chiang Y.-K., et al., 2017, ApJL, 844, L23

Cochrane R. K., Best P. N., Sobral D., Smail I., Wake D. A., Stott J. P., Geach J. E., 2017, MNRAS, 469, 2913

Cole S., Lacey C. G., Baugh C. M., Frenk C. S., 2000, MNRAS, 319, 168

Cole S., et al., 2005, MNRAS, 362, 505

Colín P., Klypin A. A., Kravtsov A. V., Khokhlov A. M., 1999, ApJ, 523, 32

Condon J. J., 1992, Annual Review of Astron and Astrophys, 30, 575

Cooke E. A., Hatch N. A., Muldrew S. I., Rigby E. E., Kurk J. D., 2014, MNRAS, 440, 3262

Cooper M. C., et al., 2008, MNRAS, 383, 1058

Coppin K., et al., 2006, MNRAS, 372, 1621

Cresci G., et al., 2015, ApJ, 799, 82

Croton D. J., et al., 2006, MNRAS, 365, 11

Cucciati O., et al., 2014, A&A, 570, A16

Cui Y., Xiang Y., Rong K., Feris R., Cao L., 2014. pp 213–219, doi:10.1109/WACV.2014.6836098

Daddi E., et al., 2007, ApJ, 670, 156

Daddi E., et al., 2009, ApJ, 694, 1517

Damen M., et al., 2011, ApJ, 727, 1

Danielson A. L. R., et al., 2017, ApJ, 840, 78

Dannerbauer H., et al., 2019, Bulletin of the American Astronomical Society, 51, 293

Darvish B., Mobasher B., Sobral D., Rettura A., Scoville N., Faisst A., Capak P., 2016, ApJ, 825, 113

Dashyan G., Choi E., Somerville R. S., Naab T., Quirk A. C. N., Hirschmann M., Ostriker J. P., 2019, MNRAS, 487, 5889

Davé R., Finlator K., Oppenheimer B. D., Fardal M., Katz N., Kereš D., Weinberg D. H., 2010, MNRAS, 404, 1355

Davies L. J. M., Bremer M. N., Stanway E. R., Husband K., Lehnert M. D., Mannering E. J. A., 2014, MNRAS, 438, 2732

Davis M., Efstathiou G., Frenk C. S., White S. D. M., 1985, ApJ, 292, 371

De Breuck C., et al., 2004, A&A, 424, 1

De Breuck C., et al., 2010, ApJ, 725, 36

De Lucia G., Blaizot J., 2007, MNRAS, 375, 2

De Lucia G., et al., 2004, ApJL, 610, L77

De Lucia G., Springel V., White S. D. M., Croton D., Kauffmann G., 2006, MNRAS, 366, 499

De Lucia G., et al., 2007, MNRAS, 374, 809

Dekel A., Birnboim Y., 2006, MNRAS, 368, 2

Dekel A., Silk J., 1986, ApJ, 303, 39

Dekel A., et al., 2009, Nature, 457, 451

Dey A., van Breugel W., Vacca W. D., Antonucci R., 1997, ApJ, 490, 698

Diener C., et al., 2013, ApJ, 765, 109

Diener C., et al., 2015, ApJ, 802, 31

Ding X., et al., 2020, ApJ, 888, 37

Donoso E., Li C., Kauffmann G., Best P. N., Heckman T. M., 2010, MNRAS, 407, 1078

Dressler A., 1980, ApJ, 236, 351

Dubinski J., 1998, ApJ, 502, 141

Dudzevičiūtė U., et al., 2020, MNRAS, 494, 3828

Dunne L., et al., 2009, MNRAS, 394, 1307

Elbaz D., Cesarsky C. J., Chanial P., Aussel H., Franceschini A., Fadda D., Chary R. R., 2002, A&A, 384, 848

Elbaz D., et al., 2007, A&A, 468, 33

Ellis R. S., Smail I., Dressler A., Couch W. J., Oemler Augustus J., Butcher H., Sharples R. M., 1997, ApJ, 483, 582

Fakhouri O., Ma C.-P., Boylan-Kolchin M., 2010, MNRAS, 406, 2267

Falder J. T., et al., 2010, MNRAS, 405, 347

Falder J. T., et al., 2011, ApJ, 735, 123

Faucher-Giguère C.-A., Kereš D., Ma C.-P., 2011, MNRAS, 417, 2982

Ferrarotti A. S., Gail H. P., 2006, A&A, 447, 553

Finkelstein S. L., Rhoads J. E., Malhotra S., Grogin N., Wang J., 2008, ApJ, 678, 655

Finkelstein S. L., et al., 2022, ApJ, 928, 52

Fixsen D. J., Dwek E., Mather J. C., Bennett C. L., Shafer R. A., 1998, ApJ, 508, 123

Förster Schreiber N. M., et al., 2018, ApJS, 238, 21

Fritz J., Franceschini A., Hatziminaoglou E., 2006, MNRAS, 366, 767

Galametz A., et al., 2012, ApJ, 749, 169

Gao Y., Solomon P. M., 2004, ApJ, 606, 271

Gao L., Loeb A., Peebles P. J. E., White S. D. M., Jenkins A., 2004, ApJ, 614, 17

García-Vergara C., Hodge J., Hennawi J. F., Weiss A., Wardlow J., Myers A. D., Hickox R., 2020, ApJ, 904, 2

Garn T., et al., 2010, MNRAS, 402, 2017

Gavazzi R., Adami C., Durret F., Cuillandre J. C., Ilbert O., Mazure A., Pelló R., Ulmer M. P., 2009, A&A, 498, L33

Gawiser E., et al., 2006a, ApJS, 162, 1

Gawiser E., et al., 2006b, ApJL, 642, L13

Gawiser E., et al., 2007, ApJ, 671, 278

Geach J. E., Smail I., Best P. N., Kurk J., Casali M., Ivison R. J., Coppin K., 2008, MNRAS, 388, 1473

Geach J. E., et al., 2016, ApJ, 832, 37

Geach J. E., et al., 2017, MNRAS, 465, 1789

Geach J., et al., 2019, Bulletin of the American Astronomical Society, 51, 549

Gehrz R., 1989, in Allamandola L. J., Tielens A. G. G. M., eds, Vol. 135, Interstellar Dust. p. 445

Gilbank D. G., Yee H. K. C., Ellingson E., Gladders M. D., Loh Y. S., Barrientos L. F., Barkhouse W. A., 2008, ApJ, 673, 742

Gilbank D. G., Gladders M. D., Yee H. K. C., Hsieh B. C., 2011, AJ, 141, 94

Gladders M. D., Yee H. K. C., 2000, AJ, 120, 2148

Gladders M. D., Yee H. K. C., 2005, ApJS, 157, 1

Glenn J., et al., 2010, MNRAS, 409, 109

González V., Labbé I., Bouwens R. J., Illingworth G., Franx M., Kriek M., Brammer G. B., 2010, ApJ, 713, 115

Greve T. R., Stern D., Ivison R. J., De Breuck C., Kovács A., Bertoldi F., 2007, MNRAS, 382, 48

Guaita L., et al., 2010, ApJ, 714, 255

Gunn J. E., Gott J. Richard I., 1972, ApJ, 176, 1

Guth A. H., Pi S. Y., 1982, Physical Review Letters, 49, 1110

Hainline L. J., Blain A. W., Smail I., Alexander D. M., Armus L., Chapman S. C., Ivison R. J., 2011, ApJ, 740, 96

Hall K. R., Crichton D., Marriage T., Zakamska N. L., Mandelbaum R., 2018, MNRAS, 480, 149

Han J., et al., 2015, MNRAS, 446, 1356

Hasselfield M., et al., 2013, Journal of Cosmology and Astroparticle Physics, 2013, 008

Hatch N. A., et al., 2011a, MNRAS, 410, 1537

Hatch N. A., Kurk J. D., Pentericci L., Venemans B. P., Kuiper E., Miley G. K., Röttgering H. J. A., 2011b, MNRAS, 415, 2993

Hatch N. A., et al., 2014, MNRAS, 445, 280

Hauser M. G., et al., 1998, ApJ, 508, 25

Hayashi M., Kodama T., Tadaki K.-i., Koyama Y., Tanaka I., 2012, ApJ, 757, 15

Hayashi M., et al., 2018, Publications of the Astronomical Society of Japan, 70, S17

Hayashi M., et al., 2020, Publications of the Astronomical Society of Japan, 72, 86

Hayashino T., et al., 2004, AJ, 128, 2073

Hayward C. C., Narayanan D., Kereš D., Jonsson P., Hopkins P. F., Cox T. J., Hernquist L., 2013, MNRAS, 428, 2529

Hennawi J. F., Prochaska J. X., Cantalupo S., Arrigoni-Battaia F., 2015, Science, 348, 779

Henry J. P., Mullis C. R., Voges W., Böhringer H., Briel U. G., Gioia I. M., Huchra J. P., 2006, ApJS, 162, 304

Hickox R. C., et al., 2012, MNRAS, 421, 284

Hilbert B., et al., 2016, ApJS, 225, 12

Hildebrand R. H., 1983, Quarterly Journal of the Royal Astronomical Society, 24, 267

Hildebrandt H., et al., 2006, A&A, 452, 1121

Hill R., et al., 2020, MNRAS, 495, 3124

Ho M., Ntampaka M., Rau M. M., Chen M., Lansberry A., Ruehle F., Trac H., 2022, Nature Astronomy, 6, 936

Hodge J. A., et al., 2013a, ApJ, 768, 91

Hodge J. A., Carilli C. L., Walter F., Daddi E., Riechers D., 2013b, ApJ, 776, 22

Hoekstra H., Bartelmann M., Dahle H., Israel H., Limousin M., Meneghetti M., 2013, Space Science Reviews, 177, 75

Hopkins P. F., Hernquist L., Cox T. J., Kereš D., 2008, ApJS, 175, 356

Hopkins P. F., Quataert E., Murray N., 2012, MNRAS, 421, 3522

Hsieh B.-C., Wang W.-H., Hsieh C.-C., Lin L., Yan H., Lim J., Ho P. T. P., 2012, ApJS, 203, 23

Hu E. M., Cowie L. L., Barger A. J., Capak P., Kakazu Y., Trouille L., 2010, ApJ, 725, 394

Hubble E. P., 1926, ApJ, 64, 321

Hubble E., 1929, Proceedings of the National Academy of Science, 15, 168

Hughes D. H., et al., 1998, Nature, 394, 241

Husband K., Bremer M. N., Stanway E. R., Davies L. J. M., Lehnert M. D., Douglas L. S., 2013, MNRAS, 432, 2869

Hwang H. S., et al., 2010, MNRAS, 409, 75

Ikarashi S., et al., 2015, ApJ, 810, 133

Intema H. T., Venemans B. P., Kurk J. D., Ouchi M., Kodama T., Röttgering H. J. A., Miley G. K., Overzier R. A., 2006, A&A, 456, 433

Ito K., et al., 2023, arXiv e-prints, p. arXiv:2301.08845

Ivison R. J., et al., 2000, ApJ, 542, 27

Ivison R. J., et al., 2002, MNRAS, 337, 1

Ivison R. J., et al., 2004, ApJS, 154, 124

Ivison R. J., et al., 2005, MNRAS, 364, 1025

Ivison R. J., et al., 2007, MNRAS, 380, 199

Ivison R. J., et al., 2013, ApJ, 772, 137

Izquierdo-Villalba D., Orsi Á. A., Bonoli S., Lacey C. G., Baugh C. M., Griffin A. J., 2018, MNRAS, 480, 1340

Jaffé Y. L., Aragón-Salamanca A., De Lucia G., Jablonka P., Rudnick G., Saglia R., Zaritsky D., 2011, MNRAS, 410, 280

Kajisawa M., Kodama T., Tanaka I., Yamada T., Bower R., 2006, MNRAS, 371, 577

Karouzos M., Jarvis M. J., Bonfield D., 2014, MNRAS, 439, 861

Kashikawa N., Kitayama T., Doi M., Misawa T., Komiyama Y., Ota K., 2007, ApJ, 663, 765

Kauffmann G., Heckman T. M., Best P. N., 2008, MNRAS, 384, 953

Kennicutt R. C. J., 1983, ApJ, 272, 54

Kennicutt Robert C. J., 1998, Annual Review of Astron and Astrophys, 36, 189

Kennicutt Robert C. J., De Los Reyes M. A. C., 2021, ApJ, 908, 61

Kennicutt R. C., Evans N. J., 2012, Annual Review of Astron and Astrophys, 50, 531

Kereš D., Katz N., Weinberg D. H., Davé R., 2005, MNRAS, 363, 2

Khostovan A. A., et al., 2015, MNRAS, 452, 3948

Khostovan A. A., Sobral D., Mobasher B., Smail I., Darvish B., Nayyeri H., Hemmati S., Stott J. P., 2016, MNRAS, 463, 2363

Khostovan A. A., et al., 2020, MNRAS, 493, 3966

Kim S., et al., 2009, ApJ, 695, 809

Kissler-Patig M., et al., 2008, A&A, 491, 941

Klaassen P. D., et al., 2020, in Marshall H. K., Spyromilio J., Usuda T., eds, Society of Photo-Optical Instrumentation Engineers (SPIE) Conference Series Vol. 11445, Ground-based and Airborne Telescopes VIII. p. 114452F (`arXiv:2011.07974`), doi:10.1117/12.2561315

Kleiner D., Pimbblet K. A., Jones D. H., Koribalski B. S., Serra P., 2017, MNRAS, 466, 4692

Kodama T., Arimoto N., Barger A. J., Aragón-Salamanca A., 1998, A&A, 334, 99

Kormendy J., Ho L. C., 2013, Annual Review of Astron and Astrophys, 51, 511

Koyama Y., Kodama T., Tadaki K.-i., Hayashi M., Tanaka M., Smail I., Tanaka I., Kurk J., 2013, MNRAS, 428, 1551

Kravtsov A. V., Klypin A. A., 1999, ApJ, 520, 437

Kravtsov A. V., Berlind A. A., Wechsler R. H., Klypin A. A., Gottlöber S., Allgood B., Primack J. R., 2004, ApJ, 609, 35

Kriek M., Conroy C., 2013, ApJL, 775, L16

Kuiper E., et al., 2011a, MNRAS, 415, 2245

Kuiper E., et al., 2011b, MNRAS, 417, 1088

Kurk J. D., et al., 2000, A&A, 358, L1

Lacey C. G., Baugh C. M., Frenk C. S., Silva L., Granato G. L., Bressan A., 2008, MNRAS, 385, 1155

Lacey C. G., Baugh C. M., Frenk C. S., Benson A. J., Orsi A., Silva L., Granato G. L., Bressan A., 2010, MNRAS, 405, 2

Lagos C. d. P., Tobar R. J., Robotham A. S. G., Obreschkow D., Mitchell P. D., Power C., Elahi P. J., 2018, MNRAS, 481, 3573

Lawrence A., et al., 2007, MNRAS, 379, 1599

Le Fèvre O., et al., 2005, A&A, 439, 845

Lehmer B. D., et al., 2005, ApJS, 161, 21

Lehmer B. D., et al., 2009, MNRAS, 400, 299

Lemaître G., 1927, Annales de la Société Scientifique de Bruxelles, 47, 49

Lemaux B. C., et al., 2014, A&A, 572, A41

Lemaux B. C., et al., 2018, A&A, 615, A77

Lemaux B. C., et al., 2022, A&A, 662, A33

Lidman C., Rosati P., Demarco R., Nonino M., Mainieri V., Stanford S. A., Toft S., 2004, A&A, 416, 829

Lilly S. J., Eales S. A., Gear W. K. P., Hammer F., Le Fèvre O., Crampton D., Bond J. R., Dunne L., 1999, ApJ, 518, 641

Lin Y.-T., Mohr J. J., 2004, ApJ, 617, 879

Long A. S., et al., 2020, ApJ, 898, 133

Lutz D., Spoon H. W. W., Rigopoulou D., Moorwood A. F. M., Genzel R., 1998, ApJL, 505, L103

Ly C., et al., 2007, ApJ, 657, 738

Ly C., Lee J. C., Dale D. A., Momcheva I., Salim S., Staudaher S., Moore C. A., Finn R., 2011, ApJ, 726, 109

Madau P., Dickinson M., 2014, Annual Review of Astron and Astrophys, 52, 415

Magnelli B., et al., 2012, A&A, 539, A155

Man Z.-Y., Peng Y.-J., Shi J.-J., Kong X., Zhang C.-P., Dou J., Guo K.-X., 2019, ApJ, 881, 74

Martín-Navarro I., Pillepich A., Nelson D., Rodriguez-Gomez V., Donnari M., Hernquist L., Springel V., 2021, Nature, 594, 187

Martinet N., et al., 2015, A&A, 575, A116

Matsuda Y., et al., 2011, MNRAS, 416, 2041

McBride J., Fakhouri O., Ma C.-P., 2009, MNRAS, 398, 1858

Mei S., et al., 2009, ApJ, 690, 42

Mei S., et al., 2023, A&A, 670, A58

Merten J., et al., 2015, ApJ, 806, 4

Miettinen O., et al., 2017, A&A, 606, A17

Miley G., De Breuck C., 2008, The Astronomy and Astrophysics Review, 15, 67

Miley G. K., et al., 2004, Nature, 427, 47

Miller N. A., et al., 2013, ApJS, 205, 13

Miller T. B., Hayward C. C., Chapman S. C., Behroozi P. S., 2015, MNRAS, 452, 878

Miller T. B., et al., 2018, Nature, 556, 469

Molina J., Ibar E., Swinbank A. M., Sobral D., Best P. N., Smail I., Escala A., Cirasuolo M., 2017, MNRAS, 466, 892

Moore B., Katz N., Lake G., Dressler A., Oemler A., 1996, Nature, 379, 613

Moorwood A. F. M., van der Werf P. P., Cuby J. G., Oliva E., 2000, A&A, 362, 9

Morselli L., et al., 2014, A&A, 568, A1

Moster B. P., Somerville R. S., Maulbetsch C., van den Bosch F. C., Macciò A. V., Naab T., Oser L., 2010, ApJ, 710, 903

Moustakas L. A., Somerville R. S., 2002, ApJ, 577, 1

Muldrew S. I., Hatch N. A., Cooke E. A., 2015, MNRAS, 452, 2528

Muzzin A., et al., 2009, ApJ, 698, 1934

Muzzin A., et al., 2012, ApJ, 746, 188

Muzzin A., et al., 2013, ApJ, 777, 18

Narayanan D., Hayward C. C., Cox T. J., Hernquist L., Jonsson P., Younger J. D., Groves B., 2010, MNRAS, 401, 1613

Narayanan D., et al., 2015, Nature, 525, 496

Nesvadba N. P. H., Bicknell G. V., Mukherjee D., Wagner A. Y., 2020, A&A, 639, L13

Neugebauer G., et al., 1984, ApJL, 278, L1

Niemi S.-M., Somerville R. S., Ferguson H. C., Huang K.-H., Lotz J., Koekemoer A. M., 2012, MNRAS, 421, 1539

Nilsson K. K., Tapken C., Møller P., Freudling W., Fynbo J. P. U., Meisenheimer K., Laursen P., Östlin G., 2009, A&A, 498, 13

Ocvirk P., Pichon C., Teyssier R., 2008, MNRAS, 390, 1326

Oke J. B., Gunn J. E., 1983, ApJ, 266, 713

Osterbrock D. E., Ferland G. J., 2006, Astrophysics of gaseous nebulae and active galactic nuclei

Ouchi M., et al., 2005, ApJL, 620, L1

Ouchi M., et al., 2008, ApJS, 176, 301

Ouchi M., et al., 2010, ApJ, 723, 869

Overzier R. A., 2016, The Astronomy and Astrophysics Review, 24, 14

Overzier R. A., et al., 2006, ApJ, 637, 58

Overzier R. A., Guo Q., Kauffmann G., De Lucia G., Bouwens R., Lemson G., 2009, MNRAS, 394, 577

Pacaud F., et al., 2016, A&A, 592, A2

Padovani P., 2017, Frontiers in Astronomy and Space Sciences, 4, 35

Padovani P., et al., 2017, The Astronomy and Astrophysics Review, 25, 2

Palunas P., Teplitz H. I., Francis P. J., Williger G. M., Woodgate B. E., 2004, ApJ, 602, 545

Papovich C., et al., 2010, ApJ, 716, 1503

Papovich C., et al., 2018, ApJ, 854, 30

Paufique J., et al., 2010, in Ellerbroek B. L., Hart M., Hubin N., Wizinowich P. L., eds, Society of Photo-Optical Instrumentation Engineers (SPIE) Conference Series Vol. 7736, Adaptive Optics Systems II. p. 77361P, doi:10.1117/12.858261

Peebles P. J. E., 1982, ApJL, 263, L1

Peng Y., Maiolino R., Cochrane R., 2015, Nature, 521, 192

Penzias A. A., Wilson R. W., 1965, ApJ, 142, 419

Perlmutter S., et al., 1998, Nature, 391, 51

Pirard J.-F., et al., 2004, in Moorwood A. F. M., Iye M., eds, Society of Photo-Optical Instrumentation Engineers (SPIE) Conference Series Vol. 5492, Ground-based Instrumentation for Astronomy. pp 1763–1772, doi:10.1117/12.578293

Pirzkal N., et al., 2013, ApJ, 772, 48

Planck Collaboration 2020, A&A, 641, A6

Planck Collaboration et al., 2016, A&A, 594, A27

Pope A., et al., 2006, MNRAS, 370, 1185

Pope A., et al., 2008, ApJ, 675, 1171

Popesso P., et al., 2009, A&A, 494, 443

Postman M., et al., 2012, ApJS, 199, 25

Press W. H., Schechter P., 1974, ApJ, 187, 425

Puget J. L., et al., 1996, A&A, 308, L5

Ramakrishnan V., et al., 2023, ApJ, 951, 119

Ramasawmy J., et al., 2022, in Zmuidzinas J., Gao J.-R., eds, Society of Photo-Optical Instrumentation Engineers (SPIE) Conference Series Vol. 12190, Millimeter, Submillimeter, and Far-Infrared Detectors and Instrumentation for Astronomy XI. p. 1219007 (`arXiv:2207.03914`), doi:10.1117/12.2627505

Ramsay S. K., Mountain C. M., Geballe T. R., 1992, MNRAS, 259, 751

Reddick R. M., Wechsler R. H., Tinker J. L., Behroozi P. S., 2013, ApJ, 771, 30

Rees M. J., Ostriker J. P., 1977, MNRAS, 179, 541

Reines A. E., Volonteri M., 2015, ApJ, 813, 82

Rho J., et al., 2008, ApJ, 673, 271

Riess A. G., et al., 1998, AJ, 116, 1009

Rigby E. E., et al., 2014, MNRAS, 437, 1882

Rubin V. C., Ford W. K. J., Thonnard N., 1980, ApJ, 238, 471

Rudnick G., et al., 2009, ApJ, 700, 1559

Sanders D. B., Mirabel I. F., 1996, Annual Review of Astron and Astrophys, 34, 749

Sanders D. B., Soifer B. T., Elias J. H., Madore B. F., Matthews K., Neugebauer G., Scoville N. Z., 1988, ApJ, 325, 74

Sargent B. A., et al., 2010, ApJ, 716, 878

Schechter P., 1976, ApJ, 203, 297

Schinnerer E., et al., 2004, AJ, 128, 1974

Schreiber C., et al., 2015, A&A, 575, A74

Schwarzschild K., 1916, Sitzungsberichte der Deutschen Akademie der Wissenschaften, pp 189–196

Scoville N., et al., 2007, ApJS, 172, 1

Scoville N., et al., 2013, ApJS, 206, 3

Scoville N., et al., 2017, ApJ, 837, 150

Seymour N., et al., 2007, ApJS, 171, 353

Seymour N., et al., 2012, ApJ, 755, 146

Shimakawa R., et al., 2018, MNRAS, 481, 5630

Shimasaku K., et al., 2003, ApJL, 586, L111

Shin J., Woo J.-H., Chung A., Baek J., Cho K., Kang D., Bae H.-J., 2019, ApJ, 881, 147

Siebenmorgen R., Carraro G., Valenti E., Petr-Gotzens M., Brammer G., Garcia E., Casali M., 2011, The Messenger, 144, 9

Sikora M., Stawarz Ł., Lasota J.-P., 2007, ApJ, 658, 815

Silk J., Rees M. J., 1998, A&A, 331, L1

Sillassen N. B., et al., 2022, A&A, 665, L7

Silva L., Granato G. L., Bressan A., Danese L., 1998, ApJ, 509, 103

Silverman J. D., et al., 2010, ApJS, 191, 124

Simpson C., Mortlock D., Warren S., Cantalupo S., Hewett P., McLure R., McMahon R., Venemans B., 2014a, MNRAS, 442, 3454

Simpson J. M., et al., 2014b, ApJ, 788, 125

Simpson J. M., et al., 2015, ApJ, 799, 81

Simpson J. M., et al., 2019, ApJ, 880, 43

Simpson J. M., et al., 2020, MNRAS, 495, 3409

Slipher V. M., 1917, Proceedings of the American Philosophical Society, 56, 403

Smail I., Ivison R. J., Blain A. W., 1997, ApJL, 490, L5

Smail I., Edge A. C., Ellis R. S., Blandford R. D., 1998, MNRAS, 293, 124

Smolčić V., et al., 2009, ApJ, 696, 24

Smolčić V., et al., 2012, A&A, 548, A4

Smolčić V., et al., 2017a, A&A, 597, A4

Smolčić V., et al., 2017b, A&A, 602, A1

Smolčić V., et al., 2017c, A&A, 602, A2

Snyder G. F., et al., 2012, ApJ, 756, 114

Sobral D., et al., 2009, MNRAS, 398, 75

Sobral D., Best P. N., Matsuda Y., Smail I., Geach J. E., Cirasuolo M., 2012, MNRAS, 420, 1926

Sobral D., Smail I., Best P. N., Geach J. E., Matsuda Y., Stott J. P., Cirasuolo M., Kurk J., 2013, MNRAS, 428, 1128

Sobral D., Best P. N., Smail I., Mobasher B., Stott J., Nisbet D., 2014, MNRAS, 437, 3516

Sobral D., et al., 2015, MNRAS, 451, 2303

Soifer B. T., Neugebauer G., 1991, AJ, 101, 354

Solomon P. M., Vanden Bout P. A., 2005, Annual Review of Astron and Astrophys, 43, 677

Somerville R. S., et al., 2018, MNRAS, 473, 2714

Speagle J. S., Steinhardt C. L., Capak P. L., Silverman J. D., 2014, ApJS, 214, 15

Springel V., Di Matteo T., Hernquist L., 2005a, MNRAS, 361, 776

Springel V., et al., 2005b, Nature, 435, 629

Stach S. M., et al., 2019, MNRAS, 487, 4648

Stach S. M., et al., 2021, MNRAS, 504, 172

Staniszewski Z., et al., 2009, ApJ, 701, 32

Starobinsky A. A., 1982, Physics Letters B, 117, 175

Steidel C. C., Adelberger K. L., Dickinson M., Giavalisco M., Pettini M., Kellogg M., 1998, ApJ, 492, 428

Steidel C. C., Adelberger K. L., Shapley A. E., Pettini M., Dickinson M., Giavalisco M., 2000, ApJ, 532, 170

Steidel C. C., Adelberger K. L., Shapley A. E., Erb D. K., Reddy N. A., Pettini M., 2005, ApJ, 626, 44

Stevans M. L., et al., 2021, ApJ, 921, 58

Stevens J. A., et al., 2003, Nature, 425, 264

Stevens J. A., Jarvis M. J., Coppin K. E. K., Page M. J., Greve T. R., Carrera F. J., Ivison R. J., 2010, MNRAS, 405, 2623

Stiavelli M., et al., 2005, ApJL, 622, L1

Stott J. P., 2022, MNRAS, 511, 2659

Stott J. P., Smail I., Edge A. C., Ebeling H., Smith G. P., Kneib J. P., Pimbblet K. A., 2007, ApJ, 661, 95

Stott J. P., Edge A. C., Smith G. P., Swinbank A. M., Ebeling H., 2008, MNRAS, 384, 1502

Stott J. P., Pimbblet K. A., Edge A. C., Smith G. P., Wardlow J. L., 2009, MNRAS, 394, 2098

Stott J. P., et al., 2020, MNRAS, 497, 3083

Sunyaev R. A., Zeldovich Y. B., 1972, Comments on Astrophysics and Space Physics, 4, 173

Swinbank A. M., et al., 2014, MNRAS, 438, 1267

Tamura Y., et al., 2009, Nature, 459, 61

Tanaka M., Kodama T., Arimoto N., Okamura S., Umetsu K., Shimasaku K., Tanaka I., Yamada T., 2005, MNRAS, 362, 268

Tanaka I., et al., 2011, Publications of the Astronomical Society of Japan, 63, 415

Tasitsiomi A., Kravtsov A. V., Wechsler R. H., Primack J. R., 2004, ApJ, 614, 533

Taylor E. N., et al., 2009, ApJS, 183, 295

Toft S., et al., 2014, ApJ, 782, 68

Toshikawa J., et al., 2016, ApJ, 826, 114

Toshikawa J., et al., 2018, Publications of the Astronomical Society of Japan, 70, S12

Toshikawa J., Malkan M. A., Kashikawa N., Overzier R., Uchiyama H., Ota K., Ishikawa S., Ito K., 2020, ApJ, 888, 89

Trainor R. F., Steidel C. C., 2012, ApJ, 752, 39

Treister E., et al., 2009, ApJ, 693, 1713

Trimble V., 1995, The Publications of the Astronomical Society of the Pacific, 107, 1133

Truemper J., 1993, Science, 260, 1769

Uchiyama H., et al., 2022, ApJ, 926, 76

Umehata H., et al., 2015, ApJL, 815, L8

Umehata H., et al., 2019, Science, 366, 97

Vale A., Ostriker J. P., 2004, MNRAS, 353, 189

Venemans B. P., et al., 2002, ApJL, 569, L11

Venemans B. P., et al., 2005, A&A, 431, 793

Venemans B. P., et al., 2007, A&A, 461, 823

Viero M. P., et al., 2013, ApJ, 779, 32

Visvanathan N., Sandage A., 1977, ApJ, 216, 214

Von Der Linden A., Best P. N., Kauffmann G., White S. D. M., 2007, MNRAS, 379, 867

Walter F., et al., 2012, Nature, 486, 233

Wang S. X., et al., 2013, ApJ, 778, 179

Wardlow J. L., et al., 2011, MNRAS, 415, 1479

Weaver J. R., et al., 2022, ApJS, 258, 11

Wechsler R. H., Gross M. A. K., Primack J. R., Blumenthal G. R., Dekel A., 1998, ApJ, 506, 19

Weiß A., et al., 2009, ApJ, 707, 1201

Weiß A., et al., 2013, ApJ, 767, 88

White S. D. M., Frenk C. S., 1991, ApJ, 379, 52

White S. D. M., Rees M. J., 1978, MNRAS, 183, 341

Wilkinson A., et al., 2017, MNRAS, 464, 1380

Williamson R., et al., 2011, ApJ, 738, 139

Wilson A. S., Colbert E. J. M., 1995, ApJ, 438, 62

Wilson G., et al., 2009, ApJ, 698, 1943

Wold M., Armus L., Neugebauer G., Jarrett T. H., Lehnert M. D., 2003, AJ, 126, 1776

Wylezalek D., et al., 2013, ApJ, 769, 79

Yajima H., et al., 2022, MNRAS, 509, 4037

Yang Y., Zabludoff A., Eisenstein D., Davé R., 2010, ApJ, 719, 1654

Yuan T., et al., 2014, ApJL, 795, L20

Zavala J. A., et al., 2019, ApJ, 887, 183

Zheng X. Z., Cai Z., An F. X., Fan X., Shi D. D., 2021, MNRAS, 500, 4354

Zwicky F., 1933, Helvetica Physica Acta, 6, 110

da Cunha E., Charlot S., Elbaz D., 2008, MNRAS, 388, 1595

da Cunha E., et al., 2015, ApJ, 806, 110

van de Voort F., Schaye J., Booth C. M., Haas M. R., Dalla Vecchia C., 2011, MNRAS, 414, 2458

van der Burg R. F. J., Muzzin A., Hoekstra H., Wilson G., Lidman C., Yee H. K. C., 2014, A&A, 561, A79